

NORTHWESTERN UNIVERSITY

Understanding Atomic Structure and Structural Evolution of Perovskite Oxides at the 2-D Limit:  
From Surface to Thin Film

A DISSERTATION

SUBMITTED TO THE GRADUATE SCHOOL  
IN PARTIAL FULFILLMENT OF THE REQUIREMENTS

for the degree

DOCTOR OF PHILOSOPHY

Field of Materials Science and Engineering

By

Tassie K. Andersen

EVANSTON, ILLINOIS

September 2018

© Copyright by Tassie K. Andersen 2018

All Rights Reserved

## ABSTRACT

### Understanding Atomic Structure and Structural Evolution of Perovskite Oxides at the 2-D Limit: From Surface to Thin Film

Tassie K. Andersen

Perovskite oxide materials for the wide array of properties that make them candidate materials for application ranging from catalysis, to electronics, to beyond-Moore computation. As many of these oxides share similar structures they can be combined in a seemingly-endless number of ways to produce the desired properties for a given application. Understanding of their surface structures and interface formation during growth however, is an area not given enough attention, especially in a class of materials that relies heavily on interfaces to produce its unique properties. The objective of this dissertation is to present theories and tools for probing and understanding the atomic structure of perovskite materials at the 2-D limit (i.e. surfaces and thin films).

In this dissertation the applicability of Pauling's rules to prediction and determination of oxide surface structures is presented. Examples of solved surface reconstructions on  $\text{SrTiO}_3$  (1 0 0), (1 1 0), and (1 1 1) are considered as well as nanostructures on these surfaces and a few other  $\text{ABO}_3$  oxide materials. These rules are found to explain atomic arrangements for reconstructions and thin films just as they apply to bulk oxide materials. Using this data and Pauling's rules, the fundamental structural units of reconstructions and their arrangement are discussed.

Pauling's rules are applied to the  $\text{SrTiO}_3$  (1 1 1) surface to solve the atomic structures of two reconstructions,  $(\sqrt{7} \times \sqrt{7})\text{R}19.1^\circ$  and  $(\sqrt{13} \times \sqrt{13})\text{R}13.9^\circ$ . These structures were determined using a combination of density functional theory and scanning tunneling microscopy data and APW+lo density functional theory minimizations and simulations. These reconstructions belong

to the same structural family made up of an interconnected, single layer of edge-sharing  $\text{TiO}_6$  and  $\text{TiO}_5$  octahedra. This family is found to include the previously-solved  $(2 \times 2)_a$  reconstruction. This reconstruction family and the calculations of surface energies for different hypothesis structures also shed light on the structure of Schottky defects observed on these reconstructed  $\text{SrTiO}_3$  (1 1 1) surfaces.

Moving from surfaces to thin films, growth of strontium cobalt oxide thin films by molecular beam epitaxy, and conditions necessary to stabilize different defect concentration phases are reported. In situ X-ray scattering is used to monitor structural evolution during growth, while in situ X-ray absorption near-edge spectroscopy is used to probe oxidation state and measure changes to oxygen vacancy concentration as a function of film thickness. Experimental results are compared to kinetically-limited thermodynamic predictions, in particular, solute trapping, with semi-quantitative agreement. Agreement between observations of dependence of cobaltite phase on oxidation activity and deposition rate, and predictions indicates that a combined experimental/theoretical approach is key to understanding phase behavior in the strontium cobalt oxide system.

To facilitate studies of thin film structure, a portable metalorganic gas delivery system was designed and constructed to interface with an existing molecular beam epitaxy chamber at beamline 33-IDE of the Advanced Photon Source. This system offers the ability to perform in situ X-ray measurements of complex oxide growth via hybrid molecular beam epitaxy. Performance of the hybrid molecular beam epitaxy system while delivering metalorganic source materials is described. The high-energy X-ray scattering capabilities of the hybrid molecular beam epitaxy system are demonstrated both on oxide films grown solely from the metalorganic



source, and  $\text{ABO}_3$  oxide perovskites containing elements from both the metalorganic source and a traditional effusion cell.

Approved by

Professor Laurence D. Marks

Department of Materials Science and Engineering

Northwestern University, Evanston, IL 60208, U.S.A

## Acknowledgement

Firstly, I would like to thank my advisors, Laurence Marks and Dillon Fong. Without their support and encouragement over the years this dissertation would not be possible. I want to thank Laurie for his wholistic approach to research: his insistence on the importance of following the science and acquiring whatever skills and knowledge are necessary to do so have shaped my approach to experiments and broadened my views. I will always appreciate how he urged me to see connections between the different areas of my work and consider the forest as well as the trees. His curiosity and critical eye have been both invaluable and inspiring. I want to thank Dillon for his depth of knowledge in guiding me and the freedom in projects he trusted me with. He has also tolerated an astonishing amount of stupid questions, and I think him for many interesting discussions. His creative approaches to complicated problems have shown me different ways of tackling hard questions and he has been a wonderful resource in navigating the professional side of my career. I also would like to thank my thesis defense committee, Professor Michael Bedzyk, Dr. John Freeland, and Professor James Rondinelli for their valuable time and discussions.

I am exceptionally grateful to all my collaborators for their help in my Ph.D studies. First and foremost, I would like to thank my colleague Dr. Seyoung Cook for the countless hours of assistance during beamtimes and many fruitful discussions. Without his help, the many beamtimes this work relied upon would not have been pleasant or productive. I want to thank Dr. Yang Liu for his guidance in learning to operate the equipment at the beamlines and his expertise in oxide growth. I would also like to thank Dr. I-Cheng Tung for his advice and assistance during beamtimes as well as for sharing his wealth of knowledge in many discussion on X-ray methods and oxide growth. I would like to thank Dr. Hawoong Hong for his unfailing patience and

contributions to beamtimes, as well as his expertise. I would like to thank Erika Benda for her mechanical knowledge and for creating beautiful CAD renderings of the hybrid molecular beam epitaxy instrumentation. I would also like to thank Dr. Bharat Jalan, Dr. Roman Engel-Herbert, Dr. Matthew Brahlek, and Dr. Craig Eaton for their valuable insight into construction and troubleshooting of the hybrid system. Furthermore, I would like to thank my collaborator at Oxford University, Professor Martin Castell, for the experimental expertise and many years of back and forth with the thorny problems of various oxide reconstructions. I would also like to thank Shuqiu Wang at Oxford for her assistance with STM images and unfailing willingness to accommodate my most specific questions.

Without the assistance of many staff members at the Advanced Photon Source beamlines this work would have been far more difficult and much less enjoyable. I would like to thank Dr. Zhan Zhang, Evguenia Karapetrova, and Roger Ranay. They have all assisted with logistics, scheduling, questions, and at times have lent a helping wrench or screwdriver. I would also like to acknowledge the staff of the Department of Materials Science and Engineering who have always been attentive and swift in their responses.

I would also like to thank all the previous and current members of the Marks group for their friendship, conversation, and engaging company. Special thanks are due to Emily Hoffman for her enthusiasm in convincing me to join the group, and Pratik Koirala for his humor and patience with all things DFT-related. For their companionship, many all-you-can-eat sushi dinners, and general commiseration I thank Betty, Lawrence, Chris, Tiffany, Alex, and Zach.

The many friends I have made during my time at Northwestern in the graduate school community, department, and the Chicago area also deserve mention- without you the time spent outside of work would be bland and I appreciate all the color and fun you have brought me.

A special thanks goes to my partner Dale, who has been a source of encouragement and consistency in my life throughout these years. He has tolerated complaints, strange working hours, and sat through all manner of presentation practices with patience and encouragement. I am very grateful that he has been there to celebrate achievements and prop me up when I need it most. I look forward to everything yet to come.

Finally, I would like to thank my family. My brother Tom has provided me with the type of perspective that only an older brother can- leading by example while knowing exactly what to say to make me smile. Thank you to my mother and father who have always cared and listened, while supporting me in all academic and creative endeavors. Their drive has always inspired me to pursue my goals with my entire focus, and their perspective has always kept me grounded. I am forever grateful for all they have done.

I would also like to officially thank my funding. The work in Chapters Four and Five was used the Extreme Science and Engineering Discovery Environment (XSEDE), which is supported by National Science Foundation grant number ACI-1548562. Specifically, it used the Bridges system, which is supported by NSF award number ACI-1445606, at the Pittsburgh Supercomputing Center (PSC) through allocation DMR160023P. The work in Chapters Six, Seven, and Eight was performed at Argonne National Laboratory, including the Advanced Photon Source, was supported by the U.S. Department of Energy (DOE), Basic Energy Sciences, under Contract

No. DE-AC02-06CH11357. I was personally supported by the U.S. Department of Energy, Office of Science, Office of Basic Energy Sciences, Materials Sciences and Engineering Division.

## List of Abbreviations

DFT	Density Functional Theory
SXRD	Surface X-ray Diffraction
XAS	X-ray Absorption Spectroscopy
MBE	Molecular Beam Epitaxy
HMBE	Hybrid Molecular Beam Epitaxy
PLD	Pulsed Laser Deposition
UHV	Ultra-High Vacuum
APS	Advanced Photon Source
XANES	X-ray Absorption Near Edge Spectroscopy
QCM	Quartz Crystal Monitor
CTR	Crystal Truncation Rod
ML	Monolayer
LDA	Local Density Approximation
GGA	Generalized Gradient
PBE	Perdew-Burke-Ernzerhof
HF	Hartree Fock
STM	Scanning Tunneling Microscopy
BVS	Bond Valence Sum
DOS	Density of States
ED-TiO <sub>4</sub>	Edge-Displaying TiO <sub>4</sub>
FD-TiO <sub>4</sub>	Face-Displaying TiO <sub>4</sub>

TED	Transmission Electron Diffraction
RT13	$(\sqrt{13} \times \sqrt{13})R33.7^\circ$
RT7	$(\sqrt{7} \times \sqrt{7})R19.1^\circ$
SCO	Sr-Co-O
AFM	Atomic Force Microscopy
BM-SCO	Brownmillerite $\text{SrCoO}_{2.5}$
P-SCO	Perovskite $\text{SrCoO}_3$
326-SCO	$\text{Sr}_3\text{Co}_2\text{O}_{6+\delta}$
BL	Bilayer
LSAT	Lanthanum aluminate- strontium aluminum tantalate
RHEED	Reflection High Energy Electron Diffraction
RGA	Residual Gas Analyzer
PID	Proportional-Integral-Derivative
TTIP	Titanium (IV) Tetraisopropoxide (TTIP)
VTIP	Vanadium (V) Triisopropoxide
EPICS	Experimental Physics and Industrial Control System
GUI	Graphical User Interface
LabVIEW	Laboratory Virtual Instrument Engineering Workbench
XRD	X-ray Diffraction



## Table of Contents

<b>ABSTRACT .....</b>	<b>3</b>
<b>Acknowledgement .....</b>	<b>7</b>
<b>List of Abbreviations .....</b>	<b>11</b>
<b>List of Figures.....</b>	<b>19</b>
<b>Chapter 1: Introduction .....</b>	<b>28</b>
1.1 Motivation and Scope.....	29
1.2 Organization .....	33
<b>Chapter 2: Background.....</b>	<b>35</b>
2.1 Perovskites .....	36
2.2 Multivalent Transition Metals .....	37
2.3 Superlattices .....	38
2.4 Brownmillerite .....	39
2.5 Ruddlesden-Popper .....	41
2.6 Oxygen Vacancies in Perovskite Materials.....	42
2.7 Surface Structures .....	43
<b>Chapter 3: Methods .....</b>	<b>46</b>

	14
3.1 Experimental Methods .....	47
3.1.1 Oxide MBE.....	47
3.1.2 MBE Chamber for in situ X-Ray Diffraction Experiments.....	48
3.1.3 Surface X-Ray Diffraction.....	51
3.1.4 X-Ray Absorption Spectroscopy .....	53
3.2 Theoretical and Computational Methods .....	54
3.2.1 DFT Methods.....	54
3.2.2 STM Simulation .....	58
<b>Chapter 4: Pauling's Rules for Oxide Surfaces .....</b>	<b>62</b>
4.1 Introduction .....	63
4.2 Pauling's Rules.....	66
4.3 Case Analyses .....	69
4.3.1 SrTiO <sub>3</sub> (1 0 0): .....	70
4.3.2 SrTiO <sub>3</sub> (1 1 0): .....	73
4.3.3 SrTiO <sub>3</sub> (1 1 1): .....	77
4.3.4 From Reconstructed Surface to Thin Film: .....	83
4.3.5 BaTiO <sub>3</sub> (1 0 0): .....	89
4.3.6 LaAlO <sub>3</sub> (1 1 0): .....	91
4.4 Discussion .....	93
<b>Chapter 5: Single Ti-Layer Reconstructions on SrTiO<sub>3</sub> (1 1 1) - A</b>	
<b>Demonstration of Pauling's Rules .....</b>	<b>98</b>
5.1 Introduction .....	99
5.2 Methods.....	101
5.2.1 STM Measurements.....	101

	15
5.2.2 DFT Calculations.....	101
5.2.3 STM Simulation .....	102
5.3 Results .....	102
5.3.1 STM of ( $\sqrt{7} \times \sqrt{7}$ )R19.1° and ( $\sqrt{13} \times \sqrt{13}$ )R13.9° .....	102
5.3.2 Structure Generation.....	105
5.3.3 DFT Results .....	108
5.3.3 STM Simulation .....	110
5.4 Discussion .....	111
5.5 Conclusions .....	115
<b>Chapter 6: Thin Film Growth of Strontium Cobaltites .....</b>	<b>117</b>
6.1 Introduction .....	119
6.2 Methods .....	120
6.2.1 Substrate Preparation.....	120
6.2.2 Thin Film Deposition.....	121
6.2.3 In situ X-Ray Scattering .....	121
6.2.3 In situ X-Ray Scattering .....	122
6.3 Results .....	122
6.3.1 Sr-Co-O Film Growth.....	122
6.3.2 Effects of Growth Rate on Thin Film Phase.....	128
6.3.3 Annealing BM-SCO Films .....	135
6.4 Discussion .....	138
6.4.1 Thermodynamics of Sr-Co-O Film Growth .....	138
6.4.2 Kinetics of Sr-Co-O Film Growth.....	142
6.4.2 Phase Evolution of SrCoO <sub>2.5</sub> upon Annealing.....	144
6.5 Conclusions .....	146

## **Chapter 7: Design, Construction, and Characterization of Delivery with a Hybrid MBE System for in situ X-Ray Characterization.....149**

7.1 Introduction .....	151
7.2 Methods .....	153
7.2.1 Sector 33-IDE MBE Chamber Details .....	153
7.2.2 Residual Gas Analyzer .....	153
7.3 Hybrid Delivery System Overview .....	154
7.3.1 Challenges .....	154
7.3.2 General Equipment Overview .....	154
7.3.3 Gas Handling .....	159
7.3.4 Control Systems.....	163
7.3.4 Safety .....	164
7.4 Performance .....	166
7.4.1 Determination of Indicator for TTIP .....	166
7.4.2 Characteristics of Gas Delivery .....	167
7.5 Additional Practical Information for Running the HMBE and Further Improvements ....	169
7.5 Conclusions .....	173

## **Chapter 8: Growth of Oxide Materials Using Hybrid MBE System with in situ X-Ray Diffraction.....175**

8.1 Introduction .....	176
8.2 Methods .....	178
8.2.1 Substrate Preparation .....	178
8.2.2 X-Ray Measurements .....	179

	17
8.3 Results .....	180
8.3.1 Growth of $\text{TiO}_2$ .....	180
8.3.2 Growth of $\text{SrTiO}_3$ .....	184
8.3.3 TTIP Reaction with $\text{SrO}$ .....	187
8.3.4 Growth of $\text{Sr}_2\text{TiO}_4$ and $\text{TiO}_2$ (anatase) .....	192
8.4 Discussion .....	196
8.5 Conclusions .....	200
<b>Chapter 9: Ongoing and Future Work .....</b>	<b>201</b>
9.1 ( $5 \times 5$ ) Reconstruction on $\text{SrTiO}_3$ (1 1 1) .....	202
9.1.1 Introduction .....	202
9.1.2 Methods .....	204
9.1.2.1 STM Measurements .....	204
9.1.2.2 DFT Calculations .....	204
9.1.2.3 STM Simulation .....	205
9.1.3 Results .....	206
9.1.3.1 STM .....	206
9.1.3.2 Structure Generation - First Round .....	206
9.1.3.3 DFT Results - First Round .....	207
9.1.3.4 STM Simulation - First Round .....	209
9.1.3.5 Round Two – Current Progress .....	210
9.1.4 Future Directions .....	210
9.2 Superlattice Growth with Hybrid MBE .....	211
9.2.1 Introduction .....	212
9.2.2 Progress .....	213
9.2.3 Future Directions .....	213
<b>Reference .....</b>	<b>216</b>

<b>Appendix A .....</b>	<b>236</b>
-------------------------	------------

## List of Figures

Figure 1.1 Complexities of atomic structure at an idealized $\text{ABO}_3$ surface illustrating a surface reconstruction, unit cell step-height terraces, simple oxygen vacancy defects, and adsorption of ‘-OH’ groups. ....	31
Figure 2.1 Perovskite structure of $\text{SrTiO}_3$ .....	37
Figure 2.2 Brownmillerite structure of $\text{SrCoO}_{2.5}$ .....	40
Figure 2.3 The Ruddlesden-Popper series of $\text{Sr}_{n+1}\text{Ti}_n\text{O}_{3n+1}$ ( $n = 1, 2, 3, \dots\infty$ ) and its perovskite and rock salt building blocks. ....	41
Figure 2.4 An example of Wood's notation showing a $(2 \times 3)$ reconstruction created by two different atomic species denoted by blue and red circles over a bulk ordering of white circles. .	44
Figure 3.1 Schematic depiction of the in situ X-ray system for hybrid MBE growth. The oxide MBE chamber is mounted on a six-circle diffractometer with the axes of motion indicated [129]. ....	49
Figure 3.2 Crystal Truncation Rods (CTRs) from surface scattering explained in terms of convolution of a perfect crystal with a step function. ....	52
Figure 3.3 Simulated STM of the $(\sqrt{13} \times \sqrt{13})\text{R}33.7^\circ$ (RT13b) reconstruction at different bias voltages indicated below the corresponding frame. The inset image in each frame is unit cell averaged STM (+3.5 V bias, 0.1 nA current) of the RT13b shown for comparison. ....	60
Figure 4.1 Idealized coordination environments for $\text{TiO}_x$ showing (from left to right) octahedral $\text{TiO}_6$ , octahedral $\text{TiO}_5[]$ , and tetrahedral $\text{TiO}_4$ . ....	70
Figure 4.2 Atomic structure of solved reconstructions on the $\text{SrTiO}_3$ (1 0 0) surface showing (a) $(2 \times 2)\text{A}$ , (b) $(2 \times 2)$ , (c) $(2 \times 1)$ , (d) $c(6 \times 2)$ , (e) $(\sqrt{13} \times \sqrt{13})\text{R}33.7^\circ$ , and (f) $c(4 \times 2)$ . $\text{TiO}_5[]$ units are red, $\text{TiO}_6$ light blue. Sr atoms are green, Ti are blue, and oxygen are red. ....	71

Figure 4.3 Atomic structure of the solved  $(2 \times 2)$  reconstruction on  $\text{SrTiO}_3$   $(1\ 0\ 0)$  viewed from the a-axis (a), and c-axis (b). In (c) a square grid is imposed on the underlying bulk  $\text{TiO}_2$  layer and in (d) the reconstruction is represented by red squares showing placement of  $\text{TiO}_5[\ ]$  units on this grid. .... 72

Figure 4.4 Atomic structure of solved reconstructions on the  $\text{SrTiO}_3$   $(1\ 1\ 0)$  surface showing (a)  $(2 \times 1)$ , (b)  $(3 \times 1)$ , (c)  $(4 \times 1)$ , (d)  $(5 \times 1)$ , (e)  $(6 \times 1)$ , (f)  $(5 \times 1)\text{A}$ , (g)  $(\infty \times 1)\text{A}$ , and (h)  $(\infty \times 1)\text{B}$ .  $\text{TiO}_6$  are light blue,  $\text{TiO}_4$  are purple. Sr atoms are green, Ti are blue, and oxygen are red. . 74

Figure 4.5 Atomic structure of the solved  $(5 \times 1)\text{A}$  reconstruction viewed from the b-axis (a), and c-axis (b). In (c) a diamond grid is imposed over the bulk layers below and in (d) the reconstruction is represented by purple diamonds and pink triangles showing placement of two different orientations of  $\text{TiO}_4$  units. .... 75

Figure 4.6 Atomic structure of solved reconstructions on  $\text{SrTiO}_3$   $(1\ 1\ 1)$  surface showing (a)  $(1 \times 2)$  – “Low”, (b)  $(2 \times 2)\text{b}$ , (c)  $(3 \times 3)$ , (d)  $(2 \times 2)\text{a}$ , (e)  $(4 \times 4)$ , and (f)  $(1 \times 1)$  – “High”.  $\text{TiO}_6$  units are light blue,  $\text{TiO}_5[\ ]$  are red, and  $\text{TiO}_4$  are purple. Sr atoms are green, Ti are blue, and oxygen are red..... 79

Figure 4.7 Atomic structure of the solved  $(2 \times 2)\text{a}$  reconstruction viewed from the b-axis (a), and c-axis (b). In (e) a triangle grid is imposed over the bulk layer below and in (f) the reconstruction is represented by blue and red triangles showing placement of  $\text{TiO}_6$  and  $\text{TiO}_5[\ ]$  units, respectively. Atomic structure of the solved  $(2 \times 2)\text{b}$  reconstruction viewed from the a-axis (c), and c-axis (d). In (g) a triangle grid is imposed over the bulk layer below and in (h) the reconstruction is represented by blue and red triangles showing placement of  $\text{TiO}_6$  and  $\text{TiO}_5[\ ]$  units, respectively and purple triangles and diamonds showing placement of  $\text{TiO}_4$  units. .... 80

Figure 4.8 Atomic structure of the solved  $c(6 \times 2)$  nanostructure on  $\text{SrTiO}_3$   $(1\ 0\ 0)$  viewed from the b-axis (a), and c-axis with a square grid imposed over the bulk layers below (e). In (f)  $\text{TiO}_6$  units are placed on top of the bulk, represented by blue squares- the structure of this layer is shown in (b). In (g)  $\text{TiO}_6/\text{TiO}_5[\ ]$  units are represented by green squares and are placed atop those



in (b) and (f)- the structure of this layer is shown in (c). In (h)  $\text{TiO}_5$  units are represented by red squares and are placed atop those in (c) and (g)- the structure and tilts of this layer is shown in (d). ..... 84

Figure 4.9 Atomic structure of the solved triline nanostructure on  $\text{SrTiO}_3$  (1 0 0) viewed from the a-axis (a), and c-axis with a square grid imposed over the underlying bulk (d). In (e)  $\text{TiO}_6$  units are represented by blue squares placed atop the grid in (d)- the structure of this layer is shown in (b). In (f)  $\text{TiO}_5$  units are represented by red squares placed atop the structure in (b) and (e)- the structure of this layer is shown in (c). ..... 86

Figure 4.10 Atomic structure of the solved  $(2 \times 4)$ a nanostructure on  $\text{SrTiO}_3$  (1 1 0) viewed from the b-axis (a), and c-axis with a diamond grid imposed (d). In (e)  $\text{TiO}_6$  units are represented by purple diamonds placed atop the grid in (d)- the structure and distortions in this layer is shown in (b). In (f)  $\text{TiO}_6$  units are represented by orange diamonds placed atop the structure in (b) and (e)- the structure of this layer is shown in (c). ..... 87

Figure 4.11 Atomic structure of reconstructions on  $\text{BaTiO}_3$  (1 0 0) surface showing  $c(2 \times 2)$  viewed down perpendicular axes in (a) and (c) and  $c(4 \times 4)$  viewed down the same perpendicular axes in (b) and (d).  $\text{TiO}_6$  units are light blue, surface  $\text{TiO}_6$  are yellow,  $\text{TiO}_5$  are navy blue, and  $\text{TiO}_3$  are pink. Ba atoms are dark green, Ti are blue, and oxygen are red. .... 90

Figure 4.12 Atomic structure of the solved reconstructions on  $\text{LaAlO}_3$  (1 1 0) surface showing  $(2 \times 1)$  in viewed down the c-axis in (a) and viewed down the b-axis in (c). Atomic structure of the solved  $(3 \times 1)$  reconstruction viewed down the c-axis in (b) and the b-axis in (d).  $\text{AlO}_6$  units are light blue, and two different orientations of  $\text{AlO}_4$  are red and purple respectively. La atoms are green, Al are blue, and oxygen are red. .... 92

Figure 5.1 (a) STM image (+2.9 V sample bias, 0.3 nA tunneling current) showing RT7 and RT13 domains. Dashed rectangle highlights region of disorder. (b) Unit-cell averaged STM images of the RT7 reconstruction (+2.1 V bias, 0.1 nA current) and (c) the RT13 reconstruction (+3.5 V bias, 1 nA current), dashed parallelograms outline unit cells of reconstructions. .... 104

Figure 5.2 Unit cells of two rotational domains of RT7 (pink) and RT13 (blue) compared to the underlying in-plane bulk unit cell of the  $\text{SrTiO}_3$  (1 1 1) surface. Atoms of strontium, titanium, and oxygen are represented by green, blue, and red circles respectively. .... 105

Figure 5.3 Three hypothetical structures for the RT7 reconstruction shown as symbolic representations based on Pauling's rules. .... 107

Figure 5.4 Six hypothetical structures for the RT13 reconstruction shown as symbolic representations based on Pauling's rules. .... 107

Figure 5.5 Surface energies in eV/(1  $\times$  1) surface unit cell plotted versus excess  $\text{TiO}_2$  per (1  $\times$  1). Results are from the revTPSS calculation, and the dotted lines show results from the convex hull construction..... 109

Figure 5.6 (a) Averaged STM image (+2.14 V sample bias, 0.10 nA tunneling current) of RT7 with simulated RT7b overlaid in the middle and (b) structure diagram with  $\text{TiO}_5[]$  octahedra in red,  $\text{TiO}_6$  octahedra in blue, and Sr atoms in green. (c, d) Show the averaged STM image and structure diagram for RT7a, respectively. (e) Averaged STM (+3.6 V bias, 0.12 nA current) of RT13, simulation RT13b overlaid to the right and (f) diagram of structure. (g, h) Show averaged STM image and structure diagram for RT13a, respectively..... 110

Figure 5.7 (a) Diagram of RT13b, (b) RT7b, and (c) (2  $\times$  2)a where  $\text{TiO}_5[]$  octahedra are red,  $\text{TiO}_6$  octahedra blue, and Sr atoms are green. (d) Grid imposed on bulk  $\text{SrTiO}_3$  (1 1 1) to codify RT13b, (e) RT7b, and (f) (2  $\times$  2)a. .... 112

Figure 5.8 (a) STM image (+2.9 V sample bias, 0.3 nA tunneling current) of defects in RT13. (b, c) Diagrams of RT13b showing possible Schottky defects where  $\text{TiO}_5[]$  octahedra are red,  $\text{TiO}_6$  octahedra blue, and Sr atoms are green. .... 114

Figure 6.1 X-ray scattering along the (0 0 L) crystal truncation rod of phase-pure  $\text{SrCoO}_{2.5}$  (a) and  $\text{Sr}_3\text{Co}_2\text{O}_{6\pm\delta}$  (326-SCO) (b) films grown on  $\text{SrTiO}_3$  (0 0 1). Film shown in (a) was grown at  $T_{\text{sub}} = 875$  K,  $p\text{O}_3 = 1.33 \times 10^{-4}$  Pa ( $1 \times 10^{-6}$  Torr), (b) was grown at  $T_{\text{sub}} = 873$  K,  $p\text{O}_2 = 1.33 \times$

$10^{-4}$  Pa ( $1 \times 10^{-6}$  Torr). XANES at the Co K-edge (c) for the films, showing they both exhibit  $\sim\text{Co}^{3+}$ , as measured at  $\mu x = 0.5$  (the intensity halfway point of normalized spectra). The energy references are from the Co metal foil and Refs. [143, 223]..... 124

Figure 6.2 Structures of the stable members of the  $\text{SrCoO}_{(3n-1)/n}$  homologous series for  $n = 2$  (a), 4 (b), 8 (c), and  $\infty$  (d) on  $\text{SrTiO}_3$  (0 0 1) and (e-h) their corresponding (calculated) X-ray scattered intensities along the (0 0 L) specular rod assuming films are coherently strained, respectively. The  $n = 4$ , and 8 members (b) and (c) have two possible orientations, shown separated by the dotted line, the (0 0 L) in (f) and (g) are an average of these two. The polyhedra corresponding to  $\text{CoO}_4$ ,  $\text{CoO}_5$ , and  $\text{CoO}_6$  are shown in cyan, blue, and violet, respectively. Strontium atoms and oxygen atoms are green and red respectively. The defect structures are expected to evolve from left to right when moving from reducing to more oxidizing conditions. .... 125

Figure 6.3 Crystal structures of the  $\text{Sr}_3\text{Co}_2\text{O}_7$  Ruddlesden-Popper (a) and the related oxygen-deficient  $\text{Sr}_3\text{Co}_2\text{O}_{6\pm\delta}$  (b) showing positions of oxygen vacancies. The polyhedra corresponding to  $\text{CoO}_5$ , and  $\text{CoO}_6$  are shown in blue, and violet, respectively. Strontium atoms and oxygen atoms are green and red respectively..... 127

Figure 6.4 Scattered X-ray intensity at the (0 0  $\frac{1}{2}$ ) position during growth (left) of three different Sr-Co-O films (a, c, e) on  $\text{SrTiO}_3$  (0 0 1) and their corresponding (0 0 L) scans of the films (right) after growth (b, d, f). Films were interrupted (marked as ‘Measure’) during growth as depicted in the inset shutter schematics of (a), (c), and (e). All growths shown were conducted at  $T_{\text{sub}} = 873$  K,  $p\text{O}_3 = 1.33 \times 10^{-4}$  Pa ( $1 \times 10^{-6}$  Torr). .... 130

Figure 6.5 Scattered X-ray intensity along the (0 0 L) specular rod showing evolution of the film structure for films interrupted after deposition of each four BLs (a), (c) or interrupted every BL (b), (d). All intensities (z-axis and color map lightness) are plotted on a normalized  $\log_{10}$  scale. Arrows in (c) and (d) indicate peak positions characteristic to the BM-SCO (pink) and 326-SCO (blue) phases while tick marks on the right axis indicate when measurements were taken. .... 131

Figure 6.6 Thickness of different phases during growth in a pure BM-SCO film (a) and the BM-SCO + 326-SCO film (b). The BM-SCO phase is indicated by the pink traces, 326-SCO phase by blue, while the overall film thickness based on CTR thickness fringes is indicated in black. Linear fits are drawn as a guide for the eye. .... 133

Figure 6.7 In situ XANES measured at the Co K-edge during growth of two films interrupted at different points throughout growth, showing a phase-pure BM-SCO film (a) interrupted after deposition of each four BL and a two-phase BM-SCO and 326-SCO film (b) interrupted after deposition of each BL. The energy references are from the Co metal foil and Refs. [143, 223] 134

Figure 6.8 Specular (0 0 L) scattering of a BM-SCO film after growth (a) at  $T_{\text{sub}} = 793 \text{ K}$  in  $1.33 \times 10^{-4} \text{ Pa}$  ( $1 \times 10^{-6} \text{ Torr}$ ) of 100%  $\text{O}_3$ , its changes upon annealing at  $5.60 \times 10^{-4} \text{ Pa}$  ( $4 \times 10^{-6} \text{ Torr}$ ) with increasing temperature from 793 to 1023 K (b), and further change upon lowering background  $p_{\text{O}_3}$  from  $5.60 \times 10^{-4} \text{ Pa}$  ( $4 \times 10^{-6} \text{ Torr}$ ) to  $1.33 \times 10^{-4} \text{ Pa}$  ( $1 \times 10^{-6} \text{ Torr}$ ) at constant temperature of 1023 K(c). .... 137

Figure 6.9 Thermodynamic phase diagram (a) showing  $p_{\text{O}_2}/a_{\text{O}_2}$  (left/right axis) for the 326-SCO  $\leftrightarrow$  BM-SCO reaction (bold line). The  $a_{\text{O}_2}$  of 100%  $\text{O}_3$  at  $1.33 \times 10^{-4} \text{ Pa}$  ( $1 \times 10^{-6} \text{ Torr}$ ) is indicated as a short, dashed line, while 100%  $\text{O}_2$  at  $1.33 \times 10^{-4} \text{ Pa}$  ( $1 \times 10^{-6} \text{ Torr}$ ) is indicated by the long, dashed line. In (b), containing an enlarged view of (a), we overlay the results for films of Sr-Co-O grown at varying  $T_{\text{sub}}$  and  $a_{\text{O}_2}$ . Open and dark circles indicate Brownmillerite and 326-SCO films, respectively, with mixtures of the two are indicated by partially-shaded circles. .... 141

Figure 7.1 Schematic of the mobile, vertical rack for the in situ hybrid MBE chamber. Views from the front (a), the back (b), and at angle (c), with the labeled components described in the text. Labelled parts are bellows-sealed pneumatic valves (A), (F), and (I), heating controllers (B), line pressure/ mechanical valve controller (C), digital I/O for pneumatic valves (D), pneumatic valve solenoids (E), scroll pump (G), pressure capacitance manometer (H), source enclosure (J), metal-sealed mechanical stepper valve (K), and exhaust vent hookup (L). .... 155

Figure 7.2 Schematic of the entire in situ hybrid MBE system, showing the placement and attachment of the vertical rack used to deliver the metalorganic precursors, relative to the oxide MBE chamber and six-circle diffractometer, as viewed from the top (a) and side (b)..... 159

Figure 7.3 Diagram of the hybrid MBE gas delivery system, indicating placement of the valves and pressure controllers. .... 160

Figure 7.4 Diagram illustrating the different temperature zones for a single hybrid MBE gas delivery line. Labels of the different valves and pressure controllers are shown in Figure 7.3. 162

Figure 7.5 Partial pressures from cracking products of the TTIP metalorganic as a function of  $m/z$ . The measurement was performed during deposition of  $\text{TiO}_2$  on  $r$ -plane  $\text{Al}_2\text{O}_3$  in the oxide MBE chamber. Inset shows an enlarged view of the higher  $m/z$  products..... 167

Figure 7.6 Partial pressure traces of selected  $m/z$  cracking products of the metalorganic precursor, TTIP, during growth of rutile  $\text{TiO}_2$ . The RGA measurements show the behavior of precursor gases within the MBE chamber upon initiating and after terminating gas delivery. The traces in (a), (b), and (c) have been re-scaled for ease of viewing. Dotted lines between traces serve as a guide to the eye; no data was recorded during this time. Measurements were taken during growth at a temperature of  $800^\circ\text{C}$ . .... 168

Figure 8.1 AFM (height) of prepared substrates for oxide growth showing a)  $r$ -plane  $\text{Al}_2\text{O}_3$  (0 1 2), b) LSAT (0 0 1), and c)  $\text{SrTiO}_3$  (0 0 1). .... 179

Figure 8.2 AFM (height) of bare  $r$ -plane  $\text{Al}_2\text{O}_3$  (0 1 2) substrate a) before and b) after growth of  $\text{TiO}_2$  and  $2\theta$  X-ray diffraction showing (1 0 1)  $[0\ 1\ 0]_{\text{TiO}_2} \parallel [0\ 1\ 2]\ [0\ 0\ 1]_{\text{Al}_2\text{O}_3}$  orientation of  $\text{TiO}_2$  film on  $\text{Al}_2\text{O}_3$ . .... 181

Figure 8.3 (a) Scattered X-ray intensity measured along the out-of-plane, 0 0 L direction for a rutile  $\text{TiO}_2$  film grown on  $\text{Al}_2\text{O}_3$  (0 1 2). (b) Change in scattered X-ray intensity during growth at the anti-Bragg position,  $H\ K\ L = 0\ 0\ \frac{1}{2}$  r. l. u., and (c) at the  $\text{TiO}_2$  (1 0 1) Bragg peak or  $H\ K\ L =$

0 0 1.42 r. l. u. The measurements were taken at the growth temperature of 600°C. Delivery of TTIP began at  $t = 0$ , measurement began at  $t = 120$  sec. .... 183

Figure 8.4 Room temperature results for two  $\text{SrTiO}_3$  films grown at 750°C on LSAT (0 0 1) with 110 mTorr TTIP under Sr fluxes of  $2.35 \times 10^{12}$  atoms/cm<sup>2</sup>\*sec (STOh1) and  $2.67 \times 10^{12}$  atoms/cm<sup>2</sup>\*sec (STOh2). (a) X-ray scattering along the specular 0 0 L direction at room temperature. (b) Scattered X-ray intensities (STOh1 on left axis, STOh2 on right) measured during growth at 750°C at the reciprocal lattice position, H K L = 0 0 ½ r. l. u. (c, d) Room temperature 2  $\mu\text{m} \times 2 \mu\text{m}$  AFM micrographs of the films STOh1 (c) and STOh2 (d)..... 186

Figure 8.5 Titanium (IV) Tetraisopropoxide Chemical Structure. .... 189

Figure 8.6 AFM images of  $\text{SrTiO}_3$  (0 0 1) with initial  $\text{TiO}_x$ -rich surfaces (a-b, e-f) and SrO islands (c-d, g-h) after annealing at 800 °C without exposure to TTIP (a-d) and after a 5-minute dose of TTIP (e-h). AFM in a, c, e, and g shows height while b, d, f, and h show phase. .... 190

Figure 8.7 Scattering along the (0 0 L) direction (a, b) of Sr-Ti-O oxide films on  $\text{SrTiO}_3$  (1 0 0) showing  $\text{Sr}_2\text{TiO}_4$ -rich (a), and mixed  $\text{Sr}_2\text{TiO}_4$  and anatase  $\text{TiO}_2$  (b). Scattered intensity measured at the H K L = 0 0 ½ (c, d) for the film whose CTR is shown in the frame directly above. All films were grown at 800°C. .... 193

Figure 8.8 Scattering along the (0 0 L) direction (a, b, c) of Sr-Ti-O oxide films on  $\text{SrTiO}_3$  (1 0 0) showing  $\text{Sr}_2\text{TiO}_4$ -rich (a), and anatase  $\text{TiO}_2$ -rich (b) films. Scattered intensity measured at the H K L = 0 0 ½ (c, d) for the film whose CTR is shown in the frame directly above. All films were grown at 800°C. .... 195

Figure 9.1 STM images showing the (5  $\times$  5) reconstruction on different samples (a) and (b) taken at 2.6V bias and 0.2 nA tunneling current. Both STM are 24.2  $\times$  12.2 nm<sup>2</sup> in area. .... 206

Figure 9.2 STM images showing the (3  $\times$  3) reconstruction (a) taken at 2.0V bias and 0.4 nA tunneling current, the (4  $\times$  4) (b) taken at 2.0V bias and 0.5 nA tunneling current, and the (5  $\times$  5) (c) taken at 2.6V bias and 0.2 nA tunneling current. All STM are 24.2  $\times$  12.2 nm<sup>2</sup> in area. .... 207

Figure 9.3 (a) Surface energies in eV/(1 × 1) surface unit cell plotted versus excess TiO<sub>2</sub> per (1 × 1). Results are from the PBEsol0 calculation, and the dotted lines show results from the convex hull construction. (b) Structure diagram of the low-energy solution with TiO<sub>5</sub> octahedra in purple, TiO<sub>6</sub> octahedra in blue, TiO<sub>4</sub> tetrahedra in purple, and Sr atoms in green. .... 208

Figure 9.4 (a) STM image of (5 × 5) reconstruction Type B, from Figure 9.1 (b), with overlaid simulated structure. (b) shows a zoomed-in view of this same STM and simulation. (c) STM image of (5 × 5) reconstruction Type A, from Figure 9.1 (a), with overlaid simulated current structure. All STM taken at 2.6V bias and 0.2 nA tunneling current. .... 209

Figure 9.5 (a) Titanium (IV) tetraisopropoxide (TTIP) and (b) vanadium (V) triisopropoxide chemical structure. .... 214

## CHAPTER 1

### **Introduction**



## 1.1 Motivation and Scope

Oxide materials contain metal cations and oxygen anions. We interact with these materials on a daily basis; the surfaces we encounter are often oxidized simply by contact with oxygen in the air itself. The family of oxide materials also encompasses diverse crystalline materials and many of these comprise transition metals, known to support a variety of different types of bonding and properties with their *d* and *f* orbital electrons.

Transition metal oxide materials are relevant to a multitude of applications including energy generation and storage [1-4], computation [5, 6], catalysis [7-14], gas sensing [15], and electronics [16-23], however effectively applying these materials to such a wide range of applications hinges upon realizing a similarly diverse set of properties. This can be done through manipulation of the structure or surface of a material or, alternatively, novel properties can be achieved by combining two oxide materials with similar crystal structures. Unfortunately, many material properties are inexorably linked such that a trade-off between particularly useful aspects exists. Luckily, there are multiple strategies for obtaining desired properties oxide material offer without sacrificing others. The multitude of transition metals, rare earth, or lanthanide cations that can be incorporated into oxides leads to a great deal of flexibility in engineering the material for these properties. Additionally, their similar crystal structures facilitate the synthesis of heterostructures to address the common trade-offs associated with materials design.

Many technologically relevant oxide materials, including those discussed herein, belong to the perovskite,  $ABO_3$ , structure family where A and B are metal cations and B is typically a transition metal. Since their structures and the size of their unit cells are quite similar, many of these materials can be combined in different permutations while retaining a perovskite-like

crystalline structure. Despite the relative simplicity of the ideal structure, there can be wide variations across the entire family of oxides allowing further customization of this general crystalline framework. The differing size ratios of A:B cations in different perovskites lead to many changes in structure beyond simply the unit cell size. These variations include octahedral tilting, rhombohedral distortion, and oxygen vacancy defects among other structural imperfections or deviations from the perfect perovskite [24, 25]. All of these features contribute complexity to observed structures.

Outside of the structural variations in perovskite-based crystals, there is one part of a material that is often overlooked despite being the one we interact with most frequently. Crystallography is often thought to concern only the periodic structure of a bulk crystal; however the surface of a crystal can be equally important. When a crystal is cleaved, the exposed surface cannot be considered to be the same as the bulk crystal. For a surface to be stable instances of atomic under or over-bonding must be eliminated and compensation must occur such that the material does not have an overall formal charge. When a degree of freedom is limited, representing a finite surface, structural determination can be challenging even in bulk single-crystals, as shown in Figure 1.1. Changes from the bulk can include but are not limited to full surface reconstructions, step-terraces, surface atomic defects such as vacancies, and adsorption of small molecules from the environment. Often more than one of these phenomenon is present on a given surface.

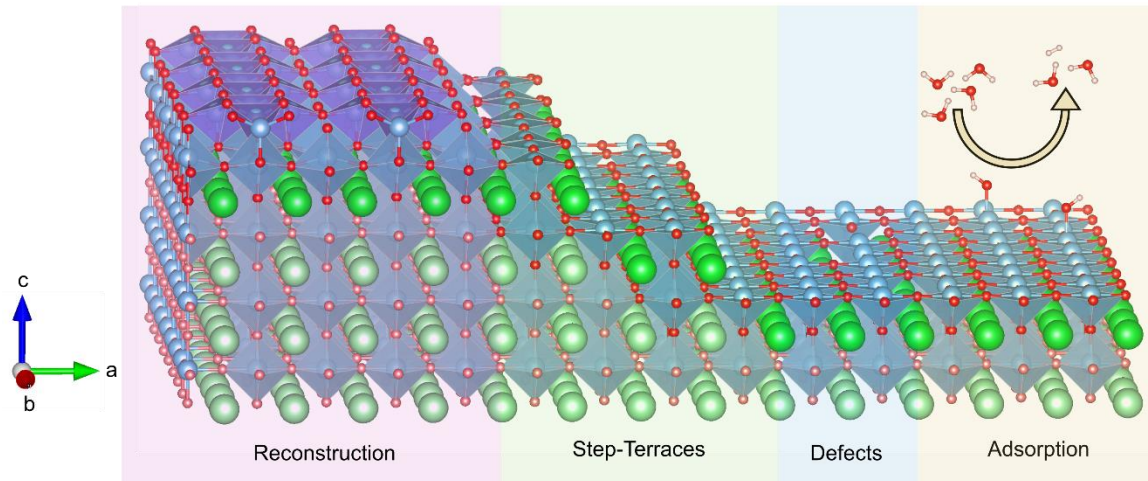


Figure 1.1 Complexities of atomic structure at an idealized  $\text{ABO}_3$  surface illustrating a surface reconstruction, unit cell step-height terraces, simple oxygen vacancy defects, and adsorption of ‘-OH’ groups.

One consequence of this complexity manifests in the observation of a multitude of surface reconstructions on perovskites including  $\text{SrTiO}_3$ ,  $\text{BaTiO}_3$ , and  $\text{LiNbO}_3$  [26-63]. It is logical to think that different surface reconstructions would lead to variations in materials grown on them and in fact, reconstructions have been demonstrated to affect the structure of films beyond the normally-considered aspects of strain and inter-diffusion [64-66]. Not only does the surface of a substrate affect thin film growth, but when different oxide materials are combined in a film the interface between them will form a unique structure. In thin films and heterostructures, the role of surfaces dominates because they are such a significant portion of the material and these interfacial regions can influence a device’s properties [16, 17, 23, 67-74]. This makes it essential to identify and target specific substrate surfaces to achieve desired properties after growth. The starting surface of a substrate goes on to form the interfacial structure of interest, and it may also affect the surface structure of the resulting thin film.

The focus of this work is on understanding the structural evolution of oxides at the 2-D limit from single crystal surfaces to thin films. Understanding the initial structures of oxide films provides a more complete picture for their use in devices. Determining the structure of common oxide growth substrates facilitates identifying the fundamental units of oxide surface structures, including differences between oxide thin films grown by homoepitaxy and those grown by heteroepitaxy. This knowledge provides a basis for understanding and predicting surface structures of common  $\text{ABO}_3$  oxides while also providing a toolset for investigating the transition from surface to thin film in oxide growth applications.

Building a complete picture of oxide surface and interface structures requires a wide variety of techniques and using these techniques in concert with each other in efficient ways is an important aspect of these investigations. A variety of techniques including density functional theory (DFT), in situ surface X-ray scattering (SXRD), X-ray absorption spectroscopy (XAS), thermodynamic calculations, oxide molecular beam epitaxy (MBE), and metalorganic hybrid molecular beam epitaxy (HMBE) were employed during this investigation. Quantum-based calculations like DFT are often accompanied by substantial computing cost in modeling surfaces while thin film growth is time-consuming and requires much trial and error. By employing the various strategies presented herein, the effort on the part of the experimenter, and the costs associated with these investigations (computation, time, etc.) can be significantly reduced. To this end a variety of cases including structure prediction on oxide surfaces, DFT of large surface reconstructions, thermodynamic calculations for understanding cobaltite thin film growth, and new tools for probing the mechanisms of HMBE are discussed as both interesting in their own right and as models for future studies of challenging systems. Investigating structurally relevant systems

and synthetically promising techniques provides a route for understanding and harnessing complexity in the family of perovskite oxide materials.

## 1.2 Organization

This work strives to unite theoretical prediction and experiment while investigating oxide structures of increasing complexity. This dissertation is presented as follows: Chapter Two covers additional background information on common structures discussed further in the subsequent sections. Chapter Three discusses the methods forming the basis of these investigations, both theoretical and experimental. After this, the thesis has two general sections: the first section, which comprises Chapters Four and Five, primarily focusing on DFT and surface reconstructions on  $\text{SrTiO}_3$ . Chapter Four focuses on the fundamental units of reconstructions on the most common truncations-  $(1\ 0\ 0)$ ,  $(1\ 1\ 0)$ , and  $(1\ 1\ 1)$ - of the  $\text{SrTiO}_3$  perovskite. Predictive rules for surface structure generation and determination strategies for common oxide substrate materials, especially  $\text{SrTiO}_3$ , serve as a starting point and foundation for this discussion. Chapter Five covers an application of the model laid out in Chapter Four and discusses solving two related reconstructions on  $\text{SrTiO}_3$   $(1\ 1\ 1)$ . The next chapters make up the second section of this dissertation, where the focus is on understanding and providing tools and techniques for thin film growth of oxide materials. Chapter Six details the growth and structural evolution of strontium cobaltite thin films via MBE within the context of thermodynamic and kinetic factors. The functional role of oxygen vacancies in these materials is investigated in the thin film growth. Chapters Seven and Eight outline the design, construction, testing, and initial experimental results of a hybrid MBE system constructed for the purpose of in situ structural evolution measurements using X-ray scattering techniques. Finally, Chapter Nine discusses ongoing work and related possible future

investigations. The experimental work performed as part of this thesis were based primarily on synchrotron X-rays provided by the Advanced Photon Source, and the beamline experiments involving oxide MBE were performed with significant help from Seyoung Cook. The contributions of co-authors, where appropriate, are indicated in the beginning pages of each chapter.

## CHAPTER 2

### **Background**

The sections of this work all deal with understanding interfaces and growth in perovskite oxide materials. As such, this section provides general background information useful for understanding the more in-depth discussion in the chapters that follow. First, the basics of the perovskite structure are discussed because all of the oxide materials investigated in this work are either perovskites or related structures. Favorable aspects of these structures are outlined including how they can incorporate a variety of properties and be combined into unique heterostructures. A number of structures related to the perovskite architecture including the Brownmillerite and Ruddlesden-Popper structures are also introduced. These crystal structures are relevant to the strontium cobaltite materials discussed in a later chapter and to oxide growth in general. Once the important features of these materials have been covered, aspects regarding their surface structures can be considered. Common nomenclature for surface structures as well as important differences between surface and bulk structures are briefly discussed. This information prepares readers for the more in-depth discussions of the nuances of perovskite-based structures and their surfaces in the chapters to follow. Information regarding experimental and theoretical methods are summarized separately in Chapter Three. Each chapter describing research contains additional specific background information and these chapters are mentioned as necessary.

## **2.1 Perovskites**

Many oxide materials of technological importance, and the majority of those discussed in this thesis, belong to the perovskite,  $ABO_3$ , structure family. In perovskites, the cation represented by A is often a member of Group I or II of the periodic table, though it can also be a lanthanide element. This cation sits in a 12-fold coordination environment with oxygen. Cations represented by B are often transition metals and are bonded to six oxygens, resulting in an octahedral



orientation. An ideal cubic perovskite structure is shown in Figure 2.1. Due to differing size ratios between A and B cations, common variations on this structure include rhombohedral distortion and octahedral rotations.

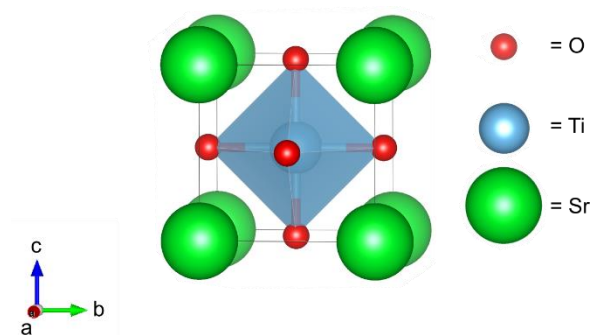


Figure 2.1 Perovskite structure of  $\text{SrTiO}_3$ .

## 2.2 Multivalent Transition Metals

Transition metals are able to support multiple valence states. This allows them to be particularly flexible in the structures they can adopt. These materials are the focus of this thesis work. Titanium and cobalt are the two transition metals discussed in the majority of investigations presented herein. Their electronic structures allow them to accommodate doping, complex cation ordering, and they can maintain their framework structure even with a large number of oxygen vacancies. While this allows great versatility, it also makes synthesis of these materials more challenging, given the large number of possible structures they can adopt. In fact, there are many factors to consider when targeting growth of a specific phase. One oxide material that provides an example of this is the family of strontium cobalt oxides,  $\text{Sr-Co-O}$ , discussed extensively in Chapter Six. Cobalt can easily take on oxidation states ranging from +2 to +4, forming bonds with 4-6 oxygen atoms in its local coordination environment. There are other transition metals that can adopt multiple valence states, including Fe and Mn [75-79], that may behave similarly. However,

cobalt is particularly sensitive to its oxygen environment and can easily switch between structures accompanying changes in oxygen content. In some cases, this results in significant changes to material properties. Since many oxide materials belong to the same structure family, it is a logical assumption to make that they could be combined in various ways through clever synthesis.

## 2.3 Superlattices

As most perovskite and perovskite-derived oxides have similar unit-cell dimensions [80, 81], they can be combined through various synthetic means to produce even more complex structures. Since epitaxial strain is low between different members of the perovskite-derived families, they can easily be layered through controlled synthesis by using a variety of deposition methods. Most commonly pulsed laser deposition (PLD) and MBE are employed to create superlattice structures. The hybrid MBE growth system introduced and discussed in Chapters Seven and 8 provides another method for creating these types of films. This synthesis method is discussed in more depth in the aforementioned chapters.

Manipulating the properties of a given film is often done by doping or mixed-cation synthesis. Doping of both the A- and B-site cations has been investigated for many perovskite systems [80, 82-88]. Higher content mixtures, such as those represented by  $A_xA'_{1-x}BO$ ,  $AB_yB'_{1-y}O$ , or even  $A_xA'_{1-x}B_yB'_{1-y}O$  alloys (as opposed to cation ordered superlattices) have also been synthesized.

With many synthesis options available and a toolset of materials that can be assembled like Legos™, film growers are able to target specific properties. In the cases of superlattices and thin films, it is often the properties of the interfaces themselves that are of interest [89, 90]. These range from application-specific properties like catalytic activity [3, 7, 8, 10-13, 91-93],

superconductivity [94-98], and metal-insulator transitions [99-101], to more exotic phenomena such as spin frustration [102, 103]. Doping and superlattice growth allow for desired properties to be incorporated, produce unique materials for studying the fundamental physics of oxides, and can serve more practical purposes such as the simple goal of improving a film's stability [75, 76, 104].

Superlattices are not just limited to combinations of different perovskites. There are many related structures that can also be combined in superlattices or grown as thin films on a perovskite substrate.

## **2.4 Brownmillerite**

Other structures that are common in the oxide materials include those derived from the parent perovskite structure. One example, which will be further discussed in the case of strontium cobalt oxides in Chapter Six, is the Brownmillerite structure. The technological relevance of this structure and further background details are contained in Chapter Six. This structure is formed from a supercell of perovskite units with ordered oxygen vacancies, creating vacancy channels in a preferential direction. The unit cell of the Brownmillerite structure is four times that of the perovskite in one direction and  $\sqrt{2}$  times in the other two directions. As such, if it is epitaxially grown on a perovskite (1 0 0) surface, its simplest unit cell will exhibit a  $45^\circ$  rotation with respect to the perovskite in-plane structure. The Brownmillerite's structure is illustrated in Figure 2.2.

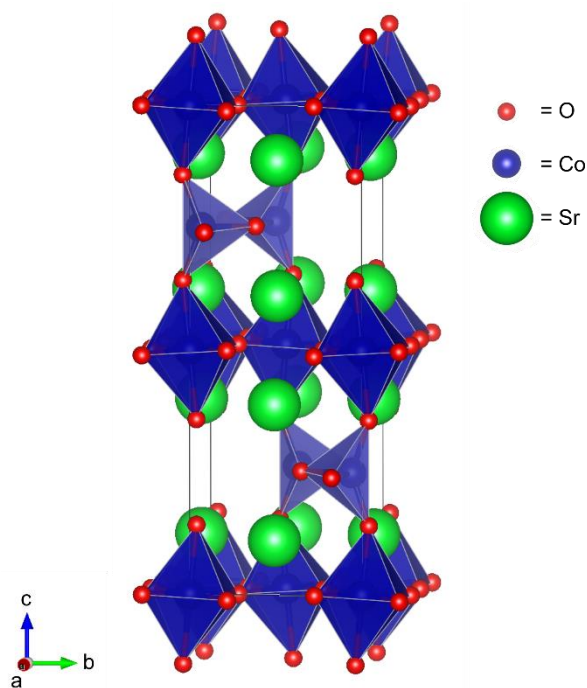


Figure 2.2 Brownmillerite structure of  $\text{SrCoO}_{2.5}$ .

The Brownmillerite structure is formed by removal of  $1/6$  of the oxygen atoms in the perovskite, written as  $\text{ABO}_{2.5}$ . The quadrupling of the unit cell in one direction is a direct consequence of the B cation adopting an alternating sequence of octahedral/tetrahedral coordination due to an alternating oxygen vacancy concentration along the  $[0\ 0\ 1]$  direction. Tetrahedral units can have different orientations within this framework and within a Brownmillerite unit cell they alternate between two of these, resulting in the quadrupled unit cell (Figure 2.2).

This structure, where oxygens are removed from the perfect perovskite, is a member of a homologous series of structures with the formula  $\text{ABO}_{(3n-1)/n}$ , with  $n = 2, 4, 8$ , theoretically increasing up to  $\infty$ . Other members of this series have been observed with different oxygen vacancy ordering [105]. While this structure is created by introducing oxygen vacancies into the perovskite,

there are other structures that rely on periodic combinations of perovskites with compatible oxide materials.

## 2.5 Ruddlesden-Popper

Another structural variation on the perovskite theme is the Ruddlesden-Popper structure. As this structure is discussed in-depth in Chapter Six it is introduced here simply to provide familiarity with its elements. This structure is created by an intergrowth of perovskite and rock salt units with cube-on-cube epitaxy. Different members of this series are created by changing the number of perovskite units in a unit cell, varying the overall ratio of perovskite to rock salt. The series of oxide compounds with this structure are represented by:  $A_{n+1}B_nO_{3n+1}$  ( $n = 1, 2, 3, \dots\infty$ ). An example of this series is shown in Figure 2.3 along with the perovskite and rock salt units that provide its building blocks.

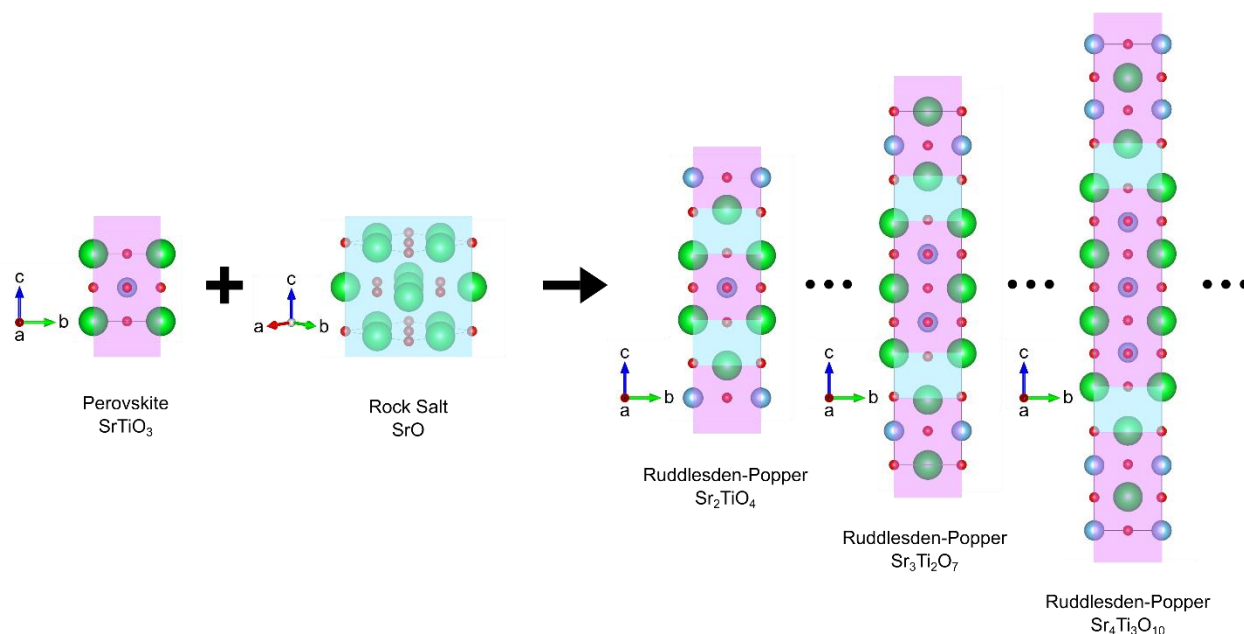


Figure 2.3 The Ruddlesden-Popper series of  $Sr_{n+1}Ti_nO_{3n+1}$  ( $n = 1, 2, 3, \dots\infty$ ) and its perovskite and rock salt building blocks.

Since this family of structures incorporates the perovskite, it can easily be integrated with

other perovskite structures. As with the parent perovskite, there is structural variation within the Ruddlesden-Popper framework. Additionally, as an oxide material with two different cations, Ruddlesden-Popper structures have many similar defects and distortions to their perovskite parent.

## **2.6 Oxygen Vacancies in Perovskite Materials**

For oxide materials, oxygen vacancies are a common functional defect. In these structures, oxygen has greater mobility while the cations maintain a relatively rigid framework [106]. The Brownmillerite structure is a good example of the importance that oxygen defects play- it is an ordered structure derived from the perovskite with vacancies. The ability of many oxide materials to lose and gain oxygen with relative ease is a desirable property in its own right, but understanding the defects present in oxide materials and controlling the extent to which they appear is of particular concern for surfaces and growth. More complex structures, like the previously-discussed Ruddlesden-Popper phases, are also prone to the formation of oxygen vacancies, sometimes resulting in additional ordering [107, 108]. As such, considering oxygen vacancies and understanding how they are formed, as well as the role they play in the resulting properties is highly relevant to all oxide materials. Oxygen vacancies are discussed in the context of synthesis in-depth in Chapter Six and additional background including the motivations for controlling these defects in cobaltite oxides are presented therein.

Oxygen vacancies represent just one type of defect in the oxide materials, though they are a very common one. In addition to the various complexities present in the bulk structure of oxides, there is also the separate matter of a materials surface. Since surfaces and interfaces are so important to the growth of superlattices and the properties of oxide materials it is important to understand their structure and features.

## 2.7 Surface Structures

The surface of a crystalline material is distinct from the bulk because the truncation of the bulk periodic structure creating a surface introduces additional degrees of freedom for the atoms exposed. In a complex crystal, like those of the perovskite oxide family, the properties and atomic arrangement at the surface can be quite different from the bulk.

Atoms will adopt a structure that minimizes their energy in a given environment whenever possible. However, when a surface is created, atoms find themselves in high-energy environments due to multiple factors which may include “dangling bonds” [109] caused by truncating the bulk crystal structure, and the charge repercussions of a polar surface [110, 111]. One way to alleviate these issues and adopt a lower energy is atomic rearrangement, resulting in surface reconstructions. Alternatively, the adsorption of small, charge-compensating species can cause reconstructions to form [112, 113]. While these phenomena are driven by the need to minimize the surface energy, the exact nature of the underlying driving forces for this rearrangement is a subject of ongoing discussion that will be touched upon in Chapter Four. Regardless of the exact reason for their formation, in all of these cases atomic rearrangements result in surface reconstructions: two-dimensional periodic structures that are different from the underlying bulk.

A reconstruction is often discussed in terms of its size in two dimensions with respect to the underlying bulk unit cell of the crystal. The underlying bulk unit cell defines the size of a  $(1 \times 1)$  reconstruction and the size of surface structures is named based on this custom. In this notation, known as Wood’s notation [114], reconstructions can be distinguished from each other and information about their relationship to the bulk unit cell can be conveyed easily. An illustrative example of a  $(2 \times 3)$  reconstruction is shown in Figure 2.4. This convention will be used throughout

this work in the names of the reconstructed surfaces discussed herein.

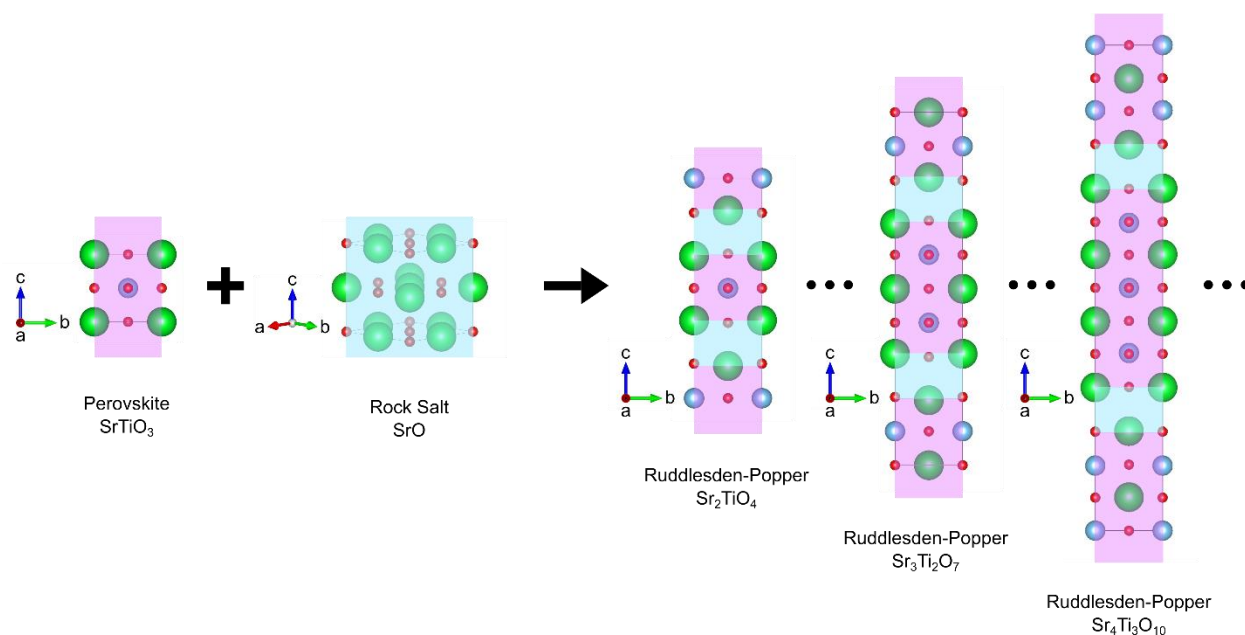


Figure 2.4 An example of Wood's notation showing a  $(2 \times 3)$  reconstruction created by two different atomic species denoted by blue and red circles over a bulk ordering of white circles.

For a given material, multiple surface reconstructions which vary in size and composition (or their relationship to the bulk ordering) are possible, as long as certain conditions (e.g. charge neutrality) are satisfied. However, different structures may be more or less stable under given conditions. For example, the stable structure might be determined by the oxygen partial pressure or the chemical potential of available species. The reconstructions present on oxide surfaces have been observed to depend on the conditions under which they form, be it through applying ultrahigh-vacuum reducing conditions, different annealing procedures, subtle variations in A:B cation stoichiometry, or synthesis conditions for nanoparticles [10, 31, 43, 47]. In some cases, it has been shown that surface reconstructions are related through dehydration, the loss of adsorbed hydroxides [112, 113].

These factors lead to considerable complexity in understanding oxide surfaces, and



determining the structure of a given surface is no small task. To this end, a number of different techniques can be employed and are often combined. Reflection high-energy electron diffraction, low-energy electron diffraction, transmission electron diffraction, and surface x-ray diffraction have all been used, combined with appropriate calculation methods, to determine structures [115-121]. Density functional theory and more sparse experimental methods such as scanning tunneling microscopy can also be combined to elucidate structures [29, 58, 122-124]. Having a variety of techniques available allows surfaces to be probed under different conditions.

Chapters Four and Five both deal with discussions of surface structures and reconstructions on perovskite oxide materials and further background information on these topics is provided therein.

## CHAPTER 3

### **Methods**

A variety of experimental and theoretical methods for prediction, property measurement, and structural determination were utilized throughout this work. Details on the important features of these methods, as well as background information helpful to their understanding and interpretation are covered in this chapter.

### **3.1 Experimental Methods**

#### **3.1.1 Oxide MBE**

The perovskite and related families of oxide materials have been produced using many different methods including wet-chemical synthesis and solid-state techniques [105, 125-127]. However, bulk-synthesis techniques lack the ability to incorporate different cation materials in a systematic manner with precise control over elemental stoichiometry at the level required for thin-film superlattices. For these cases, thin film deposition, which can be viewed as similar to additive manufacturing, is preferable.

One such technique, molecular beam epitaxy, allows material growth to be controlled by varying the flux of heated solid elemental sources. Since MBE takes place under ultra-high vacuum (UHV) conditions, the mean free path of the effusing atom is very long, and the physical barrier of shutters can be employed to control deposition. In some cases deposition is controlled such that an adsorption-controlled regime is accessed, allowing near-perfect stoichiometric control [128]. While growth via MBE is very precise, it is not quick, as a source's flux is limited by the temperature to which it can be heated.

The advantage that MBE often has over methods that produce similar qualities of crystalline materials (i.e. with low defect concentration), such as PLD, is in the flexibility afforded by multiple sources. PLD uses a ceramic target as its source and, while the stoichiometry of

elements in this target can be customized, it is not easy to deposit many different species in a desired sequence. MBE systems can have multiple metal sources, and a high degree of flexibility is present, as these sources can be precisely shuttered to produce any desired sequence of material deposition. Since many of the investigations in the work presented here were made with the aim of depositing a precise amount of material (on the order of single atomic layers) MBE was chosen as the deposition method of choice.

### **3.1.2 MBE Chamber for in situ X-Ray Diffraction Experiments**

The chamber used for molecular beam epitaxial growth in all experiments presented in this work is located at the Advanced Photon Source (APS) Sector 33-IDE. It was designed to allow for simultaneous growth and X-ray scattering measurements of thin films [129, 130]. This chamber can be used to perform reactive molecular beam epitaxy using either  $O_2$  or  $O_3$  as an oxidizing source for oxide material synthesis. A brief overview of the features and geometry of this chamber will now be discussed.

This chamber is mounted on a base that provides axes of motion equivalent to a six-circle diffractometer. These are shown in Figure 3.1.

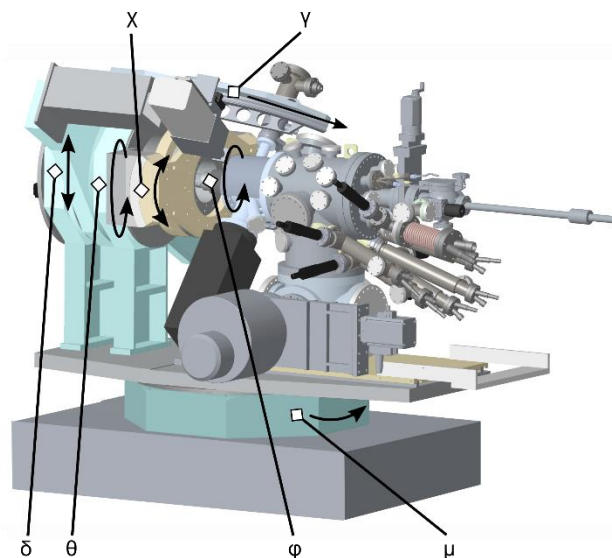


Figure 3.1 Schematic depiction of the in situ X-ray system for hybrid MBE growth. The oxide MBE chamber is mounted on a six-circle diffractometer with the axes of motion indicated [129].

The angle naming convention shown in Figure 3.1 is the same used in Ref [131]. The sample orientation is controlled by  $\phi$ ,  $\chi$ , and  $\theta$ , while the detector is controlled by  $\delta$  (parallel to  $\theta$ ), and  $\gamma$  (orthogonal). All of these circles sit on a base circle,  $\mu$ , which rotates around a vertical axis. Some of these axes of motion are restricted by physical constraints of either the chamber or the space the chamber occupies in the X-ray hutch. The “tilting” sample axis,  $\chi$ , has motion restricted to  $\pm 5^\circ$ , while the chamber’s base,  $\mu$ , can rotate approximately  $25\text{--}30^\circ$  from the configuration shown in Figure 3.1. In this chamber geometry, the growth substrate is mounted vertically with its sample normal pointed toward the right of the figure, aligned with the sample manipulating rod.

The beamline where this chamber is located is a high-energy beamline where the energies of X-rays that can be easily accessed range from 6 – 18 keV. When selecting a particular X-ray energy, we desire access to as much of reciprocal space as possible for the collection of scattering data while avoiding higher-order harmonics from the monochromator. There is limited access to X-ray energies that can be used for X-ray absorption measurements, as this beamline is optimized

for diffraction. However, if the absorption edge of interest lies within the accessible range, it is possible to perform limited X-ray absorption near-edge spectroscopy (XANES) measurements or perform diffraction measurements above and below the absorption energies of a specific, desired element. In terms of diffraction, crystal truncation rods (CTR) can be measured for any accessible reciprocal space geometry available to the motors- proper alignment is all that is required. Additionally, a specific diffraction condition can be monitored in situ during growth (i.e. the change in intensity at a specific diffraction condition can be monitored over time). While CTR measurements can be performed during growth, their collection is not always swift enough to provide utility.

Various aspects of this chamber are modified from a typical MBE chamber to allow for X-ray measurement. A beryllium window is located in the cylindrical section to allow incoming X-rays into the chamber for an angular range of  $-3^{\circ}$  to  $45^{\circ}$  with respect to the sample surface. Additionally, the sample holder stage, which uses resistive heating to control the sample temperature, can be moved in and out of the chamber from its back, such that the X-ray beam can be precisely cut in half by the sample surface at  $0^{\circ}$  incidence angle. To facilitate MBE growth, the chamber is equipped with a quartz crystal microbalance (QCM) that measures a source element's flux and can be moved to the same position as the growth substrate (the sample stage is temporarily pulled partway back, out of the chamber during calibration). All sources are directed at the sample position during growth and are equipped with shutters for controlling the deposition time and sequence of the different metals.

This chamber is specifically equipped for oxide material growth. To provide a sufficiently oxidizing environment, a leak valve is installed on the system so that  $O_2$  or  $O_3$  gas can be delivered

to the chamber during growth.  $O_3$  is provided by an ozone distiller [DCA, Finland] and can be delivered at a level of nominally 100%  $O_3$ . Alternately, the distiller can be bypassed and a mixture of 90%  $O_2$  and 10%  $O_3$  (which the ozone generator in this instrument produces) can be delivered. These gases can be delivered up to a background pressure of  $10^{-5}$  Torr before the heated metal sources used for deposition are in danger of oxidizing [132, 133]. This background pressure is also near the upper limit that the 1000 L/s turbo pump and ion pump on the chamber can control.

### 3.1.3 Surface X-Ray Diffraction

Bulk diffraction of all types (neutron, X-ray, electron) is used to determine the structure of oxides. If a source of high brilliance is utilized in X-ray diffraction the structure of the surface can also be measured [120]. Since X-rays scatter weakly when interacting with atoms they can be treated with the kinematical approximation. This, combined with Huygens principle, allows each atom to be treated as a scattering center leading to Bragg peaks from the crystal occurring when all secondary waves emitted from the scattering centers interfere constructively. This leads to a discrete grid in reciprocal (momentum) space known as the reciprocal lattice. If this is treated as being equal to the Fourier transform of the crystal lattice then the convolution theorem can be used to understand diffraction from the surface.

A crystal's surface can be represented as an infinite crystal multiplied by a step function in one direction. The Fourier transform of this step function is a  $\frac{1}{q_z}$  shape function and the diffraction pattern is determined by the convolution between the reciprocal lattice and the shape function, as shown in Figure 3.2.

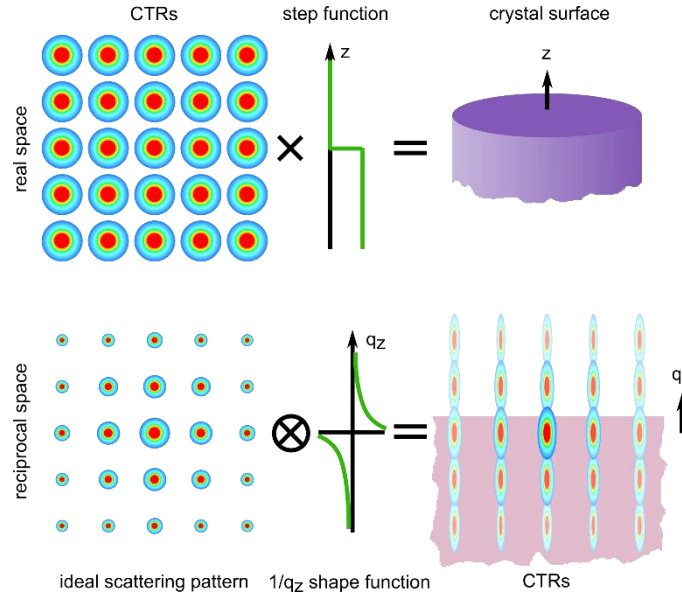


Figure 3.2 Crystal Truncation Rods (CTRs) from surface scattering explained in terms of convolution of a perfect crystal with a step function.

This leads to diffraction patterns with rods of intensity between the Bragg peaks perpendicular to the material surface, known as crystal truncation rods. Since actual crystals do not have infinitely sharp surfaces, the intensity between the Bragg peaks can vary. By applying corrections, taking into account the sample and X-ray beam geometry, the structure factor,  $F_{sum}$ , of the structure near the material's surface can be measured. This can be used to measure the thickness of a film grown on a substrate, understand the epitaxial (or non-epitaxial) relationship at an interface, find structural periodicity in the direction perpendicular to the surface, and even determine the electron density of the material using direct methods [134-136].

SXRD has been used to determine the structure and dynamics of growth for thin film materials like  $\text{Sr}_{n+1}\text{Ti}_n\text{O}_{3n+1}$ , a Ruddlesden-Popper oxide [137]. The setup utilized in this work is designed to allow in situ monitoring of specific diffraction conditions during materials growth as well as measurement of CTRs [129, 130]. These measurements are carried out at the Advanced



Photon Source (APS) at Sector 33-IDE. When SXRD results are discussed in this work, often one monolayer (ML) is mentioned. For (0 0 1)-oriented perovskite-like films, this describes an  $\text{AO}_x/\text{BO}_y$  unit. Generally, the films have low lattice mismatch with the substrate and this ML thickness is very similar to that of the out-of-plane lattice constant of the substrate.

### 3.1.4 X-Ray Absorption Spectroscopy

Another technique that can be performed in the MBE chamber is XAS. While the range of accessible energies at this beamline is limited, the absorption edges of some transition metals (and lanthanides) can be accessed as they are high enough in energy. For example, two elements that are present in structures in the following investigations include Sr and Co, both of which have accessible K-edges at 16.1 and 7.7 keV, respectively [138, 139]. With the ability to tune energies with the Si (1 1 1) monochromator at the Sector 33-IDE beamline, an energy range appropriate for XANES can be probed.

XAS measurements rely on the absorption cross-section of the element,  $\sigma$ , i.e. the probability of exciting an electron from some initial state,  $\varphi_i$ , to some final state,  $\varphi_f$ , via the absorption of photons. Applying Fermi's Golden Rule and the dipole approximation to this scenario leads to the following definition of  $\sigma$  in Equation 3.1.

$$\sigma = \frac{4\pi^2 h^2 e^2}{m^2} \frac{1}{hc h\omega} \zeta(E) |\langle \varphi_f | \hat{e} \cdot \vec{r} | \varphi_i \rangle|^2 \delta(h\omega + E_i - E_f) \quad (3.1)$$

Here,  $h$  is Plank's constant,  $c$  is the speed of light,  $h\omega$  is the incident photon energy,  $e$  and  $m$  are the charge and mass of an electron,  $\zeta(E)$  is the state density of the final state,  $\langle \varphi_f | \hat{e} \cdot \vec{r} | \varphi_i \rangle$  is the dipole matrix element,  $\delta(h\omega + E_i - E_f)$  is the delta function for the conservation of energy, in this equation bra-ket notation is used.

XAS gives information about the unoccupied density of states for an element. Quantum mechanical selection rules play a major role in the shape of XAS spectra. In the experiments presented, the transition of interest is that of a metal K-edge. In this case, the electronic transitions involved correspond to core level changes where  $1s$  electrons are promoted to  $2p$ -like final states. In general XANES interpretation is more qualitative than quantitative, but with appropriate reference materials it is possible to deduce structural information. As a simple generalization, the absorption intensity around the pre-edge region (lower energies than the K-edge) gives information on the coordination of the element in question, the edge position gives information regarding the element's oxidation state, and the near edge region contains information analogous to extended X-ray absorption fine structure as well as local structural information.

The most straightforward way to use XAS data is to compare the collected data to the body of existing literature encompassing various ligand coordinations and oxide compounds [140, 141] or other samples of known structure to perform a qualitative finger-printing of the film's electronic structure. Features of a XANES spectrum can be simulated via linear combination of spectra of the components to determine their concentration, and XANES can also be used to monitor phase transitions or reactions [142, 143].

### **3.2 Theoretical and Computational Methods**

#### **3.2.1 DFT Methods**

Computational methods can be used to better understand the structure and properties of oxide materials [144, 145]. Ab initio methods, based on quantum principles, such as DFT, can be employed for these methods. DFT is a particularly useful method in the research presented herein

due to its ability to predict and elucidate unexpected properties of surfaces and interfaces [146, 147].

Quantum calculations rely on solving the  $N$ -particle Schrödinger equation where the number of variables scales as  $N^3$  for a  $N$  electron system. The time-dependent version of this equation has the following form:

$$i\hbar \frac{\partial}{\partial t} \Psi(\vec{r}, t) = \left[ \frac{-\hbar^2}{2\mu} \nabla^2 + V(r, t) \right] \Psi(r, t) \quad (3.2)$$

Where  $\mu$  is the reduced mass of a particle (its effective mass),  $\Psi(r, t)$  is the time-dependent wave function,  $V(r, t)$  is the time-dependent energy potential, and the  $\nabla^2$  operator represents the kinetic energy. As the number of electrons in a system increases the complexity of solving the Schrödinger equation analytically does too. DFT calculations rely on the idea, proposed by Hohenberg and Kohn [148, 149], that electron density has a one-to-one correspondence with any ground state observable property of the material. DFT approximates this by solving the many-body equation as many single-body Schrödinger-like ones of the form shown below.

$$\left( -\frac{\hbar^2}{2\mu} \vec{\nabla}_m^2 + \frac{e^2}{4\pi\epsilon_0} \int \frac{\rho(\vec{r}')}{|\vec{r} - \vec{r}'|} + V_{xc} + V_{ext} \right) \psi_m(\vec{r}) = \epsilon_m \psi_m(\vec{r}) \quad (3.3)$$

To do this, the exact form of the potential energy term is desirable, but this term can only be approximated, and the description of both the exchange and correlation energies within it are challenges for DFT methods. The exchange-correlation functional,  $V_{xc}$ , is defined in many DFT codes using the local density approximation (LDA) and generalized gradient approximation (GGA) [150, 151]. The LDA assumes slow variation in electron density while GGA deals with gradients

in electron density that allow for inhomogeneous variation and localization in electronic structure. The energy density functional [150] for each of these two approximations, in its spin-resolved form, is given by:

$$E_{xc}^{LDA}[n \uparrow, n \downarrow] \int n(r) \epsilon_{xc}(n \uparrow(r), n \downarrow(r)) d^3r \quad (3.4)$$

$$E_{xc}^{GGA}[n \uparrow, n \downarrow] \int f(n \uparrow, n \downarrow, \nabla n \uparrow, \nabla n \downarrow) d^3r \quad (3.5)$$

One of the most popular GGA functionals, the PBE (Perdew-Burke-Ernzerhof) functional [152], is the basis of a revised functional used in these investigations, the PBEsol functional (the PBE functional for solids and surfaces) [153]. All the materials considered in these calculations contain transition metals, which have strongly correlated electrons due to the partial occupation of their *d*-electron orbitals coupling strongly with *2p* oxygen orbitals. These are not well-modelled by the methods described up to this point and require a further correction. A fraction of exact-exchange for the relevant orbitals is included using the Hartree-Fock (HF) method. The fraction of HF included varies on a system-by-system basis, and the value used is determined by finding the closest match to the experimental heats of formation for relevant bulk transition metal oxides for the cation in question.

The DFT package used for calculations presented in this work is WIEN2k [154]. It is an all-electron augmented plane wave plus local orbital code. Local orbitals define regions inside the muffin-tin radii while plane waves treat the interstitial regions. Within muffin-tins, the basis set used is a combination of spherical harmonics, radial functions, and local orbitals. For the plane waves to remain continuous at the boundary of the muffin-tin, there are constraints placed on this

basis set. The accuracy of this code is set by choosing the smallest muffin tin radius ( $R_{mt}$ ) and the largest k-vector ( $K_{max}$ ), often selected to provide a balance of accuracy and computation expense.

A theoretical materials structure can be relaxed with DFT to determine atomic positions, its density of states, and simulate experimental results such as XAS or scanning tunneling microscopy (STM) [154-156]. Careful construction of the units cell allows for surface energies and properties to also be calculated.

A construction known as the convex hull will be discussed at various times in the experiments presented. These graphs are made by calculating the surface energy of a relaxed reconstruction. Theoretical structures' energies can be compared to those of already-determined structures for the same material and bulk termination. These energies are then referenced to the calculated energy of the bulk material in question and any oxides making up its structure; for  $SrTiO_3$  this means that energies are referenced to that of bulk  $SrTiO_3$  and rutile  $TiO_2$ . To calculate the energy of a surface per  $(1 \times 1)$  surface unit cell, the following equation is used:

$$E_{surf} = (E_{slab} - E_{STO}N_{STO} - E_{TiO_2}N_{TiO_2}) / (2 * N_{(1 \times 1)}) \quad (3.6)$$

where  $E_{slab}$  is the total energy of the slab,  $E_{STO}$  is the energy for a single bulk  $SrTiO_3$  unit cell,  $N_{STO}$  is the number of bulk  $SrTiO_3$  unit cells present,  $E_{TiO_2}$  the total energy of bulk rutile  $TiO_2$ ,  $N_{TiO_2}$  the number of excess  $TiO_2$  units, and  $N_{(1 \times 1)}$  the number of surface  $(1 \times 1)$  unit cells. Both  $N_{STO}$  and  $N_{TiO_2}$  are determined by finding the total number of atoms in the slab construction used. When surface energy is plotted against  $TiO_2$ -excess, as in the convex hull construction, this quantity is found by normalizing to surface area such that

$$TiO_{2_{excess}} = (N_{TiO_2}) / (2 * N_{(1 \times 1)}) \quad (3.7)$$

The surface energy for different structures is calculated in this way in the following sections.

A given relaxed surface structure's viability as a possible solution can also be assessed by calculating the bond valence sum (BVS) of the surface atoms and comparing this to the BVS of the bulk material [157]. The bond valence sum is a useful parameter, and its calculation is very simple. For any single atom, the BVS is calculated using Equation 7, where the observed bond lengths,  $R_0$ , are compared to the ideal bond length,  $R_i$ , for the element when the valence is equal to 1. The empirical constant  $b = \sim 0.37\text{\AA}$  for most types of bonds.

$$V = \sum \left( \frac{R_0 - R_i}{b} \right) \quad (3.8)$$

This method is based on Pauling's rules and is used to determine the valence of an atom, or the number of electrons it uses in bonding to its neighbors [158]. It can be used to estimate the coordination of atoms [159]. However, the BVS is not appropriate as a structure prediction tool as it does not account for anion-anion interactions.

### 3.2.2 STM Simulation

STM image simulation from DFT calculated structures rely on the work of Tersoff and Hamann [160] and Bardeen's tunneling theory [161]. This theory assumes that the STM tip and sample system is the same as a metal-insulator-metal junction. Independent wavefunctions of both sides of the tunneling barrier are approximated as orthogonal. The Tersoff-Hamann approximation results when limits of low sample-tip bias and temperature are applied. In this approximation, the tunneling current,  $I_t$ , is related to the density of states (DOS) around the sample's Fermi energy,  $E_F$ , according to Equation 3.9.

$$I_t \propto \rho(\mathbf{r}, E_F) \equiv \sum_{\mu} |\psi_{\mu}(\mathbf{r})|^2 \delta(\varepsilon_{\mu} - E_F) \quad (3.9)$$

In Equation 3.9,  $\psi_{\mu}$  is the sample wavefunction, with the eigenvalue  $\varepsilon_{\mu}$ , where  $\mu$  is the probe displacement. Since this equation relies primarily on the local DOS, calculated from first-principles methods like DFT, it provides a way to simulate STM images. Unfortunately, this approximation breaks down for bias voltages higher than 100mV, making it inaccurate for insulating SrTiO<sub>3</sub> which is measured at very high bias voltage.

This theory was extended to high-bias and beyond spherical tips by Stokbro et al [162]. Their derivation, with the addition of a tip wavefunction expansion used by Chen [163] (where higher-order angular tip states are ignored) produces the modified relationship shown in Equation 3.10

$$I_t \propto \int_{E_F}^{E_F + e \cdot V_b} \kappa(\varepsilon)^{-2} \rho(\mathbf{r}, \varepsilon) d\varepsilon \quad (3.10)$$

where

$$\kappa(\varepsilon) = \hbar^{-1} \sqrt{2m_e(\varphi_t + E_F + e \cdot V_b - \varepsilon)} \quad (3.11)$$

$\kappa(\varepsilon)$  is the inverse decay length of electron states in vacuum for an energy  $\varepsilon$ ,  $\varphi_t$  is the workfunction of the tip, and  $m_e$  is the mass of an electron with charge  $e$ .

To apply this to DFT, a relaxed, converged structure where the unoccupied states between  $E_F$  and  $E_F + e \cdot V_b$  are artificially populated (weighted by a factor of  $\kappa(\varepsilon)^{-2}$ ), can be used to simulate STM images. When performing a simulation, the value of  $E_F$  must be chosen: for Nb-doped bulk SrTiO<sub>3</sub>, the Fermi energy lies at the top of the bandgap. The quantity,  $V_b$ , represents the experimental bias voltage. However, the majority of an image's contrast is due to the

topological variation of atoms at a sample surface. In light of this, as long as the DOS is integrated over a reasonable energy range, the DFT-calculated Fermi energy can be used. To illustrate this, since it can be difficult to determine the exact experimental bias voltage used, a variety of energy ranges are chosen of a similar order of magnitude as the experimental value. The energy window that best reproduces the experimental image is chosen for final simulation parameters. One such series is shown in Figure 3.3 where the simulation that best reproduces the experimental features is between 2.45 – 2.72 eV.

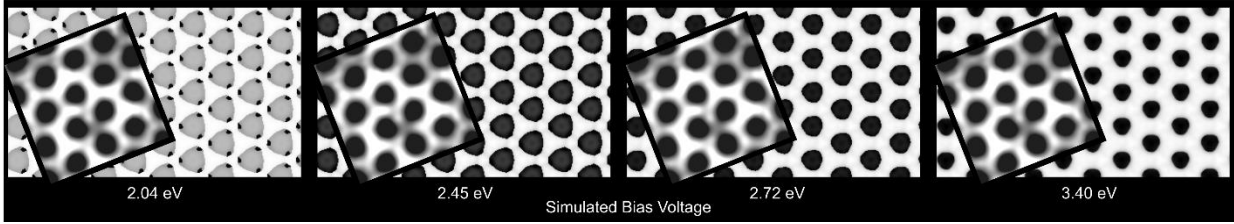


Figure 3.3 Simulated STM of the  $(\sqrt{13} \times \sqrt{13})R33.7^\circ$  (RT13b) reconstruction at different bias voltages indicated below the corresponding frame. The inset image in each frame is unit cell averaged STM (+3.5 V bias, 0.1 nA current) of the RT13b shown for comparison.

For comparison with experiments in constant-current (rather than constant height) mode, the artificial local unoccupied DOS must be sampled over a volume rather than a simple plane. Values of the sampling density for out-of-plane and in-plane intervals are chosen to provide sufficient resolution for generating a 3-D array of densities. Additionally, the experimental tip size is finite (rather than infinitesimally small), and there is instability or vibration during measurement. These effects are accounted for in a simulation by convoluting each sampled space with a radially symmetric step-function convolution, shown below in Equation 3.12.

$$F(r) = \begin{cases} 1, & r \leq R \\ 0, & r > R \end{cases} \quad (3.12)$$



Here  $r$  is the distance from the voxel of interest and  $R$  is the effective tip size, which can be varied to best match experimental data.

## CHAPTER 4

### **Pauling's Rules for Oxide Surfaces**

Some nice intro text

## 4.1 Introduction

Oxide perovskites demonstrate an array of properties [17, 70, 71, 73, 164], while having similar structures and lattice parameters [80, 81]. These factors make it appealing to combine them in increasingly creative film structures [82, 83, 89, 165, 166]. While superstructures are interesting, surfaces and interfacial structures of these materials cannot be overlooked as they often contribute disproportionately to a material's properties [7, 11, 14, 16, 23, 68, 72]. Unfortunately, understanding the atomic arrangements on surfaces producing these effects, even for bare perovskite substrates, is not easy.

The surprising array of surface reconstructions that have been observed on oxides shows the high level of complexity in surface structures. Since so many possibilities exist, determination of surface structures is an area of great interest. Structure solutions for perovskite oxides surfaces have been found using combinations of methods, particularly in the case of  $\text{SrTiO}_3$  [26-41, 44-49, 53, 56-58, 60-62, 167-169].  $\text{SrTiO}_3$  has an ideal perovskite structure and is frequently utilized as a growth substrate, making it a good example case. Three orientations: (1 0 0), (1 1 0), and (1 1 1) have also been studied on the  $\text{SrTiO}_3$  surface. These represent the challenges in perovskite oxide materials- they are insulating, two are polar, and one has mixed A/B cation termination if truncated along an idealized atomic plane. Other oxide surfaces have been studied, including  $\text{BaTiO}_3$  [43, 51, 52, 54, 55],  $\text{LaAlO}_3$  [42, 170], and  $\text{LiNbO}_3$  [59], although the number of reconstructions solved on these surfaces is far fewer.

Both experimental methods and simulation have been applied to solving reconstructions, but a theoretical framework explaining structures has been notably lacking. Understanding and

predicting oxide surface structures is traditionally approached from two directions: the first uses the underlying physics/chemistry to produce general formulations, the second consists of specific calculations (density functional schemes are typical). The first approach includes explanations focusing on surface dangling bonds [109], minimizing Coulomb forces [171], or considering aspects such as charge compensation in polar surfaces [110, 111]. These cases rely on the fundamental idea that a surface must be valence neutral (we will present an explanation regarding use of the terms “valence” and “charge” later). Neutrality can be achieved by atomic rearrangement i.e. surface reconstructions. These theories deal specifically with the surface and address the difficulty of modelling a realistic surface. However, they do not offer explanation for how surface and bulk relate. Though they point out the important fact that a surface structure has no formal charge, this information alone is not enough to produce a unique solution.

The second approach is based on ab initio calculations. In it, oxide surfaces are often described as ideal truncations of the bulk crystal. Even if oxygen vacancies are included in this model, it still represents an oversimplification that does not agree with the large body of experimental evidence regarding the nuances of oxide surfaces [39, 40, 43, 59, 63]. In addition, ab initio methods are not guaranteed in all cases to produce the correct result. The initial positions of atoms in a hypothetical structure can influence the final resulting relaxed structure, leading to non-unique solutions. Such a structure may appear reasonable despite representing a local rather than global energy minimum. Ab initio methods are also unable to correct issues arising from incorrect chemical composition of a hypothetical structure. As an example, the  $(2 \times 1)$  reconstruction on  $\text{SrTiO}_3$  (1 0 0) contains chemisorbed water [35, 112, 113], a feature that ad initio methods alone would not be able to identify. Another example is an early model for the  $c(6 \times 2)$  reconstruction

on the same surface. This model failed to include surface strontium that later, more detailed, analysis showed [32, 46]. It is possible to avoid these pitfalls by performing a global search over different possible structures. However, this requires expensive computation and generating an exhaustive list of structures is challenging. Ab initio methods can also encounter difficulty when describing strongly correlated oxides which are common in this material family [172].

Ways to predict and judge the reasonableness of atomic structures, that use a chemical approach to complement physics-based ideas are necessary. Progress in addressing this has been made considering the  $\text{SrTiO}_3$  (1 0 0) surface. Polyhedral packing of  $\text{TiO}_5$  units was first proposed with the solution of the  $\text{SrTiO}_3$  (1 0 0)  $(2 \times 1)$  surface [35]. With these units identified, many proposed arrangements were investigated with DFT calculations to conclude that low-energy arrangements minimized non-bonding oxygen interactions [173]. The bulk concept of bond valence sums was applied to understanding oxide surfaces [157]. Using these ideas and calculating hypothetical structures via DFT has led to identification of multiple structures with similar surface energy. This supports indicates that surfaces can have a 2-D network glass-like structure with short-range order if the other requirements are fulfilled [41, 49, 174].

In this chapter, we propose a general explanation based on the one outlined by Linus Pauling in 1929 [175]. Pauling's rules provides guidelines for understanding oxide surface structures. They have been shown to suit bulk structures and can be adapted and applied to oxide surfaces to explain observed surface structures. Solved reconstructions on  $\text{SrTiO}_3$  surfaces are discussed from the perspective of Pauling's rules. Common features are identified and explained within this framework, revealing similarities in structure across these otherwise disparate surfaces. Nanostructures on the  $\text{SrTiO}_3$  (1 0 0) and (1 1 0) surfaces are discussed. These thicker surface

structures begin to resemble the films present in the first stages of heteroepitaxial growth and they provide insight into interfacial structures in oxide films. Finally, the reconstructions on two other oxide surfaces,  $\text{BaTiO}_3$  (1 0 0) and  $\text{LaAlO}_3$  (1 1 0), are presented.

## 4.2 Pauling's Rules

First we present a general explanation of how Pauling's rules relate to surfaces before going into specific examples. Pauling's rules [175] were originally stated as follows:

1. "A coordinated polyhedron of anions is formed about each cation, the cation-anion distance being determined by the radius sum and the coordination number of the cation by the radius ratio."
2. "In a stable coordination structure the electric charge of each anion tends to compensate the strength of the electrostatic valence bonds reaching to it from the cations at the centers of the polyhedral of which it forms a corner; that is, for each anion"

$$\zeta = \sum_i \frac{z_i}{v_i} = \sum_i s_i \quad (4.1)$$

Where  $\zeta$  is the charge of the anion,  $z_i$  is the electric charge of a cation,  $v_i$  its coordination number, and  $s_i$  the strength of the electrostatic valence bond.

3. "The presence of shared edges, and particularly shared faces, in a coordinated structure decreases its stability; this effect is large for cations with large valence and small coordination number, and is especially large in case the radius ratio approaches the lower limit of stability of the polyhedron."
4. "In a crystal containing different cations those with large valence and small coordination number tend not to share polyhedron elements with each other."

5. “The number of essentially different kinds of constituents in a crystal tends to be small.”

These rules have already held up in bulk oxides. Only Pauling’s second rule has changed somewhat since its initial publication. A modern interpretation would be to refer it in terms of valence, rather than electrostatic charge. In all oxides (barring some superoxides or peroxides which contain  $\text{O}_2^{2-}$  ions), oxygen’s valence state is 2-, where the sign is written after the number. Electrostatic charge on oxygen is generally smaller, and the sign is written on the number’s other side (e.g. -1.5). Valence is considered in terms of the BVS model [157, 158, 176, 177]. For the limit of a totally ionic model, electrostatic charge and valence are identical, but in reality a full ionic model is unrealistic for most oxide cases.

Pauling’s second rule has been investigated in detail [157], indicating that the bond valence sum (BVS) model [157, 176-178] can qualitatively predict the relative energy of a surface structure consistent with DFT relaxation and experimental evidence. It can also give insight into adsorption or disassociation behavior by identifying whether atoms are over- or under-bonded. We argue that all Pauling’s rules similarly provide generic guidelines that oxide surfaces obey.

Pauling’s fifth rule is a logical place to start, stating “The number of essentially different kinds of constituents in a crystal tends to be small.” It implies that the number of unique units making up a surface structure is small. A surface structure can be broken down and described by a few “puzzle pieces”, not all possible combinations need to be considered.

Next the structural units are described in Pauling’s first rule. These units contain a cation surrounded by anions (oxygen). Their arrangements are described by regular chemical polyhedra. For example, bond lengths and angles in a  $\text{TiO}_4$  cation polyhedron are as similar as possible to those of an ideal tetrahedron, and so on for all coordinations. The portion of the rule explaining

the radius ratio indicates how many oxygens a cation is coordinated with in its most stable configuration; it identifies the  $x$  in any  $\text{AO}_x$ .

The last rules govern organization of units with respect to one another and combine information from Pauling's third and fourth rules. Cation polyhedra sharing faces are higher in energy than those sharing edges, which are higher in energy than those sharing corners. This effect is more pronounced for cations with higher valence and smaller coordination numbers; e.g., a tetrahedral unit of  $\text{TiO}_4$  (with  $\text{Ti}^{4+}$ ), is less likely to share a face than an edge with another  $\text{TiO}_4$  unit compared to an octahedrally coordinated  $\text{TiO}_6$  unit. Furthermore, a cation of lower valence ( $\text{Sr}^{2+}$  in  $\text{SrTiO}_3$ ), is more likely than  $\text{Ti}^{4+}\text{O}_x$  polyhedra to share faces or edges due to its lower valence and higher coordination.

These rules imply the relevance of Ising or Potts models (see also [49]). For surfaces to interface properly with atoms in the bulk, only certain sites can be occupied, and these will form a lattice. The Ising model can be used when sites are only occupied by one type of structural unit. With more structural units a Potts model becomes relevant. Potts models for simpler surface phenomena such as chemisorption or melting have been reported in the literature (e.g. [179-184]).

These guidelines are obeyed for known oxide surface structures, as will be shown in this chapter. This implies that the rules also place restrictions on the lowest energy atomic arrangements of unknown oxide surfaces. When there are many different surface structures as a function of composition, the building blocks of reconstructions can be identified and specific rules for their arrangement extracted. They also provide insight into phenomena occurring at surfaces such as the formation of nanostructures and thin film growth. These points will be addressed in the following sections.



### 4.3 Case Analyses

Specific cases and show that a large number of solved oxide surface structures follow Pauling's rules. This supports the hypothesis that they are a powerful, general approach for understanding and predicting oxide surface structures. Reconstructed (1 0 0), (1 1 0), and (1 1 1) surfaces of  $\text{SrTiO}_3$ ,  $\text{SrTiO}_3$  nanostructures, film growth on  $\text{SrTiO}_3$  (1 0 0), reconstructions on  $\text{BaTiO}_3$  (1 0 0), and reconstructions on  $\text{LaAlO}_3$  (1 1 0) will be discussed as specific examples. First, the universal features of all solved reconstructions on  $\text{SrTiO}_3$  will be outlined.

All experimentally solved reconstructions on  $\text{SrTiO}_3$  (to date) are charge and valence neutral, can be represented by the formula  $n\text{SrTiO}_3 \cdot m\text{TiO}_2$ , and have Ti-rich outer layers.

There other universal features for all the  $\text{SrTiO}_3$  reconstructions are related to Pauling's rules:

1. According to Pauling's fifth rule, a structure will minimize the number of different arrangements of its atoms. As such, structures with higher symmetry are lower in energy; higher symmetry yields fewer inequivalent atomic positions in a unit cell, and fewer bonding environments.
2. Either an Ising or Potts model can be used to consider all surfaces- an Ising model for binary systems of structural units and a Potts model for more complex ones. This relates to Pauling's fifth rule.
3. Pauling's first rule contains the radius ratio explanation. According to this a 6-fold octahedral coordination with oxygen ( $\text{TiO}_6$ ) is the lowest-energy arrangement for Ti atoms. As the surface density of Ti atoms decreases, Ti adopts coordinations with fewer oxygen atoms to maintain a continuous, periodic network on the surface- 5-fold octahedral

coordinations ( $\text{TiO}_5[\ ]$ ), and then 4-fold tetrahedral coordinations ( $\text{TiO}_4$ ) are adopted. The 5-fold octahedral coordinations are based on  $\text{TiO}_6$  units with a single oxygen vacancy. The coordinations  $\text{TiO}_x$  can adopt are shown in Figure 4.1, where their bond lengths and angles (for Ti-O) are at a minimum energy when they are as similar as possible to the ideal polyhedron; this reduces the non-bonded repulsions between oxygen atoms.

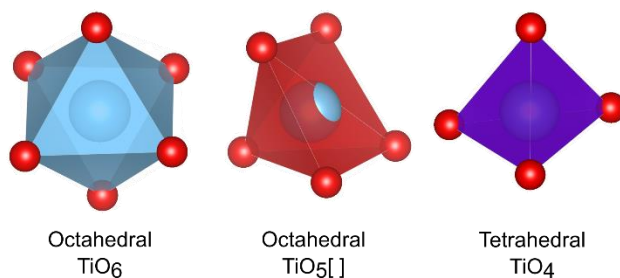


Figure 4.1 Idealized coordination environments for  $\text{TiO}_x$  showing (from left to right) octahedral  $\text{TiO}_6$ , octahedral  $\text{TiO}_5[\ ]$ , and tetrahedral  $\text{TiO}_4$ .

4. The lowest-energy sites for  $\text{TiO}_x$  unit to occupy on the  $\text{SrTiO}_3$  surface are those that represent a continuation of bulk ordering. These are referred to as “natural Ti sites” herein. These sites obey Pauling’s third and fourth rules and minimize the number of shared faces between cation polyhedra in the lower bulk layers.
5. Oxygen atoms are always coordinated to two or three cations, three mainly when they are coordinated to strontium. This follows from rules 1-3 and partially 4. As an example, if only corner-sharing occurs, then the oxygen can only be bonded to two cations. Three-fold coordination requires edge-sharing which is more likely with lower valence atoms such as strontium.

#### 4.3.1 $\text{SrTiO}_3$ (1 0 0):

$\text{SrTiO}_3$  (1 0 0) possesses many identified reconstructions. Reported and solved reconstructions are summarized in Table 4.1. The solved reconstructions shown in Figure 4.2 will be discussed in terms of Pauling's rules.

Table 4.1. Reconstructions on  $\text{SrTiO}_3$  (1 0 0) from the literature.

Reconstruction	Structure Status	Pictured	Reference/s
(1 × 1)	Observed, models proposed	n/a	[26, 29, 33, 39]
(2 × 1)	Observed and solved	Figure 4.2 (c)	[29, 33, 35, 36, 39, 56]
(2 × 2)	Observed and solved	Figure 4.2 (b)	[26, 33, 39, 45, 53, 173]
(2 × 2)A	Observed and solved	Figure 4.2 (a)	[26, 33, 39, 45, 48, 53]
c(4 × 2)	Observed and solved	Figure 4.2 (f)	[30, 36, 40]
c(4 × 4)	Observed, models proposed	n/a	[30, 40, 45]
(4 × 4)	Observed, models proposed	n/a	[45]
c(6 × 2)	Observed and solved	Figure 4.2 (d)	[30, 32, 36, 40, 46, 56]
( $\sqrt{5} \times \sqrt{5}$ )R26.6°	Observed, models proposed	n/a	[44, 45, 61, 168]
( $\sqrt{13} \times \sqrt{13}$ )R33.7°	Observed and solved	Figure 4.2 (e)	[41, 45, 56]

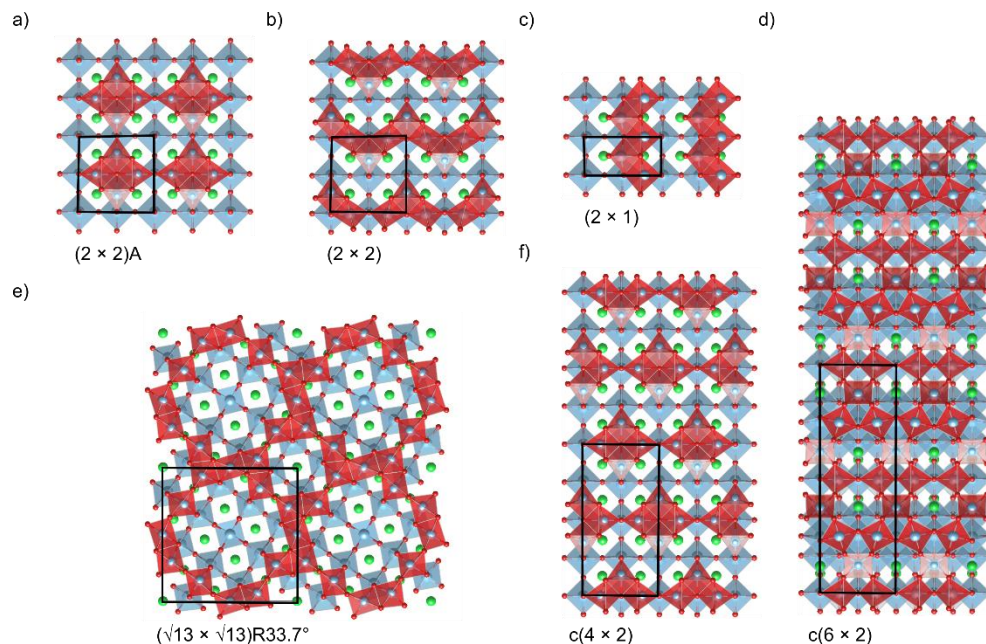


Figure 4.2 Atomic structure of solved reconstructions on the  $\text{SrTiO}_3$  (1 0 0) surface showing (a) (2 × 2)A, (b) (2 × 2), (c) (2 × 1), (d) c(6 × 2), (e) ( $\sqrt{13} \times \sqrt{13}$ )R33.7°, and (f) c(4 × 2).  $\text{TiO}_5$  units are red,  $\text{TiO}_6$  light blue. Sr atoms are green, Ti are blue, and oxygen are red.

All reported structures decorate the bulk  $\text{TiO}_2$ -plane termination of  $\text{SrTiO}_3$ . The  $(2 \times 1)$ ,  $(2 \times 2)\text{A}$ ,  $(2 \times 2)$ ,  $c(4 \times 2)$ , and  $(\sqrt{13} \times \sqrt{13})\text{R}33.7^\circ$  are formed in a Ti double-layer structure, where  $\text{TiO}_5[\ ]$  units are located on top of the bulk-like  $\text{TiO}_2$  plane. These  $\text{TiO}_5[\ ]$  have four oxygen atoms in the same plane or slightly above the central Ti. Two oxygens at opposite ends of the polyhedron are shared with bulk-like  $\text{TiO}_6$  below. Remaining oxygens are shared with other  $\text{TiO}_5[\ ]$  in the same layer. Each  $\text{TiO}_5[\ ]$  shares an oxygen atom below the central Ti with two bulk-like  $\text{TiO}_6$  below. Oxygen atoms can be shared with more than two Ti, but this configuration is unfavorable. This description outlines an Ising model, as shown as a symbolic representation in Figure 4.3, using the  $(2 \times 2)$  reconstruction as an example.

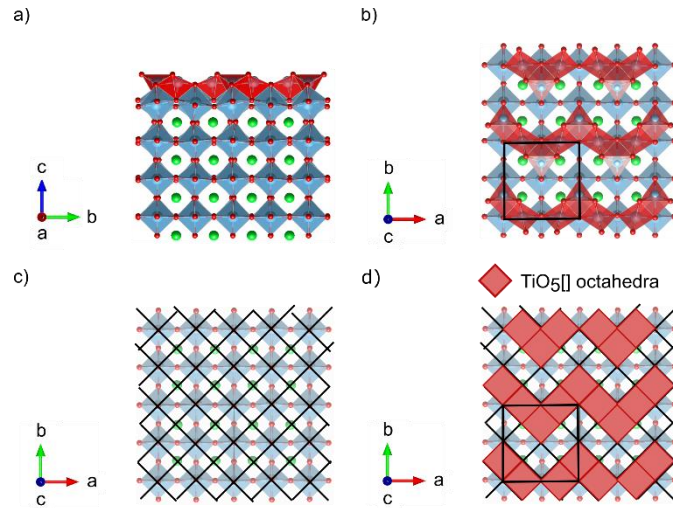


Figure 4.3 Atomic structure of the solved  $(2 \times 2)$  reconstruction on  $\text{SrTiO}_3$  (1 0 0) viewed from the a-axis (a), and c-axis (b). In (c) a square grid is imposed on the underlying bulk  $\text{TiO}_2$  layer and in (d) the reconstruction is represented by red squares showing placement of  $\text{TiO}_5[\ ]$  units on this grid.

In Figure 4.3 (a) and (b) the reconstructed surface is viewed along different axes. A grid can be drawn on the bulk-like  $\text{TiO}_2$  layer in Figure 4.3 (c). Figure 4.3 (d) shows the reconstruction is codified into a symbolic representation with one type of structural unit,  $\text{TiO}_5[\ ]$ . These occupy positions such that the Ti atom sits above an oxygen (at the imposed grid's center). Four oxygen

atoms defining the  $\text{TiO}_5$  are laterally located near the grid intersections, some closer to vacuum than the Ti atom. This is represented by red squares in Figure 4.3 (d). An Ising model is appropriate for these surfaces since there are only two options for occupation of each grid position- a  $\text{TiO}_5$  unit or nothing.

In these reconstructions there is only one coordination environment needed to describe these reconstructed surfaces:  $\text{TiO}_5$ . This follows Pauling's fifth rule, stating that the number of structural units is small. Pauling's first rule indicates that the  $\text{TiO}_5$  units, when relaxed, will have atoms at positions as close to ideal octahedra as possible.

In accordance with the third and fourth rules Pauling outlined,  $\text{TiO}_5$  units occupying the grid in Figure 4.3 (c) do not share faces with other  $\text{TiO}_x$  units. The sharing of edges between  $\text{TiO}_5$  is also minimized. As Ti-excess coverage increases in these reconstructions, a more densely-packed network of  $\text{TiO}_5$  units has increasing levels of edge sharing. Nevertheless, this minimization rule is still followed.

#### 4.3.2 $\text{SrTiO}_3$ (1 1 0):

The idealized (1 0 0) termination is charge and valence neutral, but  $\text{SrTiO}_3$  (1 1 0) possesses alternate stacking of  $(\text{SrTiO})^{4+}$  and  $(\text{O}_2)^{4-}$  layers leading to a macroscopic dipole at its polar surface. Feasible surface reconstructions must stabilize this dipole and produce a valence neutral structure. Structures observed on  $\text{SrTiO}_3$  (1 1 0) are summarized in Table 4.2. Those with solutions include the homologous  $(n \times 1)$  where  $(n = 2, 3, 4, 5, 6, \infty)$  series [34], a related  $(5 \times 1)$  reconstruction [47], and the two families of larger  $(n \times 2)$  where  $(n = 2, 3, 4, 5, 6, \infty)$  nanostructures, which will be discussed later. The  $(n \times 1)$  series and  $(5 \times 1)$ A structure are shown in Figure 4.4 [47].

Table 4.2. Reconstructions on  $\text{SrTiO}_3$  (1 1 0) from the literature.

Reconstruction	Structure Status	Pictured	Refs
$(n \times 1)$ ( $n = 2, 3, 4, 5, 6, \infty$ )	Observed and solved	Figure 4.4 (a-e, g, h)	[34, 58]
$(5 \times 1)A$	Observed and solved	Figure 4.4 (f)	[47]
$(n \times 2)a$ ( $n = 2 - 6, \infty$ )	Observed and solved	$(4 \times 2)a$ Figure 4.10	[62]
$(n \times 2)b$ ( $n = 2 - 6, \infty$ )	Observed and solved	n/a	[62]
$(2 \times 5)$	Observed	n/a	[28]
$(3 \times 4)$	Observed	n/a	[28]
$c(2 \times 6)$	Observed, models proposed	n/a	[27]
$(4 \times 4)$	Observed	n/a	[28]
$(6 \times 4)$	Observed	n/a	[28]
$(4 \times 7)$	Observed	n/a	[28]

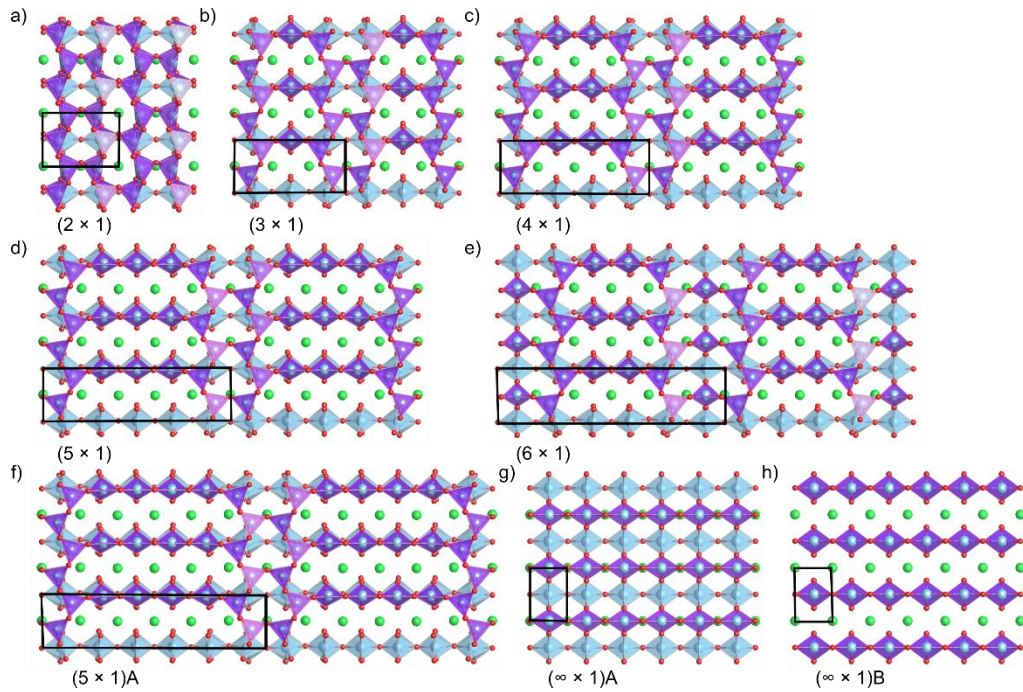


Figure 4.4 Atomic structure of solved reconstructions on the  $\text{SrTiO}_3$  (1 1 0) surface showing (a)  $(2 \times 1)$ , (b)  $(3 \times 1)$ , (c)  $(4 \times 1)$ , (d)  $(5 \times 1)$ , (e)  $(6 \times 1)$ , (f)  $(5 \times 1)A$ , (g)  $(\infty \times 1)A$ , and (h)  $(\infty \times 1)B$ .  $\text{TiO}_6$  are light blue,  $\text{TiO}_4$  are purple. Sr atoms are green, Ti are blue, and oxygen are red.

The structures in Figure 4.4 are built the same way: if  $\text{SrTiO}_3$  (1 1 0) is thought of as alternating layers of  $(\text{SrTiO})^{4+}$  and  $(\text{O}_2)^{4-}$ , the bulk  $\text{SrTiO}_3$  (1 1 0) base terminates on a  $(\text{SrTiO})^{4+}$  layer. Above this, tetrahedral  $\text{TiO}_4$  units make up the reconstruction. Each  $\text{TiO}_4$  shares (one or two)



oxygen atoms with Ti below such that a bulk-like  $(\text{O}_2)^{4-}$  layer exists between the reconstructed Ti-atoms and the bulk-like  $(\text{SrTiO})^{4+}$ ; this is a Potts model structure with two different tetrahedral units plus nothing, a total of three structural units. Remaining oxygen atoms in  $\text{TiO}_4$  units are in the same plane or closer to vacuum than the central Ti atom. This description is turned into the symbolic representation of the Potts model in Figure 4.5. The  $(5 \times 1)\text{\AA}$  reconstruction provides a comprehensive example.

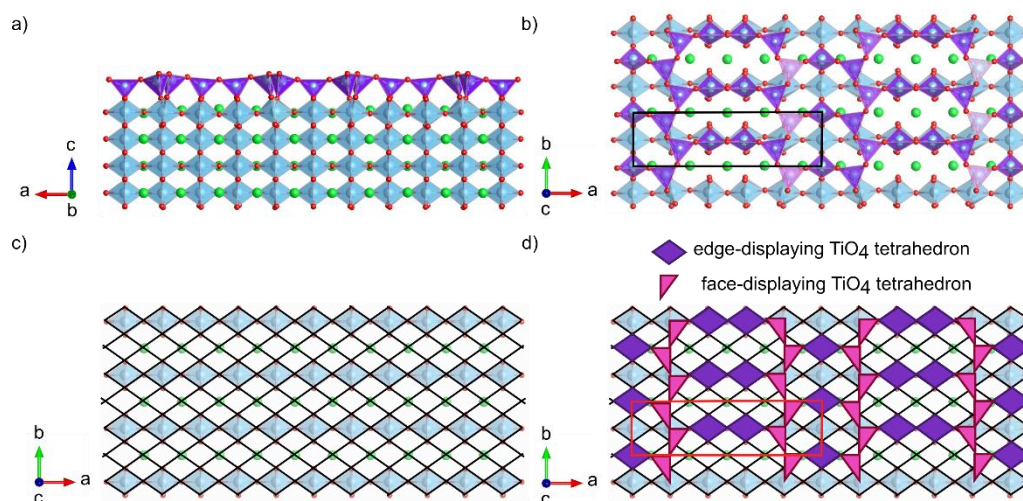


Figure 4.5 Atomic structure of the solved  $(5 \times 1)\text{\AA}$  reconstruction viewed from the b-axis (a), and c-axis (b). In (c) a diamond grid is imposed over the bulk layers below and in (d) the reconstruction is represented by purple diamonds and pink triangles showing placement of two different orientations of  $\text{TiO}_4$  units.

In Figure 4.5 (c) a diamond grid is imposed over the bulk-like  $(\text{SrTiO})^{4+}$  layer of  $\text{SrTiO}_3$   $(1\ 1\ 0)$ . Figure 4.5 (d) shows the  $(5 \times 1)\text{\AA}$  reconstruction codified into its symbolic representation. Edge-displaying  $\text{TiO}_4$  (ED- $\text{TiO}_4$ ) are indicated by purple diamonds. They occupy sites such that their Ti atom is in a grid space's center. The positions of oxygen in ED- $\text{TiO}_4$  occur at roughly the corners of the imposed grid diamonds. Two oxygens, at closest opposite diamond corners, are shared with  $\text{TiO}_6$  below. The remaining two are shared with other  $\text{TiO}_4$ . Face-displaying  $\text{TiO}_4$  (FD- $\text{TiO}_4$ ) are represented by pink triangles. The corners of these triangles represent the position of

oxygen atoms in the outermost layer. FD-TiO<sub>4</sub> occupy the grid such that one of their corners is at a grid intersection (one of two intersections at the furthest opposite diamond corners) and the other corners are at grid diamonds' centers. The Ti atom in FD-TiO<sub>4</sub> is in the center of the pink triangle. They share one oxygen atom with TiO<sub>6</sub> in the below, it is located beneath the central Ti atom. Its position is indicated by grid intersections (one of the two intersections at closest opposite diamond corners).

To satisfy Pauling's fifth rule the number of structural units must be as small as possible. This is the case we see; only ED-TiO<sub>4</sub> and FD-TiO<sub>4</sub> units make up these reconstructions. The placement of ED-TiO<sub>4</sub> and FD-TiO<sub>4</sub> dictated by the grid ensures that TiO<sub>4</sub> (in particular ED-TiO<sub>4</sub>) occupy positions most similar to bulk-like TiO<sub>6</sub>. This is favorable from an energy standpoint- if Pauling's fifth rule is taken to its extreme one expects that surface positions/coordinations mimicking those of the bulk are lower in energy. As opposed to the SrTiO<sub>3</sub> (1 0 0) surface, where TiO<sub>5</sub>[] are the basic units, these reconstructions have lower TiO<sub>x</sub> surface density. Due to this, TiO<sub>4</sub> tetrahedra are the lowest energy configuration which also creates a self-supporting network. This implies that increasing TiO<sub>x</sub> density would lead to observation of TiO<sub>5</sub>[] or TiO<sub>6</sub> units - seen in the case of TiO<sub>x</sub> nanostructures on the (1 1 0) surface,  $(n \times 2)a/b$  ( $n = 2, 3, 4, 5, 6, \infty$ ), discussed in a later section. In accordance with Pauling's first rule, each TiO<sub>4</sub> has bond lengths and angles as close to the ideal tetrahedra as possible.

As Ti coordination decreases, the adherence to the third and fourth rules becomes more extreme. This is observed in multiple aspects of these surfaces. Sharing faces between TiO<sub>4</sub> would be the most unfavorable arrangement possible, and it is never observed. While ED-TiO<sub>4</sub> share a single edge with the TiO<sub>6</sub> below, they never share edges with other TiO<sub>4</sub>. This demonstrates the



nuance captured by Pauling's rules. ED-TiO<sub>4</sub> can share an edge with a TiO<sub>6</sub> unit because the TiO<sub>6</sub> unit is not as low in coordination, and thus this type of sharing is observed more often than edge-sharing between two TiO<sub>4</sub> units. The drive to minimize shared edges also explains why these reconstructions appear to be “bridging” above the bulk material whereas TiO<sub>5</sub>[] on the (1 0 0) face are nestled closely with the layers below. The TiO<sub>5</sub>[] of the (1 0 0) surface are more likely to share edges since their coordination is higher. Finally, sharing corners between TiO<sub>4</sub> units is frequently observed. This type of sharing is expected since it is the lowest in energy.

There are some positions where TiO<sub>4</sub> units do not occur. These positions are avoided because they would not minimize face and edge sharing, or because of close proximity to Sr atoms that would lead to unfavorable cation-cation repulsion.

#### **4.3.3 SrTiO<sub>3</sub> (1 1 1):**

The SrTiO<sub>3</sub> (1 1 1) surface is the most complex of the three common terminations. This surface is polar, like (1 1 0). The material can be thought of as an alternating stack of (SrO<sub>3</sub>)<sup>4-</sup> and (Ti)<sup>4+</sup> layers. The two-dimensional Bravais lattice of this termination is hexagonal, leading to more complex symmetry in its reconstructions. The structures reported and solved on the SrTiO<sub>3</sub> (1 1 1) are summarized in Table 4.3. Of these, the most solved reconstructions and selected theoretical low-energy structures with high and low excess-TiO<sub>2</sub> coverage are shown in Figure 4.6 [49, 167].

Table 4.3. Reconstructions on  $\text{SrTiO}_3$  (1 1 1) from the literature.

Reconstruction	Structure Status	Pictured	Reference/s
$(1 \times 1)$	Observed	n/a	[37, 38, 60]
$(9/5 \times 9/5)$	Observed	n/a	[31, 57]
$(2 \times 2)$ a	Observed and solved	Figure 4.6 (d)	[49]
$(2 \times 2)$ b	Observed and solved	Figure 4.6 (b)	[49]
$(\sqrt{7} \times \sqrt{7})R19.1^\circ$	Observed	n/a	[169]
$(3 \times 3)$	Observed and solved	Figure 4.6 (c)	[31, 49, 57]
$(\sqrt{13} \times \sqrt{13})R13.9^\circ$	Observed	n/a	[169]
$(4 \times 4)$	Observed and solved	Figure 4.6 (e)	[31, 49, 57]
$(5 \times 5)$	Observed	n/a	[57]
$(6 \times 6)$	Observed	n/a	[31, 57]
$(1 \times 2)$ – “Low”	Theoretical low-energy	Figure 4.6 (a)	[49, 167]
$(1 \times 1)$ – “High”	Theoretical low-energy	Figure 4.6 (f)	[49, 167]

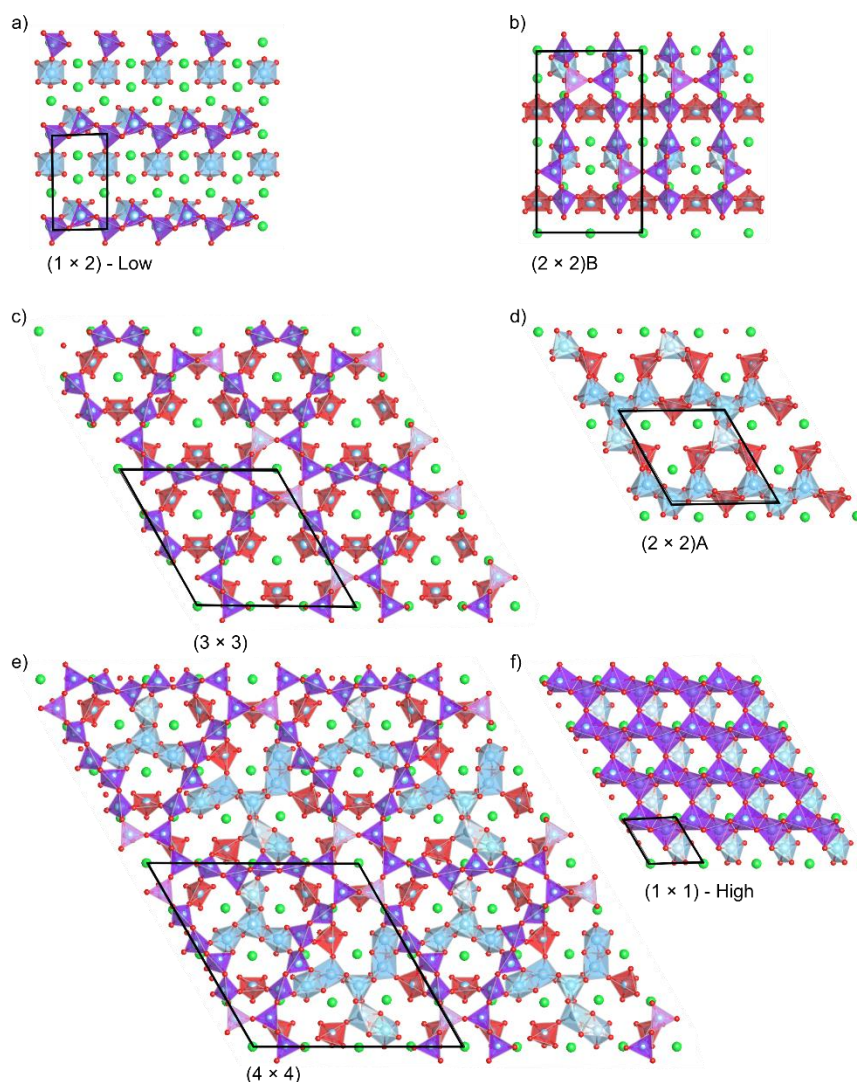


Figure 4.6 Atomic structure of solved reconstructions on  $\text{SrTiO}_3$  (1 1 1) surface showing (a)  $(1 \times 2)$  – “Low”, (b)  $(2 \times 2)$ b, (c)  $(3 \times 3)$ , (d)  $(2 \times 2)$ a, (e)  $(4 \times 4)$ , and (f)  $(1 \times 1)$  – “High”.  $\text{TiO}_6$  units are light blue,  $\text{TiO}_5$  are red, and  $\text{TiO}_4$  are purple. Sr atoms are green, Ti are blue, and oxygen are red.

In Figure 4.6 the reconstructions are built on a bulk-like  $(\text{SrO}_3)^{4-}$  layer. Reconstructions are made up of one or two Ti-containing layers. A single Ti-layer reconstruction is shown in Figure 4.6 (d). It is composed of  $\text{TiO}_6$  and  $\text{TiO}_5$  units on top of the bulk-like  $(\text{SrO}_3)^{4-}$  plane. These units have two or three oxygens in a plane above the central Ti. They share three oxygens with the  $\text{TiO}_6$

units below, ensuring bulk  $(\text{SrO}_3)^{4-}$  layer stoichiometry. All other reconstructions shown are double-layered. In the layer above the  $(\text{SrO}_3)^{4-}$  they have the same construction as the single-layered reconstructions. The Ti atoms closest to vacuum are part of  $\text{TiO}_4$  units, like those on the  $\text{SrTiO}_3$  (1 1 0) surface, with the same ED- $\text{TiO}_4$  or FD- $\text{TiO}_4$  units. These reconstructions can be represented in a symbolic Potts model shown in Figure 4.7. Figure 4.7 illustrates two examples, the  $(2 \times 2)_a$  in Figure 4.7 (a), (b), (e) and (f) and the  $(2 \times 2)_b$  in Figure 4.7 (c), (d), (g) and (h), to highlight differences between single and double Ti-layer reconstructions. The Potts model for the single Ti-layer reconstruction is made up of three units:  $\text{TiO}_6$ ,  $\text{TiO}_5[]$ , and an “empty” unit. For the double Ti-layer reconstruction the Potts model has five units:  $\text{TiO}_6$ ,  $\text{TiO}_5[]$ , ED- $\text{TiO}_4$ , FD- $\text{TiO}_4$ , and an “empty” unit.

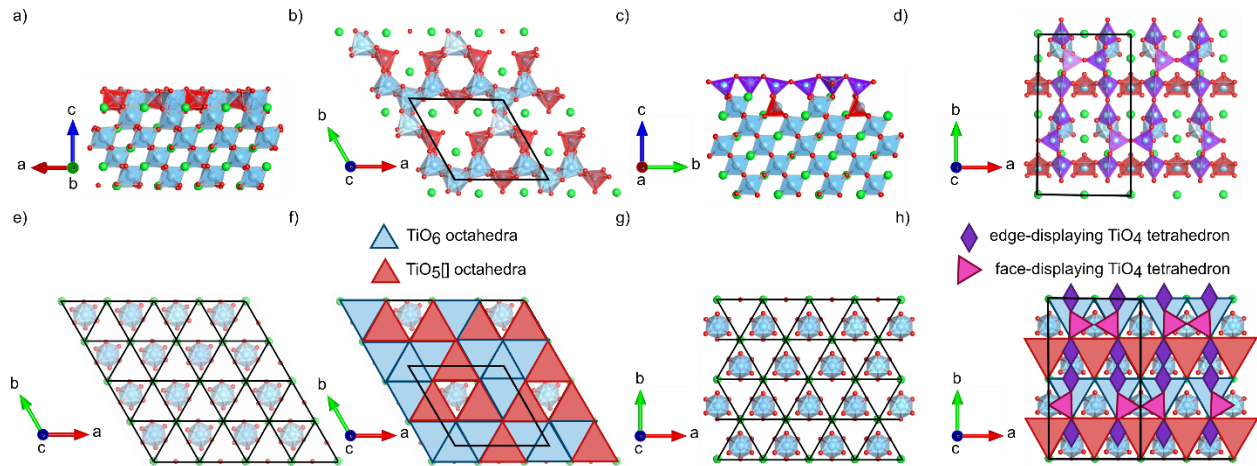


Figure 4.7 Atomic structure of the solved  $(2 \times 2)_a$  reconstruction viewed from the b-axis (a), and c-axis (b). In (e) a triangle grid is imposed over the bulk layer below and in (f) the reconstruction is represented by blue and red triangles showing placement of  $\text{TiO}_6$  and  $\text{TiO}_5[]$  units, respectively. Atomic structure of the solved  $(2 \times 2)_b$  reconstruction viewed from the a-axis (c), and c-axis (d). In (g) a triangle grid is imposed over the bulk layer below and in (h) the reconstruction is represented by blue and red triangles showing placement of  $\text{TiO}_6$  and  $\text{TiO}_5[]$  units, respectively and purple triangles and diamonds showing placement of  $\text{TiO}_4$  units.

As Figure 4.7 (e) and (g) show, a triangular grid can be imposed over the bulk-like  $(\text{SrO}_3)^{4-}$ .

A single  $\text{TiO}_x$ -layer reconstruction is shown in Figure 4.7 (a), (b), (e) and (f).  $\text{TiO}_6$  (blue triangles)

or  $\text{TiO}_5$  (red triangles) occupy any space on this grid- their Ti atom roughly in its center. All oxygens shared with the  $(\text{SrO}_3)^{4-}$  layer occur at bulk-like positions. The two or three oxygens closest to vacuum (in  $\text{TiO}_5$  or  $\text{TiO}_6$ ) are shared among two  $\text{TiO}_x$  units and occur at roughly the midpoints of the triangle's sides, offset from the oxygens below to adopt a more-ideal polygon. A double  $\text{TiO}_x$ -layered reconstruction is shown in Figure 4.7 (c), (d), (g) and (h).  $\text{TiO}_6$  and  $\text{TiO}_5$  units in these reconstructions are placed in the same way as those of the single-layer reconstruction. However, the outermost oxygen atoms in  $\text{TiO}_6$  or  $\text{TiO}_5$  can be shared by  $\text{TiO}_x$  in the same layer or with  $\text{TiO}_4$  above. The possible positions of ED- $\text{TiO}_4$  (purple diamonds) and FD- $\text{TiO}_4$  (pink triangles), similar in shape and oxygen-sharing to those on the (1 1 0) surface, are all illustrated in the example shown. In all  $\text{TiO}_4$  units, Ti occurs at the center of the purple diamond or pink triangle. ED- $\text{TiO}_4$  tetrahedra occur on two sites. On one site, furthest opposite corners of its diamond (oxygen closest to the surface) are over a grid intersection and the center of a grid triangle. The other site has the two furthest opposite corners both over the center of a grid triangle (one over a bulk Ti site and the other over a Ti-site occupied by the  $\text{TiO}_6/\text{TiO}_5$  layer). FD- $\text{TiO}_4$  units occur with one corner of the displayed face on a grid intersection and the other two corners of the displayed face at the center of two different grid triangles. The fourth oxygen is directly below the central Ti.

The variety of structures on  $\text{SrTiO}_3$  (1 1 1) is greater than that of (1 0 0) or (1 1 0). However, they can still be broken down into a small number of units as per Pauling's fifth rule. These units are similar to those on the (1 0 0) and (1 1 0) surfaces, indicating that Pauling's fifth rule applies in general to a given oxide material.  $\text{TiO}_5$  or  $\text{TiO}_6$  are arranged preferentially on the natural Ti sites indicated by open grid triangles without a bulk  $\text{TiO}_6$  in Figure 4.7 (e) and (g). Continuing the

bulk-like structure minimizes energy on the surface. Pauling's first rule is particularly relevant for these surfaces. All possible  $\text{TiO}_x$  units are present: in layers where  $\text{TiO}_x$  density is highest, the most-favorable  $\text{TiO}_6$  and  $\text{TiO}_5[]$  coordinations with geometry as close as possible to ideal octahedra are adopted. In two-layer  $\text{TiO}_x$  reconstructions, the outermost layer of lower  $\text{TiO}_x$  density does not support these structures. Instead, the  $\text{TiO}_4$  coordination is adopted to create a continuous self-supported network, like the (1 1 0) surface.

Pauling's third and fourth rules apply here in familiar ways. The only units to share polyhedra faces are  $\text{TiO}_6$  and  $\text{TiO}_5[]$ , which occasionally share a face with bulk-like layers below. Placing these in natural Ti sites reduces the occurrence of this higher-energy configuration. Also, while  $\text{TiO}_6$  and  $\text{TiO}_5[]$  units often share edges,  $\text{TiO}_4$  units almost never do. This is expected due to their low coordination and high valence. The positions at which each of these types of units occur minimize unfavorable sharing.

Something unique to the (1 1 1) surface, shown in Figure 4.6 (a), (b), and (d), is removed or added Sr atoms, necessary to satisfying the  $n\text{SrTiO}_3 \cdot m\text{TiO}_2$  condition. In a single Ti-layer reconstruction Sr atoms are removed from the bulk-like  $(\text{SrO}_3)^{4-}$  layer. For double Ti-layer reconstructions, there are no reported examples where Sr atoms are removed. However, Sr atoms can be added to the outermost  $\text{TiO}_4$ -containing layer (e.g.  $(2 \times 2)_b$  in Figure 4.6). When Sr are added it is to octahedral sites at the corners or centers of grid triangles. This placement ensures a coordination environment as close as possible to that of the bulk, as expected from Pauling's rules.

#### 4.3.4 From Reconstructed Surface to Thin Film:

The  $\text{TiO}_2$ -rich surfaces of  $\text{SrTiO}_3$  provide a robust example for how Pauling's rules apply to perovskite oxides. We will show that with increasing coverage the same rules apply, providing the connection to thin film growth.

All  $\text{TiO}_2$  nanostructures reported on  $\text{SrTiO}_3$  have structural features and periodic arrangements similar to the  $\text{SrTiO}_3$  surfaces they are grown on, showing that Pauling's rules apply to heteroepitaxial film growth. The three structures considered in detail are listed in Table 4.4.

Table 4.4. Nanostructures on  $\text{SrTiO}_3$  (1 0 0) from the literature.

Structure	Surface	Pictured	Reference/s
$c(6 \times 2)$	(1 0 0)	Figure 4.8	[30, 32, 36, 40, 46, 56]
Diline/Triline	(1 0 0)	Figure 4.9	[185, 186]
$(2 \times n)a/b$ ( $n = 2-6 \dots \infty$ )	(1 1 0)	Figure 4.10	[62]

The  $c(6 \times 2)$  reconstruction builds off of the  $\text{TiO}_2$  plane termination of  $\text{SrTiO}_3$  (1 0 0). It is “thicker” than others on this surface, with two additional  $\text{TiO}_x$  layers. It has the usual  $\text{TiO}_5[\ ]$  units on its top surface with the addition of Sr adatoms. The  $\text{TiO}_5[\ ]$  units are the same as in other  $\text{SrTiO}_3$  (1 0 0) reconstructions. The additional  $\text{TiO}_x$  layers between the  $\text{TiO}_5[\ ]$  surface and bulk-like  $\text{TiO}_6$  are fully 6-coordinated  $\text{TiO}_6$  octahedra. This structure is shown in Figure 4.8. Placement of atoms in each layer is highlighted both using the symbolic Potts model representations for Figure 4.8 (e-h) as well as the resulting structure in Figure 4.8 (a-d). In this Potts model the three elements are  $\text{TiO}_6$ ,  $\text{TiO}_5[\ ]$ , and an “empty” unit.

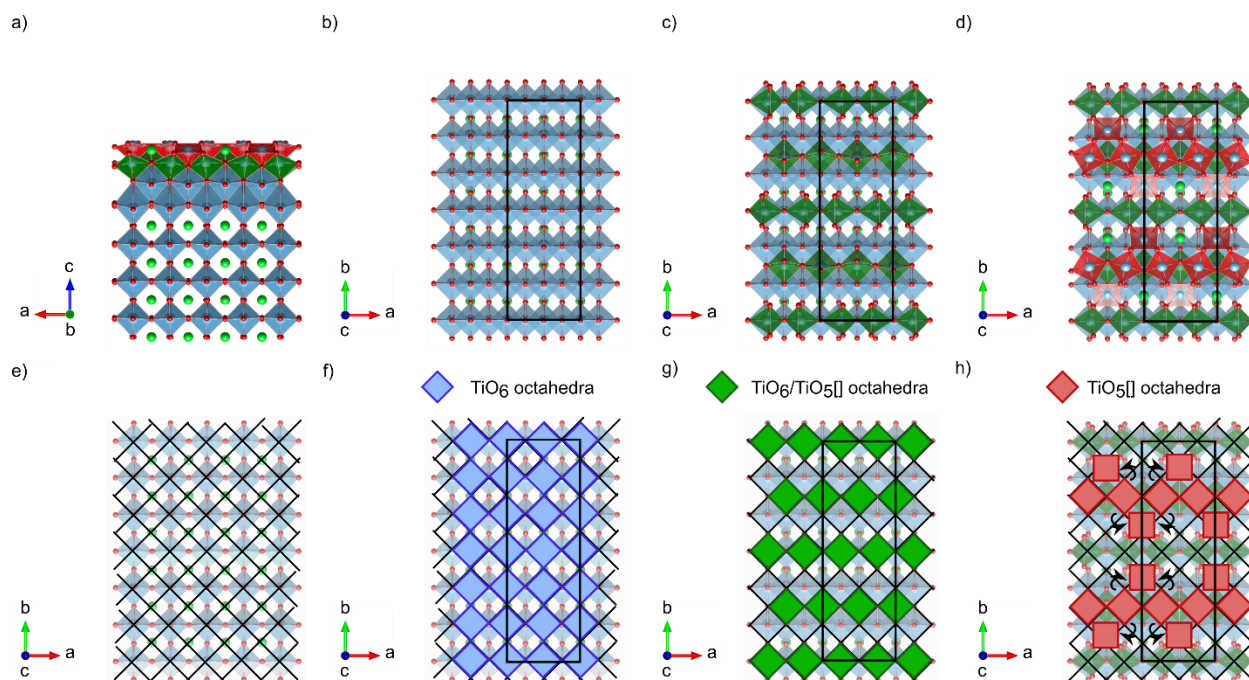


Figure 4.8 Atomic structure of the solved  $c(6 \times 2)$  nanostructure on  $\text{SrTiO}_3$  (1 0 0) viewed from the b-axis (a), and c-axis with a square grid imposed over the bulk layers below (e). In (f)  $\text{TiO}_6$  units are placed on top of the bulk, represented by blue squares- the structure of this layer is shown in (b). In (g)  $\text{TiO}_6/\text{TiO}_5[]$  units are represented by green squares and are placed atop those in (b) and (f)- the structure of this layer is shown in (c). In (h)  $\text{TiO}_5[]$  units are represented by red squares and are placed atop those in (c) and (g)- the structure and tilts of this layer is shown in (d).

Building up the  $c(6 \times 2)$  is very similar to any reconstruction previously discussed. The same grid, shown in Figure 4.8 (e), is drawn and populated with  $\text{TiO}_x$  units. These have more layers of  $\text{TiO}_x$  above and adopt a fully coordinated  $\text{TiO}_6$  geometry, shown with blue squares in Figure 4.8. Taking this layer as the new “base”, another grid can be drawn following the same rules as before. The second additional layer of  $\text{TiO}_6$  and  $\text{TiO}_5[]$  units, green squares in Figure 4.8, again occupy the same relative atomic positions that  $\text{TiO}_5[]$  units in a  $\text{SrTiO}_3$  (1 0 0) reconstruction would be expected to. If this layer had another complete layer of  $\text{TiO}_x$  units above (i.e. every available site filled) all these units would be  $\text{TiO}_6$ . However, that is not the case, leading to the presence of some  $\text{TiO}_5[]$ . This layer is then the basis of the final one, where  $\text{TiO}_5[]$  units (red



squares in Figure 4.8) are placed on top, again with the same rules as a normal  $\text{SrTiO}_3$  (1 0 0) surface reconstruction.

This reconstruction contains only  $\text{TiO}_6$  and  $\text{TiO}_5[]$  units, conforming to Pauling's fifth rule. Pauling's first rule determines which of these two coordinations a given Ti atom is in. If there are additional  $\text{TiO}_x$  units above it, the Ti atom adopts its most stable coordination,  $\text{TiO}_6$ . If it is a Ti with none above it, the  $\text{TiO}_5[]$  coordination is adopted- this is illustrated in the layer represented by green squares in Figure 4.8 (c) and (g). Furthermore, to accommodate idealized  $\text{TiO}_5[]$  coordinations while accounting for differences in surface height, some of the units in the layer represented by red squares in Figure 4.8 (d) and (h) are shifted slightly in terms of their ideal grid-determined positions. This structure also has a few additional Sr atoms at its surface. Sr adatoms on the surface follow the same placement rules as those on  $\text{SrTiO}_3$  (1 1 1); they are only present in sites allowing an octahedral coordination, agreeing with Pauling's fifth and first rules.

As with the other  $\text{SrTiO}_3$  (1 0 0) reconstructions, this structure minimizes the number of shared edges between  $\text{TiO}_x$  units. Sharing of corners is favored while sharing of faces is totally avoided, in agreement with Pauling's third and fourth rules.

$\text{TiO}_2$  nanowires, such as the diline and triline reported on  $\text{SrTiO}_3$  (1 0 0), are other structures approaching the thin film regime [185, 186]. The  $\text{TiO}_x$  di/trilines resemble the simpler  $c(4 \times 2)$   $\text{SrTiO}_3$  (1 0 0) reconstruction at their surface with the typical  $\text{TiO}_5[]$  units [112]. Between this and the bulk-like  $\text{TiO}_6$  is a single additional  $\text{TiO}_x$  layer made up of fully-coordinated  $\text{TiO}_6$ . This structure is illustrated in the case of the triline structure in Figure 4.9. The Potts model shown in Figure 4.9 has three elements:  $\text{TiO}_6$ ,  $\text{TiO}_5[]$ , and the "empty" unit.

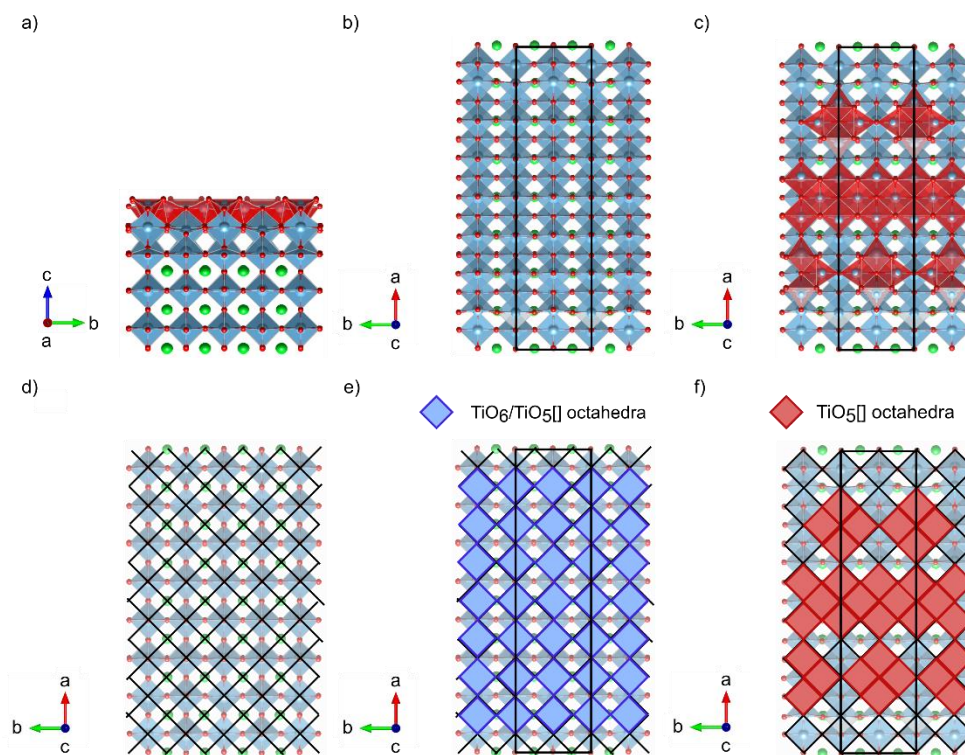


Figure 4.9 Atomic structure of the solved triline nanostructure on  $\text{SrTiO}_3$  (1 0 0) viewed from the a-axis (a), and c-axis with a square grid imposed over the underlying bulk (d). In (e)  $\text{TiO}_6$  units are represented by blue squares placed atop the grid in (d)- the structure of this layer is shown in (b). In (f)  $\text{TiO}_5[]$  units are represented by red squares placed atop the structure in (b) and (e)- the structure of this layer is shown in (c).

Building the trelines (and dilines) relies on the same principles as the  $c(6 \times 2)$  and other reconstructions on the (1 0 0) surface. The grid is shown in Figure 4.9 (d) and  $\text{TiO}_6$  (blue squares) are placed on it in Figure 4.9 (e), following the same pattern of occupation as for the  $c(6 \times 2)$ . The final layer of  $\text{TiO}_5[]$  units (red squares) are placed in Figure 4.9 (f) and occupy the same relative positions as any other previously-discussed  $\text{TiO}_5[]$ .

Pauling's rules are obeyed by the triline in much the same way as for the normal  $\text{SrTiO}_3$  (1 0 0) reconstructions and the just-discussed  $c(6 \times 2)$ . As this structure simply serves to reinforce these rules, further explanation is not necessary.

$\text{TiO}_2$  nanostructures are not unique to the  $\text{SrTiO}_3$  (1 0 0) surface. Two families,  $(2 \times n)a$

and b, where ( $n = 2, 3, 4, 5, 6, \infty$ ), observed on  $\text{SrTiO}_3$  (1 1 0) display the same ordered transition from reconstructed surface to reconstructed thin film [187]. These nanostructures have an additional  $\text{TiO}_x$  layer when compared to other reconstructions on the (1 1 0) surface. On their top surface they display  $\text{TiO}_6$  units, rather than the  $\text{TiO}_4$  often seen in other (1 1 0) reconstructions. Between this surface layer and the bulk below, there is a layer made up of  $\text{TiO}_6$  octahedra. These are the same in geometry as those on other  $\text{SrTiO}_3$  surfaces, and their placement is similar to  $\text{TiO}_4$  in other (1 1 0) reconstructions. One of these structures, the  $(2 \times 4)a$ , is shown in Figure 4.10, where each layer of the nanostructure is illustrated by the symbolic Ising model in Figure 4.10 (d-f) and with the actual structure in Figure 4.10 (a-c). Since this structure only has two units, a  $\text{TiO}_6$ , and an “empty” unit, it can be represented with the binary Ising model.

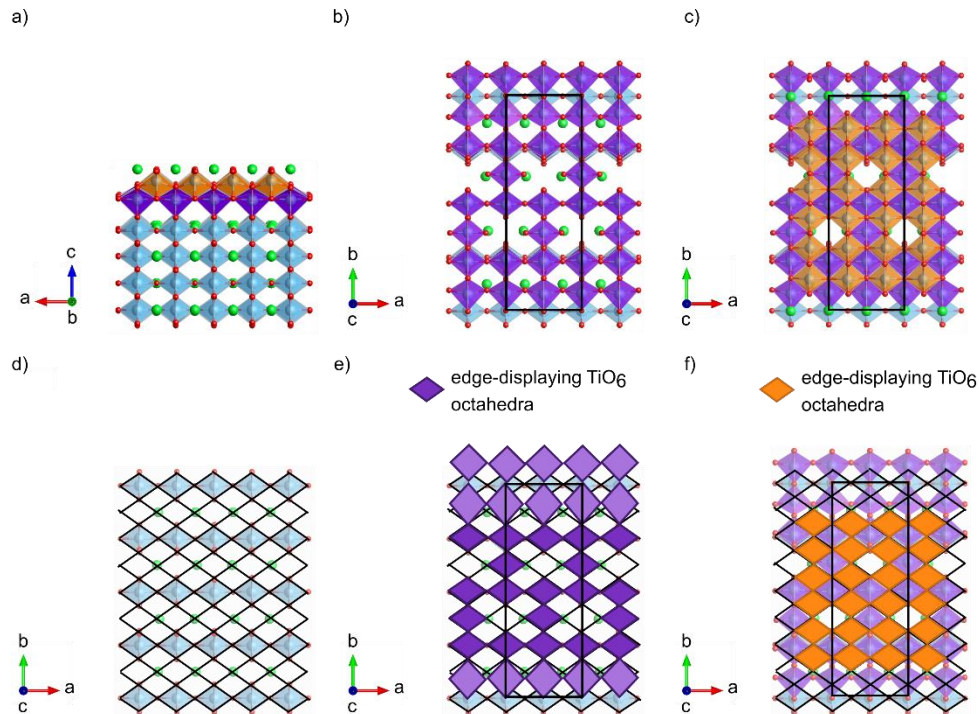


Figure 4.10 Atomic structure of the solved  $(2 \times 4)a$  nanostructure on  $\text{SrTiO}_3$  (1 1 0) viewed from the b-axis (a), and c-axis with a diamond grid imposed (d). In (e)  $\text{TiO}_6$  units are represented by purple diamonds placed atop the grid in (d)- the structure and distortions in this layer is shown in

(b). In (f)  $\text{TiO}_6$  units are represented by orange diamonds placed atop the structure in (b) and (e)- the structure of this layer is shown in (c).

Building up the  $(2 \times 4)_a$  is the same as other reconstructions on the  $\text{SrTiO}_3$  (1 1 0). The starting base is a bulk-like  $(\text{SrTiO})^{4+}$  layer. The grid drawn in Figure 4.10 (d) is identical to the ones used before on this surface. It is populated with exclusively  $\text{TiO}_6$  units in the same sites that held ED- $\text{TiO}_4$  in other (1 1 0) reconstructions. The difference between the ED- $\text{TiO}_4$  seen earlier and these  $\text{TiO}_6$  is that these units have oxygens below and above the central Ti atom. These are located at the closest opposite diamond corners (top and bottom corners)- so they can be thought of as edge-displaying  $\text{TiO}_6$ . These are visualized as purple diamonds in Figure 4.10 (e). If this layer is then used as the new base, a new grid can be drawn and more  $\text{TiO}_6$  placed to form the final layer of the reconstruction, adhering to the same rules. This final layer is visualized as orange diamonds in Figure 4.10 (f). This structure also has Sr adatoms, which are placed at sites with the same in-plane positions as bulk Sr, but at the surface.

Pauling's fifth rule is exemplified in these surfaces- the only unit making up these reconstructions is  $\text{TiO}_6$ . Additionally, its edge-displaying geometry is the same as the bulk-like layers below, making this a particularly low-energy environment. Pauling's first rule gives insight into why the  $\text{TiO}_6$  structure is adopted (rather than  $\text{TiO}_4$ ) and some of the shifting seen in the  $\text{TiO}_6$  layer depicted in Figure 4.10 (b) and (d). This nanostructure has high  $\text{TiO}_x$  density. Additionally, many  $\text{TiO}_6$  units have another  $\text{TiO}_x$  unit above them. In this case it is possible to adopt the most stable coordination according to Pauling's first rule: octahedral  $\text{TiO}_6$ . The deviations from the ideal placement shown by light purple diamonds in Figure 4.10 (e) serve to permit this low-energy configuration (as opposed to the higher-energy  $\text{TiO}_4$  alternative) and preserve the coordinations as close to ideal geometry as possible when a fully-occupied  $\text{TiO}_x$  layer does not exist.

Pauling's third and fourth rules are also obeyed in the placement of  $\text{TiO}_6$  on this surface. No faces are shared in any  $\text{TiO}_6$  units. Edge sharing is also minimized by the arrangement of these units.

As with the other thin film structures discussed, Sr adatoms decorate the surface at octahedral coordinated positions, in accordance with Pauling's fifth and first rules. In this case, Sr atoms occur above the deviated  $\text{TiO}_6$ , acting as an additional mechanism for stress relief – they are octahedrally coordinated with a larger bond length than in  $\text{TiO}_6$ .

#### 4.3.5 $\text{BaTiO}_3$ (1 0 0):

Few other perovskite oxide surfaces have been investigated with the same attention as  $\text{SrTiO}_3$ . However, there are surfaces whose reconstructions have been reported that deserve mention. One example of this is  $\text{BaTiO}_3$  (1 0 0).

The structure of  $\text{BaTiO}_3$  is a perovskite similar to  $\text{SrTiO}_3$ , although  $\text{BaTiO}_3$  deviates more dramatically from the cubic structure, experiencing a great number of structural transitions with temperature. Since it has the same stoichiometry, B-site cation, and general structure, one would expect its surface reconstructions to have similar structural features to  $\text{SrTiO}_3$ . Of the reported structures for the  $(2 \times 1)$  [52],  $(3 \times 1)$  [43],  $c(2 \times 2)$  [55],  $(\sqrt{5} \times \sqrt{5})R26.6^\circ$  [51],  $(\sqrt{13} \times \sqrt{13})R33.6^\circ$  [54], and  $c(4 \times 4)$  [55], all the proposed solutions have surfaces that are B-site rich, with a similar double-layer structure to the  $\text{SrTiO}_3$  (1 0 0) reconstructions. The similarities between the two end there, however, as these surfaces were all prepared under reducing conditions and have not all been analyzed by multiple techniques. Since they are reduced, the condition of  $n\text{BaTiO}_3 \cdot m\text{TiO}_2$  does not hold, allowing for structures with reduced oxygen content, or  $n\text{BaTiO}_3 \cdot m\text{TiO}_x$  to occur. Proposed models for two of these structures, the  $c(2 \times 2)$  and  $c(4 \times 4)$ , are shown in Figure 4.11.

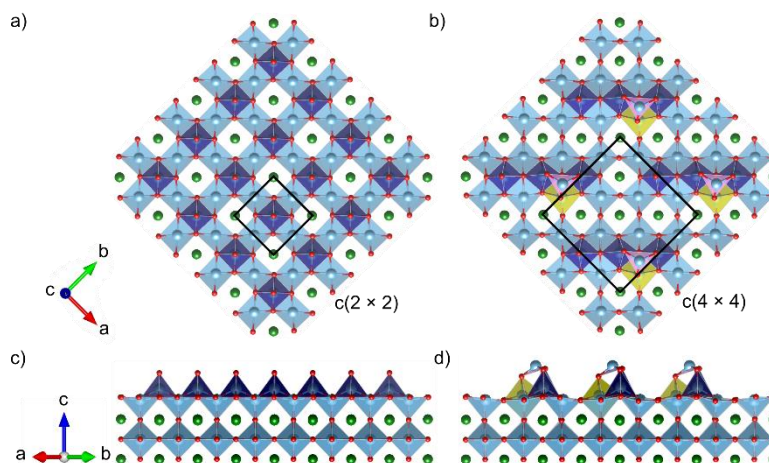


Figure 4.11 Atomic structure of reconstructions on  $\text{BaTiO}_3$  (1 0 0) surface showing  $c(2 \times 2)$  viewed down perpendicular axes in (a) and (c) and  $c(4 \times 4)$  viewed down the same perpendicular axes in (b) and (d).  $\text{TiO}_6$  units are light blue, surface  $\text{TiO}_6$  are yellow,  $\text{TiO}_5[]$  are navy blue, and  $\text{TiO}_3$  are pink. Ba atoms are dark green, Ti are blue, and oxygen are red.

From Figure 4.11 one can see that Pauling's rules are still obeyed to some extent. There are, according to the fifth rule, a small number of structural units in these reconstructions, in this case  $\text{TiO}_6$ ,  $\text{TiO}_5[]$ , and  $\text{TiO}_3$ . Bulk-like positioning of the first  $\text{TiO}_6/\text{TiO}_5[]$  layer also agrees with the implication from Pauling's rules that surface structures that continue bulk ordering are favorable. The coordination of the  $\text{TiO}_6$  and  $\text{TiO}_5[]$  units are close to ideal, as expected based on the first rule. Since these surfaces are reduced, it is reasonable to assume that the average oxidation state of Ti is also reduced. As such, the presence of  $\text{TiO}_3$  is plausible because of the highly-reduced nature of these surfaces. Additionally,  $\text{TiO}_3$  units only occur in situation with very low excess  $\text{TiO}_x$ , consistent with the other surfaces analyzed. Coordination of  $\text{TiO}_3$  should obey Pauling's rules as well, adopting the most ideal polyhedron geometry possible.

Pauling's third and fourth rules are obeyed;  $\text{TiO}_x$  units are organized such that face sharing does not occur and edge-sharing is also minimized. The  $\text{TiO}_3$  units also follow this rule, they only share corners with other  $\text{TiO}_x$ . This behavior is as-expected from their extremely low coordination

and high valence. While not enough structures have been solved to conduct the same type of analysis done on the  $\text{SrTiO}_3$  surfaces, the available information provides clues for solving additional  $\text{BaTiO}_3$  reconstructions.

These structures also illustrate another use of Pauling's rules – to raise questions with structures which appear to deviate from what is normal. For instance, both contain surface titanyl group with a  $\text{T}=\text{O}$  double bond. This is unusual, as it yields a “naked” polyhedral apex. In addition, the proposed three-fold titanium sites are not what one would expect based upon established bulk inorganic chemistry.

#### **4.3.6 $\text{LaAlO}_3$ (1 1 0):**

Moving beyond perovskites that contain titanium, the only other oxide material which has multiple reconstructions both reported and solved in a quantitative manner is  $\text{LaAlO}_3$  (1 1 0).

$\text{LaAlO}_3$  has been of interest in the oxide community since the discovery of a 2-dimensional electron gas at the  $\text{LaAlO}_3/\text{SrTiO}_3$  (1 0 0) interface [70]. Unlike  $\text{SrTiO}_3$ , where the valence of the two cations is viewed as  $+2/+4$  (Sr/Ti), in  $\text{LaAlO}_3$  it is  $+3/+3$  (La/Al). This leads to a polar surface for the  $\text{LaAlO}_3$  (1 0 0) termination. The (1 1 0) termination can also be thought of as an alternate stacking of  $(\text{LaAlO})^{4+}$  and  $(\text{O}_2)^{4-}$  layers, possessing a macroscopic electrostatic dipole similar to that of  $\text{SrTiO}_3$  (1 1 0). The parallels to the  $\text{SrTiO}_3$  surface do not end there- the two reconstructions reported on the  $\text{LaAlO}_3$  (1 1 0) surface,  $(2 \times 1)$  [170], and  $(3 \times 1)$  [42], have many similarities to the  $(n \times 1)$  reconstructions on the  $\text{SrTiO}_3$  (1 1 0) surface [34, 47]. For  $\text{LaAlO}_3$ , the solved reconstructions can be described as  $\text{Al}_2\text{O}_3$ -rich (as opposed to  $\text{TiO}_2$ -rich), and are all neutral in terms of formal charge. Ideally, they conform to the formula  $n\text{LaAlO}_3 \cdot m\text{Al}_2\text{O}_3$ , although the  $(3 \times$



1) has additional adsorbed hydrogen (i.e. -OH groups). The structures of the  $(2 \times 1)$  and  $(3 \times 1)$  are shown in Figure 4.12.

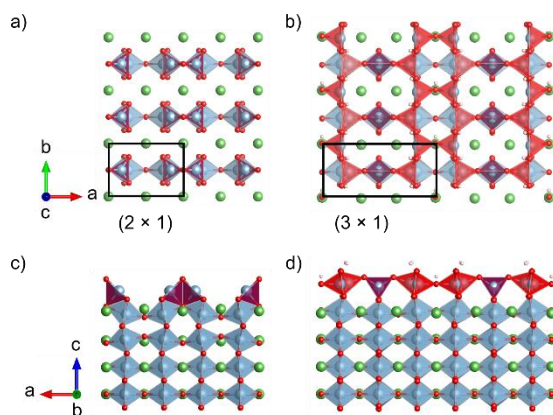


Figure 4.12 Atomic structure of the solved reconstructions on  $\text{LaAlO}_3$  (1 1 0) surface showing  $(2 \times 1)$  in viewed down the c-axis in (a) and viewed down the b-axis in (c). Atomic structure of the solved  $(3 \times 1)$  reconstruction viewed down the c-axis in (b) and the b-axis in (d).  $\text{AlO}_6$  units are light blue, and two different orientations of  $\text{AlO}_4$  are red and purple respectively. La atoms are green, Al are blue, and oxygen are red.

The reconstructions shown in Figure 4.12 are very similar to those on the  $\text{SrTiO}_3$  (1 1 0) surface with similar polyhedral elements,  $\text{AlO}_4$  and  $\text{AlO}_5$  present. This agrees with Pauling's fifth rule. Additionally, these units occur at similar positions with respect to the underlying bulk layers when compared to the  $\text{TiO}_4$  on the  $\text{SrTiO}_3$  (1 1 0) surface. These  $\text{AlO}_4$  and  $\text{AlO}_5$  are as close as possible to ideal polyhedra for these coordination numbers, in accordance with Pauling's first rule. Deviations from ideal polyhedron shapes are due more to cation repulsion and close packing of polyhedra than any other factor, as expected from Pauling's first rule. The reconstructions shown here also conform to Pauling's third and fourth rules. Face and edge sharing between  $\text{AlO}_x$  units are minimized while still conforming to the experimental unit cell size and lack of formal charge requirements.

The formula to describe charge neutral reconstructions is different for this surface than



$\text{SrTiO}_3$  (1 1 0) in B-site cation and oxygen content: i.e.  $n\text{LaAlO}_3 \cdot m\text{Al}_2\text{O}_3$  vs.  $n\text{SrTiO}_3 \cdot m\text{TiO}_2$ . As such, it may seem surprising that these reconstructions have such features. However, the fact that the same types of structural units appear on both oxide surfaces indicates that they could be codified in a very similar manner. This further reinforces the idea that Pauling's rules provide a robust framework for oxide surfaces.

While there have been surface structures solved or proposed on  $\text{LiNbO}_3$  [59], and likely other perovskite surfaces, none of these data sets contain a number of structures large enough to draw conclusions regarding their structural units. In addition, complete atomic positions are not always published, and in some theoretical works only very limited possibilities such as bulk-like terminations have been considered. We believe that as more structural information becomes available, most if not all will follow Pauling's rules; we expect that except for invalid models all real oxide surfaces will.

#### 4.4 Discussion

By using the large number of reconstructions solved on the (1 0 0), (1 1 0), and (1 1 1) orientations of  $\text{SrTiO}_3$  and a few other materials as examples, the application of Pauling's rules to oxide surfaces has been demonstrated. Although these surfaces have disparate properties, the fundamental features and structural motifs found on them are remarkably similar. All orientations of  $\text{SrTiO}_3$  exhibit families of related reconstructions based on a Ti-rich surface that most often consists of a bulk-like Ti-atom layer with additional  $\text{TiO}_x$  polyhedra sitting on top of it, creating the various electron density features often probed via STM, SXRD, or transmission electron diffraction (TED). In all cases discussed, these reconstructions can be represented by tilings of only a few different structural units in an Ising or Potts model, with polyhedra of  $\text{TiO}_6$ ,  $\text{TiO}_5$ [], and

TiO<sub>4</sub> possessing near-ideal bond Ti-O bond lengths and angles occurring consistently across different orientations. In addition, reconstructions on these surfaces follow Pauling's other rules in their specific arrangements- reducing the number of face and edge sharing polyhedral units further as the coordination number of a high valence cation, in this case Ti<sup>4+</sup>, decreases.

With a set of rules established based on Pauling's rules, the task of generating plausible solutions for additional reconstructions on this material is significantly simplified. It is even possible to generate hypothetical structural solutions for surface reconstructions where little data is present or of arbitrary unit cell dimensions. To do this the Ising or Potts models serve as a starting point for generating reconstructions on the various surfaces. In this way, Pauling's rules can be combined with simple algorithms to generate every possible solution for a given unit cell size. This has been demonstrated thoroughly on the SrTiO<sub>3</sub> (1 0 0) surface [188]. While some surfaces of SrTiO<sub>3</sub> are more complex than others, and the number of possible reconstructions quickly becomes very large as the unit cell size increases, this strategy could still be employed in cases where little information is available regarding a given structure. The combination of these rules with algorithms designed to generate permutations of possible structures offers a truly predictive capability for oxide surfaces. Even in cases of large unit cells, Pauling's rules can be used to generate realistic hypothetical structures or evaluate the likelihood of a given proposed structure. When combined with additional data including symmetry and relative surface composition from STM, SXRD, TED, or other methods, this can significantly reduce the number of candidate structures to evaluate using *ab initio* methods like DFT. Along with the simple BVS calculation method, these rules provide an alternative initial evaluation method with essentially negligible computational cost. This results in an overall reduction in computation time and expense as fewer

structures need to be considered and reconstructions with otherwise prohibitively large unit cells can be treated in a systematic manner.

Once a set of hypothetical structures are generated using an appropriate algorithm, these structures can serve as starting points for DFT relaxations. Relaxation of the structures can then be performed to compare the surface energies of different structures and determine which is lowest in energy or matches most closely with available experimental data. When a structure generated through the application of Pauling's rules is relaxed the atoms will shift some from their original positions. Whether a given  $\text{TiO}_x$  polyhedra is better-described in the end as  $\text{TiO}_4$  with long bonds to other oxygens,  $\text{TiO}_5$  or  $\text{TiO}_6$  is relevant, but not critical.

Two additional oxide surfaces,  $\text{BaTiO}_3$  (1 0 0) and  $\text{LaAlO}_3$  (1 1 0) are also shown to conform to Pauling's rules, although the bonding in the proposed  $\text{BaTiO}_3$  structures is surprising. This shows that they are applicable to oxide perovskites of different cations and oxidations states. Additionally, the cases of reduced and hydrated surfaces were briefly mentioned in these datasets. As these special cases resulted in only small deviations from the expectations laid out by Pauling's rules, they do not present a significant deviation from this framework. The paucity of data regarding solved reconstructions on other perovskite oxide surfaces is a perfect test bed which we will leave to the future.

The reconstructions presented here are thermodynamically stable structures, introducing the question of whether surfaces formed under conditions where kinetics dominate (i.e. film growth) also adhere to Pauling's rules. The available evidence says, yes, however there have not been enough studies where both the substrate surface and resultant film surface structure are considered. Those studies which the authors are currently aware involve deposition methods

including MBE, reactive (or hybrid) MBE, and PLD. These have found reconstructions to be a persistent feature in homoepitaxial  $\text{SrTiO}_3$  growth for multiple orientations. This is evidenced by the presence of the same types of reconstructions in thin films as on the “bare” surfaces. Persistence of the  $(\sqrt{13} \times \sqrt{13})R33.7^\circ$  (RT13) reconstruction on an  $\text{SrTiO}_3$  (1 0 0) substrate was observed via STM after the initial stages of PLD thin film growth. In this case, the reconstruction migrated to the surface [189]. Sub-monolayer  $\text{LaAlO}_3$  (1 0 0) growth on  $\text{SrTiO}_3$  (1 0 0) was conducted where the substrate’s RT13 reconstruction was observed to migrate, forming a thin  $\text{TiO}_2$  layer at the surface [64]. A study of homoepitaxial growth on  $\text{SrTiO}_3$  (1 0 0) considered surfaces with a  $(2 \times 2)$  or the  $c(6 \times 2)$  reconstruction and found that films grown on these surfaces had different morphologies [65]. Growth of  $\text{La}_{0.7}\text{Ca}_{0.3}\text{MnO}_3$  on  $\text{SrTiO}_3$  (1 0 0) RT13 surfaces indicated that the initial excess Ti on the surface led to films displaying a surface structure of the same periodicity even up to a thickness of 50 unit cells [66]. During the process of growth subtle variation of Sr:Ti cation ratio produces different, previously-observed, reconstructions in films grown by hybrid MBE on  $\text{SrTiO}_3$  (1 0 0) and (1 1 0) [47, 190]. The appearance of reconstructions, and the A:B cation ratio they imply, is reliable and repeatable enough that they have even been successfully used for *in situ* feedback to control  $\text{SrTiO}_3$  film stoichiometry during deposition [187]. This indicates that changing the number of fundamental  $\text{TiO}_x$  units (by varying the A:B stoichiometry) causes a surface to re-organize itself to obey Pauling’s rules.

In summary, all the available evidence points towards Pauling’s rules being applicable to perovskite surfaces, where there is currently a large enough database of well-solved structures. We see no reason why the rules should be limited to perovskites, and they should be generally applicable to other oxides. Indeed, there is no reason who one needs to limit their use to oxides,

and in fact they have been implicitly used in the silicon and related III-IV materials where similar ideas are common. These are Pauling's rules, just different types of coordination chemistry.

Surface structures which disobey Pauling's rules must be treated with caution. They might be rare exceptions, or just incorrect interpretations; this we leave to the future.

## CHAPTER 5

### **Single Ti-Layer Reconstructions on SrTiO<sub>3</sub> (1 1 1) - A Demonstration of Pauling's Rules**

This chapter shows a direct application of the guidelines determined and outlined in the previous chapter. As such, it serves as evidence that Pauling's Rules can, in fact, be applied to solving structures on the surface of  $\text{SrTiO}_3$ , and also provides an example for what that process entails.

Here, the case of the  $\text{SrTiO}_3$  (1 1 1) surface was considered. The case of these two reconstructions in particular was of interest as they possess unit cell sizes that are not integer multiples of the bulk unit cell. Pauling's rules were used, in combination with STM data, to generate hypothetical structures. These were then relaxed using DFT to determine whether they were structures with sufficiently low surface energies to be realistic. Final candidates were then compared to the STM experimental data to identify their structures.

This work was done in collaboration with colleagues at the University of Oxford in Oxford, UK, specifically Prof. Martin Castell and Shuqiu Wang. These collaborators provided the experimental STM images and also provided enhanced, averaged images of the two reconstructions discussed. Some material in this chapter is based on the work presented in "Single-Layer  $\text{TiO}_x$  Reconstructions on  $\text{SrTiO}_3$  (1 1 1):  $(\sqrt{7} \times \sqrt{7})\text{R}19.1^\circ$ ,  $(\sqrt{13} \times \sqrt{13})\text{R}13.9^\circ$ , and Related Structures" [191].

## 5.1 Introduction

Strontium titanate finds a wide variety of applications from the very basic to the complex. As a relatively idealized representation of the perovskite structure, it is often seen as a very simple material. However, with applications for its surfaces ranging from utilization as an oxide growth substrate [137, 192], an active material in catalysis [10, 11], to a functional material for oxide

electronics [16-18, 20, 22, 23], there is great interest in understanding the structure of its surfaces to use it most effectively.

The many reported and solved reconstructions on the three most common terminations of bulk  $\text{SrTiO}_3$  single-crystals, (1 0 0), (1 1 0), and (1 1 1), have already been mentioned and discussed at length in the previous section. Arguably, the most complex and least-studied of these three surfaces is that of  $\text{SrTiO}_3$  (1 1 1) where numerous reconstructions have been reported, as summarized previously in Table 4.3. However, only four reconstructions have been solved on this surface, making it the least-understood common termination. A number of additional low-energy structures have been theorized for this surface through DFT investigations, giving some additional insight into which types of structures are most likely to occur [49, 167]; common features of these reconstructions were discussed in the previous section.

In this section, the structure solutions of two previously-unsolved reconstructions, the  $(\sqrt{7} \times \sqrt{7})\text{R}19.1^\circ$  (RT7) and  $(\sqrt{13} \times \sqrt{13})\text{R}13.9^\circ$  (RT13) reconstructions on  $\text{SrTiO}_3$  (1 1 1) [169], are presented. Experimental STM images and Pauling's rules were used in conjunction to generate all the possible structures for these two unit cell sizes given the available symmetry information. DFT calculations and simulations of STM with the final, relaxed structures were then performed to identify which of the hypothetical starting points was correct. The final structures consist of a single layer of  $\text{TiO}_5$  and  $\text{TiO}_6$  units, a structure type that is shared with another previously-reported reconstruction, the  $(2 \times 2)\text{a}$  [49]. These solutions provide additional insight into the nature of defects observed in these reconstructions.



## 5.2 Methods

### 5.2.1 STM Measurements

All STM images were kindly provided by collaborators in the Castell group at Oxford University. Epi-polished single crystal  $\text{SrTiO}_3$  (1 1 1) with 0.5 wt% Nb-doping from PI-KEM, UK were prepared in a JEOL JSTM4500xt ultrahigh vacuum chamber. Since undoped  $\text{SrTiO}_3$  is an insulating material, Nb-doped samples were necessary to introduce n-type carriers that give rise to good electrical conductivity at room temperature, which is necessary for STM measurements. Samples were annealed at a base pressure of  $10^{-8}$  Pa ( $7.5 \times 10^{-11}$  Torr) for 30 minutes at 850 °C. Resistive heating was employed via a direct current passed through the sample, with the temperature monitored via optical pyrometer. For STM imaging, an etched tungsten tip was used at room temperature. Images were taken at constant current [169].

### 5.2.2 DFT Calculations

The WIEN2k code [154], described previously in Section 3.2.1, was used for all DFT calculations. Both the generalized gradient approximation, in this case PBESol [152], and the revTPSS method [193] were employed. All d-orbital electrons of the transition metal Ti atoms were treated with an on-site exact exchange of 0.5, similar to previous investigations [41]. This value was chosen by optimization and compared with experimental energies of selected  $\text{TiO}_x$  molecules [41]. Including this high level of exact exchange was shown, in previous work, to result in better calculated energy for the decomposition of  $\text{SrTiO}_3$  to SrO and  $\text{TiO}_2$ , closer magnitude of the band gap [167], and improved match of the ratio of surface free energy for  $\text{SrTiO}_3$  (0 0 1) to (1 1 0), as obtained from Wulff construction measurements [194].

Parameters for all calculations were standardized to allow comparison across different unit cell sizes. The lowest-energy unit-cell size for bulk  $\text{SrTiO}_3$  was determined separately for each of the calculation types (PBEsol vs. revTPSS), and all unit cells for a given reconstruction were adjusted to match these for their in-plane dimensions. Slabs were constructed using a  $(1 \times 1 \times 10)$  supercell where at least 1.6 nm of vacuum was present between surfaces. Each slab construction had six layers of bulk  $\text{SrTiO}_3$ . The muffin-tin atomic radii for O, Sr, and Ti atoms were 1.55, 1.71, and 2.21 Bohr radii respectively. A Brillouin-zone reciprocal space sampling equivalent to a  $(4 \times 4)$  in-plane mesh for a  $(1 \times 1)$  cell on  $(1 \ 1 \ 1)$  was used with an  $r^*k_{\text{max}}$  of 6.20. A quasi-Newton algorithm [195] was used to converge atomic positions and electron density, with overall convergence to better than 0.01 eV/ $(1 \times 1)$ . The surface energy per  $(1 \times 1)$  unit cell, the main quantity reported in this investigation, was calculated according to Equation 3.6, described earlier. Use of this method yielded an overall estimated error of 0.05 eV/ $(1 \times 1)$ .

### 5.2.3 STM Simulation

Relaxed low-energy structures found using DFT calculations were compared to experimental STM using STM simulations based on a modified Tersoff-Hamann approximation [124]. Additional information about this simulation technique can be found in Section 3.2.2.

## 5.3 Results

### 5.3.1 STM of $(\sqrt{7} \times \sqrt{7})\text{R}19.1^\circ$ and $(\sqrt{13} \times \sqrt{13})\text{R}13.9^\circ$

Imaging of samples done via STM showed the salient features of two reconstructions, RT7 and RT13, as well as the surface they occur on. In numerous images, terraces with jagged steps were visible; the edges of these steps did not follow a preferred crystallographic direction. Step

edges were found to be  $0.21 \pm 0.02$  nm in height, equivalent to the  $d_{111}$  lattice parameter (0.23 nm). Most of the surface was ordered, showing either RT7 or RT13 domains or a combination of the two. These domains could be small and present on multiple terraces; however, their sizes appeared to have no recognizable pattern, and the edges of these domains did not occur along any preferred crystallographic directions. There were also areas of the sample where significant disorder was present, and the boundaries between domains tended to be disordered as well. Figure 5.1 shows a typical STM image where both types of reconstructions are present on the same sample's surface. For the sample shown in Figure 5.1 and in other STM images, the two reconstructions were observed to have two different rotational domains. From the STM images, the periodicity of the two domains was found to be  $1.46 \pm 0.07$  nm (RT7) and  $1.99 \pm 0.09$  nm (RT13). This corresponds to a lattice coincidence with the underlying bulk  $\text{SrTiO}_3$  (1 1 1) of  $(\sqrt{7} \times \sqrt{7})\text{R}19.1^\circ$  (RT7) and  $(\sqrt{13} \times \sqrt{13})\text{R}13.9^\circ$  (RT13).

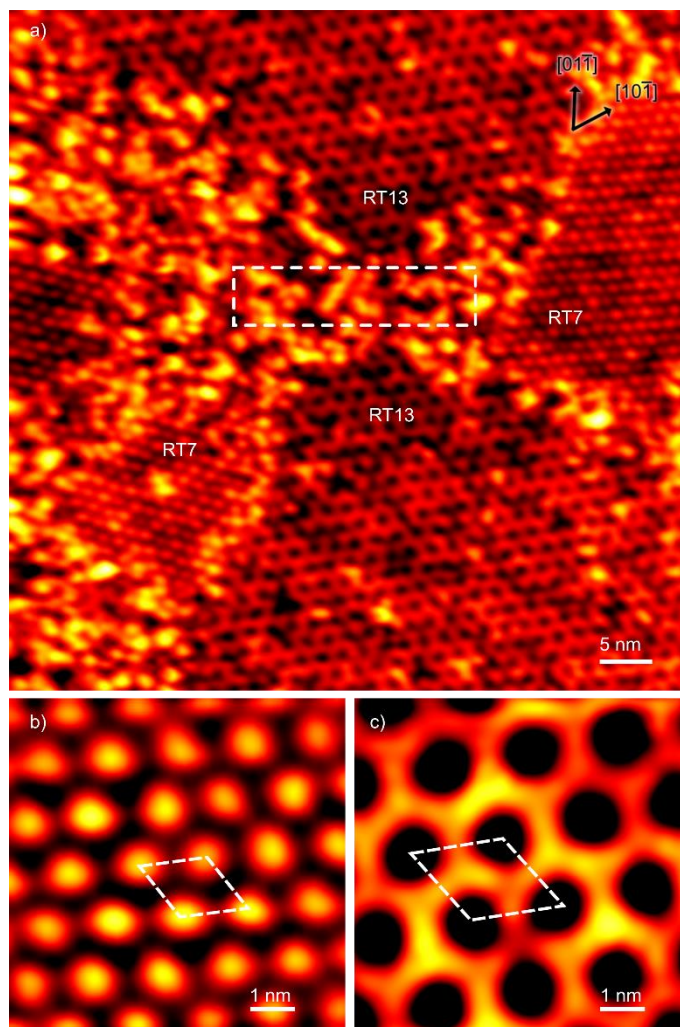


Figure 5.1 (a) STM image (+2.9 V sample bias, 0.3 nA tunneling current) showing RT7 and RT13 domains. Dashed rectangle highlights region of disorder. (b) Unit-cell averaged STM images of the RT7 reconstruction (+2.1 V bias, 0.1 nA current) and (c) the RT13 reconstruction (+3.5 V bias, 1 nA current), dashed parallelograms outline unit cells of reconstructions.

In Figure 5.1 (b) and (c), averaged STM images of the two reconstructions are shown at a larger scale to highlight their features- their unit cells are outlined by a white dashed line. The RT7, shown in Figure 5.1 (b), appears to be made up of bright dots or clusters of atoms marking out the corners of its unit cell. The RT13 is almost the opposite in contrast- instead showing an atomic arrangement that forms a honeycomb-like continuous network. While STM does not give the exact atomic positions nor provide indication of what types of atoms are present in its bright areas, this

information did provide a general starting point for these structures. Additionally, looking at the unit-cell averaged STM images in b) and c) generated using a process described elsewhere [196], p3 symmetry was identified in both of these structures.

Another representation of these reconstructions, showing how they compare to the underlying bulk  $\text{SrTiO}_3$  (1 1 1) termination and illustrating the two rotational domains, is shown below in Figure 5.2. This gives a frame of reference for how the structural hypotheses can be built up on the bulk material below and possible unit-cell origins for the two reconstructions that are considered while solving them.

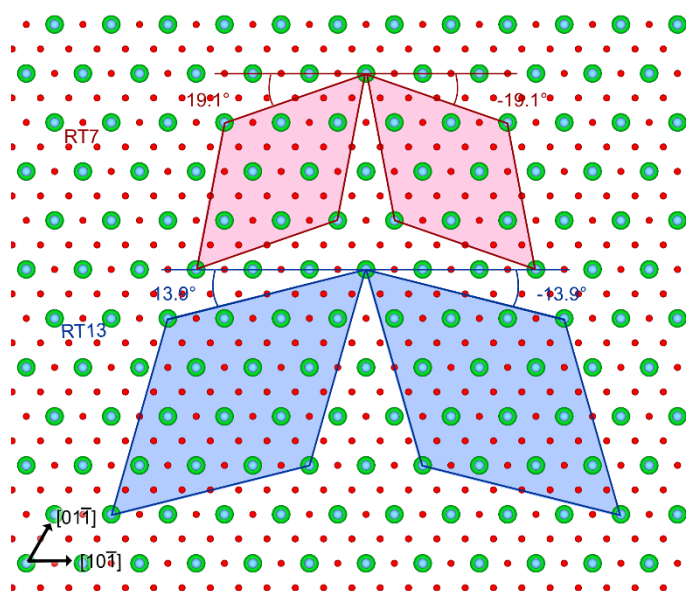


Figure 5.2 Unit cells of two rotational domains of RT7 (pink) and RT13 (blue) compared to the underlying in-plane bulk unit cell of the  $\text{SrTiO}_3$  (1 1 1) surface. Atoms of strontium, titanium, and oxygen are represented by green, blue, and red circles respectively.

### 5.3.2 Structure Generation

The Pauling's rules discussed in Chapter Four can be used, along with a few other constraints, to generate possible solutions for these reconstructions. The constraints outside of Pauling's rules that were considered are that structures on the  $\text{SrTiO}_3$  (1 1 1) are  $\text{TiO}_2$ -rich (as

determined from experimental data) [169] and are valence neutral. They follow the formula  $n\text{SrTiO}_3 \cdot m\text{TiO}_2$ .

Following the guidelines in 4.3.3, hypothetical structures were made by creating a unit cell containing bulk layers of  $\text{SrTiO}_3$  (1 1 1) that terminates on the  $(\text{SrO}_3)^{4-}$  plane. Based on the symmetry and unit cell sizes (as well as their rotations with respect to the bulk), it is not possible for these particular reconstructions to be double Ti-layer. This is due to the fact that  $\text{TiO}_4$  units in the double Ti-layer reconstructions on  $\text{SrTiO}_3$  (1 1 1) would violate the observed  $p3$  symmetry with the positions they are able to occupy according to Pauling's rules. As such, only single Ti-layered possibilities were considered.

Single Ti-layered reconstructions are made up of an interconnected network of  $\text{TiO}_5[]$  and  $\text{TiO}_6$  units. All of the possible arrangements that fulfill this requirement as well as the symmetry and stoichiometry constraints were generated for these two reconstructions. As these are relatively small unit cell sizes, this process was done by hand. However, it is possible to create an algorithm to generate these, similar to work done elsewhere [188]. This would be particularly useful in cases of increasing unit cell size where there are increasingly more structure possibilities.

All of the structures generated are shown as symbolic representations in Figure 5.3 and Figure 5.4. These representations are similar to the ones discussed in Section 4.3.3, and their main features are discussed only briefly herein. In these two figures, red triangles represent  $\text{TiO}_5[]$  units while blue triangles represent  $\text{TiO}_6$  units. Figure 5.3 shows the three possible structures for the RT7 sized reconstruction. Figure 5.4 shows all six possible structures for the RT13.

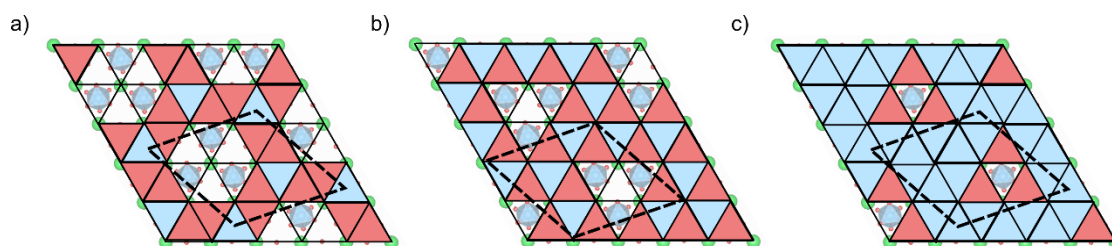


Figure 5.3 Three hypothetical structures for the RT7 reconstruction shown as symbolic representations based on Pauling's rules.

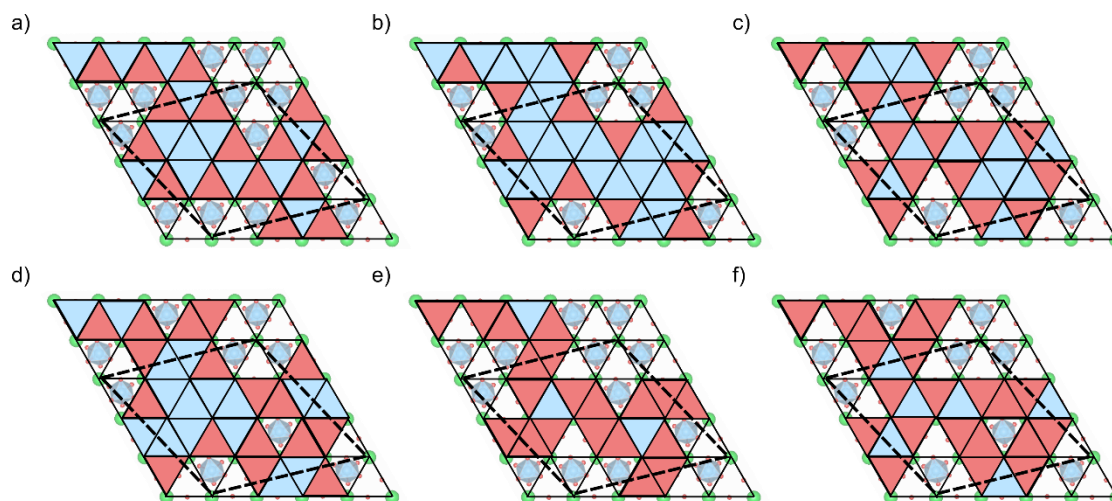


Figure 5.4 Six hypothetical structures for the RT13 reconstruction shown as symbolic representations based on Pauling's rules.

It is possible that some of the hypothetical reconstructions shown could have different unit cell origins (i.e. the same structure tiling shown by the red/blue triangles but with the bulk below shifted by a some distance). However, the possibilities shown do not include any of these original variations- when they occur the lowest energy structure has been chosen according to Pauling's rules. Specifically, the structures shown minimize the number of  $\text{TiO}_5$  or  $\text{TiO}_6$  units that share faces with  $\text{TiO}_6$  units below- this is a simple way on the  $\text{SrTiO}_3$  (1 1 1) surface to narrow down possible structures for further calculation.

### 5.3.3 DFT Results

All of the generated structures were relaxed and their surface energies calculated using DFT. To form the convex hull construction for  $\text{SrTiO}_3$  (1 1 1) reconstructions, endmembers representing different Ti-coverages are necessary to provide a benchmark for comparison. While experimentally observed and solved structures do not exist for the entire range of Ti-coverage relevant to these calculations, the next-best option was utilized. In previous investigations [49, 167], a large number of DFT calculations were conducted on hypothetical structures. Out of these a few were identified that conform to Pauling's rules and are the lowest energy structures identified for those levels of Ti-coverage. These were used to form the endpoints of the convex hull. Energies of those RT7 and RT13 hypotheses that lie on the convex hull are graphed in Figure 5.5. The structure of the endmember marked 'Low' is made up of a single layer of  $\text{TiO}_5$  units, while the one marked 'High' is composed of two layers- an interconnected ring structure of  $\text{TiO}_5$  on top of  $\text{TiO}_6$  units. The third structure to form the convex hull's boundaries is the experimentally observed and solved  $(2 \times 2)$  reconstruction. In Figure 5.5 the error bars represent the error of the DFT calculations.



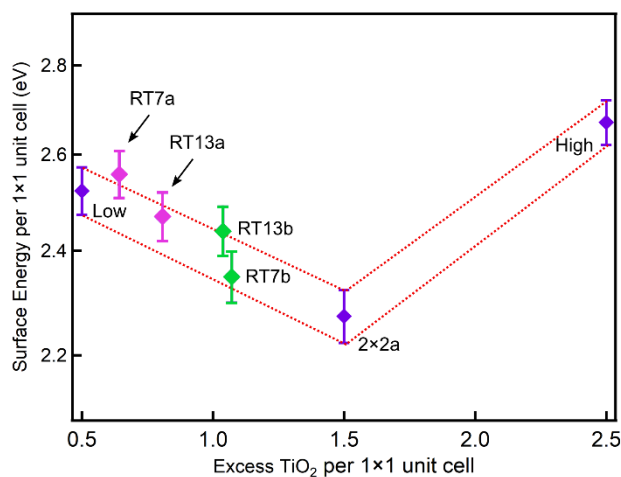


Figure 5.5 Surface energies in eV/(1 × 1) surface unit cell plotted versus excess TiO<sub>2</sub> per (1 × 1). Results are from the revTPSS calculation, and the dotted lines show results from the convex hull construction.

From an energetic perspective, all of the reconstructions plotted on this convex hull (RT7a, RT7b, RT13a, and RT13b) are theoretically possible structures. The structures of these correspond to the coded descriptions in Figure 5.3 (a) (RT7a), Figure 5.3 (b) (RT7b), Figure 5.4 (a) (RT13a), and Figure 5.4 (b) (RT13b). However, the TiO<sub>2</sub> excess for two structures, 1.071 for RT7b and 1.038 for RT13b, is similar and consistent with the STM results that showed both domains on a given sample. This reinforced the observation that identical preparation methods led to similar surface compositions, as these are both possible low-energy structures.

In the relaxed structures shown in Figure 5.5, the Ti-O bond lengths in surface TiO<sub>5</sub>[] and TiO<sub>6</sub> were both reasonable and comparable to bond lengths in the bulk material. Bonds between surface Ti and O atoms were found to be slightly longer than in the bulk (2.209 Å TiO<sub>6</sub>, and 1.994 Å TiO<sub>5</sub>[] vs 1.968 Å in bulk). This can be explained by the fact that the surface TiO<sub>x</sub> units were more tightly packed than the bulk, favoring repulsion between Ti atoms resulting in an overall expansion outwards (the least-constrained direction at the surface). The calculated bond valence

sums for these structures had Ti and O atoms at valences very close to their expected nominal 4+ and 2- values respectively [157]. Since the DFT surface energies and other easily-obtainable structural information alone were not enough to determine which of these hypotheses is correct, STM simulations were done of the relaxed structures.

### 5.3.3 STM Simulation

STM simulations of the low-energy hypotheses were conducted from their relaxed structures. The results of these simulations are compared to experimental data in Figure 5.6.

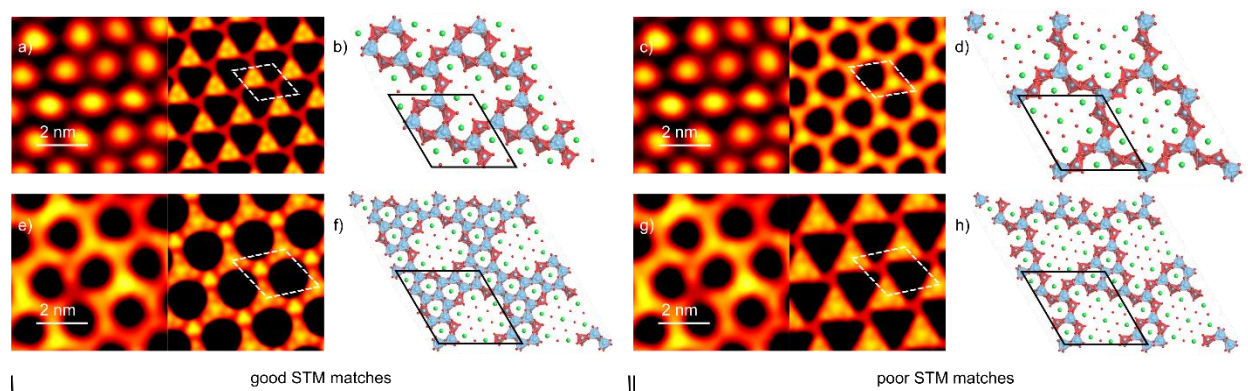


Figure 5.6 (a) Averaged STM image (+2.14 V sample bias, 0.10 nA tunneling current) of RT7 with simulated RT7b overlaid in the middle and (b) structure diagram with  $\text{TiO}_5$  octahedra in red,  $\text{TiO}_6$  octahedra in blue, and Sr atoms in green. (c, d) Show the averaged STM image and structure diagram for RT7a, respectively. (e) Averaged STM (+3.6 V bias, 0.12 nA current) of RT13, simulation RT13b overlaid to the right and (f) diagram of structure. (g, h) Show averaged STM image and structure diagram for RT13a, respectively.

The structures on the left side, RT7b (top) and RT13b (bottom), showed a good match between simulation and experimental STM. For the RT7, Figure 5.6 (a), the pattern of hexagonally close-packed dots of bright intensity was reproduced. When the simulation was compared to the atomic structure, the areas of bright contrast in the STM were attributed to the  $\text{TiO}_5/\text{TiO}_6$  ring structures present. The other possible RT7 structure, shown in Figure 5.6 (b), had a much more

open network or  $\text{TiO}_5$  and  $\text{TiO}_6$  units. This was reflected in the STM image, and the simulated contrast was almost opposite of the experimental data, making it an obviously poor match.

For the RT13 structures, the better STM match was found in Figure 5.6 (e). The characteristic honeycomb-like structure was reproduced faithfully, and comparison between the simulation and structure shows that these areas of brightness correspond very well with the denser  $\text{TiO}_5/\text{TiO}_6$  parts of the continuous network. The other hypothetical structure, Figure 5.6 (g), did not have a network with the same density and both the areas of higher  $\text{TiO}_5/\text{TiO}_6$  concentration and those with little coverage were more triangular in shape. This was also seen in the STM simulation which reproduced the triangular features rather than the hexagonal network seen in experiment.

## 5.4 Discussion

The method of generating all possible reconstructions based on the information from experimental STM and following Pauling's rules resulted in structures that were both low in energy and good matches once STM simulations were performed. These structures all consisted of a single surface layer of Ti made up on an interconnected matrix of  $\text{TiO}_5$  and  $\text{TiO}_6$  units. In the case of the RT7b reconstruction the condition of valence neutrality was maintained by removing one strontium atom per reconstruction unit cell from the  $\text{SrO}_3^{4-}$  layer directly below the  $\text{TiO}_5$  and  $\text{TiO}_6$  units. This type of removal of a Sr atom was not unique to this reconstruction, and was also reported for the  $(2 \times 2)_a$  structure on  $\text{SrTiO}_3$  (1 1 1) [49].

In fact, the  $(2 \times 2)_a$  reconstruction had many other similarities to those identified in this investigation. It was the only other experimentally observed reconstruction on this surface to display the single Ti-layer type of structure. To show the similarities between the  $(2 \times 2)_a$ , RT7b,

and RT13b structures, the three are shown below in Figure 5.7 both with their atomic structures (top) and as symbolic representations (bottom) where red triangles are  $\text{TiO}_5[\ ]$  units and blue triangles are  $\text{TiO}_6$  units. An explanation of this symbolic visualization was discussed in Section 4.3.3.

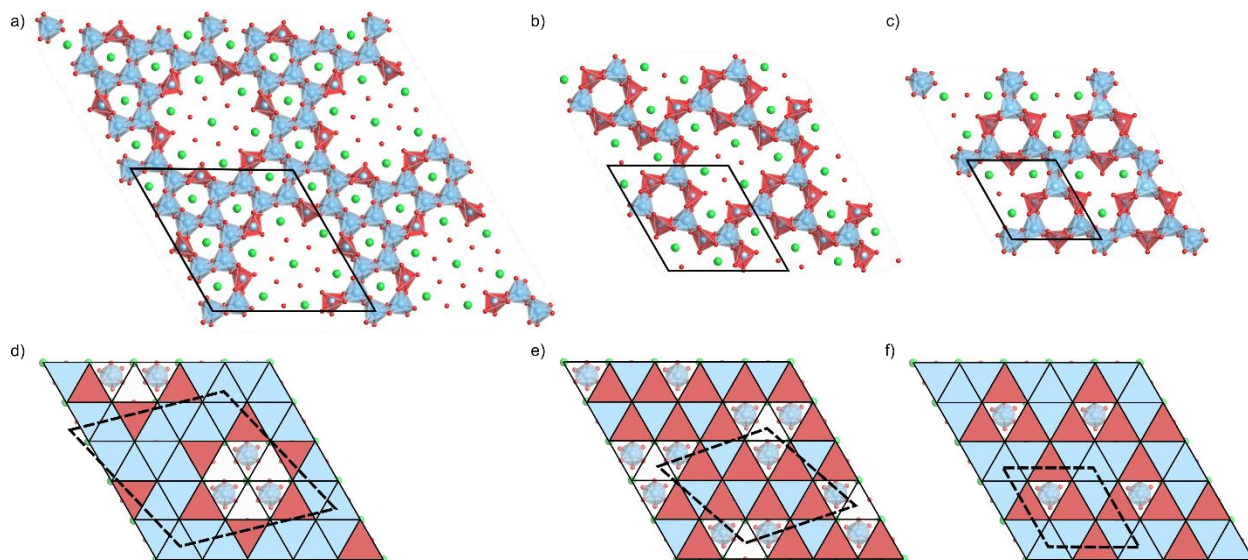


Figure 5.7 (a) Diagram of RT13b, (b) RT7b, and (c)  $(2 \times 2)a$  where  $\text{TiO}_5[\ ]$  octahedra are red,  $\text{TiO}_6$  octahedra blue, and Sr atoms are green. (d) Grid imposed on bulk  $\text{SrTiO}_3$   $(1\ 1\ 1)$  to codify RT13b, (e) RT7b, and (f)  $(2 \times 2)a$ .

Taken together, these reconstructions form a distinct family of low  $\text{TiO}_x$ -coverage reconstructions. Both solutions for the RT7 and RT13 are lower in excess  $\text{TiO}_2$  than the previously reported  $(2 \times 2)a$ , making them the lowest excess  $\text{TiO}_2$  reconstructions solved on the  $\text{SrTiO}_3$   $(1\ 1\ 1)$  surface. As the reconstructions shown in Figure 5.7 decrease in size, the concentration of  $\text{TiO}_x$  increases, forming a progressively denser  $\text{TiO}_5[\ ]/\text{TiO}_6$  network. In fact, there is another way to think about these reconstructions that reveals more about their formation and related structures, as opposed to generating them by populating atomic sites with  $\text{TiO}_5[\ ]/\text{TiO}_6$ . A hypothetical endmember structure can be imagined where all the available atomic sites on the surface are occupied by a continuous network of  $\text{TiO}_6$  units (in Figure 5.7, this would be represented by the

triangular grid being completely filled with blue triangles). This hypothetical structure satisfies the stoichiometry condition (and Pauling's rules).

If atoms were removed from this hypothetical structure to maintain the stoichiometry condition  $n\text{SrTiO}_3 \cdot m\text{TiO}_2$ , i.e., in integer amounts of  $\text{SrTiO}_3$  and  $\text{TiO}_2$ , then all of the structures seen in Figure 5.7 can be generated. Experimental STM can indicate which of these units to remove, taking some of the guesswork out of generating structures if this process is done by hand, or informing which structures are less likely if they are generated via algorithm. In cases where Sr atoms must be removed to satisfy stoichiometry, the lowest-energy positions to remove them from are those that have the highest number of neighboring  $\text{TiO}_5$  and  $\text{TiO}_6$  units. This was observed in DFT calculations and is likely due to the fact that removing Sr from these sites does little to affect the bonding environment of the nearby oxygen atoms, the atoms with the highest electronegativity.

This approach to understanding structures can be used to gain insight into experimentally-observed defects. STM of the RT13 surface is shown in Figure 5.8. There were defects present in this surface which showed up as dark areas in the STM that vary in size and placement. The structure of the outer layers was made up of  $\text{TiO}_x$  units. To maintain stoichiometry some integer number,  $n$ , of  $\text{TiO}_2$  (and/or  $\text{SrTiO}_3$ ) can be removed from this structure in a way that obeys Pauling's rules to create a new, hypothetical, defect structure. Examples of this are shown in Figure 5.8 (b), and (c). In these cases, the removed unit is indicated by a circle, and the structure that results is in the middle of the frame. In the examples shown, all maintained  $p3$  symmetry, but the experimental STM indicated that this was not necessarily required.

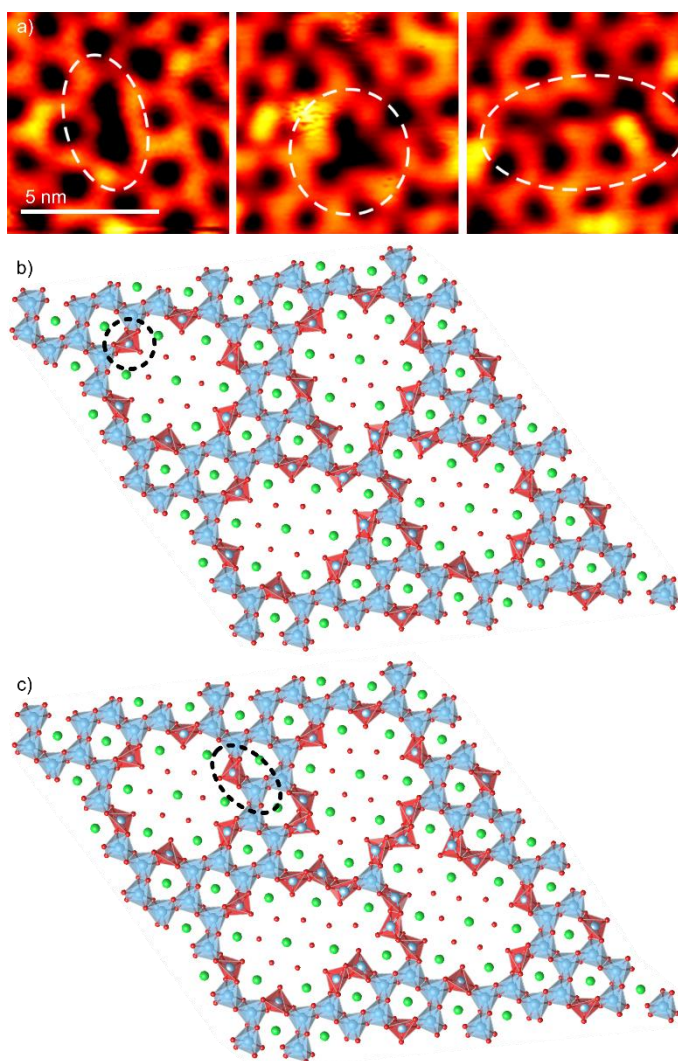


Figure 5.8 (a) STM image (+2.9 V sample bias, 0.3 nA tunneling current) of defects in RT13. (b, c) Diagrams of RT13b showing possible Schottky defects where  $\text{TiO}_5$  octahedra are red,  $\text{TiO}_6$  octahedra blue, and Sr atoms are green.

The defective structures shown in Figure 5.8 (b) and (c) were very similar to those generated in Figure 5.3 and Figure 5.4, and some were even similar to the low-energy RT13 solutions. As such, it is reasonable to conclude that they represent possible defect structures and that removal of units in any pattern to best re-create the experimental STM intensity could yield low-energy structure solutions. This indicates that the defects seen in the STM images of these

surfaces are likely to be stoichiometric Schottky defects localized at the surface of the material, as opposed to simple vacancies or interstitials.

Although the single-layered  $\text{TiO}_x$ -rich structure model does not apply to all of the  $\text{SrTiO}_3$  (1 1 1) surfaces that have been solved, conceptually it fits in well with the double-layered surfaces. It can therefore be applied to investigate hypothetical solutions for any  $\text{SrTiO}_3$  (1 1 1) surface having  $p3$  symmetry regardless of unit-cell size. The double-layered Ti-rich reconstructions such as  $(3 \times 3)$  and  $(4 \times 4)$  are a natural extension of this model- higher Ti coverage leads to a second  $\text{TiO}_x$ -rich layer made up of  $\text{TiO}_4$  units. As the amount of  $\text{TiO}_x$  on a surface increases, it is likely that a double-layered structure would be necessary to accommodate it, considering there is no great fundamental difference between the placement and types of units present in either of these surface models for  $\text{SrTiO}_3$  (1 1 1).

## 5.5 Conclusions

In this chapter, the solutions for two experimentally observed reconstructions on  $\text{SrTiO}_3$  (1 1 1), the RT7 and RT13, were determined. They were found by generating possible structures using Pauling's rules informed by the STM images, and the structures were chosen from candidates by performing DFT relaxations and STM simulations. These structures, along with the  $(2 \times 2)_a$ , were found to belong to a family whose model is easy to understand, and this model can be applied to many reconstructions and observed surface defects. The methods described in this chapter could, in the future, be used to create an algorithm for generating all possible structures within this family, given a chosen unit-cell size, vastly simplifying the process of solving reconstructions on this surface and lowering the computational burden of calculation. This direct demonstration of

Pauling's rules for oxide surfaces also indicates that descriptions of reconstructions can be unified to provide additional insight into the surfaces of a given material.



## CHAPTER 6

### **Thin Film Growth of Strontium Cobaltites**

The previous chapters focused on how the structure of oxide materials can be understood at the level of reconstructions up to several atomic layers. This provides a foundation for exploring structure in thin films while hinting at the complexity that is present in perovskite materials.

This chapter moves to structure on a larger scale- thin films. The same material family, perovskites, will be discussed as the complexity within this family is more than enough to provide opportunities for investigation. To this end, the growth and structural evolution of the strontium cobaltite, or Sr-Co-O, system is discussed in detail in this chapter.

This oxide system exhibits a complex structural interplay affected by both thermodynamic and kinetic factors. For methods where both growth environment and speed can be controlled, such as MBE deposition, there is surprising flexibility within this material system. In particular, growth behavior at varying time-scales was performed. This led to observations of the interplay between kinetic and thermodynamic drivers on a film's final structure. Post-treatment of films and the effect of this on structure is also briefly discussed.

The main tool for the measurement of films in this chapter is in situ X-ray scattering and an MBE chamber designed specifically for these types of investigations was utilized. The in situ capability of this system enables probing a film's structure at different points throughout its growth, which was used in-depth in the following investigation.

Experimental work presented herein at the APS was conducted with kind assistance from Dr. Hawoong Hong, Dr. I-Cheng Tung, and Seyoung Cook. Materials in this chapter form the basis of "Layer-by-Layer Epitaxial Growth of Defect-Engineered Strontium Cobaltites" [197], from which some figures have been reproduced.

## 6.1 Introduction

The perovskite structure of  $\text{ABO}_3$  allows incorporation of different elements in the A and B cation positions [3, 5, 6, 8, 9, 12, 23], as well as tolerating a variety of composition with regard to oxygen anions. Many B-site cations are transition metals that adopt different polyhedra according to the amount of oxygen present. The electronic structure of transition metals, where the  $d$  orbital electrons interact with the  $2p$  orbitals of oxygen anions, lies at the root of this ability. In some cases this results in materials adopting a variety of properties depending on their external environment [92, 93, 198, 199] as functional defects (oxygen vacancies) are created and moved through the material [106, 200]. Since these defects contribute to a material's properties, it becomes necessary to develop an understanding of their control.

B-site transition metals can adopt variable oxidation states, supporting a range of coordination environments and structures [201, 202]. One transition metal that shows high flexibility (by adopting oxidation states from 2+ to 4+) is cobalt, which has been studied with the aim of controlling its phase and oxidation state through synthesis [2, 93, 203]. Various oxide structures containing cobalt display high electrocatalytic activity [91, 93], reversible magnetic states [204], and controllable oxygen diffusivity [205]. One example is  $\text{SrCoO}_3$ , a ferromagnetic metallic perovskite made up of corner-sharing octahedra of  $\text{CoO}_6$  [206], and  $\text{SrCoO}_{2.5}$ , an antiferromagnetic insulator with tetrahedral and octahedral  $\text{CoO}_x$ . One can reversibly switch between these structures via a topotactic phase transition [9, 93, 207-210].

There are multiple viable methods for switching between these states [9, 93, 207-210], and controlling conditions during synthesis offers another way to achieve a desired  $\text{SrCoO}_x$  phase. For example, oxygen activity and epitaxial strain have been shown to play a role in phase determination

[9]. Most investigations of growth in this system utilized PLD with particle impingement energies ranging from 5 eV to 50 eV, which result in deposition conditions very far from equilibrium [9, 92, 93, 165, 207, 210, 211]. MBE growth differs in a number of ways: impingement energies are on the order of 0.1 eV [67], and growth rates can be much slower which allows for precise atomic and defect control [212].

In this chapter, the synthesis conditions for the stabilization of different members of the Sr-Co-O (SCO) system will be discussed. A brief investigation into post-growth annealing of the Brownmillerite phase will also be examined. In situ X-ray scattering [137] was used to probe the structure of SCO thin films at different stages of their growth. The conditions for stabilization of different phases were compared with calculated thermodynamic equilibria and kinetically-limited processes such as solute trapping [213-216]. The findings of this investigation shed light on the interplay of thermodynamic and kinetic processes in MBE and their use in predicting growth conditions for defect-engineering films with MBE.

## **6.2 Methods**

### **6.2.1 Substrate Preparation**

SrTiO<sub>3</sub> (0 0 1) substrates with low ( $< 0.1^\circ$ ) miscut [CrysTec GmbH] were prepared to produce TiO<sub>x</sub>-rich terminated substrates [217]. They were sonicated for thirty seconds each in acetone, isopropyl alcohol, and then water to de-grease and remove particles from their surface. They were then sonicated in deionized water for 10 minutes at room temperature. Etching was done by agitating for 30 seconds in a buffered hydrofluoride solution (NH<sub>4</sub>F:HF = 3:1) of pH 5-5.5 before being rinsed in deionized water. Substrates were annealed for two hours in flowing

oxygen at 1323 K. Substrates treated in this manner displayed unit cell height steps, confirmed by atomic force microscopy (AFM).

### 6.2.2 Thin Film Deposition

Films were grown using reactive MBE in the custom-built chamber introduced and discussed in Section 3.1.2. Pure oxygen or oxygen/ozone mixtures were introduced into the chamber at total pressures ranging from  $2.67 \times 10^{-5}$  to  $1.33 \times 10^{-4}$  Pa ( $2 \times 10^{-7}$  to  $1 \times 10^{-6}$  Torr). The relative ozone concentration used was varied from 10% (i.e. 10% ozone, 90% oxygen) to nominally 100%. All substrates were annealed in the background  $O_2/O_3$  at the substrate growth temperature,  $T_{sub}$ , ranging from 823-1023 K (measured by optical pyrometer) for 20 minutes before deposition. Effusion cells supplied strontium and cobalt metal vapors with fluxes that were calibrated with a QCM. The QCM calibration determined the deposition time needed for each single atomic plane (i.e. ML). Sources were shuttered according to this calculated timing in the repeated pattern of Sr -> Co -> Sr -> Co -> etc. This was chosen to favor either Brownmillerite or perovskite-structured phases that exhibit alternating MLs of Sr and Co [218-220].

### 6.2.3 In situ X-Ray Scattering

All measurements were performed at APS Sector 33-IDE. Diffraction data in this section was acquired using 7.5 keV energy unless otherwise noted (annealed samples were measured with 15 keV X-rays). X-rays were selected with a Si (1 1 1) monochromator. In situ monitoring at the anti-Bragg position (0 0  $\frac{1}{2}$ ) of the  $SrTiO_3$  substrate was performed to observe film thickness and growth mode [221]. Immediately after deposition, (0 0  $L$ ) specular rod scans were performed. Some films were interrupted periodically during growth to perform additional (0 0  $L$ ) measurements to provide detailed information on structure evolution. All reciprocal space

positions are presented in the form of  $(0\ 0\ L)$  or reciprocal lattice units (r. l. u.) where  $L$  is the out-of-plane diffraction direction relative to the room-temperature lattice parameter of  $\text{SrTiO}_3$ , 0.3905 nm, using pseudocubic (pc) indexing for all crystal structures. 2-Dimensional images of the scattered X-rays were collected using a pixel array detector [Pilatus 100 K, Dectris], and the data were reduced to background-subtracted integrated intensities [222].

### 6.2.3 In situ X-Ray Scattering

XANES measurements, across the Co  $K$ -edge, were performed to determine Co oxidation state during SCO phase growth. The intensities of the fluoresced X-rays from the films were measured using a silicon drift detector [Vortex-60EX, Hitachi] aimed at the sample from above, which was positioned at  $90^\circ$  with respect to both the sample surface and the incident X-rays. To calibrate the measured energies, a Si-PIN photodiode was used to measure the parasitic air scattering from an energy-varying incident X-ray beam transmitted through a Co metal reference foil (5  $\mu\text{m}$  thickness). An ionization chamber,  $I_0$ , was present upstream from the reference foil in order to normalize the reference spectra. Downstream of the foil another ion chamber,  $I_1$ , was used to normalize the sample spectra. To determine the oxidation state of cobalt from XANES, the midpoint of the adsorption edge's position was taken to be  $0.5\mu\text{x}$ . Two references, containing  $\text{Co}^{+2}$  and  $\text{Co}^{+3}$  [143, 223], were used as interpolation endpoints when determining the average oxidation state of films.

## 6.3 Results

### 6.3.1 Sr-Co-O Film Growth

In The SCO phase diagram has line compounds and areas of equilibrium between multiple phases [224, 225]. This complexity necessitates a narrow substrate temperature range for MBE

growth, one that is high enough for adatom mobility ( $> \sim 773$  K), but low enough to avoid decomposition into the undesirable  $\text{Sr}_6\text{Co}_5\text{O}_{15}$  hexagonal phase ( $\sim 923$  K for bulk) [226]. In the growth chamber utilized, pressure was limited to a maximum of  $\sim 10^{-4}$  Pa ( $10^{-6}$  Torr) to avoid oxidation of solid sources and provide a long enough mean-free-path for atoms. However, the  $\text{O}_2:\text{O}_3$  ratio was used to vary oxygen activity by orders of magnitude ( $10^{15}$  depending on temperature) in lieu of increasing background pressure. The growth conditions investigated yielded films of two crystalline phases both of which were epitaxial with the  $\text{SrTiO}_3$  (0 0 1) substrate. Off-specular Bragg peaks indicated both phases were coherently strained. The specular (0 0  $L$ ) X-ray scattering spectra of these phases are shown in Figure 6.1 (a) and (b) with the corresponding XANES spectra shown in Figure 6.1 (c).

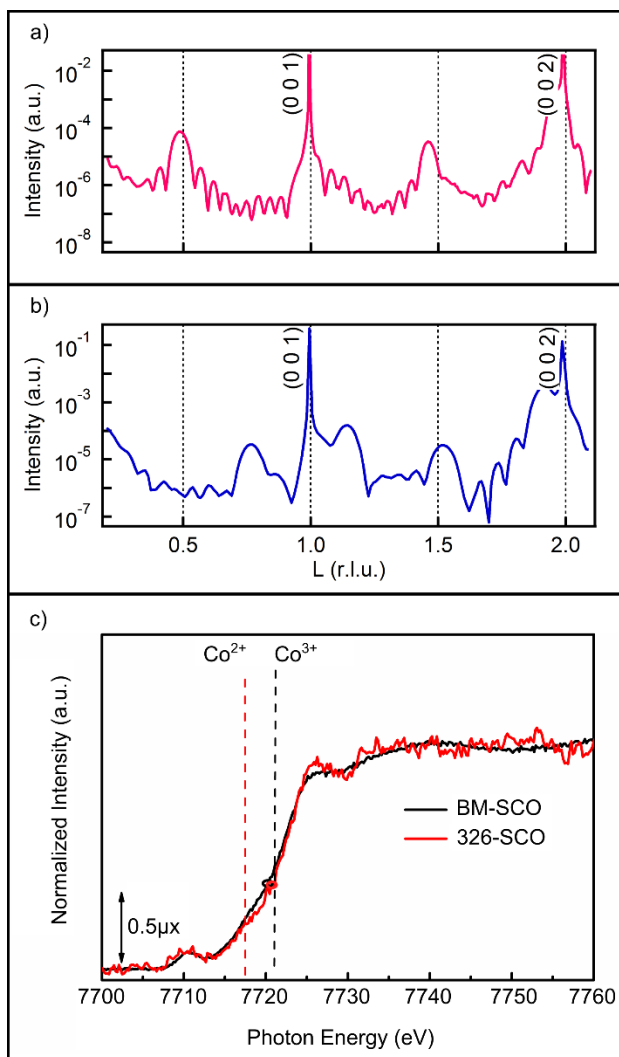


Figure 6.1 X-ray scattering along the (0 0  $L$ ) crystal truncation rod of phase-pure  $\text{SrCoO}_{2.5}$  (a) and  $\text{Sr}_3\text{Co}_2\text{O}_{6\pm\delta}$  (326-SCO) (b) films grown on  $\text{SrTiO}_3$  (0 0 1). Film shown in (a) was grown at  $T_{\text{sub}} = 875$  K,  $p\text{O}_3 = 1.33 \times 10^{-4}$  Pa ( $1 \times 10^{-6}$  Torr), (b) was grown at  $T_{\text{sub}} = 873$  K,  $p\text{O}_2 = 1.33 \times 10^{-4}$  Pa ( $1 \times 10^{-6}$  Torr). XANES at the Co K-edge (c) for the films, showing they both exhibit  $\sim\text{Co}^{3+}$ , as measured at  $\mu x = 0.5$  (the intensity halfway point of normalized spectra). The energy references are from the Co metal foil and Refs. [143, 223]

The overlay of the two traces in Figure 6.1 (c) indicates that both films contain  $\text{Co}^{3+}$ . The structure in Figure 6.1 (a) was identified as the Brownmillerite phase. Simulations of specular (0 0  $L$ ) X-ray scattering of the  $\text{SrCoO}_{(3n-1)/n}$  series (having endmembers of the Brownmillerite, BM-



SCO, and perovskite, P-SCO) are shown (along with the structures they depict) for  $n = 2, 4, 8$ , and  $\infty$  in Figure 6.2.

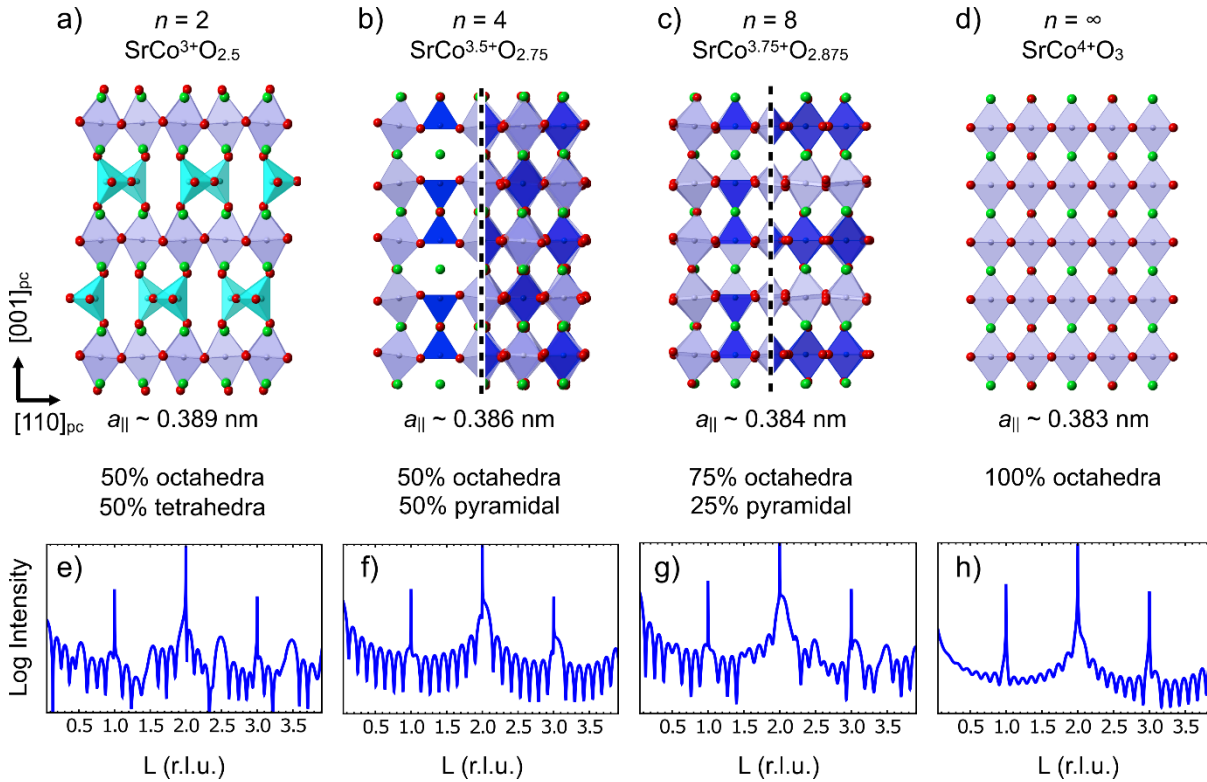


Figure 6.2 Structures of the stable members of the  $\text{SrCoO}_{(3n-1)/n}$  homologous series for  $n = 2$  (a), 4 (b), 8 (c), and  $\infty$  (d) on  $\text{SrTiO}_3$  (0 0 1) and (e-h) their corresponding (calculated) X-ray scattered intensities along the  $(0\ 0\ L)$  specular rod assuming films are coherently strained, respectively. The  $n = 4$ , and 8 members (b) and (c) have two possible orientations, shown separated by the dotted line, the  $(0\ 0\ L)$  in (f) and (g) are an average of these two. The polyhedra corresponding to  $\text{CoO}_4$ ,  $\text{CoO}_5$ , and  $\text{CoO}_6$  are shown in cyan, blue, and violet, respectively. Strontium atoms and oxygen atoms are green and red respectively. The defect structures are expected to evolve from left to right when moving from reducing to more oxidizing conditions.

The film in Figure 6.1 (a) was grown at  $T_{\text{sub}} = 875$  K using 100%  $\text{O}_3$  delivered at a pressure of  $p_{\text{O}_3} = 1.33 \times 10^{-4}$  Pa ( $1 \times 10^{-6}$  Torr). Distinctive half order peaks present at  $(0\ 0\ 1/2)$  and  $(0\ 0\ 3/2)$  in Figure 6.1 (a) were the same as those observed in simulation of the BM-SCO phase in Figure 6.2 (a) and (e). These reflections at  $(0\ 0\ m/2)$ , where  $m$  is odd, resulted from octahedral-tetrahedral

stacking along the  $[0\ 0\ 1]_{pc}$ , shown in Figure 6.2 (a). These conditions and the film's diffraction data agreed with previously-reported PLD-grown  $\text{SrCoO}_{2.5}$  films with pseudo-tetragonal structure that had in- and out-of-plane lattice parameters of  $a_t = 0.3905$  nm,  $c_{t/4} = 0.3940$  nm at room temperature [227].

Result for the film shown in Figure 6.1 (b) did not match any simulated in Figure 6.2, indicating that it was not a member of the BM-SCO to P-SCO series. This film was also grown at  $T_{sub} = 873$  K, but with 100%  $\text{O}_2$  delivered at  $p\text{O}_2 = 1.33 \times 10^{-4}$  Pa ( $1 \times 10^{-6}$  Torr). Only a small number of the Sr-Co-O phases have lattice parameters allowing coherent strain with  $\text{SrTiO}_3$  (0 0 1), one of which is the Ruddlesden-Popper,  $\text{Sr}_{n+1}\text{Co}_n\text{O}_{3n+1}$  structures [228]. This type of structure has been stabilized on perovskite substrates in other A-B-O systems [166, 229, 230]. In the SCO system the  $n = 1, 2$ , and 3 members,  $\text{Sr}_2\text{CoO}_4$ ,  $\text{Sr}_3\text{Co}_2\text{O}_7$ , and  $\text{Sr}_4\text{Co}_3\text{O}_{10}$  are stable possibilities for coherent growth on  $\text{SrTiO}_3$  (0 0 1).

Considering these, the Bragg peaks of the films were investigated. They showed periodicity of  $\sim 0.385$  in  $L$  (1.01 nm in real space). This corresponded with  $\text{Sr}_3\text{Co}_2\text{O}_7$ , having a bulk out-of-plane lattice constant of 2.022 nm given that the Bragg condition was satisfied for every (0 0 2) plane in its tetragonal unit cell (shown in Figure 6.3). The other two stable Ruddlesden-Popper phases have lattice constants of 1.233 nm, and 2.855 nm, which made them very poor matches to the observed peaks.

While the lattice parameter of the film agreed with  $\text{Sr}_3\text{Co}_2\text{O}_7$ , the XANES indicated that  $\text{Co}^{3+}$  was the species observed in this film. This implied an oxygen-deficient stoichiometry represented by  $\text{Sr}_3\text{Co}_2\text{O}_{6\pm\delta}$  (326-SCO), where  $6\pm\delta$  is very close to 6. Bulk synthesis of similar

phases including  $\text{Sr}_3\text{Co}_2\text{O}_{5.78}$ ,  $\text{Sr}_3\text{Co}_2\text{O}_{5.91}$ ,  $\text{Sr}_3\text{Co}_2\text{O}_{5.94}$ , and  $\text{Sr}_3\text{Co}_2\text{O}_{6.06}$  have been reported and their structures determined [107, 108]. This structure is shown in Figure 6.3 (b). The oxygen-deficient Ruddlesden-Popper has oxygen vacancy channels that are “taller” than those of the Brownmillerite structure but similarly run in-plane with respect to the substrate. The  $\text{CoO}_6$  octahedra of the perfect Ruddlesden-Popper are replaced by a mixture of  $\text{CoO}_6$  octahedra and  $\text{CoO}_5$  square pyramids in this structure [107].

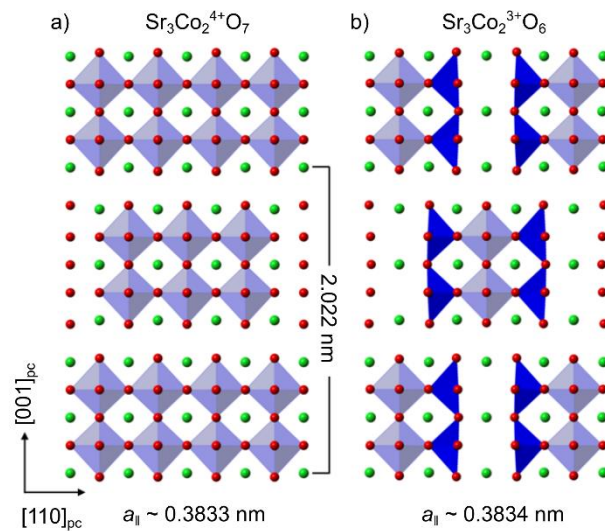


Figure 6.3 Crystal structures of the  $\text{Sr}_3\text{Co}_2\text{O}_7$  Ruddlesden-Popper (a) and the related oxygen-deficient  $\text{Sr}_3\text{Co}_2\text{O}_{6\pm\delta}$  (b) showing positions of oxygen vacancies. The polyhedra corresponding to  $\text{CoO}_5$ , and  $\text{CoO}_6$  are shown in blue, and violet, respectively. Strontium atoms and oxygen atoms are green and red respectively.

Every film across the range of conditions tested was identified as either  $\text{SrCoO}_{2.5} (0\ 0\ 1)_{\text{pc}}$ ,  $\text{Sr}_3\text{Co}_2\text{O}_{6\pm\delta} (0\ 0\ 1)_{\text{pc}}$ , or a mixture of the two. In a few films an additional peak at  $(0\ 0\ L = 1.83)$ , attributed to  $(0\ 0\ 1)$ -oriented CoO was identified. All depositions were done with a cationic ratio  $\text{Sr}:\text{Co} = 1$ , so the presence of CoO can account for the excess Co atoms missing from the 326-SCO phase. However, this peak was not observed in most of the 326-SCO films, bringing up the

question of where extra Co was located. It was possible, but at the growth temperatures investigated, highly unlikely, that CoO nanoparticles volatilized [231]. Another phenomenon, solute trapping, offers a more satisfying explanation that will be discussed in greater detail later. For now it is sufficient to note that both  $\text{SrCoO}_{2.5}$  and  $\text{Sr}_3\text{Co}_2\text{O}_{6\pm\delta}$  may be stable over a range of A:B ratios. The upper limits of solubility for cations on each other's sites has not been investigated and the Sr-Co-O phase diagram have only recently been given quantitative attention [224, 225].

### 6.3.2 Effects of Growth Rate on Thin Film Phase

To gain an understanding of the effect growth rate has on the film phase, a series of growths were observed at set conditions for an in-depth study. Films were grown using  $T_{\text{sub}} = 873$  K, and  $p_{\text{O}_3} = 1.33 \times 10^{-4}$  Pa ( $1 \times 10^{-6}$  Torr), chosen as conditions where both BM-SCO and 326-SCO were observed. The growth rate was controlled, not by changing the source flux, but by interrupting growth at different stages to collect X-ray scattering and spectroscopy data. The fastest film growth occurred without interruption (an effective growth rate of  $0.003 \text{ \AA/s}$ ); a second film was interrupted and measured after deposition of every four bilayers (BLs) (effective growth rate of  $0.002 \text{ \AA/s}$ ); and a third film was interrupted after growth of every BL (effective growth rate of  $0.001 \text{ \AA/s}$ ). This method of altering the growth rate was chosen both for practical reasons and because it allowed insight into the structural evolution at different thicknesses.

The  $(0\ 0\ L)$  X-ray scattering spectra after growth, shutter/measurement scheme, and in situ  $(0\ 0\ \frac{1}{2})$  r. l. u. intensity measured throughout growth for these three films are shown in Figure 6.4. Oscillations of the  $(0\ 0\ \frac{1}{2})$  intensity in Figure 6.4 (a), (c), and (e) corresponded with the growth of each  $\text{SrO-CoO}_x$  bilayer. The BM-SCO phase exhibited a superlattice peak at  $(0\ 0\ \frac{1}{2})$ , so it was expected that growth of this phase would result in an increase in intensity at this condition, as was

observed for the two films grown at a faster rate, Figure 6.4 (a) and (c). If the Brownmillerite structure was considered, one expected that four BLs must be grown to observe the full unit-cell and the Bragg peak at  $(0\ 0\ \frac{1}{2})$ . Before reaching this thickness the film did not have the structural periodicity required to result in superlattice peaks. Interestingly, no increase in intensity was observed at the  $(0\ 0\ \frac{1}{2})$  until at least eight BLs had been deposited. This indicated that a critical thickness of two unit-cells was necessary to observe the oxygen-vacancy ordering present in the BM-SCO phase. In the film with the slowest effective growth rate the overall intensity of the  $(0\ 0\ \frac{1}{2})$  diffraction condition was lower and its behavior was much less predictable, as shown in Figure 6.4 (e).

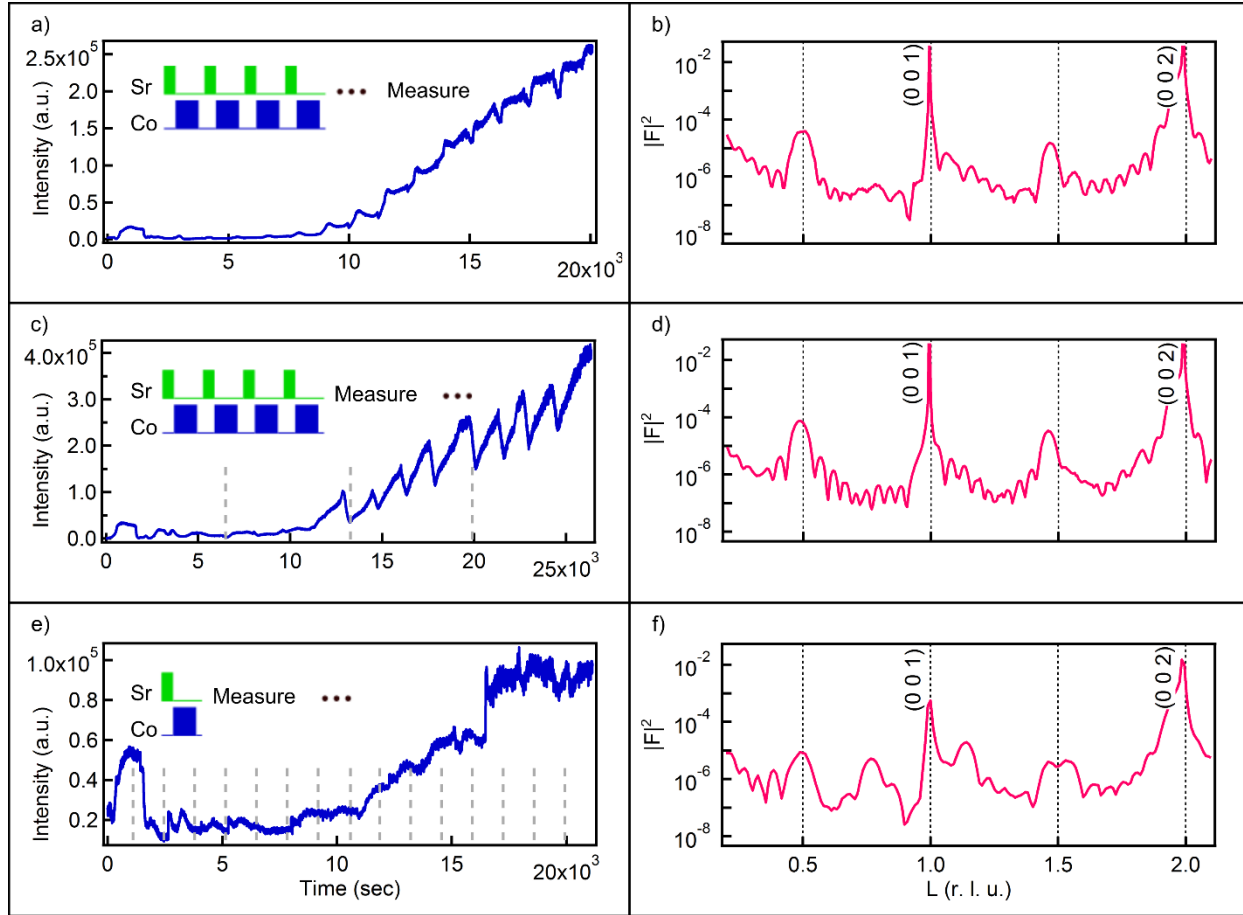


Figure 6.4 Scattered X-ray intensity at the  $(0\ 0\ \frac{1}{2})$  position during growth (left) of three different Sr-Co-O films (a, c, e) on  $\text{SrTiO}_3$   $(0\ 0\ 1)$  and their corresponding  $(0\ 0\ L)$  scans of the films (right) after growth (b, d, f). Films were interrupted (marked as ‘Measure’) during growth as depicted in the inset shutter schematics of (a), (c), and (e). All growths shown were conducted at  $T_{\text{sub}} = 873$  K,  $p\text{O}_3 = 1.33 \times 10^{-4}$  Pa ( $1 \times 10^{-6}$  Torr).

By comparing the films in Figure 6.4 (b), (d), and (f), it was determined that faster growth rates yielded films that were BM-SCO in phase while the slowest growth was a mixture of the BM-SCO and 326-SCO phases. As such, faster growth prevented decomposition of  $\text{SrCoO}_{2.5}$  into  $\text{Sr}_3\text{Co}_2\text{O}_{6\pm\delta}$  and CoO- results that agreed with PLD studies [9, 92].

Films measured at different points throughout their growth were compared to provide additional information about their structure. Figure 6.5 shows the results of this experiment with

(0 0  $L$ ) scans for the BM-SCO film interrupted every 4 BL, Figure 6.5 (a), (c), and the mixed BM-SCO + 326-SCO film interrupted every BL, Figure 6.5 (b), (d).

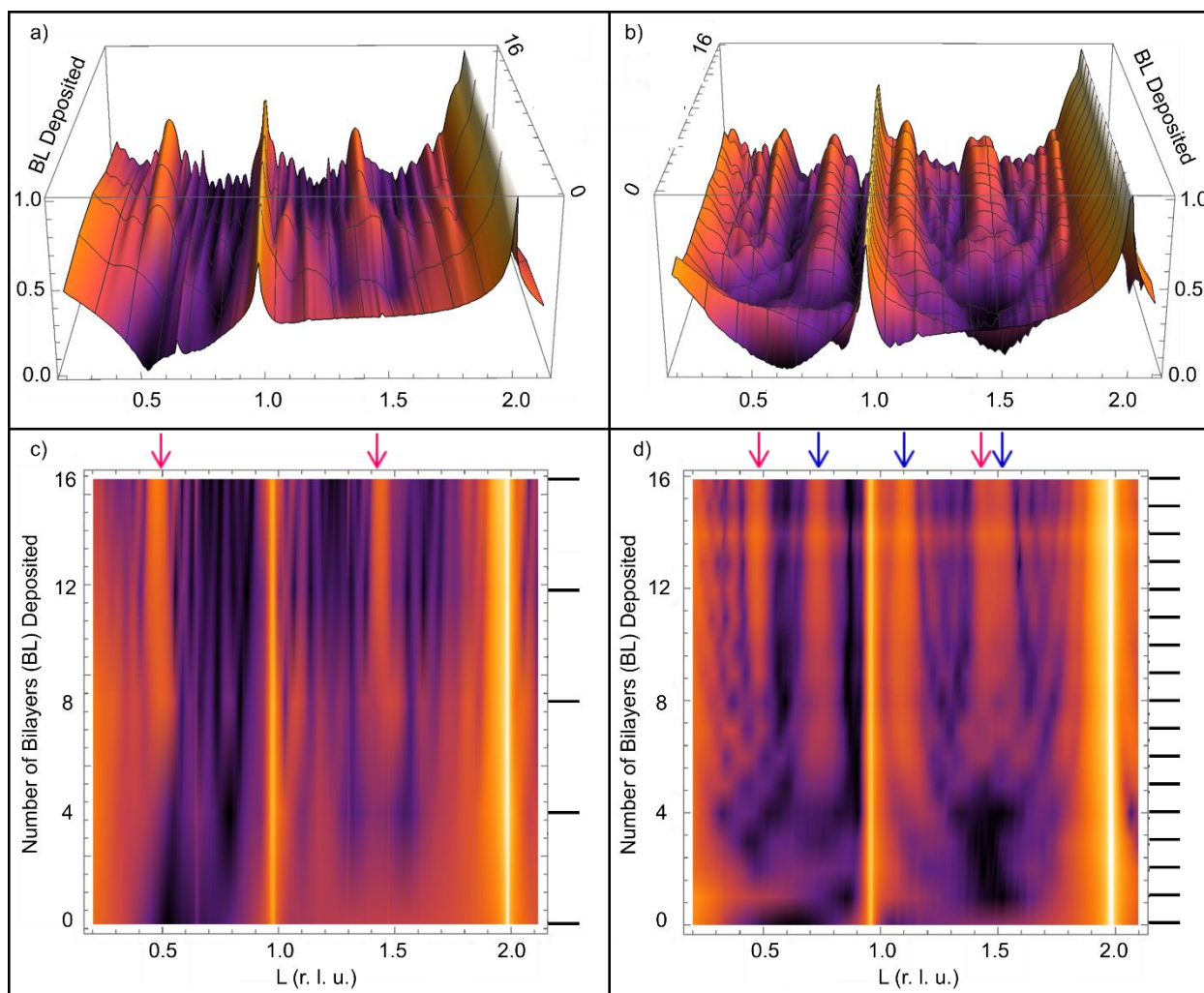


Figure 6.5 Scattered X-ray intensity along the (0 0  $L$ ) specular rod showing evolution of the film structure for films interrupted after deposition of each four BLs (a), (c) or interrupted every BL (b), (d). All intensities (z-axis and color map lightness) are plotted on a normalized  $\log_{10}$  scale. Arrows in (c) and (d) indicate peak positions characteristic to the BM-SCO (pink) and 326-SCO (blue) phases while tick marks on the right axis indicate when measurements were taken.

In Figure 6.5 (c) and (d) the BM-SCO and 326-SCO Bragg peaks are marked with pink and blue arrows respectively to aid in identification. For the BM-SCO film, Figure 6.5 (a), and (c), BM-SCO peaks became evident after deposition of 8 BL. The two-phase film, Figure 6.5 (b) and

(d), had Ruddlesden-Popper peaks near  $L = 0.77$  and  $1.14$  after deposition of about 5 BL. This was roughly the same length scale as the unit-cell for  $\text{Sr}_3\text{Co}_2\text{O}_{6\pm\delta}$ . Intensity at the BM-SCO positions did not become distinguishable from thickness fringes until deposition of roughly 8 BL. This indicated that the BM-SCO phase had a similar critical thickness for ordering whether it was in single or mixed-phase films, and that its critical thickness of ordering was larger than that of the 326-SCO phase. Once a phase was established it persisted throughout the growth, indicating that its presence was set soon after the nucleation stage and was not significantly altered by other competing phases.

To understand more about the thickness of each phase, distinct  $\text{SrCoO}_{2.5}$  and  $\text{Sr}_3\text{Co}_2\text{O}_{6\pm\delta}$  Bragg peaks were fitted with Gaussian functions. The full-width half maxima were determined, and the thickness within each phase calculated using a form of Scherrer's equation (Equation 6.1).

$$\tau = \frac{K\lambda}{\beta \cos\theta} \quad (6.1)$$

In Equation 6.1  $\tau$  was the calculated film thickness,  $K$  a dimensionless shape factor set to unity,  $\lambda$  the wavelength of X-rays,  $\beta$  the full-width half-maximum of the film peak (in radians) for the phase whose thickness is measured, and  $\theta$  was the Bragg angle (in degrees). Additionally, the total film thickness was determined from the spacing of thickness fringes measured in the  $(0\ 0\ L)$ , done for the two films shown in Figure 6.5. The results of this analysis are summarized in Figure 6.6 for the BM-SCO film (a) and the two-phase film (b). Both curves (BM-SCO phase and total thickness) were a close match in Figure 6.6 (a), indicating the out-of-plane correlation length spans the film. The data in Figure 6.6 (b) showed that the thicknesses of BM-SCO and 326-SCO increased at similar rates and their final thickness was on the same order as the total film thickness,



similar to the single-phase film. While there was no in-plane information indicated by the (0 0  $L$ ) data, this described some possible domain architectures. The most likely domain structure for the two phases was a self-assembled vertically-aligned nanocomposite [69].

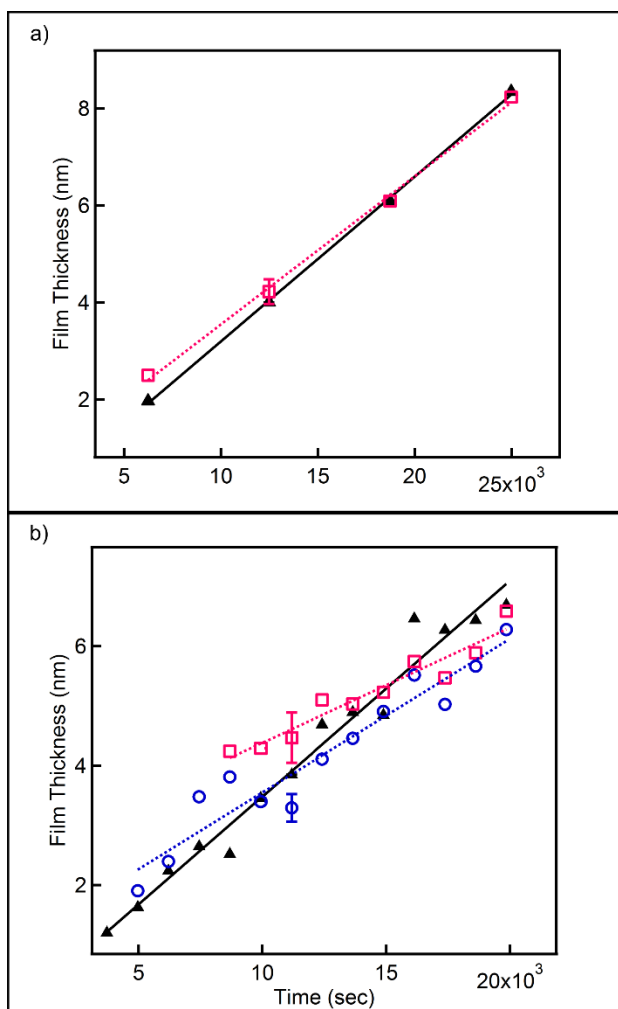


Figure 6.6 Thickness of different phases during growth in a pure BM-SCO film (a) and the BM-SCO + 326-SCO film (b). The BM-SCO phase is indicated by the pink traces, 326-SCO phase by blue, while the overall film thickness based on CTR thickness fringes is indicated in black. Linear fits are drawn as a guide for the eye.

XANES of previously-discussed films, such as those shown in Figure 6.1 (c), indicated that both the phase-pure BM-SCO and the mixed BM/326-SCO films contain  $\text{Co}^{3+}$ . In situ XANES of the films in Figure 6.5 (a) and (b) were also acquired immediately after (0 0  $L$ ) scattering data

was collected (i.e., during growth interruption) to see whether this remained true and how the oxidation state of cobalt might be affected by film thickness. The data are shown in Figure 6.7, where the BM-SCO film is presented in (a) and the mixed phase film in (b).

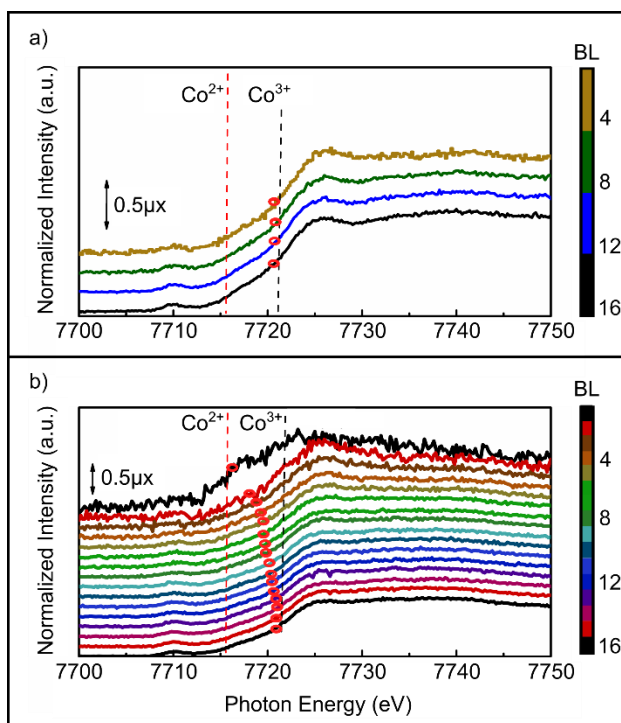


Figure 6.7 In situ XANES measured at the Co K-edge during growth of two films interrupted at different points throughout growth, showing a phase-pure BM-SCO film (a) interrupted after deposition of each four BL and a two-phase BM-SCO and 326-SCO film (b) interrupted after deposition of each BL. The energy references are from the Co metal foil and Refs. [143, 223]

Again, both of these films had Co<sup>3+</sup> as their final average oxidation state. However, the phase-pure BM-SCO film shown in Figure 6.7 (a) had a measured 3+ oxidation state at all points (taken after growth of at least 4 BLs). This indicated that, while the film was not yet ordered in the Brownmillerite structure, it had the same oxygen vacancy concentration, SrCoO<sub>2.5</sub>. Since this film was not measured more frequently, it was not possible to determine the oxidation state of its first

layer, though the Brownmillerite structure in Figure 6.3 implies that the average Co oxidation state would be 3+ after growth of only two BLs, in agreement with these observations.

The mixed phase film in Figure 6.7 (b) started off with a much lower Co oxidation state, near 2+, indicative of the first layer being CoO. This could be a tetrahedral layer like the one discussed by Meyer et al [232]. For the  $\text{Sr}_3\text{Co}_2\text{O}_{6\pm\delta}$  structure in Figure 6.3 (b), each layer containing cobalt is approximately  $\text{Co}_3\text{O}_5$ , resulting in  $\text{Co}^{3+}$  or higher for each layer. In the case of the observed growth, each deposited BL increased the observed oxidation until roughly 14 BLs were deposited and the cobalt reached an oxidation state of 3+. This hinted at a possible reason for forming a composite film under these growth conditions. The BM-SCO structure has well-defined vacancy ordering that requires the oxygen stoichiometry to be very close to  $\text{SrCoO}_{2.5}$ . Oxygen contents that vary even slightly from this will result in a distinct loss of diffraction from the half-order peaks of the BM structure (shown in Figure 6.2). The film identified as BM-SCO via diffraction, shown in Figure 6.7 (a), demonstrated this strict adherence to the  $\text{Co}^{3+}$  oxidation state. For additional oxygen vacancies to be incorporated, they must migrate into a structure that can tolerate more variation in oxygen content, such as the  $\text{Sr}_3\text{Co}_2\text{O}_{6\pm\delta}$  [107]. This migration would lead to cases where the phase fraction of  $\text{Sr}_3\text{Co}_2\text{O}_{6\pm\delta}$  increases as more oxygen vacancies are incorporated, i.e. under reducing conditions.

### 6.3.3 Annealing BM-SCO Films

The studies on growth conditions and rate gave insight into how films of pure BM-SCO or mixed BM/326-SCO can be stabilized. Controlling the growth rate provided one method of selecting between BM-SCO and 326-SCO (or producing mixed-phase films), but post-treatment of films may provide another. Additionally, post-treatment could offer a method for attaining

phases with higher cobalt oxidation states, such as the  $\text{Co}^{4+}$  found in perovskite  $\text{SrCoO}_3$ . To investigate this possibility, a related experiment was done on the annealing of Brownmillerite-phase Sr-Co-O films after their growth. For this study BM-SCO was grown on  $\text{SrTiO}_3$  (0 0 1) at  $T_{\text{sub}} = 793$  K in  $1.33 \times 10^{-4}$  Pa ( $1 \times 10^{-6}$  Torr) of 100%  $\text{O}_3$ .

The initial BM-SCO film, shown in Figure 6.8 (a), had distinctive half-order peaks characteristic of its oxygen vacancy-ordered structure. The background 100%  $\text{O}_3$  was increased from  $1.33 \times 10^{-4}$  Pa to  $5.60 \times 10^{-4}$  Pa ( $1 \times 10^{-6}$  to  $4 \times 10^{-6}$  Torr). The sample was then heated, in stages, from the growth temperature,  $T_{\text{sub}} = 793$  K, to a temperature of 1023 K. The changes in the film's structure, measured along the (0 0  $L$ ), are shown in Figure 6.8 (b). All X-ray measurements in this investigation were done with 15 keV X-rays. Keeping the sample at this temperature, the background 100%  $\text{O}_3$  was then decreased back down to its original value of  $1.33 \times 10^{-4}$  Pa ( $1 \times 10^{-6}$  Torr), the effects of which are shown in Figure 6.8 (c). This further reduction was accomplished by lowering the background 100%  $\text{O}_3$  pressure rather than additional heating due to limitations of the substrate heater.

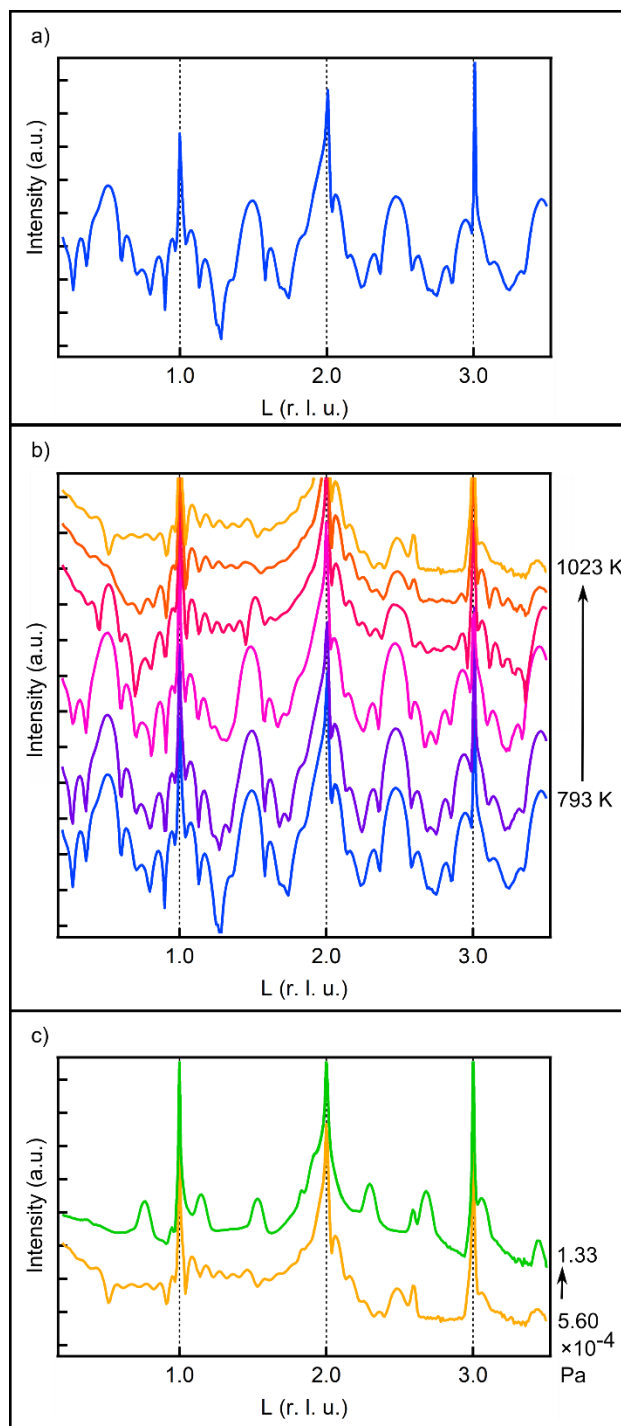


Figure 6.8 Specular (0 0 L) scattering of a BM-SCO film after growth (a) at  $T_{\text{sub}} = 793$  K in  $1.33 \times 10^{-4}$  Pa ( $1 \times 10^{-6}$  Torr) of 100%  $\text{O}_3$ , its changes upon annealing at  $5.60 \times 10^{-4}$  Pa ( $4 \times 10^{-6}$  Torr) with increasing temperature from 793 to 1023 K (b), and further change upon lowering background

$p_{O_3}$  from  $5.60 \times 10^{-4}$  Pa ( $4 \times 10^{-6}$  Torr) to  $1.33 \times 10^{-4}$  Pa ( $1 \times 10^{-6}$  Torr) at constant temperature of 1023 K(c).

Figure 6.8 (b) shows that annealing a pure BM-SCO film resulted in a weakening of intensity at the half-order peaks. This was likely due to a breakdown of ordering when oxygen vacancy migration or an overall gain/loss of oxygen in the material happened (with a loss being more likely as increasing temperatures were reducing the film). Additionally, a diffraction peak at  $(0\ 0\ L = 2.6)$ , attributed to the  $(2\ 0\ 4)$  peak of CoO, appeared. Heating the pure BM-SCO phase film caused a second phase, CoO to nucleate and grow.

When the film was subsequently reduced, by lowering the 100%  $O_3$  pressure, shown in Figure 6.8 (c), a third phase, 326-SCO, appeared. When this phase appeared, the half-order peaks of the BM-SCO were no longer visible in the film, indicating that the entire film was made up of CoO, 326-SCO, and perhaps a perovskite-like  $SrCoO_x$  phase with no oxygen vacancy ordering. These results indicated that the BM-SCO phase decomposed upon heating into CoO and 326-SCO.

## 6.4 Discussion

### 6.4.1 Thermodynamics of Sr-Co-O Film Growth

Varying the effective growth rate showed that the structure of strontium cobaltite films grown using MBE changed depending on rate. Films with faster growth rates (relative to atomic diffusion) were stable in the  $SrCoO_{2.5}$  phase while slow growth led to mixed  $SrCoO_{2.5}$  and  $Sr_3Co_2O_{6\pm\delta}$  films. Changing the deposition rate allowed for selection of the phase fraction and different growth-rates were dominated by kinetics versus thermodynamics. Mechanisms for formation of the observed phases were elucidated by comparing thermodynamic data for the Sr-Co-O system to the growth rate results.

To compare between films grown with  $O_2$  and  $O_3$ , the method outlined by Suzuki et. al. was used [233], who calculated the thermodynamic quantity of oxygen activity in ozone,  $a_{O_2}$ . The ozone to oxygen equilibrium is shown in the following chemical equation:



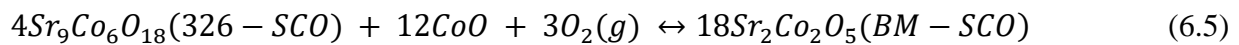
The corresponding Gibbs free energy for ozone decomposition is then

$$\Delta G^o = -RT \ln \frac{(p_{O_2}^{eq})^{3/2}}{p_{O_3}^{eq}} \quad (6.3)$$

where  $R$  is the gas constant,  $T$  is temperature, and  $p_{O_2}^{eq}$  and  $p_{O_3}^{eq}$  are equilibrium partial pressures of oxygen and ozone. This expression can be written in terms of activity of oxygen in ozone,  $a_{O_2}$

$$\Delta G^o = -RT \ln \frac{(a_{O_2} P^o)^{3/2}}{p_{O_3}} \quad (6.4)$$

where  $P^o$  is the total gas pressure. In the case of these experiments (where  $Sr/Co = 1$ ), the oxygen partial pressure for 326-SCO and BM-SCO phase coexistence,  $p_{O_2}^{eq}(326 - SCO \leftrightarrow BM - SCO)$ , can be determined from the following chemical reaction:



This reaction has a free energy of formation for  $Sr_2Co_2O_5$  (BM-SCO) given by

$$G_f^o = -RT \ln \frac{a_{BM-SCO}^{18}}{a_{326-SCO}^4 a_{CoO}^{12} (p_{O_2}^{eq}(326 - SCO \leftrightarrow BM - SCO))} \quad (6.6)$$

where  $a_{BM-SCO}$ ,  $a_{326-SCO}$ , and  $a_{CoO}$  are activities of the materials relative to the pure substances. If these are assumed to be unity,  $p_{O_2}(326 - SCO \leftrightarrow BM - SCO)$ , can be calculated. This was done for the experimental temperature and oxygen activity conditions explored using thermodynamic constants from the recent literature [224, 225, 234]. Calculations for  $p_{O_2}(326 - SCO \leftrightarrow BM - SCO)$  and  $a_{O_2}(326 - SCO \leftrightarrow BM - SCO)$  are shown in Figure 6.9. The activity of 100%  $O_3$  and 100%  $O_2$  at  $1.33 \times 10^{-4}$  Pa ( $1 \times 10^{-6}$  Torr), the most and least oxidizing conditions investigated, are shown as short and long dashed lines respectively. If the least oxidizing conditions are used, the BM-SCO phase is not favored unless  $T_{sub} < 345$ K, far too cool to produce high crystallinity using MBE. At temperatures higher than this, the 326-SCO and CoO phases are thermodynamically stable. On the other hand, using the most oxidizing condition, 100%  $O_3$ , the BM-SCO phase is stable up to growth temperatures of 835 K.



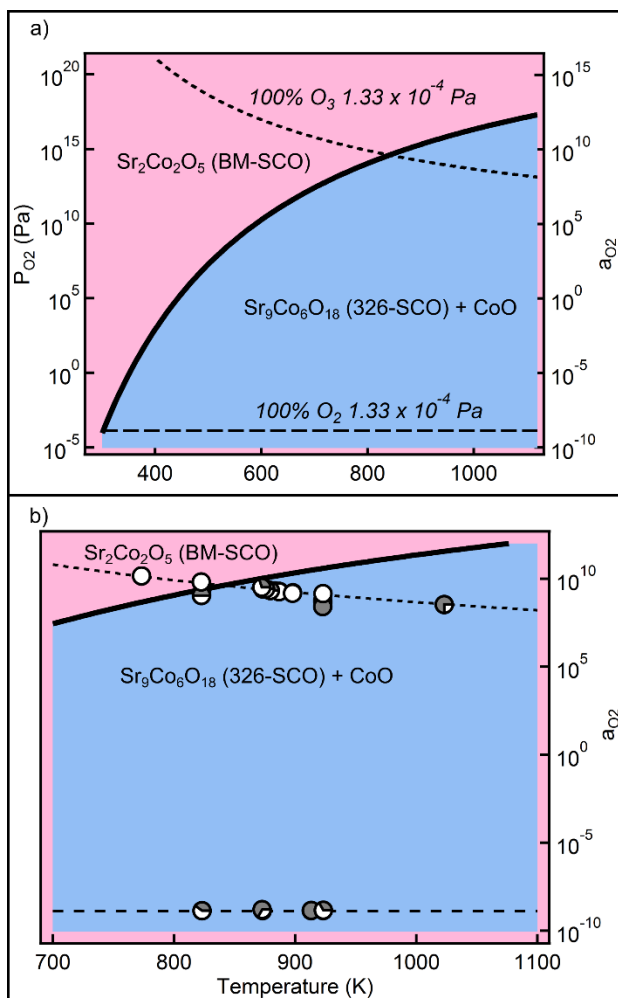


Figure 6.9 Thermodynamic phase diagram (a) showing  $p_{O_2}/a_{O_2}$  (left/right axis) for the 326-SCO  $\leftrightarrow$  BM-SCO reaction (bold line). The  $a_{O_2}$  of 100%  $\text{O}_3$  at  $1.33 \times 10^{-4} \text{ Pa}$  ( $1 \times 10^{-6} \text{ Torr}$ ) is indicated as a short, dashed line, while 100%  $\text{O}_2$  at  $1.33 \times 10^{-4} \text{ Pa}$  ( $1 \times 10^{-6} \text{ Torr}$ ) is indicated by the long, dashed line. In (b), containing an enlarged view of (a), we overlay the results for films of Sr-Co-O grown at varying  $T_{\text{sub}}$  and  $a_{O_2}$ . Open and dark circles indicate Brownmillerite and 326-SCO films, respectively, with mixtures of the two are indicated by partially-shaded circles.

Experimental growth data was overlaid on this plot in Figure 6.9 (b). Each circle represents experiments conducted at the specific conditions and the portion of gray versus white in each circle indicates the proportion of BM-SCO versus 326-SCO phase observed. White circles, indicating only the BM-SCO phase, were indeed found in the BM-SCO calculated region. However, the experimental data indicated that phase behavior in 326-SCO region was more complex. Despite

being in the 326-SCO region, the data showed that pure BM-SCO films or mixed phase BM/326-SCO films could be grown. These experiments showed that stabilizing the BM-SCO phase outside of its region of thermodynamic stability was possible but can be challenging, even when cation ratio and shutter schemes that favor the BM-SCO phase were employed. Nearer the equilibrium line, stabilization of the BM-SCO phase was easier, as indicated by the larger number of circles with white, Figure 6.9 (b). Far from the equilibrium line, especially at the 100% O<sub>2</sub> condition, it was nearly impossible to stabilize the BM-SCO phase even with fast growth. As this analysis was purely bulk thermodynamics, it did not take into consideration interface energies, epitaxial strain, or kinetic effects that may influence phase stability. However, overall there was rough agreement between the calculated phase stability regions and experiment, even when kinetic effects were totally ignored. The region near the equilibrium line was the same one probed with the series of growths made at different effective growth rates,  $V_E$ . These were conducted just inside the region of 326-SCO stability. From the scans shown in Figure 6.4, there was some critical growth velocity,  $V_C$ , above which the metal atoms deposited did not have time to nucleate the thermodynamically stable phase due to the lack of sufficient surface diffusion,  $D_S$ .

#### 6.4.2 Kinetics of Sr-Co-O Film Growth

In the experiments conducted, slow growth led to increased observation of the thermodynamically stable phase while fast growth stabilized the Brownmillerite phase. Since Brownmillerite was the structure targeted by both the A:B ratio and shutter scheme chosen, this result implied kinetic control. There was agreement between this result and two literature models for MBE growth.

One, based on alloy decomposition [235-237], stated that the stable phases and film morphology were determined by growth temperature, rate, epitaxial strain, and thermal expansion coefficients. The aspects of this model that were qualitatively observed during these growth experiments were the effects of temperature and growth velocity while forming the characteristic vertical domain structure. Epitaxial strain likely also plays a role in the stabilization of phases in this system, as films grown on Lanthanum aluminate- strontium aluminum tantalate,  $(\text{LaAlO}_3)_{0.3}(\text{Sr}_2\text{TaAlO}_6)_{0.7}$ , (LSAT) (0 0 1) under similar conditions had BM-SCO phases stable well into the calculated region of 326-SCO stability, as mentioned previously. This can likely be attributed to differences in lattice mismatch between the  $\text{SrTiO}_3$  (0 0 1) and LSAT (0 0 1) substrates [9].

A second, quantitative model that was consistent with observations presented herein is solute trapping. Solute trapping occurs when the growth rate is quick enough to prevent atoms from migrating to form thermodynamically favored phases [213-216]. This is described by the following equation:

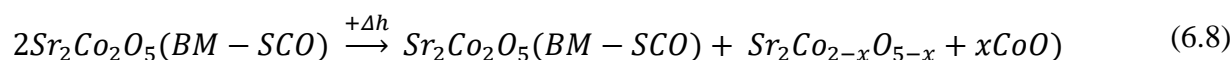
$$\frac{Va}{D} > 1 \quad (6.7)$$

where  $V$  = growth velocity,  $a$  = hopping distance, and  $D$  = interface diffusion coefficient. As such, a fast growth rate implies that the structure will be totally determined by the source shutter sequence and timing with A and B cations “frozen” in place by a growth front that advances quickly enough to prevent diffusion. For the growths presented here using different  $V_E$ , the ratio of  $Va/D$  was estimated using the self-diffusion coefficient of cobalt in cobalt,  $D_{\text{Co self}} = 3.03 \times 10^{-18} \text{ cm}^2/\text{s}$  [238] and the hopping distance  $a_{\text{Co-Co}} \sim 3 \text{ \AA}$ . Growth velocities for these films (0.001  $\text{\AA}/\text{s}$

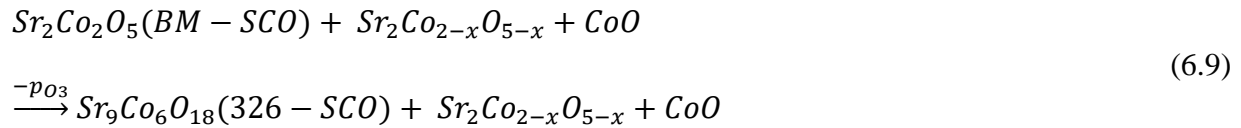
– 0.003 Å/s) resulted in  $Va/D \sim 0.1 - 0.3$ . The self-diffusion coefficient of cobalt in the oxide is smaller than in the metal, and the hopping distance of 3 Å is also a conservative estimate- actual values are likely higher. As such, the actual ratio would then be higher than those calculated. These ratios (even the ones presented based on estimates) are close enough to unity that it is likely that the process of solute trapping occurs, especially as the ratio approaches unity. All of this implies that the films grown quickly are undergoing solute trapping that allows them to maintain the BM-SCO structure.

#### 6.4.2 Phase Evolution of SrCoO<sub>2.5</sub> upon Annealing

The annealing experiments provided another way to alter the structure of a film, one that was intuitive from the calculated phase diagram and gave additional insight into the reactions between phases. Since no deposition occurred during annealing, the kinetic process of solute trapping did not have a significant effect on the film's structure during this process; it was entirely thermodynamic. According to the calculated phase map, the initial growth conditions for this film were inside the region of thermodynamic stability for the BM-SCO phase. From the calculated phase map in Figure 6.9 (a), increasing temperature at a given oxygen activity value (e.g. following the short, dashed line) will result in moving from a region where BM-SCO is stable to one where 326-SCO and the CoO phases are stable. This was observed in the film when increased temperature resulted in the appearance of the CoO phase. This change is represented by the following chemical equation:



The CoO phase was the first to nucleate when  $\text{SrCoO}_{2.5}$  was heated and some fraction of Co and O atoms precipitated out to form this secondary phase. This left the remaining  $\text{Sr}_2\text{Co}_{2-x}\text{O}_{5-x}$  with some amount,  $x$ , of vacancies. However, the BM-SCO structure was still detectable via X-ray scattering, indicating that the oxygen vacancy ordering was not totally disturbed by this process. This could be due to the CoO phase only nucleating in certain regions and the rest of the  $\text{SrCoO}_{2.5}$  remaining unchanged. When the film was subsequently further reduced (by lowering the 100%  $\text{O}_3$  background pressure), the original BM-SCO phase was no longer detected and only the 326-SCO and CoO phases remained. This can be represented by the following chemical reaction:



This chemical reaction will not be balanced as it is uncertain, from the data acquired, whether the BM-SCO phase is the only phase to decompose into the 326-SCO phase or whether some portion of the BM-SCO and the  $\text{Sr}_2\text{Co}_{2-x}\text{O}_{5-x}$  phases both decompose. In either case, at this stage, there was no remaining BM-SCO. Additionally, the phase  $\text{Sr}_2\text{Co}_{2-x}\text{O}_{5-x}$  is included in the chemical reactions shown because, upon cooling the film back to its original growth  $T_{\text{sub}} = 793$  K, some of the BM-SCO phase was recovered. If the structures of the BM-SCO and 326-SCO phases, shown in Figure 6.2 (a) and Figure 6.3 (b), are compared it is evident that they differ both in-plane and out-of-plane. As such, it is unlikely that any transition between BM-SCO and 326-SCO would be easily-reversible. Since some reversibility was observed upon heating it seems more likely that some portion of another phase,  $\text{Sr}_2\text{Co}_{2-x}\text{O}_{5-x}$ , was still present which converted back to BM-SCO, or a structure that approximated BM-SCO's oxygen vacancy ordering.

This experiment supported the validity of the calculated thermodynamic phase map in Figure 6.9. It also showed that when BM-SCO decomposes into 326-SCO and CoO, the CoO phase nucleated before any 326-SCO was observed. This observation implied that cations in the BM-SCO structure have some mobility and experience diffusion during this phase transition. Since the annealing steps were conducted on a similar timescale to the growth experiments, the idea that solute trapping (kinetics) was competing with cation diffusion (thermodynamics) was supported by this result. Additionally, CoO was observed in the annealed films, but was not present in any of the films produced by the growth rate experiments. This indicated that growth conditions and solute trapping influence the observed phases- i.e., solute trapping can keep sufficiently different phases from nucleating. In this case, CoO may not have been observed due to the existence of sufficient driving force (perhaps from interfacial energy differences) to suppress its precipitation out of the kinetically stabilized structure. Since BM-SCO and 326-SCO have very similar lattice parameters and are expected to have little to no interfacial energy between phases, they are much more compatible in a mixed-phase film where solute trapping is at play than the CoO phase would be under the same conditions, helping to explain the widespread lack of CoO observations in films that were not annealed.

## 6.5 Conclusions

The Sr-Co-O oxide growths performed via MBE provided insight into the roles of thermodynamics and kinetics on oxide phase stability in a complex system.  $\text{SrCoO}_{2.5}$  could be stabilized by both epitaxial strain and by rapid growth (films grown quickly with specific shuttering schemes favored this structure). However, if films were exposed to higher temperatures or to reducing environments during growth, the  $\text{Sr}_3\text{Co}_2\text{O}_{6\pm\delta}$  phase was stabilized, and moderate

growth rates led to nanocomposites of the two materials. Formation of observed phases was in semi-quantitative agreement with the kinetic theory of solute trapping. Additionally, thermodynamic phase diagram calculations provided guidance on experimental conditions that should be used to stabilize a desired phase. Combining thermodynamic calculations and experimental investigations of a wide range of growth environments (including growth rates) is an approach that provides additional insight into the growth of complex oxide system. This strategy can be used to target specific phases or domain architectures similar to the two-phase competition observed in the Sr-Co-O system.

The Brownmillerite  $\text{SrCoO}_{2.5}$  structure in Sr-Co-O films was observed in films with a minimum thickness of two unit cells (8 BL). Oxygen vacancies remained disordered below this thickness, but the cobalt oxidation state was set at  $\text{Co}^{3+}$  as soon as 4 BLs were deposited, observed by in situ XANES. This indicated that the overall content of oxygen vacancies in the film did not change. The  $\text{Sr}_3\text{Co}_2\text{O}_{6+\delta}$  phase nucleated with initial oxygen deficiency,  $\delta$ , and incorporated more oxygen throughout its growth up to a Co oxidation state of 3+.

In situ X-ray scattering and absorption probes facilitate investigation of deposition behavior at different growth rates. This is of interest in oxygen deficient materials where thermodynamic and kinetic factors contribute to growth behavior. The system investigated, Sr-Co-O, with its highly-variable transition metal cation and complex phase diagram, provides an example of the rich behavior that can be observed. This system shows a wide range of structure-dependent properties that are important to understand when considering the synthesis of multivalent transition metal oxides, and serves as an example of the many different possible factors that affect phase stability. Both X-ray spectroscopy and scattering give insight into physical and

chemical processes in MBE deposition, and in situ techniques can provide information necessary for defect-engineering the properties of cobaltite heterostructures.



## CHAPTER 7

### **Design, Construction, and Characterization of Delivery with a Hybrid MBE System for in situ X-Ray Characterization**

The previous chapter demonstrated the wealth of information that can be determined about the early stages of thin film growth using surface X-ray scattering methods. The structure and bonding environment of single atomic layers can be investigated and changes measured throughout synthesis.

This capability is particularly powerful in advancing the understanding of growth mechanisms for thin films if it can be applied to either the synthesis of novel materials or novel synthesis methods. While the previous chapter focused on a complex oxide system, the Sr-Co-O materials, where there is a great deal of structural flexibility due to the ease of oxygen vacancy formation (essentially investigation of an under-studied material), this chapter focuses on the latter problem: applying these measurement techniques to novel synthesis methods.

This chapter discusses the development and results obtained from a “hybrid” MBE System. This system delivers a metalorganic source, in the gas phase, to a traditional MBE chamber, allowing a metalorganic chemical vapor deposition-like capability to be added to the growth. The instrument discussed in this chapter is not the first of its kind and is based on metalorganic molecular beam epitaxy instruments, but it is the first to be integrated with in situ surface X-ray scattering capabilities that allow the mechanisms of synthesis to be investigated using a technique that has not been previously applied.

The work in this chapter would not have been possible without the advice of Dr. Bharat Jalan, Dr. Roman Engel-Herbert, and Dr. Matthew Brahlek who provided information on the design of their existing hybrid MBE systems and troubleshooting advice. Erika Benda at the APS provided invaluable expertise for system design and creation of all computer aided design models. Initial design, all assembly, interfacing with existing beamline software and an existing beamline

oxide MBE chamber, as well as testing, and initial results were all performed by the author of this thesis. Materials in this chapter form the basis of the publication “Development of a hybrid molecular beam epitaxy deposition system for in situ surface X-ray studies” [239], from which figures are reproduced.

## **7.1 Introduction**

As the degree of complexity and the range of desirable properties increase for oxides finding use in new applications including solar cells [1, 4], sensors [15], electrochemical supercapacitors [21], and other packaged devices [2, 3, 19], synthesis methods must also advance to produce these materials. To these ends, flexible synthesis with both a high degree of precision and the potential for scale-up, to meet industrial fabrication requirements are desirable. Currently many methods with the appropriate levels of precision suffer from being time-consuming or are limited in terms of the elements that can be incorporated. One way to address this is by combining desirable aspects of multiple growth methods- this is, in fact, the approach used in HMBE where both metalorganic and solid metal sources are utilized.

Implementing a metalorganic source into traditional MBE offers a few advantages. While the solid metal sources of MBE limit the elements that can be deposited (as some sources require unrealistically high temperatures), multiple metalorganic precursor compounds are also available that can provide these elements. Additionally, metalorganic sources have chemical functionality built in and do not necessarily rely on the extreme oxidizing environment provided by ozone or an oxygen plasma [218, 220, 240] necessary in normal MBE to produce a stoichiometric oxidized film. Such extreme environments often lead to oxidation of the solid metal sources themselves in MBE, and avoiding this allows for increased efficiency and stoichiometric control [132, 133]. For

these reasons incorporating metalorganic deposition into UHV chambers was first investigated in the 1980s [241-244]. Initial synthesis focused on semiconductor materials, specifically the III/V family, before expanding to include materials for high  $T_c$ -superconductors [96]. Early hybrid systems did not produce oxides, but within the past ten years interest in these synthesis methods has renewed, and their use expanded to include a much wider range of oxide materials, especially those of the diverse perovskite families [245-248].

Although HMBE is being rediscovered as a method for oxide synthesis, the specifics mechanisms of growth are still areas where relatively little study has been conducted. In situ X-ray scattering with a synchrotron X-ray source, a tool discussed in previous Sections 3.1.2, 3.1.3, and 3.1.4, is well-suited for investigation of synthesis [249-251]. The very high brilliance available from a synchrotron source permits surface X-ray scattering with techniques including grazing incidence X-ray scattering and spectroscopy [252], the measurement of CTRs from poor scattering materials or very thin films, observation of otherwise-inaccessible fractional-order peaks, and diffuse scattering to be applied to films only a few atomic layers thick. By combining these different approaches, information on defects, surface reconstructions, island sizes and distribution, and domains in a film can be investigated and information about the mechanisms of growth across length scales obtained, sometimes simultaneously. The in situ capability allows evolution of these features to be tracked in real time during film growth, offering additional insight into complex mechanisms and processes.

This section describes the system constraints, design, testing, and initial results from a HMBE metalorganic delivery system for in situ SXRD at Sector 33-IDE of the APS. The goal of this system is to provide access to SXRD techniques to perform detailed studies of growth

mechanisms in HMBE and allow comparison with other growth methods (especially traditional MBE). The only prior in situ information on HMBE growth has come from reflection high energy electron diffraction (RHEED) measurements [253, 254], so this system allows for comparison with these data sets while facilitating investigation into atomic-scale processes with a variety of diffraction conditions and scales during complex oxide thin film growth.

## **7.2 Methods**

### **7.2.1 Sector 33-IDE MBE Chamber Details**

The oxide MBE chamber that this metalorganic delivery system was designed to interface with is housed at Sector 33-IDE of the APS. This chamber is mounted on a six-circle diffractometer to provide the axes of motion necessary to reach relevant diffraction conditions for in situ SXRD. This system (the chamber and the diffractometer) and its possible motions are shown in Figure 3.1 (in Section 3.1.2) [129, 130]. The typical base pressure for MBE growth in this chamber is in the  $10^{-9}$  Torr range and the vacuum is maintained by a roughing pump and 1000 l/s turbo pump. Growth substrates in this chamber are mounted on a sample arm that provides resistive heating. The components of this growth chamber, the same one utilized in Chapter Six are discussed in greater detail in Section 3.1.2.

### **7.2.2 Residual Gas Analyzer**

To monitor presence and levels of precursor metalorganic gas in the growth chamber, a residual gas analyzer (RGA) / mass spectrometer [Stanford Research Systems, USA] was used. When collecting survey data on the RGA (i.e., measuring which mass-to-charge ratio ( $m/z$ ) values were present in the chamber and at what levels). First, a mass range of  $1 \pm 99$  amu can be scanned to survey the whole environment. It can also be run in a mode where specific  $m/z$  values are

followed over time to track changes in their levels- the use of this second measurement mode is described in the following text.

### **7.3 Hybrid Delivery System Overview**

#### **7.3.1 Challenges**

As this delivery system was designed to interface with an existing MBE chamber and X-ray measurement setup, the design had to meet specific constraints during its development. First, it had to conform to the strict geometric layout of the existing chamber and accommodate diffraction measurements with a further requirement that it must be easy to attach without significant modification of the chamber. To explore a greater variety of sources and material architectures, the use of two different metalorganic sources during deposition was desirable. To accommodate the different vapor pressures of the two sources the delivery lines and injectors for each source had to be separately maintained at specific temperatures. Finally, as this experimental station is contained within a concrete hutch at the APS (to prevent exposure to X-rays), most of the controls must be accessible remotely and integrated into existing computer systems/programs. The next section, detailing the design and overview of the created instrument, will address these concerns roughly in the order they have been presented.

#### **7.3.2 General Equipment Overview**

The entire gas delivery system is mounted on a vertically-oriented rack made of an 80/20 T-slotted aluminum frame, mounted on wheels to allow it to move when clamped to the diffractometer stage. This vertical organization was chosen to provide a small footprint. All components of the delivery system including piping, valves, meters, controls, and miscellaneous

electronics are permanently attached to the frame, and efforts were made to organize components so that the heaviest ones are nearest to the ground for stability.

The important parts of the system attached to the vertical rack are shown and labelled in Figure 7.1. What follows is a brief description of the pieces of equipment and their purpose.

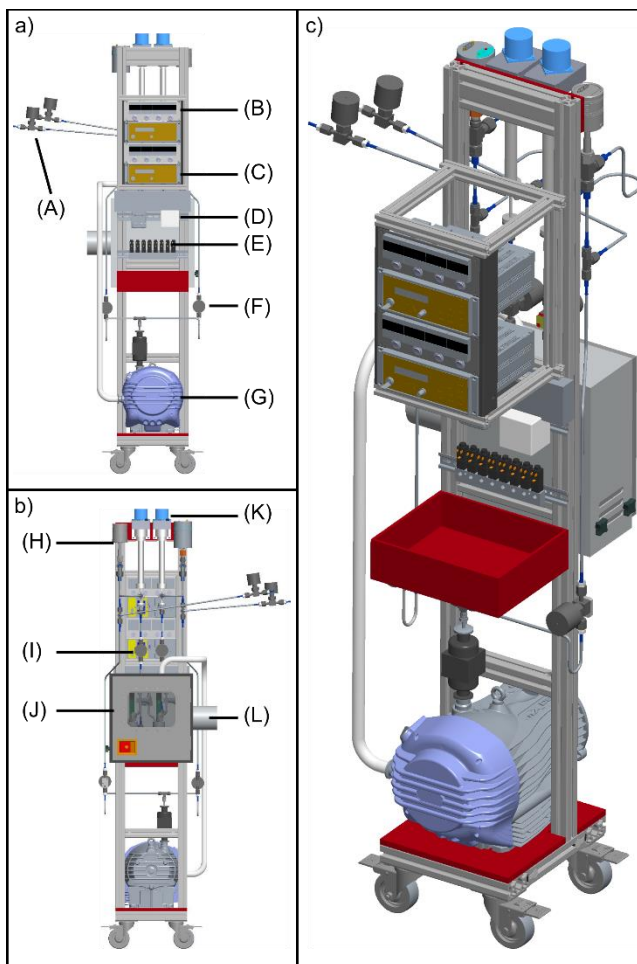


Figure 7.1 Schematic of the mobile, vertical rack for the in situ hybrid MBE chamber. Views from the front (a), the back (b), and at angle (c), with the labeled components described in the text. Labelled parts are bellows-sealed pneumatic valves (A), (F), and (I), heating controllers (B), line pressure/ mechanical valve controller (C), digital I/O for pneumatic valves (D), pneumatic valve solenoids (E), scroll pump (G), pressure capacitance manometer (H), source enclosure (J), metal-sealed mechanical stepper valve (K), and exhaust vent hookup (L).

At the bottom of the rack sits a scroll pump [Edwards Vacuum, UK] (Figure 7.1 G) with a peak speed of 6.2 m<sup>3</sup>/h, which achieves an ultimate vacuum of 0.015 Torr. This pump can be used to evacuate the delivery lines (or some section of them) during source installation or baking of lines between runs. It also provides an exhaust, and the pump's exhaust is integrated with the exhaust air system that the source enclosure feeds into (Figure 7.1 L) via a flexible piece of ductwork. Two sources are contained in the stainless-steel enclosure [Applied Energy Systems, USA] (Figure 7.1 J) that provides both ventilation for use with hazardous or flammable gases (Figure 7.1 L) and a physical blast-proof barrier. All piping (1/4 inch stainless-steel) is attached to the frame for support, generally at the points where valves or other equipment is placed. Pneumatic bellows-sealed valves [Swagelok, USA] (Figure 7.1 A, F and I) are used for isolating different parts of the line and rapid on/off or switching between sources. These valves are controlled by solenoids (Figure 7.1 E) and a digital data acquisition I/O device [National Instruments, USA] (Figure 7.1 D) that supports remote communication. Each source line has a metal-sealed control valve with a stepper motor [MKS Instruments, USA] (Figure 7.1 H), which will be referred to as a mechanical leak valve from here on out. Additionally, each line has a pressure capacitance manometer [MKS Instruments] (Figure 7.1 H) with a 1 Torr range that provides feedback to the mechanical leak valve located at the top of the rack. On one line the pressure capacitance manometer is rated to operate up to 50 °C, while the other line has an internally-heated version that operates at 200 °C. The control loops are governed by self-tuning/digital proportional-integral-derivative (PID) pressure controllers [MKS Instruments, USA] (Figure 7.1 C) which are mounted opposite the mechanical leak valves near the rack's top. The entirety of the delivery lines and any component that gas travels through are heated (not shown in Figure 7.1 but discussed in a



subsequent section) and this is controlled by a bank of autotuned PID/ on-off controllers [Omega Engineering, USA] (Figure 7.1 B), which are mounted in the same area as the mechanical leak valve controllers. This placement of the controllers was chosen for two reasons: the first being that this height puts all displays at roughly eye level for an operator; the second that their weight helps to balance out the source enclosure on the rack's other side. For convenience, a shelf for the storage of miscellaneous small tools, power strips for controllers, and other low-power components are positioned at the center of the rack.

Now that the nature of the components has been discussed, some of the reasoning for their placement and practical aspects of the vertical rack will be covered. The relevant design challenges, outlined earlier, are the prospects of interfacing with an existing chamber and allowing for the range of motion required during X-ray scattering measurements. In general, components were mounted to the rack to distribute weight evenly across both sides and heavier objects were positioned closer to the rack's bottom to reduce instability during motion. The heaviest components are the scroll pump, source enclosure, and controllers (in roughly that order), the pieces of equipment whose position has been chosen most carefully. Piping was laid out to reduce the length of delivery lines as much as possible given the other geometric constraints of this system. The in-use configuration of the system is shown in Figure 7.2, highlighting its compact footprint and how it interfaces with the growth chamber. Where the piping meets the UHV chamber a custom showerhead dual injector [Riber, USA] meets the chamber's conflat flange in a position normally reserved for a Knudsen cell MBE source. This injector was designed so that both source lines entered the chamber at the same position while maintaining independent heating from one another. The conflat chosen for delivery is one that has a straight line-of-sight to the substrate's

growth position. When in use, the rack is fixed rigidly to the stage base of the diffractometer on which the MBE chamber sits, as shown in Figure 7.2. This attachment is modular, made of steel slotted strut channel, and is removed from the diffractometer base when the HMBE is not in use. The green arm in Figure 7.2 shows where and how this attachment is done- the placement is a precaution necessary to follow the  $\pi$ -axis motion (shown in Figure 3.1) of the chamber and diffractometer during measurements. This axis of motion can sweep out an angle of up to  $30^\circ$ , which is equivalent to an arc of 3-4 feet in terms of the rack's motion across the experiment hutch's floor. All piping is fully modular, using VCR metal gasket face seal fittings [Swagelok, USA]. This ensures that parts can be easily swapped, in case maintenance or cleaning is necessary and allows the final length of piping (between the rack and MBE chamber) to be replaced to interface with chambers of different geometries. The wheeled base also provides portability to this system and it can be easily moved to different experimental setups as needed.

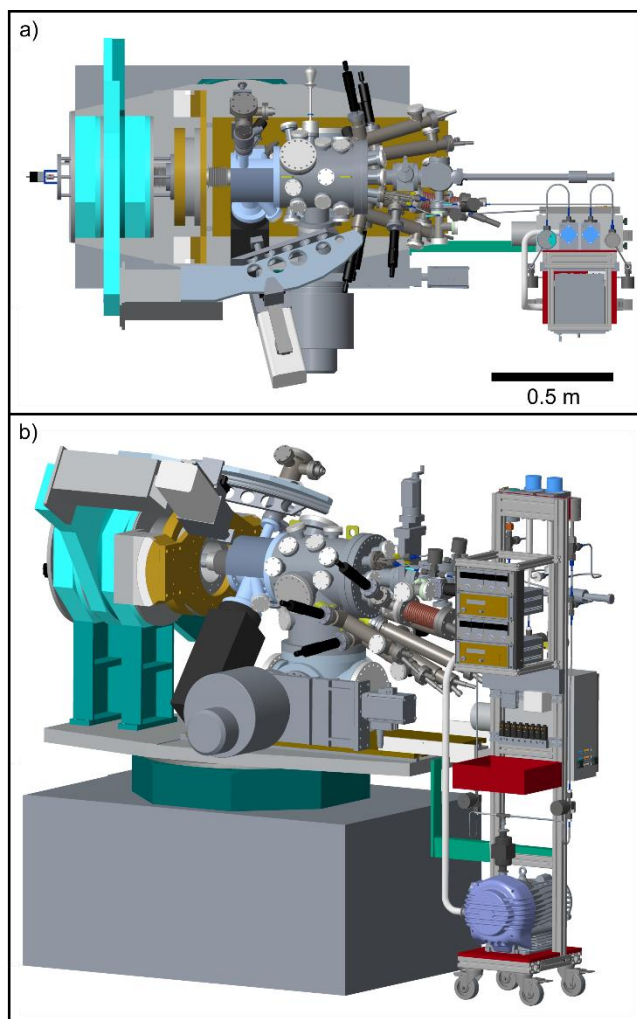


Figure 7.2 Schematic of the entire in situ hybrid MBE system, showing the placement and attachment of the vertical rack used to deliver the metalorganic precursors, relative to the oxide MBE chamber and six-circle diffractometer, as viewed from the top (a) and side (b).

### 7.3.3 Gas Handling

The gas handling system was designed to address the need to deliver two different metalorganic source gases into the UHV chamber. Since no carrier gas is employed, the flux from each source is maintained by regulating pressure in the delivery line and adjusting the mechanical leak valve accordingly while all components of the delivery system are held at constant temperature. Flux from a source can either be directed into the growth chamber or to the exhaust

system via the scroll pump by changing the configuration of the pneumatic valves. A schematic of the delivery system and the valves/ controllers is presented in Figure 7.3.

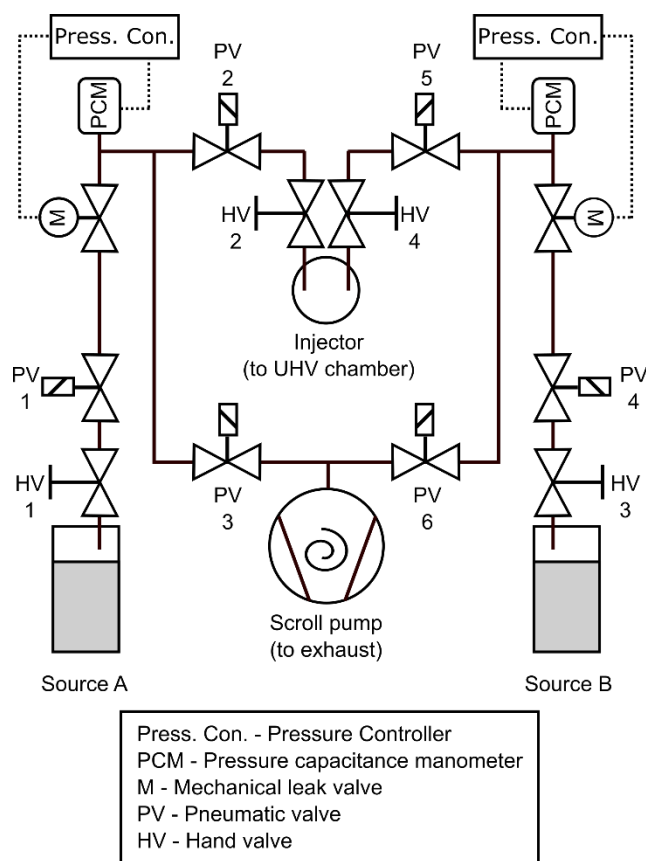


Figure 7.3 Diagram of the hybrid MBE gas delivery system, indicating placement of the valves and pressure controllers.

Source bottles contain the metalorganic precursors, generally in liquid form. All precursors used in these investigations constitute the B-site cation of the perovskite,  $\text{ABO}_3$ . Two examples of precursors discussed are titanium (IV) tetraisopropoxide (TTIP) and vanadium (V) triisopropoxide (VTIP). As mentioned, there is no precursor gas used for delivery, and as such the source temperature and resulting vapor pressure provide the concentration gradient necessary for delivery. The main control loop, a feedback/control loop between the mechanical leak valve and pressure capacitance manometer, allows a steady vapor flux to be achieved. During delivery,  $\text{O}_2$  or  $\text{O}_3$  can

be provided to the chamber via leak valve if necessary- generally to a level that results in a  $1 \times 10^{-6}$  Torr pressure in the growth chamber. Subsequent metalorganic delivery is done at pressures in the 100 mTorr range in the delivery line and  $1-2 \times 10^{-5}$  Torr range in the growth chamber (measured via ion gauge). Delivering metalorganics at a higher pressure could lead to overwhelming the roughing and turbo pumps and should be avoided.

Since the sources are effectively separate (having their own piping, control equipment, and injector nozzles), they can operate independently. This means they can deliver flux at different rates and in any order desired. The procedure for switching between sources is designed to ensure a constant gas flow to either the chamber or exhaust and prevent fluctuations in pressure during switching. Switching adheres to the following procedure: while source A is delivered to the chamber, source B is directed to the exhaust via the scroll pump at the cart's base; when the two are switched their destinations are exchanged. Any source directed to the exhaust passes through a particulate filter placed at the inlet to the scroll pump. The exhaust of the scroll pump is integrated into the hazardous gas ventilation system at beamline 33-ID (where this experimental setup is housed). While the main purpose of the pneumatic valve is switching, it also facilitates isolation of different parts of the piping during modification, source replacement, leak checking, or bake-out. Two hand valves meant for isolation of the entire piping system are located at either of its terminal ends, one directly downstream of the source and the other directly upstream of the UHV chamber injector.

Each delivery line is heated in different zones. This is shown in the diagram of Figure 7.4, where one line's temperature zones and the equipment within them are indicated. As proximity to the growth chamber decreases (zone A leads to zone B etc.), the temperature ( $T$ ) of the line

increases, such that  $T_{\text{zone A}} < T_{\text{zone B}} < T_{\text{zone C}} < T_{\text{zone D}}$ . The exact temperature values are chosen such that sufficient vapor pressure is present for the delivery flux desired while avoiding thermal decomposition of metalorganic species. The TTIP source is presented as an example. The source temperature,  $T_{\text{zone A}}$ , is kept at 72 °C, which provides a calculated vapor pressure  $P_{\text{eq, TTIP}} = 3836.4$  mTorr ( $5.0479 \times 10^{-3}$  atm) [255] in the headspace. The subsequent zones increase in temperature according to the following scheme:  $T_{\text{zone B}} = 85$  °C,  $T_{\text{zone C}} = 95$  °C, and  $T_{\text{zone D}} = 115$  °C. From a practical standpoint, while it is possible to control the temperature of the two lines of the dual injector ( $T_{\text{zone D}}$ ) separately, it is difficult to maintain a large difference ( $>50$  °C) in temperature between them due to their proximity.

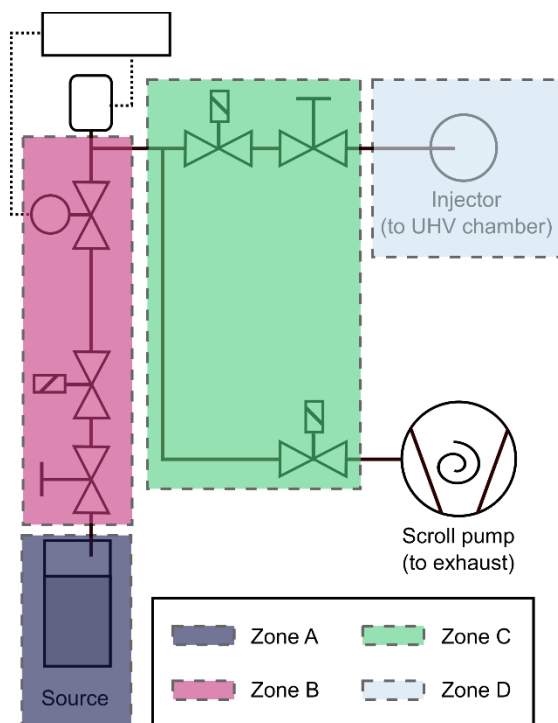


Figure 7.4 Diagram illustrating the different temperature zones for a single hybrid MBE gas delivery line. Labels of the different valves and pressure controllers are shown in Figure 7.3.

Since flux relies solely on the line pressure (and source vapor pressure), precision and accuracy are both important in the temperature control of different zones. To ensure a high level

of control each zone has a dedicated PID temperature controller. These controllers were found to maintain line temperature, once heated and stabilized, to within  $\pm 0.5$  °C. Lines are heated with heating tape wrapped uniformly and insulated with layers of aluminum foil to avoid hot or cold spots along their length. The temperature of the lines at various points along their length should be checked when the system is first heated to ensure that there are no large inconsistencies within a given zone. As mentioned previously, one of the delivery lines has an internally heated pressure capacitance manometer that operates at 200 °C. This was chosen to allow for one line to be used for “colder” sources while the other is used for “hotter” sources. This heated manometer allows sources that would easily condense to be utilized because the electronics of the other manometer are only rated for operation up to  $\sim 50$  °C.

#### **7.3.4 Control Systems**

One of the challenges discussed previously was that the growth chamber is set up to perform X-ray measurements at a synchrotron facility. As such, it is housed in a concrete hutch that cannot be entered during measurements; this necessitates that all monitoring and control of the HMBE during growth and in situ measurements must be done remotely through interfaced computers and existing systems at the beamline. The control loop of the mechanical leak valve and the pressure capacitance manometer is integrated using software built on Experimental Physics and Industrial Control System (EPICS) [256]. This platform was used because it is already in place on the beamline computers to control diffractometer motion and record diffraction data- hence both systems can be controlled from the same interface and their settings stored in one shared record. A dedicated graphical user interface (GUI) was developed for control of the mechanical leak valve. Through this, the leak valve can either be opened to a specified percentage of its fully

open value, or a desired line pressure can be set and used for PID control. Additionally, the PID settings can be altered via the GUI and multiple setpoints (of multiple types) stored in memory for quick switching between states.

The other valves on the delivery lines are all pneumatic on/off valves controlled via the Laboratory Virtual Instrument Engineering Workbench (LabVIEW™) software [257]. Using LabVIEW™, two different GUIs were written: one for individual control of each on/off valve independently according to any desired configuration, and one where specific, pre-set, valve schemes can be selected. The GUI with pre-written schemes is intended for quick switching between sources and routine actions like initiating or terminating delivery from a source. The other GUI is necessary to allow for more complicated schemes or isolation of specific piping areas during installation, pump-down, or bake-out of the system. The EPICS and LabVIEW™ systems were designed to work in tandem, allowing for the most flexibility compatibility.

#### **7.3.4 Safety**

The main safety concerns with this system are related to the high temperatures at which the delivery lines are maintained and the specific chemical hazards associated with the metalorganic sources being utilized. As some parts of the system may be maintained at temperatures nearing 120 °C, care should be taken around the piping and thermally insulated gloves should always be worn when operating hand valves. It is also necessary to check that all wiring and power around the chamber are not in direct contact with any heated lines. As the HMBE changes position during measurement, the full extent of its motion should be checked to ensure that it is unhindered before use.



Exposure to any sources should only occur in an environment where proper ventilation is present to ensure a constant flow of any potentially hazardous material away from operators. If a source bottle is filled by hand, appropriate precautions (a hood with proper airflow or the use of a glovebox if appropriate) should be taken and appropriate personal protective equipment worn depending on the source material. Installation or removal of a source bottle or bubbler from the delivery system should be done only when the entire instrument is at room temperature. The following procedure should be used for replacing a source:

The bubbler should be isolated by closing its hand valve. The rest of the piping should be evacuated to exhaust until any buildup of excess vapor pressure is eliminated. Some sources are air sensitive and if the growth chamber is not under UHV (i.e. if it is currently vented) a positive backflow of nitrogen can be provided. If this is not possible the valve directly downstream of the source should be closed so that as little of the piping is exposed to air as possible. After removal, any VCR fittings that were opened should be inspected for damage or oxidation/corrosion and replaced as necessary.

Installation of a source follows the reverse of the procedure described above. Again, either a positive flow of nitrogen should be present or all delivery line valves should be closed. Once the new source is installed, all piping (up to the source bottle) should be evacuated via exhaust before opening the bubbler's hand valve. If baking of the system is desired, this is the best opportunity to carry it out. An appropriate baking temperature for this system is 110-120 °C to drive off water and organics while staying within the temperature range that can be easily maintained by the heating elements. Once the source valve is opened, both the lines and source can be heated to the desired temperature while the exhaust vent is still open to prevent excess pressure buildup. When

the desired temperature for the source is attained the main mechanical leak valve (and the exhaust) can be closed to ready the system for normal delivery operation.

## 7.4 Performance

### 7.4.1 Determination of Indicator for TTIP

When the source bottle is first installed, or has not been in use for a significant amount of time, there can be a build-up of organic decomposition products in its headspace. This means that seeing an increase in pressure on the growth chamber's ion gauge is sufficient to determine whether the physical piping and valves are functioning, but not sufficient to indicate whether TTIP (or another source) is present in the chamber at the desired levels for deposition. For this purpose, an RGA was used to determine the cracking products of species present in the chamber and their levels during metalorganic delivery. In this hybrid system the gaseous precursor behaves in a manner more similar to the leaked  $O_2/O_3$  than the solid metal MBE sources. Upon injection into the chamber, it provides a background pressure of precursor in the entire UHV chamber. To obtain an accurate measurement while avoiding interference with the flight path of MBE effusion cell sources, the RGA was located at a similar distance from the sources as the growth substrate but to one side of the chamber (close to the turbo pump inlet). TTIP was delivered at a chamber pressure of  $1 \times 10^{-5}$  Torr and the mass spectrum collected is shown in Figure 7.5. Investigations conducted on  $TiO_2$  growth with TTIP and titanium tetrachloride [258] report that the mass-to-charge ratio ( $m/z$ ) = 45, corresponding to  $[CH_3CHOH]^+$  [258, 259], is a cracking product of the TTIP source-used to track its presence. However, in our investigations, this proved to be an unreliable indicator of the presence of TTIP, perhaps due to additional hydrocarbons present in the bubbler headspace contributing to its signal. As such, the lowest  $m/z$  cracking products of TTIP that contained some

portion of Ti were considered. These are  $[\text{TiO}]^+$  at  $m/z = 64$  and  $[\text{TiO}(\text{OH})]^+$  at  $m/z = 81$  [258]. According to the inset in the top right of Figure 7.5,  $m/z = 81$  has a stronger signal of the two. This peak was observed under all cases where films containing Ti were reliably grown, and so it serves as an adequate indicator of the level of TTIP.

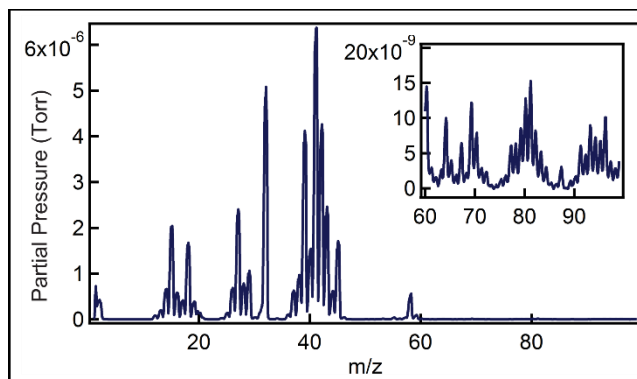


Figure 7.5 Partial pressures from cracking products of the TTIP metalorganic as a function of  $m/z$ . The measurement was performed during deposition of  $\text{TiO}_2$  on r-plane  $\text{Al}_2\text{O}_3$  in the oxide MBE chamber. Inset shows an enlarged view of the higher  $m/z$  products.

#### 7.4.2 Characteristics of Gas Delivery

After TTIP was verified in the chamber, the behavior of the metalorganic vapor during delivery could be characterized. Additionally, the stability of the flux over a long period of time was measured. To do this, time-dependent RGA tracking of selected  $m/z$  cracking products of TTIP was initiated while the chamber contained only a substrate heated to a growth temperature of 800 °C, to obtain a baseline. The mechanical leak valve was then opened, using the control mode where a selected line pressure is maintained (the common mode for a typical growth) and delivery of TTIP was tracked for approximately 30 minutes while a sample was grown. The various cracking products selected for measurement, and the results of this experiment, are shown in

Figure 7.6. Different panels are used so that cracking products at very different orders of magnitude of partial pressure can be visualized and compared easily.

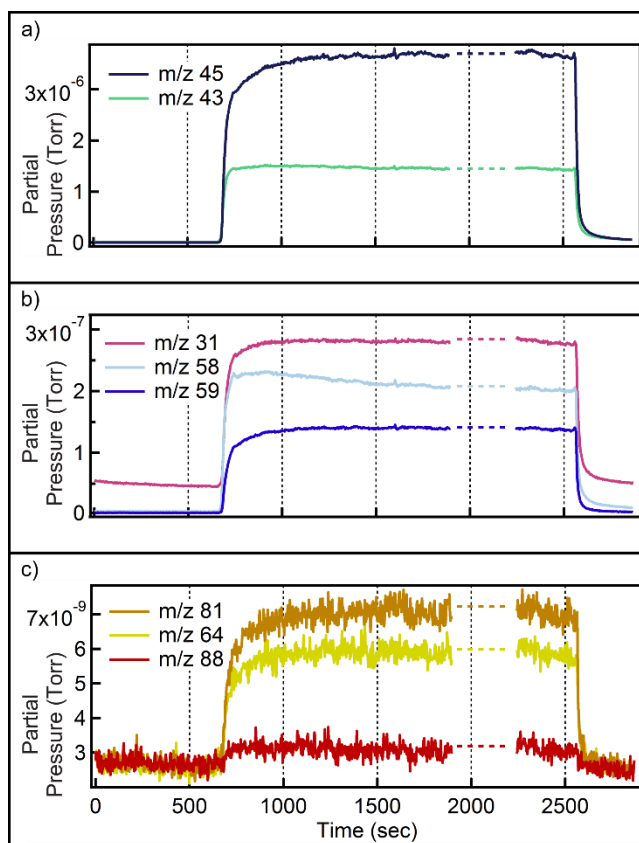


Figure 7.6 Partial pressure traces of selected  $m/z$  cracking products of the metalorganic precursor, TTIP, during growth of rutile  $\text{TiO}_2$ . The RGA measurements show the behavior of precursor gases within the MBE chamber upon initiating and after terminating gas delivery. The traces in (a), (b), and (c) have been re-scaled for ease of viewing. Dotted lines between traces serve as a guide to the eye; no data was recorded during this time. Measurements were taken during growth at a temperature of  $800^\circ\text{C}$ .

The baseline acquired before TTIP delivery was initiated, shown in the first 600 seconds of Figure 7.6, indicates that there was no significant level of the cracking products present (at least within the instrument's detection limit). This indicates that the HMBE does not have any leaks into the UHV system when its valves are in the "closed" position. After about 660 seconds of measurement in Figure 7.6, the TTIP valve is opened. There is a very quick increase when the valve is opened, followed by a slower increase up to a stable level. When deposition is initiated, it

takes roughly 100 seconds for the cracking products to reach 80-98% of their stable level, although this time varies somewhat depending on which  $m/z$  value is tracked. After the initial, quick increase, there is a much slower leveling off that occurs over the next ~450 seconds before all products tracked in this experiment reached their saturated levels, and any further change becomes indistinguishable from noise in the measurement. For the rest of the time measured, the level of TTIP partial pressure is stable until delivery is terminated, 2000 seconds after it began (at the time marked as 2600 sec in Figure 7.6). Once delivery is ended, the level of metalorganic drops immediately and becomes indistinguishable from its original, baseline, amount after 120-180 seconds. Each of the cracking products tracked behaves in a similar manner, although some take longer to reach a stable flux level than others during delivery. In the case of  $m/z$  values where the overall partial pressure is much lower (like  $m/z = 64, 81, \text{ and } 88$ ), it is possible that the initial increase to stable levels may appear slower simply because the values measured are closer to the instrument's detection limit, but there is no current way to verify or disprove this.

## **7.5 Additional Practical Information for Running the HMBE and Further Improvements**

The HMBE system delivers metalorganic gases well, and the growth of oxide materials has been demonstrated (see next chapter). However, there is additional information that an experimenter operating the equipment should be aware of when using it. This section includes general hints and tips for operating the HMBE determined over the course of a few years and many uses. It also provides suggestions for further improvement of the system and presents some pieces of information that might benefit future users to pursue more thoroughly.

As a general note, the HMBE system has many controllers, valves, and heating elements that use power supplies or cords for remote communications. These should be connected with care

to ensure that the entire assembly is still free to move during measurements. Future efforts should be made to consolidate power cords and sources and ensure that no heating elements rely on variable autotransformers (Variacs)- rather that they are all controlled via the controller bank. In particular, the heating element contained within the injector cannot currently be controlled by the heating controller- even setting the controller to a very low power output value brings the injector to a higher temperature than is desirable ( $>200\text{ }^{\circ}\text{C}$ ). Currently a Variac at a very low power percentage setting is used (10-15%), however, using a different controller for this element could eliminate this issue.

When a new source bubbler is used for the first time, or a source is used that has been inactive for a long period of time (typically half a year or more), it is necessary to evacuate the source headspace. This has been reported for other HMBE systems [260] and is due to the fact that over time the metalorganic compounds of the source decompose and the bubbler headspace fills with organic compounds. These compounds do not frequently contain the metal cation desired for synthesis. As such, if they are not evacuated, they create the illusion of source vapor pressure (the delivery lines will read a pressure, as will the ion gauge of the growth chamber), but no films can be grown. Use of an RGA is recommended to determine whether the gas entering the chamber contains cracking products of the metalorganic source and whether cracking products carrying the desired cation are present. If they are not, the headspace of the bubbler should be evacuated further. For this purpose, the cart pump and exhaust of the hutch can be used. It is recommended that the source bottle be cooled below the temperature used for normal delivery, and cooling to room temperature or below (with dry ice) is recommended. The delivery lines should be kept hot. Under these conditions the bubbler should be pumped until there is very little line pressure read on the

lines- this can take hours or even overnight. Once complete, the exhaust pump can be closed and the source re-heated to perform growth.

When performing delivery with the HMBE, the mechanical leak valve should not be immediately set to the desired line pressure. This is because the PID settings of the controller do not allow it to anticipate how quickly the gas flux increases and an initial burst of gas at a high pressure can be easily released into the growth chamber. Not only can this overwhelm the chamber's pumping capability but it can also release a significant amount of vapor pressure from the source itself, which may then not recover quickly enough to ensure stable delivery. There are two ways to counteract this. The first method outlined is the one used for most of the experiments presented herein, while the second is a suggested method that could be pursued and refined by future users.

1. The mechanical leak valve can be controlled in two modes; the normal mode of control is to set a desired line pressure and allow the valve to adjust as necessary to maintain that pressure. The other mode is to set the mechanical leak valve to a desired position- in this mode the line pressure is not directly controlled. The valve can then be slowly opened in this 'position' control mode while the line pressure is monitored. Once the line pressure is close to the desired setting, the mode of control can be switched to 'pressure' mode. For subsequent depositions, a 'position' control mode can be set with a position near the mechanical valve's initial position during the previous growth (at the same desired line pressure). This can be used initially to get the valve close to the correct position, and then the control mode can be switched back to 'pressure' mode.

2. The pneumatic valve closest to the chamber and the mechanical leak valve are closed.

The scroll pump should be on and running. All other pneumatic valves, including the one leading to the pump and exhaust, can then be opened. The mechanical leak valve can then be opened, following the procedure outlined in (1), until the line reads the desired pressure reliably. At this point, the pneumatic valve to the exhaust pump should be closed and the pneumatic valve closest to the chamber opened, switching the gas flow from the exhaust to the growth chamber. The specifics and exact valve scheme/timing of this method has not been extensively tested.

After delivery has occurred for the amount of time required for growth of a film, the base pressure of the growth chamber will have risen, even when the mechanical leak valve is closed and delivery terminated. This is due to the buildup of organics within the chamber from the metalorganic source that cannot be evacuated quickly. This is not a cause for alarm, but it does indicate that baking of the chamber after use with HMBE is necessary to prevent organics from interfering with growth of other materials. In addition, the delivery of metalorganic sources can affect the delivery rate of metals from the effusion cells. Observations of this have been made and the following example pertains to Sr, a very low-temperature source. It is likely that a higher-temperature source would not have such obvious effects, but this has not yet been investigated. Before growth of a material, the flux of the metal effusion cells is always calculated from measurements of the QCM. These values are then used to determine shutter timing, if necessary. A single source, where the effusion cell temperature is constant, often has a stable flux for over 8 hours. However, after deposition with the TTIP metalorganic source, the sample was removed and the flux of this same Sr source was measured immediately. It was found to be significantly lower,



eventually recovering over time, reaching its initial reading (the same as before growth). If the source was briefly “flashed” (i.e. the temperature was raised by about 20 °C for ten or so minutes and then lowered back to its original temperature), the rate of recovery to the original flux was much quicker. While the exact causes of this are unknown, it is likely that organic material from the metalorganic’s decomposition is depositing on the exposed surface of the Sr metal source. It may be oxidizing the source or simply forming an adsorbed layer that makes its vaporization slow. In either case, while it does not necessarily prevent growth and can be compensated for, this effect is not well understood and could be investigated further.

## **7.5 Conclusions**

The design concerns outlined for the modification of an existing MBE chamber to allow metallorganic source deposition are addressed by the HMBE instrumentation developed. Additionally, the characteristics of gas delivery with this system have been investigated and its general operation discussed. The results shown demonstrate the function and outline the principles behind a HMBE system integrated with an in situ X-ray diffraction setup.

This instrument is suited to performing diffraction-based investigations of oxide HMBE growth. Its strengths lie in its ability to measure the substrate’s surface before growth, track specific diffraction conditions, and measure SXRD of the film grown. This data can be combined with direct methods if a large area of reciprocal space is measured to determine many features of film and substrate/film interface structure. Additionally, the in situ data collected can be compared to other studies where RHEED data have been recorded to understand and compare the two, obtaining additional information about the strengths and weaknesses of both techniques and providing additional information about growth mechanisms to form a more complete picture of

the processes and dynamics involved. Initial experiments to these effects are discussed further in the next chapter.

## CHAPTER 8

### **Growth of Oxide Materials Using Hybrid MBE System with in situ X-Ray Diffraction**

Discussion in the last chapter focused on outlining the constraints, design, function, and initial characterization of gas delivery using a custom metalorganic source delivery system designed for hybrid molecular beam epitaxy growth.

The use of the assembled system will be discussed in this follow-up chapter. While this HMBE system can be used to grow novel oxides, the primary goal here is to better our understanding of the underlying mechanisms behind HMBE growth, for a variety of precursors and materials.

The focus of this chapter is growth of a variety of materials, and what can be learnt about them in situ X-ray scattering capabilities of this particular system (in comparison to other systems).

Experimental work presented herein was conducted at the APS with kind assistance from Dr. Hawoong Hong and Seyoung Cook. Work discussed in this chapter forms the basis of “Development of a hybrid molecular beam epitaxy deposition system for in situ surface X-ray studies” [239] from which some figures have been reproduced.

## **8.1 Introduction**

Capabilities of HMBE for oxide material growth are expanding as new precursor metalorganics are investigated [245, 248, 253, 260-274]. HMBE also facilitates some unique experiments including combinatorial growth [248] and production of films with stoichiometry that can be indistinguishable from bulk [246]. The potential of HMBE as a growth method for oxides is promising beyond fundamental research too, as it offers very flexible deposition modes and has a greater potential for scale-up than traditional MBE due to its increased speed and the reliable composition control provided by accessing a “growth window” [245, 253, 268].

As different families of metalorganic sources are used for oxide synthesis in HMBE the questions surrounding growth mechanisms and the role that a metalorganic's functionality plays in synthesis become more important. Sources of the isopropoxide family (TTIP, VTIP) have been used in synthesis of Ti and V-containing oxides [245, 246, 248, 253, 254, 261-269, 272-274], while other processes include using hexamethylditin radicals to supply Sn [270, 271]. In a conventional UHV chamber, equipped with only RHEED monitoring, the specifics of synthesis with these metalorganics were previously only hypothetical.

In order to most effectively utilize any synthesis method, an understanding of the growth mechanisms is desirable. To this end an HMBE system integrated with a chamber designed for SXRD was developed and assembled, described in the previous chapter. This system provides complementary information to in situ RHEED setups [275] while enabling additional diffraction information to be collected from off-specular conditions either in situ or following deposition. The combination of information available from this system enables the investigation of the reaction of metalorganic precursors with a substrate's surface, the influence of a starting surface's features, and growth modes.

In this chapter, growth of a binary and ternary oxide using the HMBE delivery system designed and assembled by the author is demonstrated. The types of data obtainable with the assembled system is introduced. Additional experiments probing the reaction of the TTIP precursor with a surface are also presented along with some cases of growth in the Sr-Ti-O oxide system where additional factors are at play in determining the phases observed. These growths open the door to additional experiments with this HMBE system and shed light on aspects of HMBE growth that have not been investigated in detail before.

## 8.2 Methods

### 8.2.1 Substrate Preparation

R-plane  $\text{Al}_2\text{O}_3$  (0 1 2) substrates [CrysTec, GmbH] were washed and annealed before use. They were ultrasonicated for thirty seconds each in acetone, isopropyl alcohol, and then water to de-grease and remove particles from their surface. After drying, they were annealed at 1100 °C in air for one hour. Atomic force microscopy (AFM) measurements were taken to confirm the presence of a step-terrace geometry and that the surfaces were free of large particles. An AFM image showing the surface of a typical  $\text{Al}_2\text{O}_3$  (0 1 2) substrate before growth is shown in Figure 8.1 (a).

LSAT (0 0 1) substrates [CrysTec, GmbH] were not annealed at any point. They were washed to remove any grease or residue present from the commercial cutting and polishing process. They were sonicated for thirty seconds each in acetone, then methanol, and then finally isopropyl alcohol. They were then dried, and AFM measurements were performed to determine whether the surface was free of debris. An AFM image showing the surface of a typical LSAT (0 0 1) substrate before growth is shown in Figure 8.1 (b).

$\text{SrTiO}_3$  (0 0 1) substrates with low miscut ( $< 0.1^\circ$ ) [CrysTec GmbH] were prepared following the same method outlined in Section 6.2.1 to produce  $\text{TiO}_x$ -rich terminated substrates. To produce substrates with SrO islands on the surface, the preparation method used was identical but the annealing time was increased by 4 hours to 5 hours in total. An AFM image showing the surface of a typical  $\text{SrTiO}_3$  (0 0 1)  $\text{TiO}_x$ -rich substrate before growth is shown in Figure 8.1 (c).

All substrates were loaded into the UHV chamber for MBE growth and heated to the desired  $T_{sub}$  for the given film material.

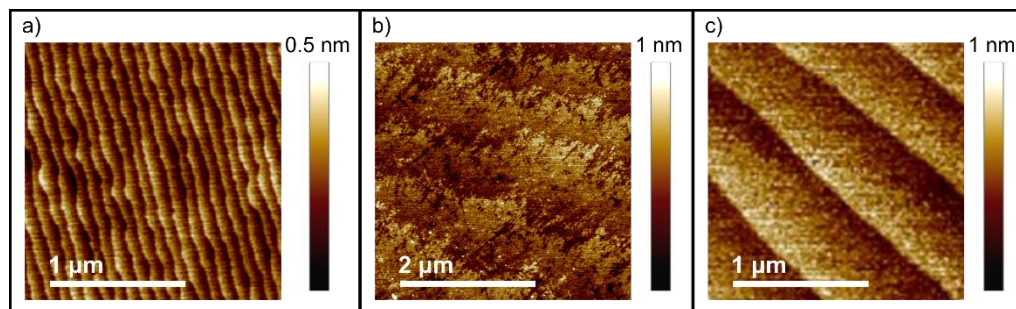


Figure 8.1 AFM (height) of prepared substrates for oxide growth showing a) r-plane  $\text{Al}_2\text{O}_3$  (0 1 2), b) LSAT (0 0 1), and c)  $\text{SrTiO}_3$  (0 0 1).

### 8.2.2 X-Ray Measurements

All measurements were performed at APS Sector 33-IDE. Diffraction data presented in this section were acquired using 15 keV energy X-rays selected with a Si (1 1 1) monochromator. Monochromatic X-rays, such as those employed during these experiments, have been previously been observed to have no effect on growth behavior with metalorganic precursors [221, 276-281] unlike highly focused [282] or non-monochromatic X-rays. In situ monitoring of specific diffraction conditions was conducted during growths as discussed in the relevant results sections. All reciprocal space positions discussed in this section are presented in the form of (0 0  $L$ ) in reciprocal lattice units (r. l. u.), where  $L$  is the out-of-plane diffraction direction relative to the sample being measured and the positions are indexed with respect to the substrate material in question ( $\text{Al}_2\text{O}_3$ ,  $\text{SrTiO}_3$ , LSAT, etc. as discussed later). 2-Dimensional images of the scattered X-rays were collected using a pixel array detector [Pilatus 100 K, Dectris] and reduced to background-subtracted integrated intensities [222].

## 8.3 Results

### 8.3.1 Growth of TiO<sub>2</sub>

Having confirmed the delivery of TTIP using the HMBE system and characterized its behavior in the previous chapter, the simplest material to grow is one that requires use of only the metalorganic source. The binary oxide TiO<sub>2</sub> fits this criteria and growth of TiO<sub>2</sub> on r-plane Al<sub>2</sub>O<sub>3</sub> (0 1 2) substrates [CrysTec, GmbH] serves as an appropriate demonstration.

Films were grown first using a variety of substrate temperatures,  $T_{sub}$ , to determine the optimal conditions and to verify the phase and orientation of TiO<sub>2</sub>. AFM was used to investigate the morphology of films. In Figure 8.2 AFM and  $\theta$ -2 $\theta$ -scan X-ray diffraction (XRD) from a TiO<sub>2</sub> film are shown, results collected on a lab-source Cu-anode diffractometer [PANalytical, Netherlands]. The morphology of the film, Figure 8.2 (b), shows small domains, indicating that at this film thickness, growth does not take place by a layer-by-layer process as it does not maintain the unit-cell height steps of the prepared substrate in Figure 8.2 (a). The diffraction peaks attributed to the film in Figure 8.2 (c) indicate that TiO<sub>2</sub> takes the rutile structure and adopts the orientation relationship of  $(1\ 0\ 1)\ [0\ 1\ 0]_{TiO_2} \parallel (0\ 1\ 2)\ [0\ 0\ 1]_{Al_2O_3}$ . This agrees with published results for HMBE growth of TiO<sub>2</sub> [265].



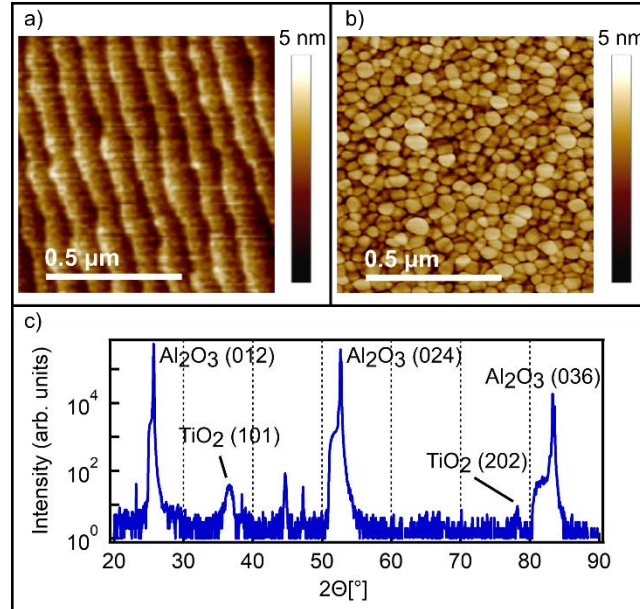


Figure 8.2 AFM (height) of bare r-plane  $\text{Al}_2\text{O}_3$  (0 1 2) substrate a) before and b) after growth of  $\text{TiO}_2$  and  $2\theta$  X-ray diffraction showing (1 0 1)  $[0\ 1\ 0]_{\text{TiO}_2} \parallel [0\ 1\ 2]_{\text{Al}_2\text{O}_3}$  orientation of  $\text{TiO}_2$  film on  $\text{Al}_2\text{O}_3$ .

The first growths using the HMBE's capability for in situ X-ray diffraction were conducted using the  $\text{TiO}_2$  growths as a test. Two films of  $\text{TiO}_2$  were grown, and real-time diffraction data from two different reciprocal space conditions were collected alongside the specular out-of-plane scattering, both shown in Figure 8.3. In the CTR shown in Figure 8.3 (a), the r. l. u. refers to the (0 1 2) room temperature d-spacing of  $\text{Al}_2\text{O}_3$ , 0.174 nm. Both traces in Figure 8.3 (a) have the same diffraction features, and if converted to the appropriate scale in  $2\theta[^\circ]$ , their peaks can be compared to determine that both films contain only rutile  $\text{TiO}_2$  with the same orientation as those presented earlier in Figure 8.2 (c). The two films shown,  $\text{TiO}_2\text{h1}$  and  $\text{TiO}_2\text{h2}$ , were both grown at  $T_{\text{sub}} = 600\ ^\circ\text{C}$  with line pressures of 75 mTorr and 50 mTorr TTIP respectively. During growth of  $\text{TiO}_2\text{h1}$  the diffraction condition monitored was the  $\text{H K L} = 0\ 0\ \frac{1}{2}$  r. l. u. position, the results of which are shown in Figure 8.3 (b). This anti-Bragg position is very sensitive to the growth of epitaxial layers and changes in surface roughness. For layer-by-layer growth, regular oscillations,

whose period indicates the time necessary to deposit a single atomic layer, would be observed for heteroepitaxial growth such as this. Its intensity can also be compared to previous RHEED studies [265] where a similar diffraction condition is typically monitored (while providing more complex information due to the differences between electron and X-ray diffraction). The film labelled TiO<sub>2</sub>h2 was monitored at the film peak, TiO<sub>2</sub> (1 0 1) condition, H K L = 0 0 1.42 r. l. u. to monitor the evolution of the crystal as a function of film thickness. The thickness of these films was calculated using a form of Scherrer's equation (Equation 8.1):

$$\tau = \frac{K\lambda}{\beta \cos \theta} \quad (8.1)$$

In Equation 8.1,  $\tau$  is the calculated film thickness in nm,  $K$  is a dimensionless shape factor set to unity,  $\lambda$  is the wavelength of incident X-rays in nm,  $\beta$  is the full-width half-maximum of the TiO<sub>2</sub> film peak (in radians), and  $\theta$  is the Bragg angle (in degrees). Using Equation 1, the film thickness of TiO<sub>2</sub>h1 was found to be 40 nm, while the thickness of sample TiO<sub>2</sub>h2 was 24 nm. This method has errors associated with it due to the sampling density of the scans in reciprocal space; however the thicknesses calculated are very close to those that would be expected from a linear relationship between TTIP line pressure and film thickness. This indicates that the source flux is reliable and growth rate can be predicted for a given line pressure (given specific HMBE temperature zones).

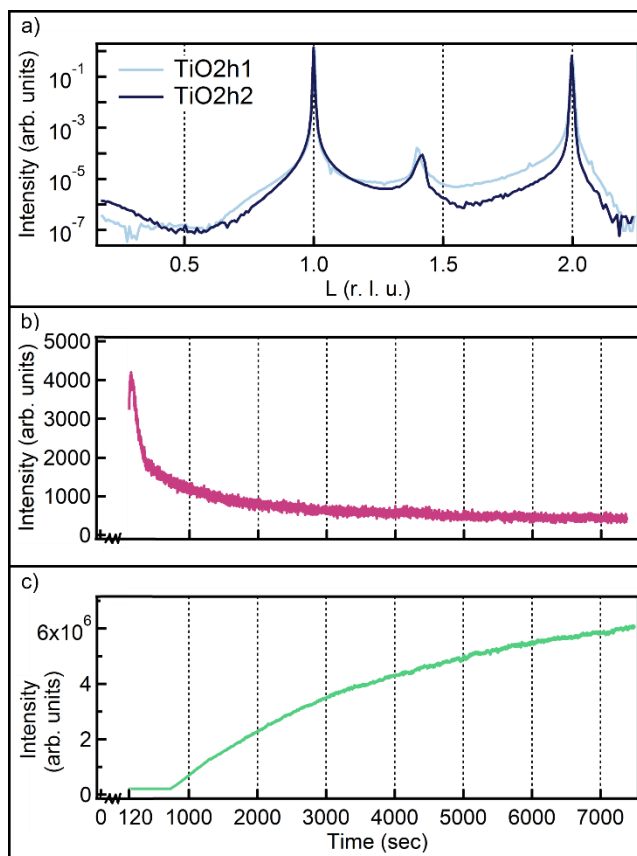


Figure 8.3 (a) Scattered X-ray intensity measured along the out-of-plane,  $0\ 0\ L$  direction for a rutile  $\text{TiO}_2$  film grown on  $\text{Al}_2\text{O}_3$  ( $0\ 1\ 2$ ). (b) Change in scattered X-ray intensity during growth at the anti-Bragg position,  $H\ K\ L = 0\ 0\ \frac{1}{2}$  r. l. u., and (c) at the  $\text{TiO}_2$  ( $1\ 0\ 1$ ) Bragg peak or  $H\ K\ L = 0\ 0\ 1.42$  r. l. u. The measurements were taken at the growth temperature of  $600^\circ\text{C}$ . Delivery of TTIP began at  $t = 0$ , measurement began at  $t = 120$  sec.

These successful experiments demonstrate that the HMBE chamber can be used for the intended experiments- combining growth using metalorganics with the in situ capabilities of the SXRD experimental setup to investigate the growth of oxide films and associated processes. Since SXRD can be approximated by the kinematic single-scattering approximation, quantitative information on different length scales can be obtained from diffraction results. This data can be compared to RHEED growth studies [275]. While RHEED data is more frequently collected, SXRD has some notable benefits. The freedom of motion associated with this SXRD MBE

chamber allows a wide range of reciprocal space diffraction conditions to be accessed and measured, some of which are challenging or even impossible to access with RHEED due simply to the geometry of measurements and differences in scattering. An example of this is the monitoring of the  $\text{TiO}_2$  (1 0 1) film Bragg peak in Figure 8.3 (c), a condition which would be difficult to specifically track using RHEED.

### 8.3.2 Growth of $\text{SrTiO}_3$

Once the efficacy of delivering TTIP and producing Ti-containing films had been established, the next step was to demonstrate the desired functionality- a tool for studying HMBE growth. This necessitates simultaneous use of both the metalorganic and a solid effusion cell MBE source. To this end, the next material was chosen such that it incorporated Ti (allowing the same source to be used) and was a member of the technologically relevant  $\text{ABO}_3$  perovskite oxide family.  $\text{SrTiO}_3$  satisfied these conditions, so it was chosen.

LSAT (0 0 1) substrates [CrysTec GmbH] were chosen for growth of  $\text{SrTiO}_3$ . These were used instead of  $\text{SrTiO}_3$  substrates to improve the visibility of film thickness fringes in the SXRD measurements- allowing the thickness and lattice parameter of the grown films to be more easily determined. During deposition, the metalorganic was supplied by a TTIP source, and Sr was supplied via effusion cell. The resulting specular (0 0  $L$ ) CTR, time-resolved scattering at the anti-Bragg position (0 0  $\frac{1}{2}$ ), and AFM images of two films grown are shown in Figure 8.4 and labelled STOh1 and STOh2, respectively. In the plot presented in Figure 8.4 (a), the r. l. u. are referenced to room temperature LSAT (0 0 1) with a lattice constant of 0.387 nm. All films of  $\text{SrTiO}_3$  grown on LSAT (0 0 1) were observed to have the orientation (0 0 1)  $[\text{0 0 1}]_{\text{SrTiO}_3} \parallel (\text{0 0 1}) [\text{0 0 1}]_{\text{LSAT}}$ . The two samples were grown under identical environmental conditions with  $T_{\text{sub}} = 750^\circ\text{C}$  and a

delivery line pressure of 110 mTorr. To change the A:B stoichiometry of the two samples, the Sr flux (measured using a quartz crystal microbalance) was altered slightly. For STOh1, the flux was  $2.35 \times 10^{12}$  atoms/cm<sup>2</sup>•sec and for STOh2 it was slightly higher at  $2.67 \times 10^{12}$  atoms/cm<sup>2</sup>•sec. The film peaks for each of the two growths are shown in Figure 8.4 (a), slightly to the left of the substrate's Bragg peaks, and these were used to calculate the lattice parameter for each film. As an ABO<sub>3</sub> film approaches the ideal A:B = 1 stoichiometry ratio, its lattice parameter shrinks; an excess in either cation would be reflected as a slightly-expanded lattice parameter compared to the ideal value. The measured c-lattice parameters were 0.401 nm and 0.395 nm at room temperature for STOh1 and STOh2. The ideal c-lattice parameter for coherently strained SrTiO<sub>3</sub> on LSAT is calculated to be 0.393 nm, assuming a bulk-like Poisson's ratio of  $\nu = 0.23$ ; therefore STOh2 has stoichiometry closer to the ideal A:B = 1. The root mean squared roughness of the two samples was also calculated from AFM data and it was found to be 0.28 nm for STOh1 and 0.15 nm for STOh2.

The AFM image of sample STOh2, Figure 8.4 (d), shows unit-cell height steps and terraces. The closeness of the lattice parameter to ideal, the lower surface roughness, and the better film ordering are all direct consequences of the STOh2 film having an A:B cation ratio closer to the ideal stoichiometry than the STOh1 film. While any one finding alone could be used as an indicator, taken together a strong case can be made that high-quality surfaces of SrTiO<sub>3</sub> can be achieved using HMBE growth. In addition, the thickness of each film was calculated from the thickness fringes visible in Figure 8.4 (a), and they were found to be 10.9 and 7.5 nm for STOh1 and STOh2. This is unsurprising- while the growth rate of STOh1 was slower, the total growth time was longer, indicated by the in situ scattering in Figure 8.4 (b).

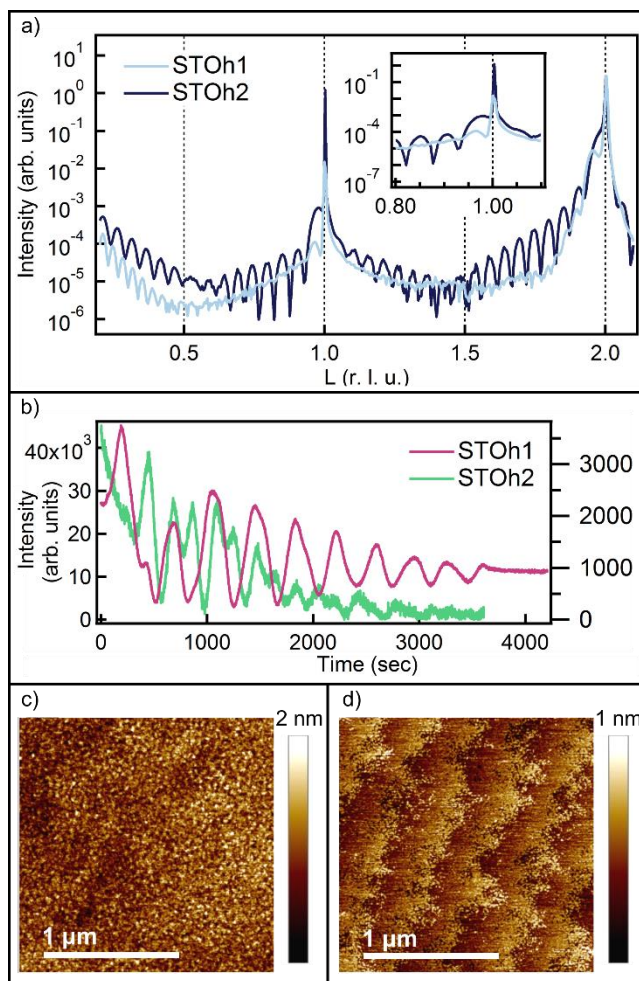


Figure 8.4 Room temperature results for two  $\text{SrTiO}_3$  films grown at  $750^\circ\text{C}$  on LSAT (0 0 1) with 110 mTorr TTIP under Sr fluxes of  $2.35 \times 10^{12}$  atoms/ $\text{cm}^2 \cdot \text{sec}$  (STOh1) and  $2.67 \times 10^{12}$  atoms/ $\text{cm}^2 \cdot \text{sec}$  (STOh2). (a) X-ray scattering along the specular 0 0  $L$  direction at room temperature. (b) Scattered X-ray intensities (STOh1 on left axis, STOh2 on right) measured during growth at  $750^\circ\text{C}$  at the reciprocal lattice position,  $H K L = 0 0 \frac{1}{2}$  r. l. u. (c, d) Room temperature  $2 \mu\text{m} \times 2 \mu\text{m}$  AFM micrographs of the films STOh1 (c) and STOh2 (d).

Unlike the growth of  $\text{TiO}_2$  presented in the previous section, the anti-Bragg scattering in Figure 8.4 (b) shows oscillations associated with the growth for these two films. Both STOh1 and STOh2 show growth oscillations, and the amount of time needed to deposit one unit-cell of  $\text{SrTiO}_3$  can be determined by measuring the period of these oscillations. For both films, the oscillations die out over the course of growth, indicating that the A:B stoichiometry is not perfect or that the

film may be growing at a rate where pure step-flow does not dominate, since the film is accumulating more defects and roughness as it becomes thicker. Additionally, the features of the oscillation, particularly in sample STOh2, are not what would be expected from perfect layer-by-layer growth. It lacks the expected oscillations of similar or slowly decreasing height that have a repeated period. Instead it shows what looks like double peaks repeated. Although the body of data on X-ray scattering at the  $(0\ 0\ \frac{1}{2})$  diffraction condition is much smaller than that of RHEED, making quantification difficult, X-ray scattering at this position can reveal features of the film that are not as easily-determined from RHEED oscillations alone. The current difficulty in quantifying X-ray scattering at the  $(0\ 0\ \frac{1}{2})$  position, in combination with the encouraging CTR scans and AFM showing well-defined thickness fringes and low roughness films, makes collection of this type of data particularly compelling for this system. High-quality films can clearly be grown, and by using a combination of these measuring methods, more can be learned about their in situ growth behavior. This HMBE system supports these investigations; its HMBE growth capability has been demonstrated by these  $\text{SrTiO}_3$  films and its potential to investigate oxide systems by collecting valuable in situ SXRD will provide insight into the synthesis of multifunctional oxide materials.

### **8.3.3 TTIP Reaction with SrO**

One of the reasons that HMBE is desirable over traditional MBE is the incorporation of chemical functionality that metalorganic sources bring to synthesis. Ideally, this should facilitate growth of perfectly stoichiometric films under the proper conditions, as growth will be occurring in an adsorption-limited regime. The incorporation of metalorganic functionality ideally widens the condition set necessary for achieving this adsorption-limited regime. One case of this has been reported in the growth of  $\text{SrTiO}_3$  with a growth window [245].

The hypothesized mechanism for growth of  $\text{SrTiO}_3$  using TTIP as an HMBE source, according to investigations by others [245, 246, 264], is summarized in the explanation that follows. Under ideal conditions ( $T_{\text{sub}}$ , flux ratio of Sr and TTIP), Sr is deposited onto the substrate and either forms SrO or simply deposits as metallic Sr atoms. It can be oxidized either by the growth environment (with a background pressure of  $\text{O}_2$  or  $\text{O}_3$  present) or by release of oxygen from the decomposition of TTIP in the chamber. When a TTIP molecule (shown in Figure 8.5) comes close to the substrate, it decomposes and reacts with any Sr or SrO on the surface to form  $\text{SrTiO}_3$ . The TTIP molecule can provide enough oxygen for stoichiometric growth (i.e. growth without significant oxygen vacancies) because there are plenty of available oxygen atoms already bonded to the central Ti atom. According to this mechanism, if the delivery rates of the two sources are correct, excess TTIP will simply not react (as it has a much lower chance of reacting with  $\text{SrTiO}_3$  or  $\text{TiO}_2$  on the surface). At some point of increase in TTIP flux, it is reasonable to assume that this no longer holds, as  $\text{TiO}_2$  can be grown using just the TTIP flux alone. This mechanism leads to the hypothesis that there is a window of flux ratios where adsorption-controlled growth dominates and excess TTIP will simply not be incorporated into the film.



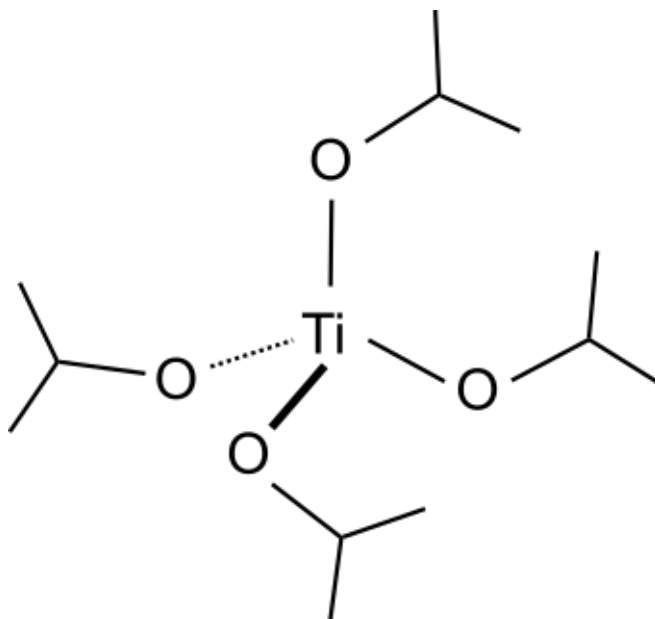


Figure 8.5 Titanium (IV) Tetraisopropoxide Chemical Structure.

To investigate whether this is a sensible reaction hypothesis, a simple experiment with  $\text{SrTiO}_3$  substrates was done. By careful control of the surface preparation method of  $\text{SrTiO}_3$  substrates, atomically flat surfaces that are  $\text{TiO}_x$ -rich can be prepared [217]. However, if an  $\text{SrTiO}_3$  substrate is annealed for too long or at too high of a temperature, segregation of SrO islands at the surface will be observed [283-286]. This offers an opportunity to probe the mechanism of TTIP reactions with a surface and, to this end, an experiment was designed with two sets of  $\text{SrTiO}_3$  (0 0 1) substrates where slightly different procedures were used to prepare the surface. The results of this experiment are summarized by the AFM images shown in Figure 8.6.

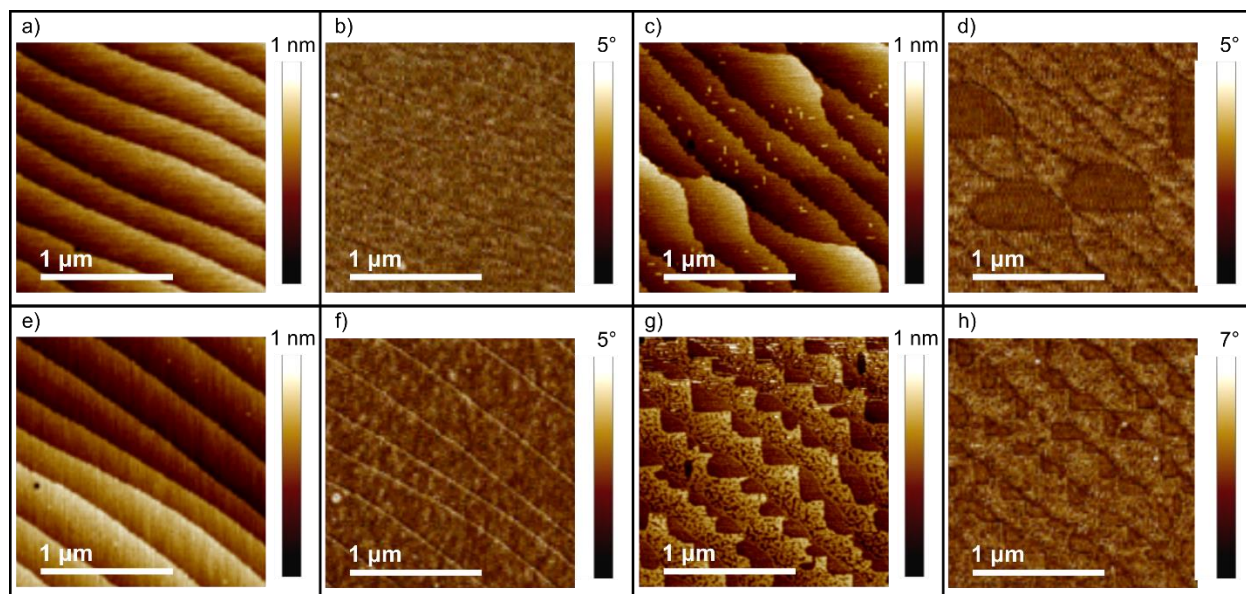


Figure 8.6 AFM images of  $\text{SrTiO}_3$  (0 0 1) with initial  $\text{TiO}_x$ -rich surfaces (a-b, e-f) and SrO islands (c-d, g-h) after annealing at 800 °C without exposure to TTIP (a-d) and after a 5-minute dose of TTIP (e-h). AFM in a, c, e, and g shows height while b, d, f, and h show phase.

One substrate set had  $\text{TiO}_x$ -rich surfaces, shown in Figure 8.6 (a) and (b), and was prepared using the methods normally followed for  $\text{SrTiO}_3$  (0 0 1) preparation. The other was annealed for four hours longer and had islands of precipitated SrO visible on its surface according to the AFM height and phase data, as illustrated in Figure 8.6 (c) and (d). The SrO islands appear as places where the unit-cell steps are bowed outwards in Figure 8.6 (c), and the fact that they are most likely of a different composition than the surrounding surface is obvious in the phase contrast of Figure 8.6 (d). To test how TTIP reacts to form  $\text{SrTiO}_3$  these substrates were used for a test growth. They were heated to  $T_{\text{sub}} = 800$  °C in  $1 \times 10^{-6}$  Torr  $\text{O}_2$  and exposed to TTIP flux for five minutes, which was kept constant between the two samples. Additional samples with similar starting morphology to the ones shown in Figure 8.6 (a-d) were also heated to the same  $T_{\text{sub}}$  for the same amount of time that growth occurred and cooled to provide a control experiment. The control substrates did not differ in appearance after heating in vacuum, and no major changes in

composition or surface morphology were observed.

After exposure to TTIP the substrates' morphology was investigated again using AFM. The resulting surfaces are shown in Figure 8.6 (e-h). The  $\text{TiO}_x$ -rich terminated substrates, Figure 8.6 (e) and (f), showed no obvious change, while the substrates with SrO islands had changed significantly, as seen in Figure 8.6 (g) and (h). The resulting morphology is much more regular, and resembles a step-terrace geometry with regularly spaced jagged edges and small pits or voids were also observed on the step-terraces. While it is impossible to determine the chemical composition from AFM alone, it is reasonable to hypothesize that the TTIP reacted with the SrO islands to change their morphology to something more closely resembling partial unit-cell coverage of a step-growth type growth mechanism. The roughness of these samples was changed very little from their pre-deposition measurement and was also very similar to the unchanged  $\text{TiO}_x$ -rich substrates. This indicates that a layer-by-layer growth mode is more reasonable, although the voids indicate that it's not necessarily the step edges that form the active sites where layers of  $\text{SrTiO}_3$  are propagated.

These samples confirm that, under the correct conditions, TTIP is much more likely to react with SrO already present on the sample surface rather than to deposit and grow  $\text{TiO}_2$ . This gives credence to the mechanism discussed earlier where the chemical functionality of the TTIP metalorganic source allows it to react in an adsorption-controlled manner with Sr during growth of  $\text{SrTiO}_3$  using HMBE. Conducting simple experiments of this nature and combining them with the in situ X-ray diffraction capabilities of the chamber the metalorganic delivery system was designed for can elucidate details of growth like these for a variety of systems.

### 8.3.4 Growth of $\text{Sr}_2\text{TiO}_4$ and $\text{TiO}_2$ (anatase)

Most oxide materials of technological relevance are members or derivatives of the perovskite,  $\text{ABO}_3$ , structure family. To grow films of these materials, it is critical that the gas source supplied by HMBE can be used in conjunction with traditional effusion cell solid metal sources. To demonstrate this ability, the Sr-Ti-O system of oxides was chosen due to its structural flexibility and the abundance of information available on its properties and phases. Growth of the binary oxide,  $\text{TiO}_2$ , and the ternary oxide,  $\text{SrTiO}_3$ , have both been demonstrated. However, there are many other structural members of the Sr-Ti-O oxide family. The following data concerns growth of the endmember Ruddlesden-Popper phase,  $\text{Sr}_2\text{TiO}_4$ .

Films of Sr-Ti-O were grown on  $\text{SrTiO}_3$  (0 0 1) substrates prepared to have  $\text{TiO}_x$ -rich surfaces. Out-of-plane scattering and in situ diffraction of the (0 0  $\frac{1}{2}$ ) condition for two selected films grown at identical TTIP flux and varying Sr flux conditions can be seen in Figure 8.7. In Figure 8.7 (a) and (b), the r. l. u's are referenced to room temperature  $\text{SrTiO}_3$  (0 0 1) having a lattice constant of 0.391 nm. All films were grown under identical environmental conditions with  $T_{\text{sub}} = 800$  °C, with a background pressure of  $1 \times 10^{-6}$  Torr  $\text{O}_2$ , and a line pressure of 55 mTorr TTIP (or a pressure of  $9 \times 10^{-6}$  Torr according to the growth chamber ion gauge). Varying the Sr flux delivered to the MBE growth chamber allowed the films grown to be  $\text{Sr}_2\text{TiO}_4$ -rich as in Figure 8.7 (a) and (c) and mixed  $\text{Sr}_2\text{TiO}_4$  and anatase  $\text{TiO}_2$  as in Figure 8.7 (b) and (d) in composition [287, 288]. The film shown in Figure 8.7 (a) and (c) was grown with a Sr flux of  $2.23 \times 10^{12}$  atoms/cm<sup>2</sup>•sec, while the film shown in Figure 8.7 (b) and (d) had a Sr flux of half that value,  $1.12 \times 10^{12}$  atoms/cm<sup>2</sup>•sec. All films grown displayed the orientation of  $\text{Sr}_2\text{TiO}_4$  and anatase  $\text{TiO}_2$  on  $\text{SrTiO}_3$  of (1 0 0)  $[1\ 0\ 0]_{\text{film phase}} \parallel (1\ 0\ 0)\ [1\ 0\ 0]_{\text{SrTiO}_3}$ . The thickness of each film was calculated

from the full-width half-maximum of the film peaks and found to be 27.5 nm for the film shown in Figure 8.7 (a) and (c), while the one shown in Figure 8.7 (b) and (d) was 13.8 nm thick.

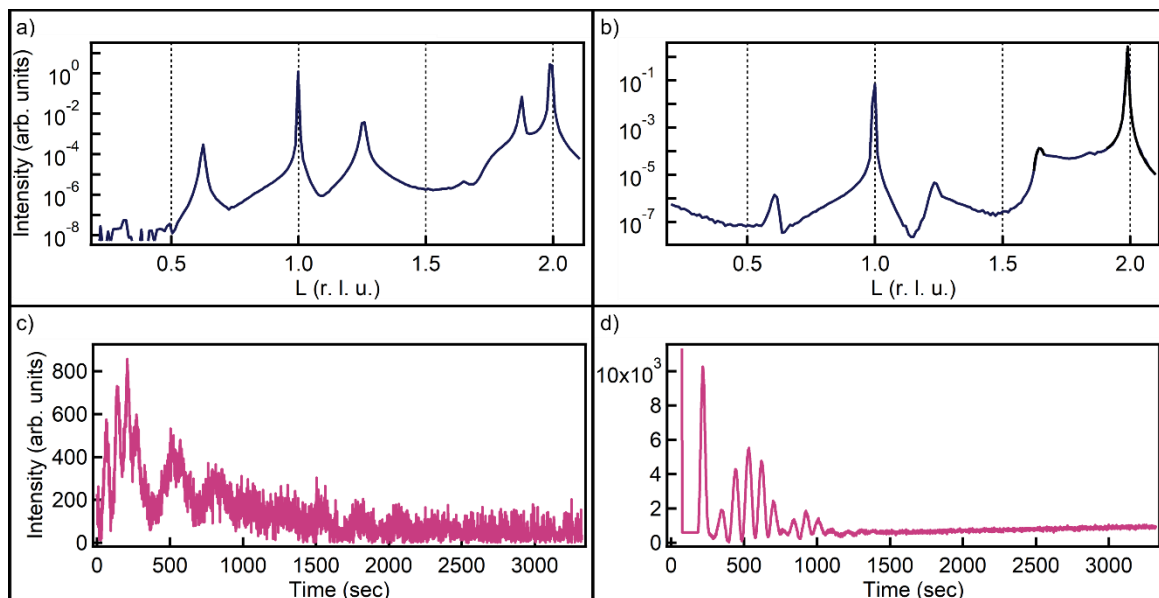


Figure 8.7 Scattering along the  $(0\ 0\ L)$  direction (a, b) of Sr-Ti-O oxide films on  $\text{SrTiO}_3$   $(1\ 0\ 0)$  showing  $\text{Sr}_2\text{TiO}_4$ -rich (a), and mixed  $\text{Sr}_2\text{TiO}_4$  and anatase  $\text{TiO}_2$  (b). Scattered intensity measured at the  $H\ K\ L = 0\ 0\ \frac{1}{2}$  (c, d) for the film whose CTR is shown in the frame directly above. All films were grown at  $800^\circ\text{C}$ .

Both films in Figure 8.7 show oscillations associated with the growth at the anti-Bragg position  $(0\ 0\ \frac{1}{2})$ . As both are plotted on the same timescale, it is clear that in both cases there are initial oscillations that die off over time. However, the oscillations are very different in character, with those in Figure 8.7 (d) having a “beating” pattern. In RHEED measurements, “beating” patterns are often associated with non-stoichiometry. However, in this case, as the “beating” gives a second periodicity to the oscillation pattern (it can be imagined as oscillations with both a primary and secondary period) it is more likely that this can be attributed to competition between two phases of material present in this film-  $\text{Sr}_2\text{TiO}_4$  and anatase  $\text{TiO}_2$ . The in situ scan in Figure 8.7 (c) are notably more noisy than those in Figure 8.7 (d), most likely due to the overall difference in

scattered X-ray intensity.

Films of Sr-Ti-O were also grown on LSAT (0 0 1) substrates. Out-of-plane scattering and in situ diffraction of the (0 0  $\frac{1}{2}$ ) condition for two selected films grown at identical TTIP flux and varying Sr flux conditions can be seen in Figure 8.8. In Figure 8.8 (a) and (b), the r. l. u. are referenced to room temperature LSAT (0 0 1) having a lattice constant of 0.387 nm. All films were grown under identical environmental conditions, the same as those used for the growths on SrTiO<sub>3</sub> (0 0 1) with  $T_{sub} = 800$  °C, a background pressure of  $8 \times 10^{-6}$  Torr O<sub>2</sub>, and a line pressure of 30 mTorr TTIP (or a pressure of  $2 \times 10^{-6}$  Torr according to the growth chamber ion gauge). Varying the Sr flux delivered to the MBE growth chamber allowed the films grown to be Sr<sub>2</sub>TiO<sub>4</sub>-rich as in Figure 8.8 (a) and (c) and anatase TiO<sub>2</sub>-rich as in Figure 8.8 (b) and (d) in composition. The film shown in Figure 8.8 (a) and (c) was grown with a Sr flux of  $1.37 \times 10^{12}$  atoms/cm<sup>2</sup>•sec, while the film shown in Figure 8.8 (b) and (d) had a Sr flux of  $1.12 \times 10^{12}$  atoms/cm<sup>2</sup>•sec. All films grown displayed the same orientation of Sr<sub>2</sub>TiO<sub>4</sub> and anatase TiO<sub>2</sub> on LSAT of (1 0 0) [1 0 0]<sub>film</sub> phase || (1 0 0) [1 0 0]<sub>LSAT</sub>. The thickness of each film was calculated from the full-width half-maximum of the film peaks and found to be 10.7 nm for the film shown in Figure 8.8 (a) and (c), while the one shown in Figure 8.8 (b) and (d) was 3.6 nm thick.

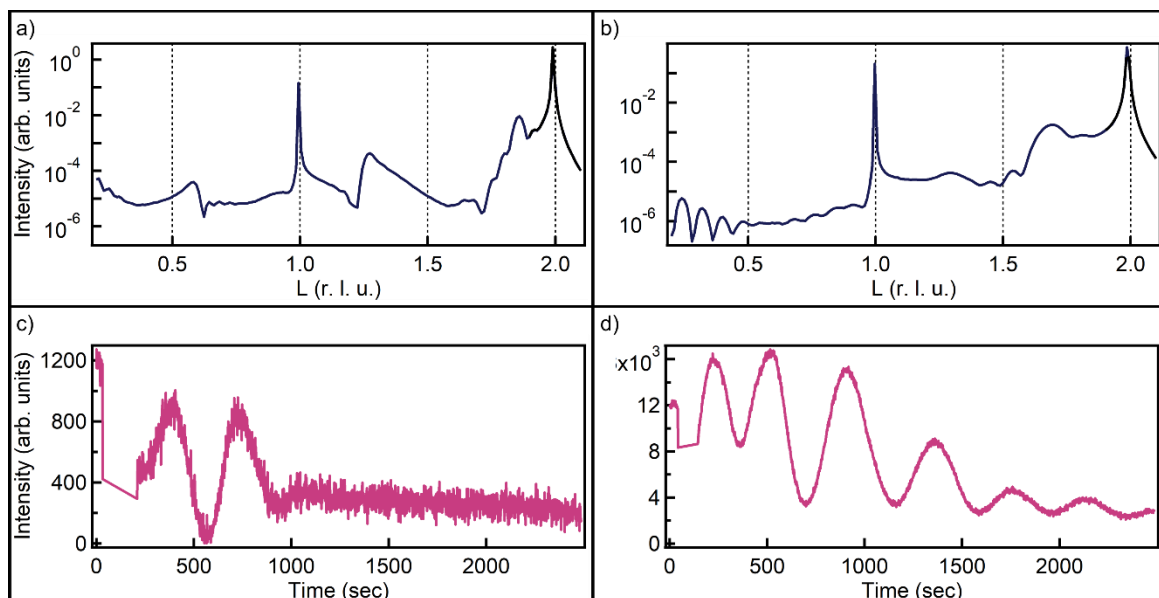


Figure 8.8 Scattering along the  $(0\ 0\ L)$  direction (a, b, c) of Sr-Ti-O oxide films on  $\text{SrTiO}_3$   $(1\ 0\ 0)$  showing  $\text{Sr}_2\text{TiO}_4$ -rich (a), and anatase  $\text{TiO}_2$ -rich (b) films. Scattered intensity measured at the  $H\ K\ L = 0\ 0\ \frac{1}{2}$  (c, d) for the film whose CTR is shown in the frame directly above. All films were grown at  $800^\circ\text{C}$ .

Both of the films in Figure 8.8 show oscillations associated with growth at the anti-Bragg position  $(0\ 0\ \frac{1}{2})$ . The oscillations for the sample shown in Figure 8.8 (d) last for the duration of the growth, whereas those in c) die off more quickly. Thickness fringes are also visible in the sample shown in Figure 8.8 (b), indicating that it is well-ordered. This sample is primarily made up of anatase  $\text{TiO}_2$ , as very little diffraction from any  $\text{Sr}_2\text{TiO}_4$  was observed, and the persistence of oscillations indicates that there was little competition between phases in growth of this sample. The differences in noise in the in situ scattered X-ray intensity in Figure 8 (c) and (d) are attributed to the differences in overall intensity.

This set of growth results indicates that the hybrid gas delivery system can be used in tandem with the typical effusion cell solid metal sources of the MBE chamber to which it is coupled to investigate growth conditions that have not been thoroughly characterized in the past.

The author of this thesis is unaware of any reports of  $\text{Sr}_2\text{TiO}_4$  films grown using HMBE, and in particular where the competing material phases are  $\text{Sr}_2\text{TiO}_4$  and anatase  $\text{TiO}_2$ .

#### 8.4 Discussion

This HMBE system is capable of growing materials by itself as a stand-alone delivery system for metalorganics (demonstrated with growth of  $\text{TiO}_2$ ) or coupled with traditional MBE effusion cells ( $\text{SrTiO}_3$  growth). The findings for both growths agree with previous reports both in terms of the identified growth conditions, the quality of films produced, and the properties (morphology, lattice parameter) of those films [245, 265].

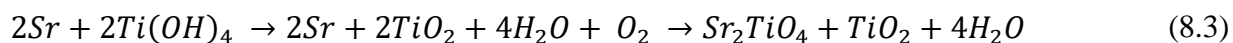
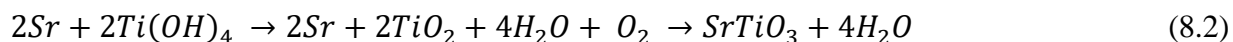
The mechanism of the TTIP reaction with SrO has also been investigated. While these experiments were not conducted with the aid of in situ X-ray diffraction or the collection of CTRs, they still shed light on the processes occurring. They agree with proposed mechanisms, although they give no specific indication as to whether the actual process occurring during Sr-Ti-O growth by HMBE relies on reaction with already-oxidized SrO islands or whether TTIP can react with metallic Sr atoms on the surface. This is a possible area for future study, although the general assertion that the functional capability of the metalorganic source aids in its synthesis reaction holds based on the results found. Additionally, the idea that adsorption-limited growth is occurring when conditions of A:B flux are correct is also supported by the lack of reaction of a small dosage of TTIP observed on the Ti-rich  $\text{SrTiO}_3$  (0 0 1) surface.

Possibly the most interesting set of growth studies were those yielding films of  $\text{Sr}_2\text{TiO}_4$  and anatase  $\text{TiO}_2$ . These films were observed to be rich in either of the two phases or have mixed character. These findings at first seem similar to those in Chapter Six where the Sr-Co-O system is discussed. One would assume that having a film that is  $\text{Sr}_2\text{TiO}_4$  rich or  $\text{TiO}_2$  rich would indicate



that the Sr:Ti ratio is heavily skewed towards one of the two cations. In that case, a perfect Sr:Ti ratio of 1:1 should yield films of SrTiO<sub>3</sub>. However, since films of Sr<sub>2</sub>TiO<sub>4</sub> mixed with TiO<sub>2</sub> are observed (and seem to contain no portion of SrTiO<sub>3</sub>) this argument doesn't capture the full picture.

When TTIP and Sr metal react together, different phases can be formed; one possibility is that SrTiO<sub>3</sub> will be grown while another is that some mixture of Sr<sub>2</sub>TiO<sub>4</sub> and anatase TiO<sub>2</sub> will grow. The two can be compared by looking at the two different reaction paths that could be followed during this synthesis. The main decomposition product of the TTIP precursor was calculated according to thermodynamic and Density Functional methods to be Ti(OH)<sub>4</sub> up to a temperature of 1000 K, covering the range of the synthesis reported herein [289]. The two relevant equations are shown in Equations 8.2 and 8.3.



Since all the reactants and some of the products are identical between these two equations, a few things can be gleaned from Equations 2 and 3. First, the proportion of oxygen consumed in these reactions is identical no matter the products, so preference for one reaction over the other is not expected to depend on oxygen concentration or activity in this system, unlike Sr-Co-O oxide synthesis. The second is that these equations can be more readily compared by preserving only the relevant different products. The relevant reaction is re-written in Equation 8.4.



Thermodynamic values can be located for the species in this equation and calculated at

different temperatures to determine the Gibb's free energy. Values for this calculation are shown in Table 8.1.

Table 8.1. Enthalpy of Formation (in  $\text{kJ}\cdot\text{mol}^{-1}$ ), Entropy (in  $\text{J}\cdot\text{K}^{-1}\cdot\text{mol}^{-1}$ ), for  $\text{TiO}_2$ ,  $\text{SrTiO}_3$ ,  $\text{Sr}_2\text{TiO}_4$ , and the Reaction in Equation 8.4 as well as Gibb's Free Energy of Equation 8.4 (in  $\text{kJ}\cdot\text{mol}^{-1}$ )

T (K)	TiO <sub>2</sub> (anatase) [234]		SrTiO <sub>3</sub> [290]		Sr <sub>2</sub> TiO <sub>4</sub> [290]		Equation 8.4 Reaction		
	$\Delta H_f^\circ$	S	$\Delta H_f^\circ$	S	$\Delta H_f^\circ$	S	$\Delta H_f^\circ$	S	$\Delta G_f^\circ$
298	-938.7	49.8	-1672.3	108.8	-2287.4	159	118.6	-8.8	121.2
300	-938.6	50.2	-1672.2	109.4	-2287.1	159.9	118.6	-8.7	121.3
400	-932.6	67.4	-1661.5	139.9	-2271.7	204.0	118.8	-8.2	122.1
500	-926.0	82.2	-1650.0	165.6	-2255.1	241.1	119.0	-7.9	122.9
600	-919.0	94.9	-1638.0	187.5	-2237.9	272.6	119.2	-7.6	123.7
700	-911.9	105.9	-1625.7	206.5	-2220.2	299.8	119.4	-7.2	124.4
800	-904.6	115.7	-1613.2	223.2	-2202.2	323.8	119.6	-6.9	125.1
900	-897.1	124.4	-1600.5	238.2	-2183.9	345.3	119.9	-6.6	125.8
1000	-889.6	132.3	-1587.6	251.7	-2165.5	364.7	120.1	-6.3	126.5
1100	-882.0	139.6	-1574.7	264.0	-2146.9	382.5	120.4	-6.0	127.1
1200	-874.4	146.2	-1561.6	275.4	-2128.1	398.8	120.7	-5.8	127.7
1300	-866.8	152.3	-1548.5	285.9	-2109.2	413.9	121.0	-5.6	128.2
1400	-859.1	158.0	-1535.3	295.7	-2090.2	428.0	121.3	-5.3	128.8
1500	-851.4	163.3	-1522.0	304.8	-2071.0	441.3	121.6	-5.1	129.3
1600	-843.8	168.2	-1508.7	313.5	-2051.7	453.7	121.9	-5.0	129.8
1700	-836.0	172.9	-1495.2	321.6	-2032.3	465.5	122.1	-4.8	130.3
1800	-828.3	177.3	-1481.7	329.3	-2012.8	476.7	122.4	-4.7	130.8

The calculated values indicate that the  $\text{SrTiO}_3$  phase would be favored for all calculated temperatures as the Gibb's free energy of this reaction is always positive. While this is consistent with the results where  $\text{SrTiO}_3$  films were successfully grown on LSAT substrates presented earlier in the chapter at similar substrate temperatures, it does not help explain the  $\text{Sr}_2\text{TiO}_4$  and anatase  $\text{TiO}_2$  phase films observed.

To explain the observations another possibility relying on Ostwald's principle [291] and differences in nucleation between the possible phases serves well. Ostwald's principle implies that

it is not always the most thermodynamically stable phase which nucleates first. Instead, it is the state that is closest in energy to the reactants (i.e., the one with the lowest energy barrier). Explanations for this include that Ostwald's principle minimizes the production of entropy in a system [292]. It can also be explained as a consequence of irreversible thermodynamics paired with structural effects- phases more similar in structure to the precursors are more likely to form first [293]. While the theoretical explanation for this phenomenon may remain incomplete, and it is uncertain which explanation applies most readily to the growth presented herein, it is a phenomenon that has nevertheless been observed experimentally in many cases [294-297]. If Equation 8.2 is studied more closely, it is evident that one of the final reaction products,  $\text{TiO}_2$ , is a product of decomposition of the  $\text{Ti}(\text{OH})_4$  species from the TTIP precursor. This implies that  $\text{TiO}_2$  is a natural intermediate state in this reaction. Since  $\text{TiO}_2$  is present in the final film, the change in energy from the reactants to form the combination of  $\text{Sr}_2\text{TiO}_4$  and  $\text{TiO}_2$  is surely less than the change to form the more stable  $\text{SrTiO}_3$  phase.

This thermodynamic explanation can additionally be coupled with a kinetic one. If the  $\text{TiO}_2$  (or the  $\text{Sr}_2\text{TiO}_4$ ) phase is nucleated early on in the reaction, perhaps due to an initial excess of TTIP or a concentration of TTIP/Sr in the chamber that favors its nucleation over that of  $\text{SrTiO}_3$ , then this will likely influence the phase growth of the entirety of the film. Similar effects have been observed in MBE growth of GaN of different structural phases [298].

Determining the exact cause behind the observation of the  $\text{Sr}_2\text{TiO}_4$  and anatase  $\text{TiO}_2$  films rather than  $\text{SrTiO}_3$  would require additional experimentation, and factors such as the deposition process (how valves and shutter are opened, etc.) as well as additional environmental conditions could be investigated.

## 8.5 Conclusions

The assembled HMBE system has been used to grow a variety of different oxide compounds in the Sr-Ti-O family. Both binary ( $\text{TiO}_2$ ) and ternary ( $\text{SrTiO}_3$ ) oxides have been produced, as well as a member of the Ruddlesden-Popper series ( $\text{Sr}_2\text{TiO}_4$ ). In addition, the reaction mechanism of TTIP metalorganic precursor has been investigated. The in situ X-ray scattering data collected at the anti-Bragg position ( $0\ 0\ \frac{1}{2}$ ) has already revealed information about the different films grown and could be compared with RHEED studies to improve understanding of a variety of syntheses.

Growth with the HMBE clearly relies, in part, on the functionality of the supplied metalorganic species. It is also may be affected by aspects such as the delivery process itself, so perfecting the control schemes and developing reliable standard operating procedures is vital to replicating experimental results with this deposition equipment.

The additional degree of freedom that the HMBE system provides in delivering a different kind of source material allows for X-ray in situ studies to be done on a wide variety of oxide materials and insight to be gained both in reference to oxide growth and also regarding metalorganic synthesis.

In addition to the areas for future study mentioned in this chapter, investigation with different source materials (e.g., vanadium-containing sources) or the delivery of more than one metalorganic during a given synthesis are exciting areas of future investigation possible with this system.

## CHAPTER 9

### **Ongoing and Future Work**

The work discussed so far has all been completed and published. Explanations have been proposed for the observations made. However, there are areas where either work was begun on related projects or where promising future work could be completed building off of the research presented herein. In particular, there are two cases discussed in this chapter where ongoing and future work are worth pursuing.

## **9.1 ( $5 \times 5$ ) Reconstruction on $\text{SrTiO}_3$ (1 1 1)**

The case of a particularly large ( $5 \times 5$ ) reconstruction observed on  $\text{SrTiO}_3$  (1 1 1) presents a good opportunity to apply the techniques discussed in previous chapters (Chapters Four and Five). This work was begun before the comprehensive explanations in Chapter Four were formulated and was not finished due to lack of computation time. However, hypothetical structures for a ( $5 \times 5$ ) reconstruction are proposed in this chapter. These were identified after an initial round of calculations eliminated less-likely structures. The structures proposed could be used to continue refinement of this large reconstruction. This work was done in collaboration with colleagues at the University of Oxford in Oxford, UK, specifically Prof. Martin Castell, Dr. Bruce C. Russell, and Prof. Shams ur Rahman.

### **9.1.1 Introduction**

The common substrate material,  $\text{SrTiO}_3$ , displays a multitude of reconstructions already discussed in Chapters Four and Five. The application of Pauling's rules has also been demonstrated. They provide insight into solving reconstructions on oxide surfaces. Among the solved reconstructions is a series of ( $n \times n$ ) reconstructions of increasing size [49, 57]. Both ( $5 \times 5$ ) and ( $6 \times 6$ ) members have been experimentally observed but their structure is still unknown. Since these are double Ti-layered reconstructions on  $\text{SrTiO}_3$  (1 1 1) (as opposed to the single-layered Ti-

reconstructions in Chapter Five), applying Pauling's rules to this case results in additional complexity. With a large unit cell and a double-layered reconstruction there are a large number of possible structures generated, even when following Pauling's rules.

These large reconstructions also present a computational challenge. In the WIEN2k package used in these investigations [154], the rate-limiting step is a diagonalization of a  $(M \times M)$  matrix. Slab unit-cell constructions of the  $(5 \times 5)$  structure can contain anywhere from 80-110 unique atoms. For a unit cell containing 80 unique atoms related by symmetry operations, this can correspond to a matrix of  $(M \times M)$  size where  $M = 90,000$ . This generally leads to a case where a large amount of memory is required on cores utilized for a calculation.

Even relatively small unit-cell constructions (e.g. ten atoms) contain thousands of variables in a DFT calculation. These variables fall into two types: those for electron density, and those for atomic positions. Luckily, using an iterative DFT method often allows convergence of these calculations within 20-40 iterations rather than thousands. This is related to the fact that convergence depends on the number of clusters of eigenvalues as well as the width of clusters of an underlying Jacobian when a Quasi-Newton method is utilized [195, 299-302]. The number of clusters of electron density depends on dielectric band structure, in general containing a limited number of clusters and scaling weakly with the number of atoms [303-309]. The width of clusters may or may not scale in the same fashion. Though this method eliminates the double-loop common in most DFT calculations by combining the electronic and atomic clusters, its performance with increasingly large unit cell sizes is not yet fully investigated. It is possible that these calculations scale sub-linearly with the number of atoms.

In addition, the utilization of hybrid functionals includes some fraction of Hartree-Fock

exchange on specific electrons, namely those with *d* or *f*-orbital character [310]. However, including this incurs additional computation expense and a balance of accuracy and practicality must be considered. The efforts presented herein to solve the  $(5 \times 5)$  reconstruction deal with these challenges, and a strategy incorporating multiple rounds of structure generation, DFT relaxation, and comparison with experimental STM is presented as a way to approach this and similar investigations. Different computation parameters at different stages of the investigation as well as different unit-cell sizes are used to reduce cost and provide a practical guide to tackling DFT calculations of this scale. This case serves as an example for not only approaching problems of this scale but could also provide a performance benchmark for the WIEN2k package (or any other utilized to perform calculations).

### **9.1.2 Methods**

#### **9.1.2.1 STM Measurements**

Epi-polished single crystal  $\text{SrTiO}_3$  (1 1 1) with 0.5 wt% Nb-doping (to provide conductivity for STM measurement) from PI-KEM, UK were prepared in a JEOL JSTM4500xt ultrahigh vacuum chamber. Samples were sputtered in  $\text{Ar}^+$  for 20 minutes at 0.5 keV in a UHV base pressure of  $10^{-8}$  Pa. For STM imaging, an etched tungsten tip was used at room temperature. Images were taken at constant current [57].

#### **9.1.2.2 DFT Calculations**

The WIEN2k code [154] was used for all DFT calculations. Both the generalized gradient approximation, in this case PBEsol [152], and the revTPSS method [193] were investigated. All *d*-orbital electrons of Ti atoms were treated with an on-site exact exchange of 0.5, similar to previous investigations [41].



Parameters for all calculations were standardized to allow comparison across unit cell sizes. The lowest-energy unit-cell size for bulk  $\text{SrTiO}_3$  was determined separately for each of the calculation types (PBEsol vs. revTPSS) and all unit cells for a given reconstruction were adjusted to match the in-plane dimensions. Slabs were constructed using a  $(1 \times 1 \times 7)$  supercell where at least 1.6 nm of vacuum was present between surfaces. DFT calculations were performed in two rounds, where the initial screening used parameters that were optimized for speed rather than accuracy. For this round, fewer layers of bulk  $\text{SrTiO}_3$  (1 1 1) were modelled. The resulting slab unit-cells contained 80-85 unique atoms. First-round calculations had muffin-tin radii of 1.50, 1.68 and 2.00 bohr radii for O, Ti and Sr respectively. A second, more accurate, round of calculations was performed with the muffin-tin atomic radii of 1.55, 1.71, and 2.21 bohrs for O, Sr, and Ti atoms, respectively. For the second round, additional layers of bulk  $\text{SrTiO}_3$  (1 1 1) were added. The resulting slab unit-cells contained 100-105 unique atoms. For all calculations, a Brillouin-zone reciprocal space sampling equivalent to a  $(4 \times 4)$  in-plane mesh for a  $(1 \times 1)$  cell on (1 1 1) was used with an  $r^*k_{\text{max}}$  of 4.75 for the first round and 6.20 for the second round. A quasi-Newton algorithm [195] was used to converge atomic positions and electron density, and a convergence better than 0.01 eV/ $(1 \times 1)$  was achieved. The surface energy per  $(1 \times 1)$  unit cell, the main quantity reported in this investigation, was calculated according to Equation 3.6, described earlier. Use of this method yielded an overall estimated error of 0.05 eV/ $(1 \times 1)$ .

### 9.1.2.3 STM Simulation

Relaxed low-energy structures found using DFT calculations were compared to experimental STM using STM simulations based on a modified Tersoff-Hamann approximation [124]. Additional information about this simulation technique can be found in Section 3.2.2.

### 9.1.3 Results

#### 9.1.3.1 STM

All experimental STM images were kindly provided by collaborators in the Castell group at Oxford University. Experimental STM images of the  $(5 \times 5)$  reconstruction revealed features of their structure as well as the surfaces they occupied. Large flat terraces with little disorder were observed. Terraces had step edge heights of  $0.224 \pm 0.12$  nm, corresponding to the  $d_{111}$  lattice parameter of  $\text{SrTiO}_3$  (1 1 1). Step edges had preferential alignment along the  $\langle 110 \rangle$  lattice directions. On some samples or regions of a given sample, both a  $(5 \times 5)$  and a  $(6 \times 6)$  reconstruction were observed in neighboring domains. The reconstruction was observed to have one mirror plane and 3-fold symmetry. The periodicity of the reconstruction was measured as  $2.70 \pm 0.12$  nm, leading to the  $(5 \times 5)$  assignment. This was confirmed with LEED, which produced a characteristic pattern for the reconstruction [57]. Two different STM images of observed  $(5 \times 5)$  reconstructed areas are shown in Figure 9.1.

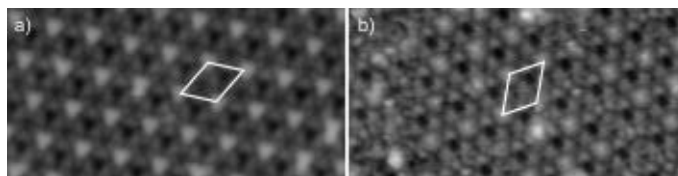


Figure 9.1 STM images showing the  $(5 \times 5)$  reconstruction on different samples (a) and (b) taken at 2.6V bias and 0.2 nA tunneling current. Both STM are  $24.2 \times 12.2$  nm<sup>2</sup> in area.

#### 9.1.3.2 Structure Generation - First Round

From the STM, the space group  $p\bar{3}m1$  was assigned to represent the observed symmetry. The integer-multiple size of the unit cell and the mirror-plane symmetry are similar to those observed in previously-solved  $(3 \times 3)$  and  $(4 \times 4)$  reconstructions. Some features of the STM, shown in Figure 9.2, are also similar.

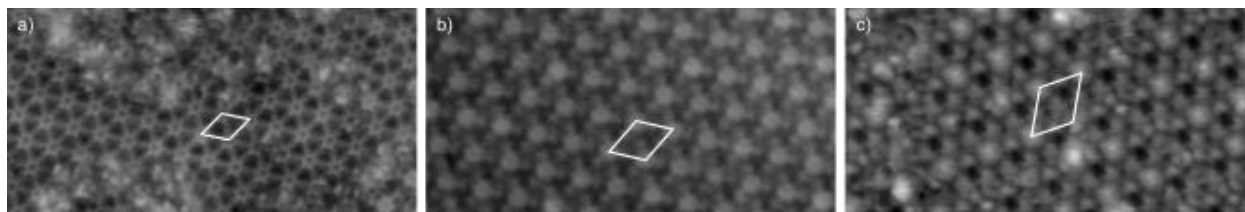


Figure 9.2 STM images showing the  $(3 \times 3)$  reconstruction (a) taken at 2.0V bias and 0.4 nA tunneling current, the  $(4 \times 4)$  (b) taken at 2.0V bias and 0.5 nA tunneling current, and the  $(5 \times 5)$  (c) taken at 2.6V bias and 0.2 nA tunneling current. All STM are  $24.2 \times 12.2 \text{ nm}^2$  in area.

The STM of the reconstructions shown in Figure 9.2 all have similar features. They are made up of a bright ring-like feature, easily observed in Figure 9.2 (b). Between these ring-like features are bright connecting lines, creating a pattern of rings connected to each other by six bright lines. Due to these similarities, the structures of the  $(3 \times 3)$  and  $(4 \times 4)$  reconstructions, along with the considerations of Pauling's rules (discussed in Chapter Four) were taken into account when generating hypothetical structures. For this structure, an underlying layer of  $\text{TiO}_5$  and  $\text{TiO}_6$  units, topped with an outer layer of  $\text{TiO}_4$  tetrahedra was considered. This was chosen for its agreement with the  $(3 \times 3)$  and  $(4 \times 4)$  reconstructions. Since this is a large unit-cell, not all possible structures could be generated easily. Only those that matched the features of similar, smaller reconstructions and the STM intensity data were generated. Additionally, the STM data only provide accurate guidance for atomic placements in the outermost  $\text{TiO}_x$  layer, in this case the  $\text{TiO}_4$  tetrahedra. As such, the structure of the underlying  $\text{TiO}_5$  and  $\text{TiO}_6$  layer is less certain, and a number of different possible motifs were generated for calculations.

### 9.1.3.3 DFT Results - First Round

Computation parameters for the initial round of structures were optimized to improve the speed of calculation as a large number of possibilities were considered. In these calculations, no portion of exact exchange was used to reduce computation cost for the large unit-cells.

Additionally, fewer layers of bulk  $\text{SrTiO}_3$  (1 1 1) were included, thereby reducing the total number of atoms in a unit cell to roughly 80-85 unique positions. The other parameters used are outlined in Section 9.1.2.2. All the structures were relaxed and surface energies were calculated using DFT. The same convex hull construction discussed in Section 5.3.3 was calculated and is shown below in Figure 9.3.

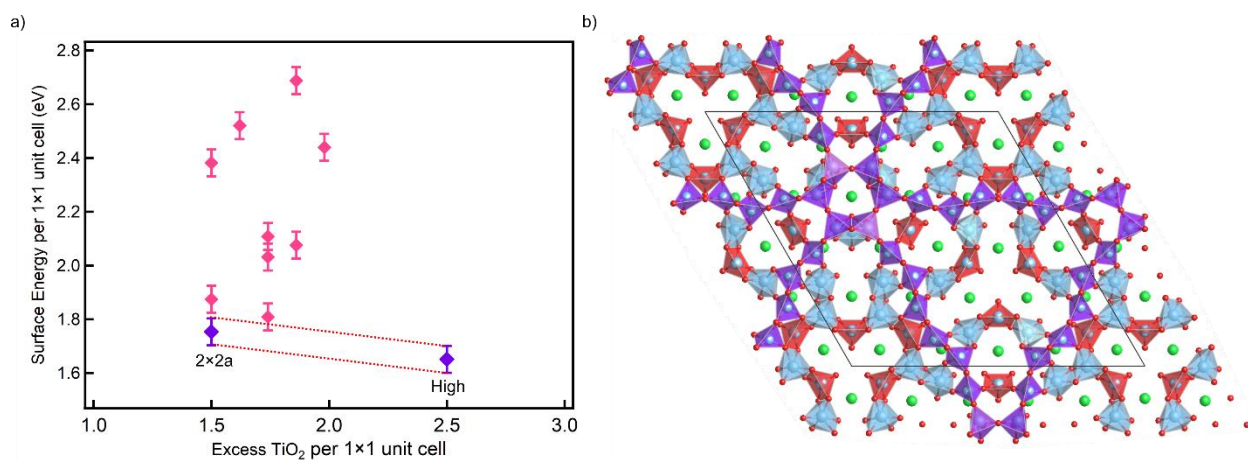


Figure 9.3 (a) Surface energies in eV/( $1 \times 1$ ) surface unit cell plotted versus excess  $\text{TiO}_2$  per ( $1 \times 1$ ). Results are from the PBEsol0 calculation, and the dotted lines show results from the convex hull construction. (b) Structure diagram of the low-energy solution with  $\text{TiO}_5$  octahedra in purple,  $\text{TiO}_6$  octahedra in blue,  $\text{TiO}_4$  tetrahedra in red, and Sr atoms in green.

The convex hull in Figure 9.3 differs in shape and calculated energy from the one shown in Figure 5.5 because no portion of exact-exchange was included for Ti  $d$ -orbital electrons. This shifts the reference calculations and leads to the observed differences. However, the principle of the convex hull still applies. As such, only structures that are close in energy to the purple endmembers in Figure 9.3 represent possible low-energy solutions. Of the twelve structures considered, only the one shown in Figure 9.3 (b) was close enough to the convex hull to warrant further investigation.

### 9.1.3.4 STM Simulation - First Round

The single low-energy structure found was used to simulate STM images. It was compared to experimental STM of the two different  $(5 \times 5)$  reconstructions. These results are shown in Figure 9.4 where (a) and (b) both show STM of the  $(5 \times 5)$  reconstruction that has similar features to the previously-solved  $(3 \times 3)$  and  $(4 \times 4)$ . The STM shown in Figure 9.4 (c) is much different.

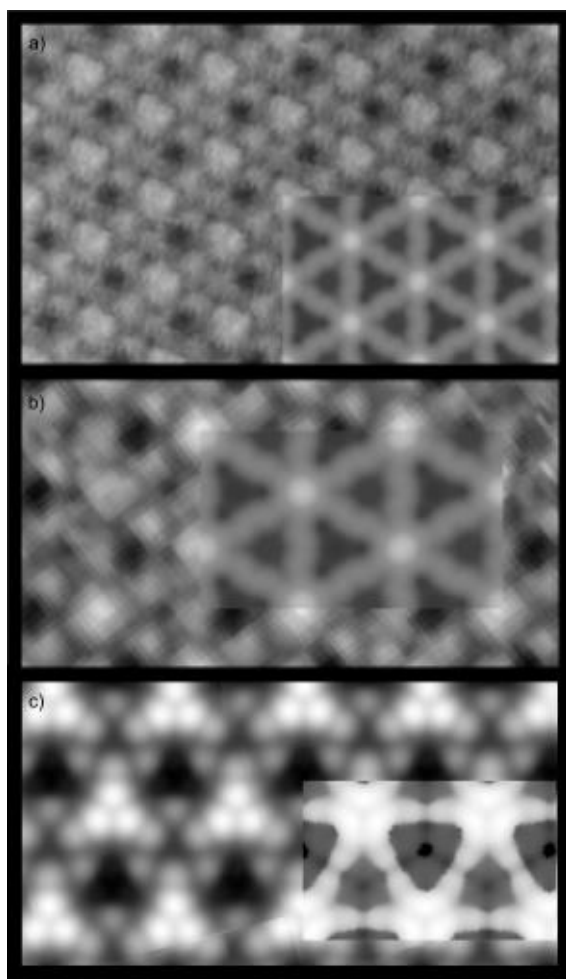


Figure 9.4 (a) STM image of  $(5 \times 5)$  reconstruction Type B, from Figure 9.1 (b), with overlaid simulated structure. (b) shows a zoomed-in view of this same STM and simulation. (c) STM image of  $(5 \times 5)$  reconstruction Type A, from Figure 9.1 (a), with overlaid simulated current structure. All STM taken at 2.6V bias and 0.2 nA tunneling current.

The STM simulations for this structure are a good match for the one shown in Figure 9.4

(a) and (b) but are a poor match for Figure 9.4 (c). The central ring-like feature of the structure matches all experimental STM data well, but the placement and shape of the connecting lines between rings does not agree with the STM of the second type of  $(5 \times 5)$  shown in Figure 9.4 (c). As such, a second round of structure generation and calculations is necessary to determine this structure.

#### **9.1.3.5 Round Two – Current Progress**

The first low-energy structure was used as a basis, along with Pauling's rules, for generating additional hypothetical reconstructions. These preserve the ring-like feature while varying the placement and shape of the connecting  $\text{TiO}_4$  tetrahedra chains between rings. Only preliminary calculations have been performed up to this point, so the additional structures generated have not been compared to the convex hull construction as of yet. The parameters for DFT relaxations of these structures follow those presented in Section 9.1.2.2, this time including the exact-exchange mentioned. These parameters are equivalent to those used in the earlier Section 5.2.2 where the RT7 and RT13 reconstructions were solved. More layers of bulk  $\text{SrTiO}_3$  (1 1 1) were also included, resulting in unit cells of roughly 100-105 unique atomic positions. Currently, some but not all of these structures have been partially relaxed, and it is impossible to determine which represent the best solutions from this iteration of hypothetical options.

#### **9.1.4 Future Directions**

The second round of generated structures should be relaxed, via DFT, using the parameters outlined in Section 9.1.2.2. If any of these are close to the convex hull they can be considered as possible solutions. STM simulations should be performed to compare them to experiment. If one of these structures is a good match to the experimental STM in Figure 9.4 (c), then it should be

considered the second solution for the  $(5 \times 5)$  reconstruction. If none of the low-energy solutions are good matches in terms of the STM, it may be worth simulating STM of the higher-energy hypotheses to determine whether or not they have structural features that might create a better match. Then, a third round of structural hypotheses can be generated to include the relevant features and the process continued as necessary to discover the solution.

When both solutions are determined, they should be compared to each other. The difference in energy between the two should be determined. It would be worthwhile to see whether the two solutions are related to each other and whether it might be possible for a phase transition to occur between the two under certain conditions. This could be calculated by considering the chemical potential in different preparation environments and the DFT results.

The structures and strategies investigated here could also serve as a guide for solving other large-scale reconstructions on  $\text{SrTiO}_3$  surfaces, in particular the observed  $(6 \times 6)$   $\text{SrTiO}_3$  (1 1 1) reconstruction. This author suspects that the  $(n \times n)$  series has common structural features and that a pattern relating these could be determined if enough of the structures are solved.

## **9.2 Superlattice Growth with Hybrid MBE**

Another area of ongoing and future work involves the hybrid MBE system built and tested by the author. While this system is mostly assembled, there are some additional hardware modifications that still need to be made to utilize its full capacity. Once this is finished additional materials can be grown with its hybrid capability. Of particular interest would be growth of superlattices or superstructures containing more than one species of transition metal cation. To do this, two different metalorganic sources would be utilized in one growth. This is the main area of future work proposed for the HMBE system discussed in this chapter.

### 9.2.1 Introduction

Hybrid MBE offers many advantages to conventional MBE and other thin-film deposition methods such as PLD, as discussed previously Chapters Seven and Eight. A hybrid MBE system was designed and constructed by the author to investigate the growth mechanisms and in situ structural evolution of HMBE-grown films. These experiments have already led to the initial results discussed in detail in Chapter Eight. However, there are many additional materials and superstructure architectures that this system's design allows the growth of. These materials move beyond simple Ti-containing oxides and are good candidates for future study.

As Chapter Eight mentions, materials with cations other than titanium have been grown via HMBE. One of the most promising of these is the vanadium-containing family of oxides, including  $\text{VO}_2$  and  $\text{SrVO}_3$ .  $\text{VO}_2$  is a material in which a metal-insulator transition can be induced near room temperature [22, 311, 312], a property that has been achieved reproducibly in films grown via HMBE [313]. This property makes  $\text{VO}_2$  attractive for use in detectors, terahertz devices, and charge oscillators for computing [314-316]. The perovskite  $\text{SrVO}_3$  is a conductive metal with strong electron correlation [269, 317], a property common to many transition metal oxides. Dimensional confinement in this material can be used to induce a metal-insulator transition [318-322]. Studies of the compound's structural changes during this transition and experiments on thin films indicate that defects play a large role in disrupting these properties [323-325]. As such, the desirable properties in both these materials depend on growth methods that lead to low defect concentrations in films [313], making HMBE a method of choice for their synthesis.

The challenges of reducing defects and understanding structural evolution in oxides with a phase diagram as complex as  $\text{VO}_2$  or  $\text{SrVO}_3$  makes studying this material with the capabilities of



in situ X-rays especially attractive. As such, this material was chosen as a candidate for future experiments using the HMBE system developed for use at the APS. To conduct these experiments, the current system must be further tested and the growth conditions for vanadium oxide materials determined with use of a VTIP precursor. The current progress towards these goals and the future steps that must be taken to investigate these materials further are outlined in the following sections.

### **9.2.2 Progress**

The design of the HMBE system was designed and assembled and its functionality in growing Ti-based materials has been explored in Chapters Seven and Eight. However, the design of this system includes two delivery lines, each utilizing a different metalorganic source. The second delivery line's piping has been cut and fasteners for it purchased. All the necessary parts in terms of valves, controllers, etc. have also been purchased. The temperature controller for the second line has also been assembled.

### **9.2.3 Future Directions**

To produce films with more than one cation material, both lines need to be assembled and their performance verified. To this end, the second delivery line, needs to be assembled and mounted to the HMBE frame. Heating tapes need to be installed and the function of valves with interfacing software (EPICs and LabVIEW™) needs to be verified. It can then be used to perform studies similar to those presented in Section 7.4.1, where the delivery of TTIP was verified and characterized.

The first precursor for use in these experiments will be VTIP. This precursor was chosen for a number of reasons. First, its chemical structure, shown in Figure 9.5 (a), has the same functional groups as that of TTIP, shown in Figure 9.5 (b). As such, its decomposition behavior is

expected to be similar to that of TTIP, allowing for incorporation of oxygen into films without the need for a background oxygen pressure during growth.

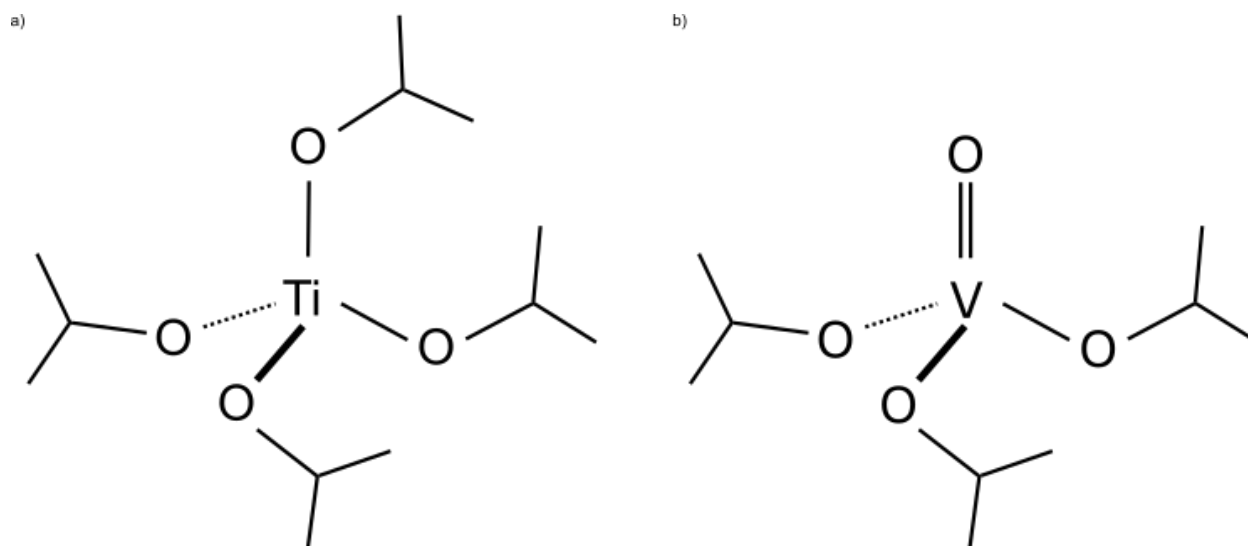


Figure 9.5 (a) Titanium (IV) tetraisopropoxide (TTIP) and (b) vanadium (V) triisopropoxide chemical structure.

VTIP also has a high vapor pressure even at low temperatures [326-328], making its use in a system with no carrier gas feasible. That being said, the first steps are to perform investigations similar to those outlined in Section 7.4.1, where an RGA was used to determine a precursor cracking product that reliably indicated the cation's presence.

Other researchers have performed investigations using VTIP as a precursor for HMBE growth of  $\text{VO}_2$ ,  $\text{SrVO}_3$ ,  $\text{LaVO}_3$ , and  $\text{CaVO}_3$  [248, 253, 269, 273, 274, 329, 330]. Since vanadium has a variable oxidation state and vanadium oxide has a complex phase diagram [331], oxygen stoichiometry control can be difficult in these materials. As such, molecular oxygen was supplied during their growth, indicating that the VTIP precursor alone may not be sufficient to produce fully oxidized films depending on the desired species. The referenced work provides a starting point for experimental growth conditions. This provides initial conditions that can be used for

testing the system both for functioning of the precursor delivery lines and for more complex material growths.

The goal of having two delivery lines is superlattice growth or film doping; any type of simultaneous or sequential deposition of two different cations requires a two-line system. The case of doping is arguably simpler as both sources can be delivered at different pressures to desired levels. This should serve as a starting place for novel material growth with the HMBE, as there is a lot of flexibility in producing films of different cation doping levels. To achieve this type of growth, especially in the case of superlattices, the switching of precursor lines must be investigated and an experimental procedure developed. If superlattices of high precision are desired, developing methods to determine a switching scheme similar to the shuttering schemes used in MBE is also necessary. These challenges should be the focus of future experiments in this area. Developing strategies to address these challenges will allow growth of a wide variety of materials with the hybrid MBE system.

## References

- [1] I. Grinberg, D.V. West, M. Torres, G. Gou, D.M. Stein, L. Wu, G. Chen, E.M. Gallo, A.R. Akbashev, P.K. Davies, J.E. Spanier, A.M. Rappe, Perovskite oxides for visible-light-absorbing ferroelectric and photovoltaic materials, *Nature*, 503 (2013) 509-512.
- [2] C. Sun, R. Hui, J. Roller, Cathode materials for solid oxide fuel cells: A review, *Journal of Solid State Electrochemistry*, 14 (2010) 1125-1144.
- [3] E.D. Wachsman, K.T. Lee, Lowering the temperature of solid oxide fuel cells, *Science*, 334 (2011) 935-939.
- [4] J. You, L. Meng, T.-B. Song, T.-F. Guo, Y. Yang, W.-H. Chang, Z. Hong, H. Chen, H. Zhou, Q. Chen, Y. Liu, N.D. Marco, Y. Yang, Improved air stability of perovskite solar cells via solution-processed metal oxide transport layers, *Nature Nanotechnology*, 11 (2016) 75.
- [5] R.K. Cavin, P. Lugli, V.V. Zhirnov, Science and engineering beyond Moore's law, *Proceedings of the IEEE*, 100 (2012) 1720-1749.
- [6] Y. Zhou, S. Ramanathan, Mott memory and neuromorphic devices, *Proceedings of the IEEE*, 103 (2015) 1289-1310.
- [7] G. Centi, S. Perathoner, Catalysis by layered materials: A review, *Microporous and Mesoporous Materials*, 107 (2008) 3-15.
- [8] Z. Feng, W.T. Hong, D.D. Fong, Y.-L. Lee, Y. Yacoby, D. Morgan, Y. Shao-Horn, Catalytic activity and stability of oxides: The role of near-surface atomic structures and compositions, *Accounts of Chemical Research*, 49 (2016) 966-973.
- [9] H. Jeon, W.S. Choi, M.D. Biegalski, C.M. Folkman, I.-C. Tung, D.D. Fong, J.W. Freeland, D. Shin, H. Ohta, M.F. Chisholm, H.N. Lee, Reversible redox reactions in an epitaxially stabilized  $\text{SrCoO}_x$  oxygen sponge, *Nature Materials*, 12 (2013) 1057-1063.
- [10] Y. Lin, J. Wen, L. Hu, R.M. Kennedy, P.C. Stair, K.R. Poeppelmeier, L. Marks, Synthesis-dependent atomic surface structures of oxide nanoparticles, *Physical Review Letters*, 111 (2013) 156101.
- [11] J.G. Mavroides, J.A. Kafalas, D.F. Kolesar, Photoelectrolysis of water in cells with  $\text{SrTiO}_3$  anodes, *Applied Physics Letters*, 28 (1976) 241-243.
- [12] J.T. Mefford, R. Xi, M.A. Artem, G.H. William, D. Sheng, M.K. Alexie, P.J. Keith, J.S. Keith, Water electrolysis on  $\text{La}_{1-x}\text{Sr}_x\text{CoO}_{3-\delta}$  perovskite electrocatalysts, *Nature Communications*, 7 (2016) 11053.
- [13] J. Suntivich, K.J. May, H.A. Gasteiger, J.B. Goodenough, Y. Shao-Horn, A perovskite oxide optimized for oxygen evolution catalysis from molecular orbital principles, *Science*, 334 (2011) 1383-1385.
- [14] T.K. Townsend, N.D. Browning, F.E. Osterloh, Nanoscale strontium titanate photocatalysts for overall water splitting, *ACS Nano*, 6 (2012) 7420-7426.
- [15] H.-J. Kim, J.-H. Lee, Highly sensitive and selective gas sensors using p-type oxide semiconductors: Overview, *Sensors & Actuators: B. Chemical*, 192 (2014) 607-627.
- [16] H.Y. Hwang, Y. Iwasa, M. Kawasaki, B. Keimer, N. Nagaosa, Y. Tokura, Emergent phenomena at oxide interfaces, *Nature Materials*, 11 (2012) 103-113.
- [17] J. Mannhart, D.G. Schlom, Oxide interfaces- An opportunity for electronics, *Science*, 327 (2010) 1607-1611.

- [18] J.M. Rondinelli, S.J. May, J.W. Freeland, Control of octahedral connectivity in perovskite oxide heterostructures: An emerging route to multifunctional materials discovery, *MRS Bulletin*, 37 (2012) 261-270.
- [19] A. Sawa, Resistive switching in transition metal oxides, *Materials Today*, 11 (2008) 28-36.
- [20] H. Takagi, H.Y. Hwang, An emergent change of phase for electronics, *Science*, 327 (2010) 1601-1602.
- [21] G. Wang, L. Zhang, J. Zhang, A review of electrode materials for electrochemical supercapacitors, *Chemical Society Reviews*, 41 (2012) 797-828.
- [22] Z. Yang, C. Ko, S. Ramanathan, Oxide electronics utilizing ultrafast metal-insulator transitions, *Annual Review of Materials Research*, 41 (2011) 337-367.
- [23] P. Zubko, S. Gariglio, M. Gabay, P. Ghosez, J.-M. Triscone, Interface physics in complex oxide heterostructures, *Annual Review of Condensed Matter Physics*, 2 (2011) 141-165.
- [24] T. Ishihara, Structure and properties of perovskite oxides, in: *Perovskite Oxide for Solid Oxide Fuel Cells*, Springer, 2009, pp. 1-16.
- [25] M.A. Peña, J.L.G. Fierro, Chemical structures and performance of perovskite oxides, *Chemical reviews*, 101 (2001) 1981-2018.
- [26] J.E.T. Andersen, P.J. Møller, Impurity-induced 900° C ( $2 \times 2$ ) surface reconstruction of SrTiO<sub>3</sub> (100), *Applied Physics Letters*, 56 (1990) 1847-1849.
- [27] H. Bando, Y. Aiura, Y. Haruyama, T. Shimizu, Y. Nishihara, Structure and electronic states on reduced SrTiO<sub>3</sub> (110) surface observed by scanning-tunneling-microscopy and spectroscopy, *Journal of Vacuum Science & Technology B: Microelectronics and Nanometer Structures Processing, Measurement, and Phenomena*, 13 (1995) 1150-1154.
- [28] J. Brunen, J. Zegenhagen, Investigation of the SrTiO<sub>3</sub> (110) surface by means of LEED, scanning tunneling microscopy and Auger spectroscopy, *Surface Science*, 389 (1997) 349-365.
- [29] M.R. Castell, Scanning tunneling microscopy of reconstructions on the SrTiO<sub>3</sub>(001) surface, *Surface Science*, 505 (2002) 1-13.
- [30] M.R. Castell, Nanostructures on the SrTiO<sub>3</sub>(001) surface studied by STM, *Surface Science*, 516 (2002) 33-42.
- [31] A.N. Chiamonti, C.H. Lanier, L.D. Marks, P.C. Stair, Time, temperature, and oxygen partial pressure-dependent surface reconstructions on SrTiO<sub>3</sub> (111): A systematic study of oxygen-rich conditions, *Surface Science*, 602 (2008) 3018-3025.
- [32] J. Ciston, H.G. Brown, A.J. D'Alfonso, P. Koirala, C. Ophus, Y. Lin, Y. Suzuki, H. Inada, Y. Zhu, L.J. Allen, L.D. Marks, Surface determination through atomically resolved secondary-electron imaging, *Nature Communications*, 6 (2015) 7358.
- [33] B. Cord, R. Courths, Electronic study of SrTiO<sub>3</sub> (001) surfaces by photoemission, *Surface Science*, 162 (1985) 34-38.
- [34] J.A. Enterkin, A.K. Subramanian, B.C. Russell, M.R. Castell, K.R. Poeppelmeier, L.D. Marks, A homologous series of structures on the surface of SrTiO<sub>3</sub> (110), *Nature Materials*, 9 (2010) 245.
- [35] N. Erdman, K.R. Poeppelmeier, M. Asta, O. Warschkow, D.E. Ellis, L.D. Marks, The structure and chemistry of the TiO<sub>2</sub>-rich surface of SrTiO<sub>3</sub> (001), *Nature*, 419 (2002) 55.
- [36] N. Erdman, O. Warschkow, M. Asta, K.R. Poeppelmeier, D.E. Ellis, L.D. Marks, Surface structures of SrTiO<sub>3</sub> (001): A TiO<sub>2</sub>-rich reconstruction with a  $c(4 \times 2)$  unit cell, *Journal of the American Chemical Society*, 125 (2003) 10050-10056.

- [37] A. Gömann, K. Gömann, M. Frerichs, V. Kempter, G. Borchardt, W. Maus-Friedrichs, Electronic structure and topography of annealed SrTiO<sub>3</sub> (111) surfaces studied with MIES and STM, *Applied Surface Science*, 252 (2005) 196-199.
- [38] Y. Haruyama, Y. Aiura, H. Bando, Y. Nishihara, H. Kato, Annealing temperature dependence on the electronic structure of the reduced SrTiO<sub>3</sub> (111) surface, *Journal of Electron Spectroscopy and Related Phenomena*, 88 (1998) 695-699.
- [39] Q.D. Jiang, J. Zegenhagen, SrTiO<sub>3</sub> (001) surfaces and growth of ultra-thin GdBa<sub>2</sub>Cu<sub>3</sub>O<sub>7-x</sub> films studied by LEED/AES and UHV-STM, *Surface Science*, 338 (1995) L882-L888.
- [40] Q.D. Jiang, J. Zegenhagen, c(6 × 2) and c(4 × 2) reconstruction of SrTiO<sub>3</sub> (001), *Surface Science*, 425 (1999) 343-354.
- [41] D.M. Kienzle, A.E. Becerra-Toledo, L.D. Marks, Vacant-site octahedral tilings on SrTiO<sub>3</sub> (001), the ( $\sqrt{13} \times \sqrt{13}$ )R33.7° surface, and related structures, *Physical Review Letters*, 106 (2011) 176102.
- [42] D.M. Kienzle, P. Koirala, L.D. Marks, Lanthanum aluminate (110) 3 × 1 surface reconstruction, *Surface Science*, 633 (2015) 60-67.
- [43] A.M. Kolpak, D. Li, R. Shao, A.M. Rappe, D.A. Bonnell, Evolution of the structure and thermodynamic stability of the BaTiO<sub>3</sub> (001) surface, *Physical Review Letters*, 101 (2008) 036102.
- [44] T. Kubo, H. Nozoye, Surface structure of SrTiO<sub>3</sub> (100)-( $\sqrt{5} \times \sqrt{5}$ )R26.6°, *Physical Review Letters*, 86 (2001) 1801-1804.
- [45] T. Kubo, H. Nozoye, Surface structure of SrTiO<sub>3</sub> (100), *Surface Science*, 542 (2003) 177-191.
- [46] C.H. Lanier, A. van de Walle, N. Erdman, E. Landree, O. Warschkow, A. Kazimirov, K.R. Poeppelmeier, J. Zegenhagen, M. Asta, L.D. Marks, Atomic-scale structure of the SrTiO<sub>3</sub> (001)-c(6 × 2) reconstruction: Experiments and first-principles calculations, *Physical Review B*, 76 (2007) 045421.
- [47] F. Li, Z. Wang, S. Meng, Y. Sun, J. Yang, Q. Guo, J. Guo, Reversible transition between thermodynamically stable phases with low density of oxygen vacancies on the SrTiO<sub>3</sub> (110) surface, *Physical Review Letters*, 107 (2011) 036103.
- [48] Y. Lin, A.E. Becerra-Toledo, F. Silly, K.R. Poeppelmeier, M.R. Castell, L.D. Marks, The (2 × 2) reconstructions on the SrTiO<sub>3</sub> (001) surface: A combined scanning tunneling microscopy and density functional theory study, *Surface Science*, 605 (2011) L51-L55.
- [49] L.D. Marks, A.N. Chiaramonti, S.U. Rahman, M.R. Castell, Transition from order to configurational disorder for surface reconstructions on SrTiO<sub>3</sub> (111), *Physical Review Letters*, 114 (2015) 226101.
- [50] M.S.M. González, M.H. Aguirre, E. Morán, M.Á. Alario-Franco, V. Perez-Dieste, J. Avila, M.C. Asensio, In situ reduction of (100) SrTiO<sub>3</sub>, *Solid State Sciences*, 2 (2000) 519-524.
- [51] J.M.P. Martinez, E.H. Morales, W.A. Saidi, D.A. Bonnell, A.M. Rappe, Atomic and electronic structure of the BaTiO<sub>3</sub> (001) ( $\sqrt{5} \times \sqrt{5}$ )R26.6° surface reconstruction, *Physical Review Letters*, 109 (2012) 256802.
- [52] H.L. Meyerheim, A. Ernst, K. Mohseni, I.V. Maznichenko, S. Ostanin, F. Klimenta, N. Jedrecy, W. Feng, I. Mertig, R. Felici, J. Kirschner, BaTiO<sub>3</sub> (001)-(2 × 1): Surface structure and spin density, *Physical Review Letters*, 108 (2012) 215502.

- [53] P.J. Møller, S.A. Komolov, E.F. Lazneva, Selective growth of a MgO (100)-c(2 × 2) superstructure on a SrTiO<sub>3</sub> (100)-(2 × 2) substrate, *Surface Science*, 425 (1999) 15-21.
- [54] E.H. Morales, D.A. Bonnell, On the relationship between surface reconstructions and step edge stability on BaTiO<sub>3</sub> (001), *Surface Science*, 609 (2013) 62-66.
- [55] E.H. Morales, J.M.P. Martirez, W.A. Saidi, A.M. Rappe, D.A. Bonnell, Coexisting surface phases and coherent one-dimensional interfaces on BaTiO<sub>3</sub> (001), *ACS Nano*, 8 (2014) 4465-4473.
- [56] M. Naito, H. Sato, Reflection high-energy electron diffraction study on the SrTiO<sub>3</sub> surface structure, *Physica C: Superconductivity*, 229 (1994) 1-11.
- [57] B.C. Russell, M.R. Castell, Surface of sputtered and annealed polar SrTiO<sub>3</sub> (111): TiO<sub>x</sub>-Rich (*n* × *n*) reconstructions, *Journal of Physical Chemistry C*, 112 (2008) 6538-6545.
- [58] B.C. Russell, M.R. Castell, Reconstructions on the polar SrTiO<sub>3</sub> (110) surface: Analysis using STM, LEED, and AES, *Physical Review B*, 77 (2008) 245414.
- [59] S. Sanna, S. Rode, R. Hölscher, S. Klassen, C. Marutschke, K. Kobayashi, H. Yamada, W. Schmidt, A. Kühnle, Charge compensation by long-period reconstruction in strongly polar lithium niobate surfaces, *Physical Review B*, 88 (2013) 115422.
- [60] S. Sekiguchi, M. Fujimoto, M. Nomura, S.-B. Cho, J. Tanaka, T. Nishihara, M.-G. Kang, H.-H. Park, Atomic force microscopic observation of SrTiO<sub>3</sub> polar surface, *Solid State Ionics*, 108 (1998) 73-79.
- [61] H. Tanaka, T. Matsumoto, T. Kawai, S. Kawai, Interaction of oxygen vacancies with O<sub>2</sub> on a reduced SrTiO<sub>3</sub> (100)  $\sqrt{5} \times \sqrt{5}$ -R26.6° surface observed by STM, *Surface Science*, 318 (1994) 29-38.
- [62] Z. Wang, A. Loon, A. Subramanian, S. Gerhold, E. McDermott, J.A. Enterkin, M. Hieckel, B.C. Russell, R.J. Green, A. Moewes, J. Guo, P. Blaha, M.R. Castell, U. Diebold, L.D. Marks, Transition from reconstruction toward thin film on the (110) surface of strontium titanate, *Nano letters*, 16 (2016) 2407-2412.
- [63] Z.L. Wang, A.J. Shapiro, Studies of LaAlO<sub>3</sub> (100) surfaces using RHEED and REM. II:  $\sqrt{5} \times \sqrt{5}$  surface reconstruction, *Surface Science*, 328 (1995) 159-169.
- [64] T. Ohsawa, M. Saito, I. Hamada, R. Shimizu, K. Iwaya, S. Shiraki, Z. Wang, Y. Ikuhara, T. Hitosugi, A single-atom-thick TiO<sub>2</sub> nanomesh on an insulating oxide, *ACS Nano*, 9 (2015) 8766-8772.
- [65] S.-h. Phark, Y.J. Chang, T. Won Noh, Selective growth of perovskite oxides on SrTiO<sub>3</sub> (001) by control of surface reconstructions, *Applied Physics Letters*, 98 (2011) 161908.
- [66] R. Shimizu, T. Ohsawa, K. Iwaya, S. Shiraki, T. Hitosugi, Epitaxial growth process of La<sub>0.7</sub>Ca<sub>0.3</sub>MnO<sub>3</sub> thin films on SrTiO<sub>3</sub> (001): thickness-dependent inhomogeneity caused by excess Ti atoms, *Crystal Growth & Design*, 14 (2014) 1555-1560.
- [67] F. Baiutti, G. Gregori, Y. Wang, Y.E. Suyolcu, G. Cristiani, P.A. van Aken, J. Maier, G. Logvenov, Cationic redistribution at epitaxial interfaces in superconducting two-dimensionally doped lanthanum cuprate films, *ACS Applied Materials and Interfaces*, 8 (2016) 27368-27375.
- [68] S. Gariglio, J.-M. Triscone, Oxide interface superconductivity, *Comptes Rendus Physique*, 12 (2011) 591-599.
- [69] J.L. Macmanus - Driscoll, Self - assembled heteroepitaxial oxide nanocomposite thin film structures: Designing interface - induced functionality in electronic materials, *Advanced Functional Materials*, 20 (2010) 2035-2045.

- [70] A. Ohtomo, H.Y. Hwang, A high-mobility electron gas at the  $\text{LaAlO}_3/\text{SrTiO}_3$  heterointerface, *Nature*, 427 (2004) 423.
- [71] M. O'Sullivan, J. Hadermann, M.S. Dyer, S. Turner, J. Alaria, T.D. Manning, A.M. Abakumov, J.B. Claridge, M.J. Rosseinsky, Interface control by chemical and dimensional matching in an oxide heterostructure, *Nature Chemistry*, 8 (2016) 347-353.
- [72] N. Reyren, S. Thiel, A.D. Caviglia, L.F. Kourkoutis, G. Hammerl, C. Richter, C.W. Schneider, T. Kopp, A.S. Rüetschi, D. Jaccard, M. Gabay, D.A. Muller, J.M. Triscone, J. Mannhart, Superconducting interfaces between insulating oxides, *Science*, 317 (2007) 1196-1199.
- [73] S. Tsui, A. Baikalov, J. Cmaidalka, Y.Y. Sun, Y.Q. Wang, Y.Y. Xue, C.W. Chu, L. Chen, A.J. Jacobson, Field-induced resistive switching in metal-oxide interfaces, *Applied Physics Letters*, 85 (2004) 317-319.
- [74] R. Wang, D. Fong, F. Jiang, M. Highland, P. Fuoss, C. Thompson, A. Kolpak, J. Eastman, S. Streiffer, A. Rappe, Reversible chemical switching of a ferroelectric film, *Physical review letters*, 102 (2009) 047601.
- [75] A. Aguadero, D. Pérez-Coll, C. De la Calle, J.A. Alonso, M.J. Escudero, L. Daza,  $\text{SrCo}_{1-x}\text{Sb}_x\text{O}_{3-\delta}$  perovskite oxides as cathode materials in solid oxide fuel cells, *Journal of Power Sources*, 192 (2009) 132-137.
- [76] A. Aguadero, M. Retuerto, F. Jiménez-Villacorta, M.T. Fernandez-Diaz, J.A. Alonso, Evolution of cobalt spin states and magnetic coupling along the  $\text{SrCo}_{1-x}\text{Sb}_x\text{O}_{3-\delta}$  system: Correlation with the crystal structure, *Physical Chemistry Chemical Physics*, 13 (2011) 12835-12843.
- [77] J.P. Hodges, S. Short, J.D. Jorgensen, X. Xiong, B. Dabrowski, S.M. Mini, C.W. Kimball, Evolution of oxygen-vacancy ordered crystal structures in the perovskite series  $\text{Sr}_n\text{Fe}_n\text{O}_{3n-1}$  ( $n=2, 4, 8$ , and  $\infty$ ), and the relationship to electronic and magnetic properties, *Journal of Solid State Chemistry*, 151 (2000) 190-209.
- [78] M. Sikora, C. Kapusta, K. Knížek, Z. Jiráček, C. Autret, M. Borowiec, C.J. Oates, V. Procházka, D. Rybicki, D. Zajac, X-ray absorption near-edge spectroscopy study of Mn and Co valence states in  $\text{LaMn}_{1-x}\text{Co}_x\text{O}_3$  ( $x=0-1$ ), *Physical Review B*, 73 (2006) 094426.
- [79] B.C. Tofield, C. Greaves, B.E.F. Fender, The  $\text{SrFeO}_{2.5}$ – $\text{SrFeO}_{3.0}$  system. evidence of a new phase  $\text{Sr}_4\text{Fe}_4\text{O}_{11}$  ( $\text{SrFeO}_{2.75}$ ), *Materials Research Bulletin*, 10 (1975) 737-745.
- [80] H.D. Megaw, Crystal structure of double oxides of the perovskite type, *Proc. Phys. Soc.*, 58 (1946) 133.
- [81] D.G. Schlom, L.-Q. Chen, C.J. Fennie, V. Gopalan, D.A. Muller, X. Pan, R. Ramesh, R. Uecker, Elastic strain engineering of ferroic oxides, *MRS Bull.*, 39 (2014) 118-130.
- [82] H.U. Anderson, Review of p-type doped perovskite materials for SOFC and other applications, *Solid State Ionics*, 52 (1992) 33-41.
- [83] J.P. Attfield, Structure–property relations in doped perovskite oxides, *Int. J. Inorg. Mater.*, 3 (2001) 1147-1152.
- [84] N. De Mathan, E. Husson, P. Gaucher, A. Morell, Modification of the B-site order of  $\text{PbMg}_{13}\text{Nb}_{23}\text{O}_3$  ceramics by thermal annealing or by La-doping, *Materials Research Bulletin*, 25 (1990) 427-434.



- [85] T. Ishihara, H. Matsuda, Y. Takita, Effects of rare earth cations doped for La site on the oxide ionic conductivity of LaGaO<sub>3</sub>-based perovskite type oxide, *Solid State Ionics*, 79 (1995) 147-151.
- [86] J. Kreisel, A.M. Glazer, G. Jones, P.A. Thomas, L. Abello, G. Lucazeau, An X-ray diffraction and Raman spectroscopy investigation of A-site substituted perovskite compounds: the (Na<sub>1-x</sub>K<sub>x</sub>)<sub>0.5</sub>Bi<sub>0.5</sub>TiO<sub>3</sub> (0 ≤ x ≤ 1) solid solution, *Journal of Physics: Condensed Matter*, 12 (2000) 3267.
- [87] D. Lybye, F.W. Poulsen, M. Mogensen, Conductivity of A-and B-site doped LaAlO<sub>3</sub>, LaGaO<sub>3</sub>, LaScO<sub>3</sub> and LaInO<sub>3</sub> perovskites, *Solid State Ionics*, 128 (2000) 91-103.
- [88] M. Mori, Y. Hiei, T. Yamamoto, Control of the thermal expansion of strontium - doped lanthanum chromite perovskites by B - site doping for high - temperature solid oxide fuel cell separators, *Journal of the American Ceramic Society*, 84 (2001) 781-786.
- [89] L. Bjaalie, B. Himmetoglu, L. Weston, A. Janotti, C.G. Van de Walle, Oxide interfaces for novel electronic applications, *New J. Phys.*, 16 (2014) 025005.
- [90] S. Stemmer, S. James Allen, Two-dimensional electron gases at complex oxide interfaces, *Annu. Rev. Mater. Res.*, 44 (2014) 151-171.
- [91] M. Ezbiri, K.M. Allen, M.E. Gálvez, R. Michalsky, A. Steinfeld, Design principles of perovskites for thermochemical oxygen separation, *ChemSusChem*, 8 (2015) 1966-1971.
- [92] H. Jeon, Z. Bi, W.S. Choi, M.F. Chisholm, C.A. Bridges, M.P. Paranthaman, H.N. Lee, Orienting oxygen vacancies for fast catalytic reaction, *Advanced Materials*, 25 (2013) 6459-6463.
- [93] Q. Lu, B. Yildiz, Voltage-controlled topotactic phase transition in thin-film SrCoO<sub>x</sub> monitored by in situ X-ray diffraction, *Nano Letters*, 16 (2016) 1186-1193.
- [94] J.G. Bednorz, K.A. Müller, Possible high T<sub>c</sub> superconductivity in the Ba– La– Cu– O system, *Zeitschrift für Physik B Condensed Matter*, 64 (1986) 189-193.
- [95] R.J. Cava, B. Batlogg, J.J. Krajewski, R. Farrow, L.W. Rupp Jr, A.E. White, K. Short, W.F. Peck, T. Kometani, Superconductivity near 30 K without copper: the Ba<sub>0.6</sub>K<sub>0.4</sub>BiO<sub>3</sub> perovskite, *Nature*, 332 (1988) 814.
- [96] K. Endo, S. Saya, S. Misawa, S. Yoshida, Preparation of yttrium barium copper oxide superconducting films by metalorganic molecular beam epitaxy, *Thin Solid Films*, 206 (1991) 143-145.
- [97] F.S. Galasso, *Perovskites and high-T<sub>c</sub> superconductors*, Gordon and Breach Science Publishers, New York, New York, 1990.
- [98] Y. Maeno, H. Hashimoto, K. Yoshida, S. Nishizaki, T. Fujita, J.G. Bednorz, F. Lichtenberg, Superconductivity in a layered perovskite without copper, *Nature*, 372 (1994) 532.
- [99] K.H. Ahn, T. Lookman, A.R. Bishop, Strain-induced metal–insulator phase coexistence in perovskite manganites, *Nature*, 428 (2004) 401.
- [100] M. Imada, A. Fujimori, Y. Tokura, Metal-insulator transitions, *Reviews of Modern Physics*, 70 (1998) 1039.
- [101] J.B. Torrance, P. Lacorre, A.I. Nazzari, E.J. Ansaldo, C. Niedermayer, Systematic study of insulator-metal transitions in perovskites RNiO<sub>3</sub> (R= Pr, Nd, Sm, Eu) due to closing of charge-transfer gap, *Physical Review B*, 45 (1992) 8209.
- [102] T. Kimura, T. Goto, H. Shintani, K. Ishizaka, T.-H. Arima, Y. Tokura, Magnetic control of ferroelectric polarization, *Nature*, 426 (2003) 55.

- [103] T. Kimura, S. Ishihara, H. Shintani, T. Arima, K.T. Takahashi, K. Ishizaka, Y. Tokura, Distorted perovskite with  $e_g^1$  configuration as a frustrated spin system, *Physical Review B*, 68 (2003) 060403.
- [104] O.A. Savinskaya, A.P. Nemudry, A.N. Nadeev, S.V. Tsybulya, Synthesis and study of the thermal stability of  $\text{SrFe}_{1-x}\text{M}_x\text{O}_{3-z}$  (M= Mo, W) perovskites, *Solid State Ionics*, 179 (2008) 1076-1079.
- [105] L. Karvonen, H. Yamauchi, M. Karppinen, Homologous series of  $\text{SrCoO}_{(3n-1)/n}$  perovskites obtained through  $\text{Br}_2$  oxygenation of  $\text{SrCoO}_{2.5}$ , *Chemistry of Materials*, 20 (2008) 7143-7147.
- [106] C. Mitra, T. Meyer, H.N. Lee, F.A. Reboredo, Oxygen diffusion pathways in Brownmillerite  $\text{SrCoO}_{2.5}$ : Influence of structure and chemical potential, *The Journal of Chemical Physics*, 141 (2014) 084710.
- [107] S.E. Dann, M.T. Weller, Structure and oxygen stoichiometry in  $\text{Sr}_3\text{Co}_2\text{O}_{7-y}$  ( $0.94 \leq y \leq 1.22$ ), *Journal of Solid State Chemistry*, 115 (1995) 499-507.
- [108] L. Viciu, H.W. Zandbergen, Q. Xu, Q. Huang, M. Lee, R.J. Cava, Structure and magnetic properties of the orthorhombic  $n=2$  Ruddlesden–Popper phases  $\text{Sr}_3\text{Co}_2\text{O}_{5+\delta}$  ( $\delta=0.91, 0.64$  and  $0.38$ ), *Journal of Solid State Chemistry*, 179 (2006) 500-511.
- [109] M.D. Pashley, Electron counting model and its application to island structures on molecular-beam epitaxy grown GaAs (001) and ZnSe (001), *Phys. Rev. B: Condens. Matter*, 40 (1989) 10481-10487.
- [110] J. Goniakowski, F. Finocchi, C. Noguera, Polarity of oxide surfaces and nanostructures, *Rep. Prog. Phys.*, 71 (2008) 016501.
- [111] C. Noguera, Polar oxide surfaces, *Journal of Physics: Condensed Matter*, 12 (2000) R367-R410.
- [112] A.E. Becerra-Toledo, M.R. Castell, L.D. Marks, Water adsorption on  $\text{SrTiO}_3$  (001): I. Experimental and simulated STM, *Surface Science*, 606 (2012) 762-765.
- [113] A.E. Becerra-Toledo, J.A. Enterkin, D.M. Kienzle, L.D. Marks, Water adsorption on  $\text{SrTiO}_3$  (001): II. Water, water, everywhere, *Surface Science*, 606 (2012) 791-802.
- [114] E.A. Wood, Vocabulary of surface crystallography, *Journal of applied physics*, 35 (1964) 1306-1312.
- [115] E.A. Soares, C.M.C. de Castilho, V.E. de Carvalho, Advances on surface structural determination by LEED, *Journal of Physics: Condensed Matter*, 23 (2011) 303001.
- [116] R. Herger, P.R. Willmott, O. Bunk, C.M. Schlepütz, B.D. Patterson, B. Delley, V.L. Shneerson, P.F. Lyman, D.K. Saldin, Surface structure of  $\text{SrTiO}_3$  (001), *Physical Review B*, 76 (2007) 195435.
- [117] N.J.C. Ingle, A. Yuskauskas, R. Wicks, M. Paul, S. Leung, The structural analysis possibilities of reflection high energy electron diffraction, *Journal of Physics D: Applied Physics*, 43 (2010) 133001.
- [118] D.M. Kienzle, L.D. Marks, Surface transmission electron diffraction for  $\text{SrTiO}_3$  surfaces, *Cryst. Eng. Comm.*, 14 (2012) 7833-7839.
- [119] L.D. Marks, W. Sinkler, E. Landree, A feasible set approach to the crystallographic phase problem, *Acta Crystallographica Section A: Foundations of Crystallography*, 55 (1999) 601-612.
- [120] I.K. Robinson, D.J. Tweet, Surface X-ray diffraction, *Reports on Progress in Physics*, 55 (1992) 599.

- [121] M.M. Woolfson, H.-f. Fan, Physical and non-physical methods of solving crystal structures, Cambridge University Press, Cambridge, New York, 1995.
- [122] A.E. Becerra-Toledo, M.S.J. Marshall, M.R. Castell, L.D. Marks,  $c(4 \times 2)$  and related structural units on the  $\text{SrTiO}_3$  (001) surface: Scanning tunneling microscopy, density functional theory, and atomic structure, *The Journal of Chemical Physics*, 136 (2012) 214701.
- [123] H. Onishi, Y. Iwasawa, Reconstruction of  $\text{TiO}_2$  (110) surface: STM study with atomic-scale resolution, *Surf. Sci.*, 313 (1994) L783-L789.
- [124] J. Tersoff, D.R. Hamann, *Scanning Tunneling Microscopy*, Springer, 1985.
- [125] V. Cascos, L. Troncoso, J.A. Alonso, New families of  $\text{M}^{n+}$ -doped  $\text{SrCo}_{1-x}\text{M}_x\text{O}_{3-\delta}$  perovskites performing as cathodes in solid-oxide fuel cells, *International Journal of Hydrogen Energy*, 40 (2015) 11333-11341.
- [126] K. Huang, M. Feng, J.B. Goodenough, Sol - gel synthesis of a new oxide - ion conductor Sr - and Mg - doped  $\text{LaGaO}_3$  perovskite, *Journal of the American Ceramic Society*, 79 (1996) 1100-1104.
- [127] S. Kaliaguine, A. Van Neste, V. Szabo, J.E. Gallot, M. Bassir, R. Muzychuk, Perovskite-type oxides synthesized by reactive grinding: Part I. Preparation and characterization, *Applied Catalysis A: General*, 209 (2001) 345-358.
- [128] D.G. Schlom, J.H. Haeni, J. Lettieri, C.D. Theis, W. Tian, J.C. Jiang, X.Q. Pan, Oxide nano-engineering using MBE, *Materials Science and Engineering: B*, 87 (2001) 282-291.
- [129] H. Hong, T.C. Chiang, A six-circle diffractometer system for synchrotron X-ray studies of surfaces and thin film growth by molecular beam epitaxy, *Nuclear Instruments and Methods in Physics Research Section A: Accelerators, Spectrometers, Detectors and Associated Equipment*, 572 (2007) 942-947.
- [130] J.H. Lee, I.-C. Tung, S.-H. Chang, A. Bhattacharya, D.D. Fong, J.W. Freeland, H. Hong, In situ surface/interface X-ray diffractometer for oxide molecular beam epitaxy, *Review of Scientific Instruments*, 87 (2016) 013901.
- [131] M. Lohmeier, E. Vlieg, Angle calculations for a six-circle surface X-ray diffractometer, *Journal of Applied Crystallography*, 26 (1993) 706-716.
- [132] E.S. Hellman, E.H. Hartford Jr, Effects of oxygen on the sublimation of alkaline earths from effusion cells, *Journal of Vacuum Science & Technology B: Microelectronics Processing and Phenomena*, 12 (1994) 1178-1180.
- [133] Y.S. Kim, N. Bansal, C. Chaparro, H. Gross, S. Oh, Sr flux stability against oxidation in oxide-molecular-beam-epitaxy environment: Flux, geometry, and pressure dependence, *Journal of Vacuum Science and Technology A: Vacuum, Surfaces and Films*, 28 (2010) 271-276.
- [134] E. Bengu, M. Salud, L.D. Marks, Model-independent inversion of x-ray or neutron reflectivity data, *Physical Review B*, 63 (2001) 195414.
- [135] L. Marks, E. Bengu, C. Collazo-Davila, D. Grozea, E. Landree, C. Leslie, W. Sinkler, Direct methods for surfaces, *Surface review and Letters*, 5 (1998) 1087-1106.
- [136] Y. Yacoby, M. Sowwan, E. Stern, J.O. Cross, D. Brewe, R. Pindak, J. Pitney, E.M. Dufresne, R. Clarke, Direct determination of epitaxial interface structure in  $\text{Gd}_2\text{O}_3$  passivation of GaAs, *Nature Materials*, 1 (2002) 99.
- [137] J.H. Lee, G. Luo, I.C. Tung, S.H. Chang, Z. Luo, M. Malshe, M. Gadre, A. Bhattacharya, S.M. Nakhmanson, J.A. Eastman, H. Hong, J. Jellinek, D. Morgan, D.D. Fong, J.W. Freeland,

Dynamic layer rearrangement during growth of layered oxide films by molecular beam epitaxy, *Nature Materials*, 13 (2014) 879-883.

[138] S. Brennan, P.L. Cowan, A suite of programs for calculating x - ray absorption, reflection, and diffraction performance for a variety of materials at arbitrary wavelengths, *Review of Scientific Instruments*, 63 (1992) 850-853.

[139] W.T. Elam, B.D. Ravel, J.R. Sieber, A new atomic database for X-ray spectroscopic calculations, *Radiation Physics and Chemistry*, 63 (2002) 121-128.

[140] D.G. Castner, P.R. Watson, I.Y. Chan, X-ray absorption spectroscopy, X-ray photoelectron spectroscopy, and analytical electron microscopy studies of cobalt catalysts. 1. Characterization of calcined catalysts, *The Journal of Physical Chemistry*, 93 (1989) 3188-3194.

[141] F.M.F. De Groot, M. Abbate, J. Van Elp, G.A. Sawatzky, Y.J. Ma, C.T. Chen, F. Sette, Oxygen 1s and cobalt 2p X-ray absorption of cobalt oxides, *Journal of Physics: Condensed Matter*, 5 (1993) 2277.

[142] L. Karvonen, M. Valkeapää, R.-S. Liu, J.-M. Chen, H. Yamauchi, M. Karppinen, O-K and Co-L XANES study on oxygen intercalation in perovskite  $\text{SrCoO}_{3-\delta}$ , *Chemistry of Materials*, 22 (2009) 70-76.

[143] A. Piovano, G. Agostini, A.I. Frenkel, T. Bertier, C. Prestipino, M. Ceretti, W. Paulus, C. Lamberti, Time resolved in situ XAFS study of the electrochemical oxygen intercalation in  $\text{SrFeO}_{2.5}$  Brownmillerite structure: comparison with the homologous  $\text{SrCoO}_{2.5}$  system, *The Journal of Physical Chemistry C*, 115 (2010) 1311-1322.

[144] E. Bousquet, N.A. Spaldin, P. Ghosez, Strain-induced ferroelectricity in simple rocksalt binary oxides, *Physical Review Letters*, 104 (2010) 037601.

[145] L. Giordano, F. Cinquini, G. Pacchioni, Tuning the surface metal work function by deposition of ultrathin oxide films: Density functional calculations, *Physical Review B*, 73 (2006) 045414.

[146] J.D. Burton, E.Y. Tsymbal, Highly spin-polarized conducting state at the interface between nonmagnetic band insulators:  $\text{LaAlO}_3/\text{FeS}_2$  (001), *Physical Review Letters*, 107 (2011) 166601.

[147] G. Song, W. Zhang, First-principles study on the phase diagram and multiferroic properties of  $(\text{SrCoO}_3)_1/(\text{SrTiO}_3)_1$  superlattices, *Scientific Reports*, 4 (2014) 4564.

[148] P. Hohenberg, W. Kohn, Inhomogeneous electron gas, *Physical Review*, 136 (1964) B864.

[149] W. Kohn, L.J. Sham, Self-consistent equations including exchange and correlation effects, *Physical review*, 140 (1965) A1133.

[150] J.P. Perdew, K. Burke, Y. Wang, Generalized gradient approximation for the exchange-correlation hole of a many-electron system, *Physical Review B*, 54 (1996) 16533.

[151] J.P. Perdew, W. Yue, Accurate and simple density functional for the electronic exchange energy: Generalized gradient approximation, *Physical review B*, 33 (1986) 8800.

[152] J.P. Perdew, K. Burke, M. Ernzerhof, Generalized gradient approximation made simple, *Physical Review Letters*, 77 (1996) 3865-3868.

[153] L.D. Marks, Registry and UHV transmission electron diffraction of surfaces, *Ultramicroscopy*, 45 (1992) 145-154.

[154] P. Blaha, K. Schwarz, G.K.H. Madsen, D. Kvasnicka, J. Luitz, WIEN2k, an augmented plane wave+ local orbitals program for calculating crystal properties, Universität Wien, Austria, 2010.

- [155] L. Pardini, V. Bellini, F. Manghi, C. Ambrosch-Draxl, First-principles calculation of X-ray dichroic spectra within the full-potential linearized augmented planewave method: An implementation into the Wien2k code, *Computer Physics Communications*, 183 (2012) 628-636.
- [156] K. Schwarz, P. Blaha, Solid state calculations using WIEN2k, *Computational Materials Science*, 28 (2003) 259-273.
- [157] J.A. Enterkin, A.E. Becerra-Toledo, K.R. Poeppelmeier, L.D. Marks, A chemical approach to understanding oxide surfaces, *Surface Science*, 606 (2012) 344-355.
- [158] N.E. Brese, M. O'keeffe, Bond-valence parameters for solids, *Acta Crystallographica Section B: Structural Science*, 47 (1991) 192-197.
- [159] I.D. Brown, What factors determine cation coordination numbers?, *Acta Crystallographica Section B: Structural Science*, 44 (1988) 545-553.
- [160] J. Tersoff, D.R. Hamann, Theory and application for the scanning tunneling microscope, *Physical Review Letters*, 50 (1983) 1998.
- [161] J. Bardeen, Tunnelling from a many-particle point of view, *Physical Review Letters*, 6 (1961) 57.
- [162] K. Stokbro, U. Quaade, F. Grey, Electric field effects in scanning tunneling microscope imaging, *Applied Physics A: Materials Science & Processing*, 66 (1998) S907-S910.
- [163] C.J. Chen, *Introduction to scanning tunneling microscopy*, 2 ed., Oxford University Press on Demand, 1993.
- [164] J. Suntivich, H.A. Gasteiger, N. Yabuuchi, H. Nakanishi, J.B. Goodenough, Y. Shao-Horn, Design principles for oxygen-reduction activity on perovskite oxide catalysts for fuel cells and metal-air batteries, *Nature Chem.*, 3 (2011) 546.
- [165] H.M. Christen, G. Eres, Recent advances in pulsed-laser deposition of complex oxides, *J. Phys.: Condens. Matter* 20 (2008) 264005.
- [166] J.H. Haeni, C.D. Theis, D.G. Schlom, W. Tian, X.Q. Pan, H. Chang, I. Takeuchi, X.-D. Xiang, Epitaxial growth of the first five members of the  $\text{Sr}_{n+1}\text{Ti}_n\text{O}_{3n+1}$  Ruddlesden–Popper homologous series, *Appl. Phys. Lett.*, 78 (2001) 3292-3294.
- [167] L.D. Marks, A.N. Chiaramonti, F. Tran, P. Blaha, The small unit cell reconstructions of  $\text{SrTiO}_3$  (111), *Surf. Sci.*, 603 (2009) 2179-2187.
- [168] M.S. Martin-Gonzalez, M.H. Aguirre, E. Moran, M.A. Alario-Franco, V. Perez-Dieste, J. Avila, M.C. Asensio, In situ reduction of (100)  $\text{SrTiO}_3$ , *Solid State Sci.*, 2 (2000) 519-524.
- [169] B.C. Russell, M.R. Castell,  $(\sqrt{13} \times \sqrt{13})\text{R}13.9^\circ$  and  $(\sqrt{7} \times \sqrt{7})\text{R}19.1^\circ$  reconstructions of the polar  $\text{SrTiO}_3$  (111) surface, *Phys. Rev. B: Condens. Matter*, 75 (2007) 155433.
- [170] P. Koirala, A. Gulec, E. Steele, L.D. Marks, Al rich (111) and (110) surfaces of  $\text{LaAlO}_3$ , In Press, (2018).
- [171] D. Wolf, Reconstruction of NaCl surfaces from a dipolar solution to the Madelung problem, *Phys. Rev. Lett.*, 68 (1992) 3315.
- [172] P. Novák, J. Kuneš, L. Chaput, W.E. Pickett, Exact exchange for correlated electrons, *Phys. Status Solidi B* 243 (2006) 563-572.
- [173] O. Warschkow, M. Asta, N. Erdman, K.R. Poeppelmeier, D.E. Ellis, L.D. Marks,  $\text{TiO}_2$ -rich reconstructions of  $\text{SrTiO}_3$  (001): a theoretical study of structural patterns, *Surface Science*, 573 (2004) 446-456.

- [174] W.H. Zachariasen, The atomic arrangement in glass, *J. Am. Chem. Soc.*, 54 (1932) 3841-3851.
- [175] L. Pauling, The principles determining the structure of complex ionic crystals, *J. Am. Chem. Soc.*, 51 (1929) 1010-1026.
- [176] I.D. Brown, *The chemical bond in inorganic chemistry : The bond valence model*, Oxford ; New York : Oxford University Press, Oxford ; New York, 2002.
- [177] I.D. Brown, Recent developments in the methods and applications of the bond valence model, *Chem. Rev.*, 109 (2009) 6858-6919.
- [178] I.D. Brown, D. Altermatt, Bond-valence parameters obtained from a systematic analysis of the Inorganic Crystal Structure Database, *Acta Crystallogr., Sect. B*, 41 (1985) 244-247.
- [179] K. Binder, D.P. Landau, Square Lattice Gases with 2-Body and 3-Body Interactions - a Model for the Adsorption of Hydrogen on Pd(100), *Surface Science*, 108 (1981) 503-525.
- [180] M.W. Conner, C. Ebner, Solid physically adsorbed films: A Potts lattice-gas-model study, *Physical review. B, Condensed matter*, 36 (1987) 3683-3692.
- [181] C.S. Jayanthi, Surface melting in a Potts lattice-gas model, *Physical review. B, Condensed matter*, 44 (1991) 427-430.
- [182] M.A. Zaluskakotur, The Kinetic Potts-Model in the Description of Surface Dynamics, *Surface Science*, 265 (1992) 196-208.
- [183] C. Dobrowolny, L. Laanait, J. Ruiz, Surface transitions of the semi-infinite Potts model II: The low bulk temperature regime, *J Stat Phys*, 116 (2004) 1405-1434.
- [184] C. Dobrowolny, L. Laanait, J. Ruiz, Surface transitions of the semi-infinite Potts model I: The high bulk temperature regime, *J Stat Phys*, 114 (2004) 1269-1302.
- [185] M.S.J. Marshall, A.E. Becerra-Toledo, L.D. Marks, M.R. Castell, Surface and defect structure of oxide nanowires on SrTiO<sub>3</sub>, *Phys. Rev. Lett.*, 107 (2011) 086102.
- [186] M.S.J. Marshall, A.E. Becerra-Toledo, D.J. Payne, R.G. Egdell, L.D. Marks, M.R. Castell, Structure and composition of linear TiO<sub>x</sub> nanostructures on SrTiO<sub>3</sub> (001), *Phys. Rev. B: Condens. Matter* 86 (2012) 125416.
- [187] Z. Wang, J. Feng, Y. Yang, Y. Yao, L. Gu, F. Yang, Q. Guo, J. Guo, Cation stoichiometry optimization of SrTiO<sub>3</sub> (110) thin films with atomic precision in homogeneous molecular beam epitaxy, *Appl. Phys. Lett.*, 100 (2012) 051602.
- [188] S. Cook, L.D. Marks, Ab initio predictions of TiO<sub>2</sub> double-layer SrTiO<sub>3</sub> (001) surface reconstructions, submitted, (2018).
- [189] R. Shimizu, K. Iwaya, T. Ohsawa, S. Shiraki, T. Hasegawa, T. Hashizume, T. Hitosugi, Atomic-scale visualization of initial growth of homoepitaxial SrTiO<sub>3</sub> thin film on an atomically ordered substrate, *ACS Nano*, 5 (2011) 7967-7971.
- [190] A.P. Kajos, S. Stemmer, Surface reconstructions in molecular beam epitaxy of SrTiO<sub>3</sub>, *Appl. Phys. Lett.*, 105 (2014) 191901.
- [191] T.K. Andersen, S. Wang, M.R. Castell, D.D. Fong, L.D. Marks, Single-Layer TiO<sub>x</sub> Reconstructions on SrTiO<sub>3</sub> (111):( $\sqrt{7} \times \sqrt{7}$ ) R19. 1° ,( $\sqrt{13} \times \sqrt{13}$ ) R13. 9° , and Related Structures, *Surface Science*, (2018).
- [192] A. Biswas, P.B. Rossen, C.H. Yang, W. Siemons, M.-H. Jung, I.K. Yang, R. Ramesh, Y.H. Jeong, Universal Ti-rich termination of atomically flat SrTiO<sub>3</sub> (001), (110), and (111) surfaces, *Applied Physics Letters*, 98 (2011) 051904.

- [193] V.N. Staroverov, G.E. Scuseria, J. Tao, J.P. Perdew, Comparative assessment of a new nonempirical density functional: Molecules and hydrogen-bonded complexes, *Journal of Chemical Physics*, 119 (2003) 12129-12137.
- [194] J.A. Enterkin, A chemical approach to understanding oxide surface structure and reactivity, in: *Materials Science & Engineering*, Northwestern University, Evanston, Illinois, 2010.
- [195] L.D. Marks, Fixed-point optimization of atoms and density in DFT, *Journal of Chemical Theory and Computation*, 9 (2013) 2786-2800.
- [196] L. Jones, H. Yang, T.J. Pennycook, M.S.J. Marshall, S. Van Aert, N.D. Browning, M.R. Castell, P.D. Nellist, Smart Align—a new tool for robust non-rigid registration of scanning microscope data, *Advanced Structural and Chemical Imaging*, 1 (2015) 8.
- [197] T.K. Andersen, S. Cook, G. Wan, H. Hong, L.D. Marks, D.D. Fong, Layer-by-layer epitaxial growth of defect-engineered strontium cobaltites, *ACS Applied Materials & Interfaces*, 10 (2018) 5949-5958.
- [198] Y.-I. Lee, J. Kleis, J. Rossmeisl, Y. Shao-horn, D. Morgan, Prediction of solid oxide fuel cell cathode activity with first-principles descriptors, *Energy & Environmental Science*, 4 (2011) 3966-3970.
- [199] N.A. Spaldin, M. Fiebig, The renaissance of magnetoelectric multiferroics, *Science*, 309 (2005) 391-392.
- [200] S.V. Kalinin, A. Borisevich, D. Fong, Beyond condensed matter physics on the nanoscale: The role of ionic and electrochemical phenomena in the physical functionalities of oxide materials, *ACS Nano*, 6 (2012) 10423-10437.
- [201] G. Van der Laan, R.A.D. Patrick, C.M.B. Henderson, D.J. Vaughan, Oxidation state variations in copper minerals studied with Cu 2p X-ray absorption spectroscopy, *Journal of Physics and Chemistry of Solids*, 53 (1992) 1185-1190.
- [202] M. Wilke, F. Farges, P.-E. Petit, G.E. Brown Jr, F. Martin, Oxidation state and coordination of Fe in minerals: An Fe K-XANES spectroscopic study, *American Mineralogist*, 86 (2001) 714-730.
- [203] A. Tarancón, M. Burriel, J. Santiso, S.J. Skinner, J.A. Kilner, Advances in layered oxide cathodes for intermediate temperature solid oxide fuel cells, *Journal of Materials Chemistry*, 20 (2010) 3799-3813.
- [204] C.K. Xie, Y.F. Nie, B.O. Wells, J.I. Budnick, W.A. Hines, B. Dabrowski, Magnetic phase separation in  $\text{SrCoO}_x$  ( $2.5 \leq x \leq 3$ ), *Applied Physics Letters*, 99 (2011) 052503.
- [205] Y.-L. Lee, D. Lee, X.R. Wang, H.N. Lee, D. Morgan, Y. Shao-Horn, Kinetics of oxygen surface exchange on epitaxial Ruddlesden–Popper phases and correlations to first-principles descriptors, *The Journal of Physical Chemistry Letters*, 7 (2016) 244-249.
- [206] Y. Long, Y. Kaneko, S. Ishiwata, Y. Taguchi, Y. Tokura, Synthesis of cubic  $\text{SrCoO}_3$  single crystal and its anisotropic magnetic and transport properties, *Journal of Physics: Condensed Matter*, 23 (2011) 245601.
- [207] N. Ichikawa, M. Iwanowska, M. Kawai, C. Calers, W. Paulus, Y. Shimakawa, Reduction and oxidation of  $\text{SrCoO}_{2.5}$  thin films at low temperatures, *Dalton Transactions*, 41 (2012) 10507-10510.
- [208] R. Le Toquin, W. Paulus, A. Cousson, C. Prestipino, C. Lambert, Time-resolved in situ studies of oxygen intercalation into  $\text{SrCoO}_{2.5}$ , performed by neutron diffraction and X-ray absorption spectroscopy, *Journal of the American Chemical Society*, 128 (2006) 13161-13174.

- [209] L. Nianpeng, Z. Pengfei, Z. Qinghua, Q. Ruimin, H. Qing, L. Hao-Bo, W. Yujia, G. Jingwen, Z. Ding, D. Zheng, L. Zhuolu, W. Meng, Y. Shuzhen, Y. Mingzhe, A. Elke, Z. Shuyun, Y. Wanli, G. Lin, N. Ce-Wen, W. Jian, T. Yoshinori, Y. Pu, Electric-field control of tri-state phase transformation with a selective dual-ion switch, *Nature*, 546 (2017) 124-128.
- [210] O.T. Tambunan, K.J. Parwanta, S.K. Acharya, B.W. Lee, C.U. Jung, Y.S. Kim, B.H. Park, H. Jeong, J.-Y. Park, M.R. Cho, Y.D. Park, W.S. Choi, D.-W. Kim, H. Jin, S. Lee, S.J. Song, S.-J. Kang, M. Kim, C.S. Hwang, Resistance switching in epitaxial  $\text{SrCoO}_x$  thin films, *Applied Physics Letters*, 105 (2014) 063507.
- [211] P.R. Willmott, J.R. Huber, Pulsed laser vaporization and deposition, *Reviews of Modern Physics*, 72 (2000) 315-328.
- [212] D.G. Schlom, Perspective: Oxide Molecular-Beam Epitaxy Rocks!, *Apl Materials*, 3 (2015) 062403.
- [213] M.J. Aziz, Interface attachment kinetics in alloy solidification, *Metallurgical and Materials Transactions A*, 27 (1996) 671-686.
- [214] J.C. Baker, J.W. Cahn, Solute trapping by rapid solidification, *Acta Metallurgica*, 17 (1969) 575-578.
- [215] W.J. Boettinger, J.H. Perepezko, *Fundamentals of Rapid Solidification*, 1985.
- [216] X. Han, B.J. Spencer, A nonlinear model for surface segregation and solute trapping during planar film growth, *Journal of Applied Physics*, 101 (2007) 084302.
- [217] G. Koster, B.L. Kropman, G.J.H.M. Rijnders, D.H.A. Blank, H. Rogalla, Quasi-ideal strontium titanate crystal surfaces through formation of strontium hydroxide, *Applied Physics Letters*, 73 (1998) 2920-2922.
- [218] J.N. Eckstein, D.G. Schlom, E.S. Hellman, K.E. Von Dessonneck, Z.J. Chen, C. Webb, F. Turner, J.S. Harris Jr, M.R. Beasley, T.H. Geballe, Epitaxial growth of high - temperature superconducting thin films, *Journal of Vacuum Science & Technology B: Microelectronics Processing and Phenomena*, 7 (1989) 319-323.
- [219] J.N. Eckstein, I. Bozovic, K.E. Von Dessonneck, D.G. Schlom, J.S. Harris Jr, S.M. Baumann, Atomically Layered Heteroepitaxial Growth of Single - Crystal Films of Superconducting  $\text{Bi}_2\text{Sr}_2\text{Ca}_2\text{Cu}_3\text{O}_x$ , *Applied physics letters*, 57 (1990) 931-933.
- [220] D.G. Schlom, A.F. Marshall, J.T. Sizemore, Z.J. Chen, J.N. Eckstein, I. Bozovic, K.E. Von Dessonneck, J.S. Harris, J.C. Bravman, Molecular beam epitaxial growth of layered Bi-Sr-Ca-Cu-O compounds, *Journal of Crystal Growth*, 102 (1990) 361-375.
- [221] G.B. Stephenson, J.A. Eastman, O. Auciello, A. Munkholm, C. Thompson, P.H. Fuoss, P. Fini, S.P. DenBaars, J.S. Speck, Real-time X-ray scattering studies of surface structure during metalorganic chemical vapor deposition of GaN, *MRS Bulletin*, 24 (1999) 21-25.
- [222] C.M. Schlepütz, R. Herger, P.R. Willmott, B.D. Patterson, O. Bunk, C. Brönnimann, B. Henrich, G. Hülsen, E.F. Eikenberry, Improved data acquisition in grazing - incidence X - ray scattering experiments using a pixel detector, *Acta Crystallographica Section A: Foundations of Crystallography*, 61 (2005) 418-425.
- [223] G.E. Sterbinsky, P.J. Ryan, J.W. Kim, E. Karapetrova, J.X. Ma, J. Shi, J.C. Woicik, Local Atomic and Electronic Structures of Epitaxial Strained  $\text{LaCoO}_3$  Thin Films, *Physical Review B*, 85 (2012) 020403.
- [224] O. Jankovský, D. Sedmidubský, J. Vitek, P. Šimek, Z. Sofer, Phase Diagram of the Sr-Co-O System, *Journal of the European Ceramic Society*, 35 (2015) 935-940.



- [225] W.-W. Zhang, M. Chen, E. Povoden-Karadeniz, P.V. Hendriksen, Thermodynamic modeling of the Sr–Co–Fe–O System, *Solid State Ionics*, 292 (2016) 88-97.
- [226] C. De La Calle, A. Aguadero, J.A. Alonso, M.T. Fernández-Díaz, Correlation between reconstructive phase transitions and transport properties from SrCoO<sub>2.5</sub> Brownmillerite: A neutron diffraction study, *Solid State Sciences*, 10 (2008) 1924-1935.
- [227] A. Muñoz, C. de La Calle, J.A. Alonso, P.M. Botta, V. Pardo, D. Baldomir, J. Rivas, Crystallographic and magnetic structure of SrCoO<sub>2.5</sub> Brownmillerite: Neutron study coupled with band-structure calculations, *Physical Review B*, 78 (2008) 054404.
- [228] X.L. Wang, H. Sakurai, E. Takayama-Muromachi, Synthesis, structures, and magnetic properties of novel Ruddlesden-Popper homologous series Sr<sub>n+1</sub>Co<sub>n</sub>O<sub>3n+1</sub> (n=1,2,3,4, and ∞), *Journal of Applied Physics*, 97 (2005) 10M519.
- [229] W. Tian, J.H. Haeni, D.G. Schlom, E. Hutchinson, B.L. Sheu, M.M. Rosario, P. Schiffer, Y. Liu, M.A. Zurbuchen, X.Q. Pan, Epitaxial growth and magnetic properties of the first five members of the layered Sr<sub>n+1</sub>Ru<sub>n</sub>O<sub>3n+1</sub> oxide series, *Applied Physics Letters*, 90 (2007) 022507.
- [230] W. Tian, X.Q. Pan, J.H. Haeni, D.G. Schlom, Transmission electron microscopy study of n = 1–5 Sr<sub>n+1</sub>Ti<sub>n</sub>O<sub>3n+1</sub> epitaxial thin films, *Journal of Materials Research*, 16 (2001) 2013-2026.
- [231] K. Nishio, H.Y. Hwang, Y. Hikita, Thermodynamic guiding principles in selective synthesis of strontium iridate Ruddlesden-Popper epitaxial films, *APL Materials*, 4 (2016) 036102.
- [232] T.L. Meyer, H. Jeen, X. Gao, J.R. Petrie, M.F. Chisholm, H.N. Lee, Symmetry-driven atomic rearrangement at a Brownmillerite-perovskite interface, *Advanced Electronic Materials*, 2 (2016) 1500201.
- [233] R.O. Suzuki, T. Ogawa, K. Ono, Use of ozone to prepare silver oxides, *Journal of the American Ceramic Society*, 82 (1999) 2033-2038.
- [234] M.W. Chase, NIST-JANAF Thermochemical Tables, Fourth Edition, 4 ed., American Institute of Physics, 1998.
- [235] F. Léonard, R.C. Desai, Alloy decomposition and surface instabilities in thin films, *Physical Review B*, 57 (1998) 4805-4815.
- [236] F. Léonard, R. Desai, Spontaneous Decomposition and Ordering During Epitaxial Growth, *Thin Solid Films*, 357 (1999) 46-52.
- [237] M.A. McCoy, R.W. Grimes, W.E. Lee, Phase stability and interfacial structures in the SrO–SrTiO<sub>3</sub> system, *Philosophical Magazine A*, 75 (1997) 833-846.
- [238] W. Bussmann, C. Herzig, W. Rempp, K. Maier, H. Mehrer, Isotope effect and self - diffusion in face - centred cubic cobalt, *Physica Status Solidi (a)*, 56 (1979) 87-97.
- [239] T.K. Andersen, S. Cook, E. Benda, H. Hong, L.D. Marks, D.D. Fong, Development of a hybrid molecular beam epitaxy deposition system for in situ surface x-ray studies, *Review of Scientific Instruments*, 89 (2018) 033905.
- [240] D.D. Berkley, B.R. Johnson, N. Anand, K.M. Beauchamp, L.E. Conroy, A.M. Goldman, J. Maps, K. Mauersberger, M.L. Mecartney, J. Morton, M. Tuominen, Y.-J. Zhang, In situ formation of superconducting YBa<sub>2</sub>Cu<sub>3</sub>O<sub>7-x</sub> thin films using pure ozone vapor oxidation, *Applied Physics Letters*, 53 (1988) 1973-1975.
- [241] M.B. Panish, Molecular beam epitaxy of GaAs and InP with gas sources for As and P, *Journal of the Electrochemical Society*, 127 (1980) 2729-2733.

- [242] E. Tokumitsu, Y. Kudou, M. Konagai, K. Takahashi, Molecular beam epitaxial growth of GaAs using trimethylgallium as a gallium source, *Journal of Applied Physics*, 55 (1984) 3163-3165.
- [243] W.T. Tsang, A review of CBE, MOMBE and GSMBE, *Journal of Crystal Growth*, 111 (1991) 529-538.
- [244] E. Veuhoff, W. Pletschen, P. Balk, H. Lüth, Metalorganic CVD of GaAs in a molecular beam system, *Journal of Crystal Growth*, 55 (1981) 30-34.
- [245] B. Jalan, P. Moetakef, S. Stemmer, Molecular beam epitaxy of SrTiO<sub>3</sub> with a growth window, *Applied Physics Letters*, 95 (2009) 032906.
- [246] J.M. LeBeau, R. Engel-Herbert, B. Jalan, J. Cagnon, P. Moetakef, S. Stemmer, G.B. Stephenson, Stoichiometry optimization of homoepitaxial oxide thin films using X-ray diffraction, *Applied Physics Letters*, 95 (2009) 142905.
- [247] K. Masaki, H. Isshiki, T. Kimura, Erbium–silicon–oxide crystalline films prepared by MOMBE, *Optical Materials*, 27 (2005) 876-879.
- [248] H.-T. Zhang, L. Zhang, D. Mukherjee, Y.-X. Zheng, R.C. Haislmaier, N. Alem, R. Engel-Herbert, Wafer-scale growth of VO<sub>2</sub> thin films using a combinatorial approach, *Nature Communications*, 6 (2015) 8475.
- [249] Z. Feng, Y. Yacoby, M.J. Gadre, Y.-L. Lee, W.T. Hong, H. Zhou, M.D. Biegalski, H.M. Christen, S.B. Adler, D. Morgan, Y. Shao-Horn, Anomalous interface and surface strontium segregation in (La<sub>1-y</sub>Sr<sub>y</sub>)<sub>2</sub>CoO<sub>4±δ</sub>/La<sub>1-x</sub>Sr<sub>x</sub>CoO<sub>3-δ</sub> heterostructured thin films, *Journal of Physical Chemistry Letters*, 5 (2014) 1027-1034.
- [250] A. Gray, Y. Liu, H. Hong, T.C. Chiang, X-ray diffraction studies of trilayer oscillations in the preferred thickness of In films on Si(111), *Physical Review B*, 87 (2013) 195415.
- [251] M. Holt, M. Sutton, P. Zschack, H. Hong, T.C. Chiang, Dynamic fluctuations and static speckle in critical X-ray scattering from SrTiO<sub>3</sub>, *Physical Review Letters*, 98 (2007) 065501.
- [252] P.H. Fuoss, S. Brennan, Surface Sensitive X-Ray Scattering, *Annual Review of Materials Science*, 20 (1990) 365-390.
- [253] M. Brahlek, L. Zhang, C. Eaton, H.-T. Zhang, R. Engel-Herbert, Accessing a growth window for SrVO<sub>3</sub> thin films, *Applied Physics Letters*, 107 (2015) 143108.
- [254] H.T. Zhang, L.R. Dedon, L.W. Martin, R. Engel-Herbert, Self-regulated growth of LaVO<sub>3</sub> thin films by hybrid molecular beam epitaxy, *Applied Physics Letters*, 106 (2015) 233102.
- [255] K.L. Siefering, G.L. Griffin, Growth kinetics of CVD TiO<sub>2</sub>: influence of carrier gas, *Journal of the Electrochemical Society*, 137 (1990) 1206-1208.
- [256] Description of the open source Experimental Physics and Industrial Control System (EPICS) can be found at <http://www.aps.anl.gov/epics/>.
- [257] LabVIEW - National Instruments, National Instruments, 2017, [www.ni.com/en-us/shop/labview.html](http://www.ni.com/en-us/shop/labview.html).
- [258] A. Rahtu, M. Ritala, Reaction mechanism studies on titanium isopropoxide-water atomic layer deposition process, *Chemical Vapor Deposition*, 8 (2002) 21-28.
- [259] V.R. Anderson, A.S. Cavanagh, A.I. Abdulagatov, Z.M. Gibbs, S.M. George, Waterless TiO<sub>2</sub> atomic layer deposition using titanium tetrachloride and titanium tetraisopropoxide, *Journal of Vacuum Science & Technology A*, 32 (2014) 01A114.

- [260] M. Brahlek, A.S. Gupta, J. Lapano, J. Roth, H.T. Zhang, L. Zhang, R. Haislmaier, R. Engel - Herbert, Frontiers in the growth of complex oxide thin films: Past, present, and future of hybrid MBE, *Advanced Functional Materials*, 28 (2018) 1702772.
- [261] R.C. Haislmaier, E.D. Grimley, M.D. Biegalski, J.M. LeBeau, S. Troler - McKinstry, V. Gopalan, R. Engel - Herbert, Unleashing strain induced ferroelectricity in complex oxide thin films via precise stoichiometry control, *Advanced Functional Materials*, 26 (2016) 7271-7279.
- [262] C.A. Jackson, S. Stemmer, Interface-induced magnetism in perovskite quantum wells, *Physical Review B*, 88 (2013) 180403.
- [263] C.A. Jackson, J.Y. Zhang, C.R. Freeze, S. Stemmer, Quantum critical behaviour in confined SrTiO<sub>3</sub> quantum wells embedded in antiferromagnetic SmTiO<sub>3</sub>, *Nature Communications*, 5 (2014) 4258.
- [264] B. Jalan, J. Cagnon, T.E. Mates, S. Stemmer, Analysis of carbon in SrTiO<sub>3</sub> grown by hybrid molecular beam epitaxy, *Journal of Vacuum Science & Technology A: Vacuum, Surfaces, and Films*, 27 (2009) 1365-1368.
- [265] B. Jalan, R. Engel-Herbert, J. Cagnon, S. Stemmer, Growth modes in metal-organic molecular beam epitaxy of TiO<sub>2</sub> on r-plane sapphire, *Journal of Vacuum Science and Technology A: Vacuum, Surfaces and Films*, 27 (2009) 230-233.
- [266] Y. Matsubara, K.S. Takahashi, Y. Tokura, M. Kawasaki, Single-crystalline BaTiO<sub>3</sub> films grown by gas-source molecular beam epitaxy, *Applied Physics Express*, 7 (2014) 125502.
- [267] P. Moetakef, D.G. Ouellette, J.Y. Zhang, T.A. Cain, S.J. Allen, S. Stemmer, Growth and properties of GdTiO<sub>3</sub> films prepared by hybrid molecular beam epitaxy, *Journal of Crystal Growth*, 355 (2012) 166-170.
- [268] P. Moetakef, J.Y. Zhang, S. Raghavan, A.P. Kajdos, S. Stemmer, Growth window and effect of substrate symmetry in hybrid molecular beam epitaxy of a Mott insulating rare earth titanate, *Journal of Vacuum Science & Technology A: Vacuum, Surfaces, and Films*, 31 (2013) 041503.
- [269] J.A. Moyer, C. Eaton, R. Engel - Herbert, Highly conductive SrVO<sub>3</sub> as a bottom electrode for functional perovskite oxides, *Advanced Materials*, 25 (2013) 3578-3582.
- [270] A. Prakash, J. Dewey, H. Yun, J.S. Jeong, K.A. Mkhoyan, B. Jalan, Hybrid molecular beam epitaxy for the growth of stoichiometric BaSnO<sub>3</sub>, *Journal of Vacuum Science & Technology A: Vacuum, Surfaces, and Films*, 33 (2015) 060608.
- [271] A. Prakash, P. Xu, X. Wu, G. Haugstad, X. Wang, B. Jalan, Adsorption-controlled growth and the influence of stoichiometry on electronic transport in hybrid molecular beam epitaxy-grown BaSnO<sub>3</sub> films, *Journal of Materials Chemistry C*, 5 (2017) 5730-5736.
- [272] P. Xu, D. Phelan, J. Seok Jeong, K. Andre Mkhoyan, B. Jalan, Stoichiometry-driven metal-to-insulator transition in NdTiO<sub>3</sub>/SrTiO<sub>3</sub> heterostructures, *Applied Physics Letters*, 104 (2014) 082109.
- [273] H.-T. Zhang, M. Brahlek, X. Ji, S. Lei, J. Lapano, J.W. Freeland, V. Gopalan, R. Engel-Herbert, High-quality LaVO<sub>3</sub> films as solar energy conversion material, *ACS Applied Materials & Interfaces*, 9 (2017) 12556-12562.
- [274] L. Zhang, Y. Zhou, L. Guo, W. Zhao, A. Barnes, H.-T. Zhang, C. Eaton, Y. Zheng, M. Brahlek, H.F. Haneef, N.J. Podraza, M.H.W. Chan, V. Gopalan, K.M. Rabe, R. Engel-Herbert, Correlated metals as transparent conductors, *Nature Materials*, 15 (2016) 204-210.

- [275] M.C. Sullivan, M.J. Ward, A. Gutiérrez-Llorente, E.R. Adler, H. Joress, A. Woll, J.D. Brock, Complex oxide growth using simultaneous in situ reflection high-energy electron diffraction and X-ray reflectivity: When is one layer complete?, *Applied Physics Letters*, 106 (2015) 031604.
- [276] R. Boichot, L. Tian, M.-I. Richard, A. Crisci, A. Chaker, V. Cantelli, S. Coindeau, S. Lay, T. Ouled, C. Guichet, C.W. Chu, N. Aubert, G. Ciatto, E. Blanquet, O. Thomas, J.-L. Deschanvres, D.D. Fong, H. Renevier, Evolution of crystal structure during the initial stages of ZnO atomic layer deposition, *Chemistry of Materials*, 28 (2016) 592-600.
- [277] D.D. Fong, J.A. Eastman, S.K. Kim, T.T. Fister, M.J. Highland, P.M. Baldo, P.H. Fuoss, In situ synchrotron x-ray characterization of ZnO atomic layer deposition, *Applied Physics Letters*, 97 (2010) 191904.
- [278] F. Jiang, A. Munkholm, R.-V. Wang, S.K. Streiffer, C. Thompson, P.H. Fuoss, K. Latifi, K.R. Elder, G.B. Stephenson, Spontaneous oscillations and waves during chemical vapor deposition of InN, *Physical review letters*, 101 (2008) 086102.
- [279] M.V.R. Murty, S.K. Streiffer, G.B. Stephenson, J.A. Eastman, G.-R. Bai, A. Munkholm, O. Auciello, C. Thompson, In situ X-ray scattering study of PbTiO<sub>3</sub> chemical-vapor deposition, *Applied Physics Letters*, 80 (2002) 1809-1811.
- [280] M.-I. Richard, M.J. Highland, T.T. Fister, A. Munkholm, J. Mei, S.K. Streiffer, C. Thompson, P.H. Fuoss, G.B. Stephenson, In situ synchrotron X-ray studies of strain and composition evolution during metal-organic chemical vapor deposition of InGaN, *Applied Physics Letters*, 96 (2010) 051911.
- [281] R.-V. Wang, F. Jiang, D.D. Fong, G.B. Stephenson, P.H. Fuoss, J.A. Eastman, S.K. Streiffer, K. Latifi, C. Thompson, In situ X-ray studies of metal organic chemical vapor deposition of PbZr<sub>x</sub>Ti<sub>1-x</sub>O<sub>3</sub>, *Thin Solid Films*, 515 (2007) 5593-5596.
- [282] S.O. Hruszkewycz, M. Allain, M.V. Holt, C.E. Murray, J.R. Holt, P.H. Fuoss, V. Chamard, High-resolution three-dimensional structural microscopy by single-angle Bragg ptychography, *Nature materials*, 16 (2017) 244.
- [283] Y. Liang, D.A. Bonnell, Structures and chemistry of the annealed SrTiO<sub>3</sub> (001) surface, *Surface Science*, 310 (1994) 128-134.
- [284] K. Szot, W. Speier, Surfaces of reduced and oxidized SrTiO<sub>3</sub> from atomic force microscopy, *Physical Review B*, 60 (1999) 5909.
- [285] K. Szot, W. Speier, U. Breuer, R. Meyer, J. Szade, R. Waser, Formation of micro-crystals on the (100) surface of SrTiO<sub>3</sub> at elevated temperatures, *Surface Science*, 460 (2000) 112-128.
- [286] H. Wei, L. Beuermann, J. Helmbold, G. Borchardt, V. Kempter, G. Lilienkamp, W. Maus-Friedrichs, Study of SrO segregation on SrTiO<sub>3</sub> (100) surfaces, *Journal of the European Ceramic Society*, 21 (2001) 1677-1680.
- [287] K. Shibuya, S. Mi, C.-L. Jia, P. Meuffels, R. Dittmann, Sr<sub>2</sub>TiO<sub>4</sub> layered perovskite thin films grown by pulsed laser deposition, *Applied Physics Letters*, 92 (2008) 241918.
- [288] S. Yamamoto, T. Sumita, T. Yamaki, A. Miyashita, H. Naramoto, Characterization of epitaxial TiO<sub>2</sub> films prepared by pulsed laser deposition, *Journal of Crystal Growth*, 237 (2002) 569-573.
- [289] P. Buerger, D. Nurkowski, J. Akroyd, S. Mosbach, M. Kraft, First-principles thermochemistry for the thermal decomposition of titanium tetraisopropoxide, *The Journal of Physical Chemistry A*, 119 (2015) 8376-8387.

- [290] K.T. Jacob, G. Rajitha, Thermodynamic properties of strontium titanates:  $\text{Sr}_2\text{TiO}_4$ ,  $\text{Sr}_3\text{Ti}_2\text{O}_7$ ,  $\text{Sr}_4\text{Ti}_3\text{O}_{10}$ , and  $\text{SrTiO}_3$ , *The Journal of Chemical Thermodynamics*, 43 (2011) 51-57.
- [291] W. Ostwald, Studien über die Bildung und Umwandlung fester Körper, *Zeitschrift für physikalische Chemie*, 22 (1897) 289-330.
- [292] R.A. Van Santen, The Ostwald step rule, *The Journal of Physical Chemistry*, 88 (1984) 5768-5769.
- [293] T. Threlfall, Structural and thermodynamic explanations of Ostwald's rule, *Organic process research & development*, 7 (2003) 1017-1027.
- [294] E.J. Essene, D.R. Peacor, Clay mineral thermometry- a critical perspective, *Clays and Clay Minerals*, 43 (1995) 540-553.
- [295] A. Levin, T.O. Mason, L. Adler-Abramovich, A.K. Buell, G. Meisl, C. Galvagnion, Y. Bram, S.A. Stratford, C.M. Dobson, T.P.J. Knowles, E. Gazit, Ostwald's rule of stages governs structural transitions and morphology of dipeptide supramolecular polymers, *Nature Communications*, 5 (2014) 5219.
- [296] P.R. ten Wolde, D. Frenkel, Homogeneous nucleation and the Ostwald step rule, *Physical Chemistry Chemical Physics*, 1 (1999) 2191-2196.
- [297] M. Yoshioka, B.C. Hancock, G. Zografi, Crystallization of indomethacin from the amorphous state below and above its glass transition temperature, *Journal of Pharmaceutical Sciences*, 83 (1994) 1700-1705.
- [298] B.M. Shi, M.H. Xie, H.S. Wu, N. Wang, S.Y. Tong, Transition between wurtzite and zinc-blende GaN: An effect of deposition condition of molecular-beam epitaxy, *Applied Physics Letters*, 89 (2006) 151921.
- [299] D.P. Bertsekas, *Nonlinear programming*, Athena Scientific, Belmont, Massachusetts, 1999.
- [300] D.P. Bertsekas, *Constrained optimization and Lagrange multiplier methods*, Academic Press, New York, New York, 2014.
- [301] C.T. Kelley, *Iterative methods for optimization*, Siam, Philadelphia, Pennsylvania, 1999.
- [302] J. Nocedal, S. Wright, *Numerical optimization*, Springer, New York, USA, 2006.
- [303] A. Baldereschi, E. Tosatti, Dielectric band structure of solids, *Solid State Communications*, 29 (1979) 131-135.
- [304] R. Car, E. Tosatti, S. Baroni, S. Leelaprute, Dielectric band structure of crystals: General properties and calculations for silicon, *Physical Review B*, 24 (1981) 985.
- [305] J.D. Castro, R.B. Muniz, L.E. Oliveira, A model calculation of the dielectric band structure of diamond and silicon, *Physica Status Solidi (b)*, 158 (1990) 743-752.
- [306] S. Galamic - Mulaomerovic, C.D. Hogan, C.H. Patterson, Eigenfunctions of the inverse dielectric functions and response functions of silicon and argon, *Physica Status Solidi (a)*, 188 (2001) 1291-1296.
- [307] K.-M. Ho, J. Ihm, J.D. Joannopoulos, Dielectric matrix scheme for fast convergence in self-consistent electronic-structure calculations, *Physical Review B*, 25 (1982) 4260.
- [308] M.S. Hybertsen, S.G. Louie, Ab initio static dielectric matrices from the density-functional approach. I. Formulation and application to semiconductors and insulators, *Physical Review B*, 35 (1987) 5585.
- [309] H.F. Wilson, D. Lu, F. Gygi, G. Galli, Iterative calculations of dielectric eigenvalue spectra, *Physical Review B*, 79 (2009) 245106.

- [310] F. Tran, P. Blaha, K. Schwarz, P. Novák, Hybrid exchange-correlation energy functionals for strongly correlated electrons: Applications to transition-metal monoxides, *Physical Review B*, 74 (2006) 155108.
- [311] J. Jeong, N. Aetukuri, T. Graf, T.D. Schladt, M.G. Samant, S.S. Parkin, Suppression of metal-insulator transition in VO<sub>2</sub> by electric field-induced oxygen vacancy formation, *Science*, 339 (2013) 1402-1405.
- [312] M. Nakano, K. Shibuya, D. Okuyama, T. Hatano, S. Ono, M. Kawasaki, Y. Iwasa, Y. Tokura, Collective bulk carrier delocalization driven by electrostatic surface charge accumulation, *Nature*, 487 (2012) 459.
- [313] H. Paik, J.A. Moyer, T. Spila, J.W. Tashman, J.A. Mundy, E. Freeman, N. Shukla, J.M. Lapano, R. Engel-Herbert, W. Zander, J. Schubert, Transport properties of ultra-thin VO<sub>2</sub> films on (001) TiO<sub>2</sub> grown by reactive molecular-beam epitaxy, *Applied Physics Letters*, 107 (2015) 163101.
- [314] T. Driscoll, H.-T. Kim, B.-G. Chae, B.-J. Kim, Y.-W. Lee, N.M. Jokerst, S. Palit, D.R. Smith, M. Di Ventra, D.N. Basov, Memory metamaterials, *Science*, 325 (2009) 1518-1521.
- [315] H. Jerominek, F. Picard, N.R. Swart, M. Renaud, M. Levesque, M. Lehoux, J.-S. Castonguay, M. Pelletier, G. Bilodeau, D. Audet, Micromachined uncooled VO<sub>2</sub>-based IR bolometer arrays, in: *Infrared Detectors and Focal Plane Arrays IV*, International Society for Optics and Photonics, 1996, pp. 60-72.
- [316] N. Shukla, A. Parihar, E. Freeman, H. Paik, G. Stone, V. Narayanan, H. Wen, Z. Cai, V. Gopalan, R. Engel-Herbert, D.G. Schlom, A. Raychowdhury, S. Datta, Synchronized charge oscillations in correlated electron systems, *Scientific Reports*, 4 (2014) 4964.
- [317] A. Fujimori, I. Hase, H. Namatame, Y. Fujishima, Y. Tokura, H. Eisaki, S. Uchida, K. Takegahara, F.M.F. De Groot, Evolution of the spectral function in Mott-Hubbard systems with d 1 configuration, *Physical Review Letters*, 69 (1992) 1796.
- [318] M. Gu, S.A. Wolf, J. Lu, Two - dimensional Mott insulators in SrVO<sub>3</sub> ultrathin films, *Advanced Materials Interfaces*, 1 (2014) 1300126.
- [319] V. Pardo, W.E. Pickett, Electron confinement, orbital ordering, and orbital moments in d<sup>0</sup>-d<sup>1</sup> oxide heterostructures, *Physical Review B*, 81 (2010) 245117.
- [320] J.H. Park, J.M. Coy, T.S. Kasirga, C. Huang, Z. Fei, S. Hunter, D.H. Cobden, Measurement of a solid-state triple point at the metal-insulator transition in VO<sub>2</sub>, *Nature*, 500 (2013) 431.
- [321] K. Yoshimatsu, K. Horiba, H. Kumigashira, T. Yoshida, A. Fujimori, M. Oshima, Metallic quantum well states in artificial structures of strongly correlated oxide, *Science*, 333 (2011) 319-322.
- [322] K. Yoshimatsu, T. Okabe, H. Kumigashira, S. Okamoto, S. Aizaki, A. Fujimori, M. Oshima, Dimensional-crossover-driven metal-insulator transition in SrVO<sub>3</sub> ultrathin films, *Physical Review Letters*, 104 (2010) 147601.
- [323] K. Byczuk, W. Hofstetter, D. Vollhardt, Mott-hubbard transition versus Anderson localization in correlated electron systems with disorder, *Physical Review Letters*, 94 (2005) 056404.
- [324] E. Freeman, G. Stone, N. Shukla, H. Paik, J.A. Moyer, Z. Cai, H. Wen, R. Engel-Herbert, D.G. Schlom, V. Gopalan, S. Datta, Nanoscale structural evolution of electrically driven insulator to metal transition in vanadium dioxide, *Applied Physics Letters*, 103 (2013) 263109.

- [325] P.A. Lee, T.V. Ramakrishnan, Disordered electronic systems, *Reviews of Modern Physics*, 57 (1985) 287.
- [326] X. Chen, E. Pomerantseva, K. Gregorczyk, R. Ghodssi, G. Rubloff, Cathodic ALD  $V_2O_5$  thin films for high-rate electrochemical energy storage, *RSC Advances*, 3 (2013) 4294-4302.
- [327] N.K. Nandakumar, E.G. Seebauer, Low temperature chemical vapor deposition of nanocrystalline  $V_2O_5$  thin films, *Thin Solid Films*, 519 (2011) 3663-3668.
- [328] K.L. Siefering, G.L. Griffin, Chemical vapor deposition of vanadium oxide thin films, *Journal of The Electrochemical Society*, 136 (1989) 897-898.
- [329] C. Eaton, J.A. Moyer, H.M. Alipour, E.D. Grimley, M. Brahlek, J.M. LeBeau, R. Engel-Herbert, Growth of  $SrVO_3$  thin films by hybrid molecular beam epitaxy, *Journal of Vacuum Science & Technology A: Vacuum, Surfaces, and Films*, 33 (2015) 061504.
- [330] H.-T. Zhang, C. Eaton, H. Ye, R. Engel-Herbert, Phase stabilization of  $VO_2$  thin films in high vacuum, *Journal of Applied Physics*, 118 (2015) 185306.
- [331] H. Katzke, P. Tolédano, W. Depmeier, Theory of morphotropic transformations in vanadium oxides, *Physical Review B*, 68 (2003) 024109.

## Appendix A

### \*.cif Files for RT7 and RT13 Structure Solutions

#### RT7a:

```

data_Wien2k_Data
_cell_length_a    14.634685
_cell_length_b    14.634685
_cell_length_c    24.174980
_cell_angle_alpha  90.000000
_cell_angle_beta   90.000000
_cell_angle_gamma 120.000000
_cell_measurement_temperature 0.0
_diffrn_ambient_temperature 0.0
_symmetry_space_group_name_H-M      'P-3      '
_symmetry_space_group_number 147

_refine_date  '12- 2-2018'
_refine_method 'generated from Wien2k code'
_refine_special_details
;
Structure converted from Wien2k struct file, Version 9.1
Title 'rt7a'
;

loop_
_symmetry_equiv_pos_as_xyz
  +x,+y,+z
  -y,+x-y,+z
  -x+y,-x,+z
  -x,-y,-z
  +y,-x+y,-z
  +x-y,+x,-z
loop_
_atom_site_label
_atom_site_type_symbol
_atom_site_fract_x
_atom_site_fract_y
_atom_site_fract_z
_atom_site_U_iso_or_equiv
Ti001  Ti  0.71447945  0.14286449  0.99846405  0.05000000
Ti002  Ti  0.00000000  0.00000000  0.00000000  0.05000000
Ti003  Ti  0.90659344  0.38282917  0.09163983  0.05000000
Ti004  Ti  0.33333333  0.66666667  0.09368496  0.05000000
Ti005  Ti  0.80859639  0.75866821  0.90338976  0.05000000
Ti006  Ti  0.38609637  0.48267147  0.19310085  0.05000000
Ti007  Ti  0.66666667  0.33333333  0.17774589  0.05000000
Ti008  Ti  0.24065532  0.04840018  0.18033042  0.05000000
Ti009  Ti  0.00000000  0.00000000  0.29171413  0.05000000
Ti010  Ti  0.66666667  0.33333333  0.29377125  0.05000000
Ti011  Ti  0.22211882  0.07185270  0.29404308  0.05000000
Ti012  Ti  0.43264184  0.27938523  0.27562812  0.05000000
Sr013  Sr  0.95119708  0.18760688  0.04177669  0.05000000
Sr014  Sr  0.42560820  0.29005182  0.13590223  0.05000000

```



```

Sr015  Sr  0.92471863  0.38893781  0.23077967  0.05000000
Sr016  Sr  0.33333333  0.66666667  0.23524678  0.05000000
Sr017  Sr  0.80337261  0.71921718  0.74830863  0.05000000
Sr018  Sr  0.15685552  0.43967639  0.14578257  0.05000000
Sr019  Sr  0.00000000  0.00000000  0.14037507  0.05000000
Sr020  Sr  0.52376137  0.90413581  0.04891899  0.05000000
Sr021  Sr  0.66666667  0.33333333  0.04313734  0.05000000
O0022  O   0.28687257  0.35300207  0.14276780  0.05000000
O0023  O   0.12665427  0.92167254  0.15438174  0.05000000
O0024  O   0.20916863  0.63424211  0.13703282  0.05000000
O0025  O   0.01658193  0.49981158  0.85969515  0.05000000
O0026  O   0.65402649  0.95642274  0.85999091  0.05000000
O0027  O   0.67215074  0.82369356  0.05350419  0.05000000
O0028  O   0.39700842  0.86532882  0.95223279  0.05000000
O0029  O   0.30749549  0.26989936  0.04437826  0.05000000
O0030  O   0.29794356  0.75340902  0.04498932  0.05000000
O0031  O   0.77746248  0.42971285  0.23167414  0.05000000
O0032  O   0.82357147  0.25529953  0.04467827  0.05000000
O0033  O   0.57864639  0.60527975  0.04398733  0.05000000
O0034  O   0.66950793  0.44588266  0.13595403  0.05000000
O0035  O   0.10765648  0.50875998  0.22606939  0.05000000
O0036  O   0.19435326  0.73200326  0.23033128  0.05000000
O0037  O   0.81383130  0.64246587  0.22451270  0.05000000
O0038  O   0.13385986  0.07973345  0.23965473  0.05000000
O0039  O   0.01918864  0.26900106  0.25233389  0.05000000
O0040  O   0.97410179  0.59189483  0.24459255  0.05000000
O0041  O   0.87934153  0.96991283  0.04825351  0.05000000
O0042  O   0.86302376  0.08441221  0.13233904  0.05000000
O0043  O   0.02301493  0.12351860  0.33008054  0.05000000
O0044  O   0.30616597  0.20792814  0.32103354  0.05000000
O0045  O   0.72841731  0.47420485  0.32058708  0.05000000
#End data_Wien2k_Data

```

**RT7b:**

```

data_Wien2k_Data
_cell_length_a  14.634685
_cell_length_b  14.634685
_cell_length_c  24.174980
_cell_angle_alpha  90.000000
_cell_angle_beta  90.000000
_cell_angle_gamma 120.000000
_cell_measurement_temperature 0.0
_diffraction_temperature 0.0
_symmetry_space_group_name_H-M      'P-3      '
_symmetry_space_group_number 147

_refine_date  ' 5-10-2017'
_refine_method 'generated from Wien2k code'
_refine_special_details
;
Structure converted from Wien2k struct file, Version 9.1
Title 'rt7b'
;

```

```

loop_
_symmetry_equiv_pos_as_xyz
  +x,+y,+z
  -y,+x-y,+z
  -x+y,-x,+z
  -x,-y,-z
  +y,-x+y,-z
  +x-y,+x,-z
loop_
_atom_site_label
_atom_site_type_symbol
_atom_site_fract_x
_atom_site_fract_y
_atom_site_fract_z
_atom_site_U_iso_or_equiv
Ti001  Ti  0.71639216  0.14324560  0.00017942  0.05000000
Ti002  Ti  0.00000000  0.00000000  0.00000000  0.05000000
Ti003  Ti  0.90560865  0.37933317  0.09356082  0.05000000
Ti004  Ti  0.33333333  0.66666667  0.09167136  0.05000000
Ti005  Ti  0.81320111  0.76437552  0.90490048  0.05000000
Ti006  Ti  0.38033916  0.48026641  0.17914369  0.05000000
Ti007  Ti  0.66666667  0.33333333  0.17612934  0.05000000
Ti008  Ti  0.23760301  0.04873316  0.19407383  0.05000000
Ti009  Ti  0.66666667  0.33333333  0.29577992  0.05000000
Ti010  Ti  0.44805785  0.30194677  0.27718687  0.05000000
Ti011  Ti  0.38868760  0.47894094  0.29601003  0.05000000
Ti012  Ti  0.16628561  0.44774691  0.27773469  0.05000000
Sr013  Sr  0.38049378  0.47455817  0.04383966  0.05000000
Sr014  Sr  0.86446764  0.58054835  0.13749237  0.05000000
Sr015  Sr  0.45973338  0.08805307  0.23502318  0.05000000
Sr016  Sr  0.95053032  0.17077639  0.75779994  0.05000000
Sr017  Sr  0.28376227  0.85981629  0.13887872  0.05000000
Sr018  Sr  0.00000000  0.00000000  0.84439798  0.05000000
Sr019  Sr  0.66666667  0.33333333  0.04312645  0.05000000
Sr020  Sr  0.23451290  0.04796138  0.04810303  0.05000000
O0021  O   0.63403344  0.91102790  0.13591569  0.05000000
O0022  O   0.06982996  0.20777191  0.14539737  0.05000000
O0023  O   0.38278762  0.58410006  0.13085537  0.05000000
O0024  O   0.50264576  0.51918939  0.85941095  0.05000000
O0025  O   0.05935770  0.70332459  0.85540788  0.05000000
O0026  O   0.17259625  0.85129193  0.04731196  0.05000000
O0027  O   0.13293200  0.53280629  0.95272251  0.05000000
O0028  O   0.72675915  0.03881829  0.04780322  0.05000000
O0029  O   0.25159543  0.54202383  0.04287376  0.05000000
O0030  O   0.57082820  0.35296375  0.23141902  0.05000000
O0031  O   0.74439302  0.56837856  0.04656687  0.05000000
O0032  O   0.55537024  0.22621149  0.13661270  0.05000000
O0033  O   0.42183071  0.90694079  0.23251722  0.05000000
O0034  O   0.50754827  0.78648378  0.22758245  0.05000000
O0035  O   0.82474856  0.17597166  0.23930500  0.05000000
O0036  O   0.90517138  0.87027946  0.23585752  0.05000000
O0037  O   0.25803104  0.93866721  0.24202807  0.05000000
O0038  O   0.63084383  0.00437455  0.23271370  0.05000000
O0039  O   0.38897561  0.97022882  0.04782843  0.05000000

```

```

O0040 O 0.46078812 0.61363778 0.32790693 0.05000000
O0041 O 0.46470947 0.41428319 0.32218282 0.05000000
O0042 O 0.01444121 0.89870444 0.04731549 0.05000000
O0043 O 0.92460425 0.77367620 0.14302323 0.05000000
O0044 O 0.72655095 0.47451564 0.31864218 0.05000000
O0045 O 0.24529037 0.39752637 0.31805565 0.05000000
#End data_Wien2k_Data

```

### RT13a:

```

data_Wien2k_Data
_cell_length_a 19.943713
_cell_length_b 19.943713
_cell_length_c 24.186845
_cell_angle_alpha 90.000000
_cell_angle_beta 90.000000
_cell_angle_gamma 120.000000
_cell_measurement_temperature 0.0
_diffraction_ambient_temperature 0.0
_symmetry_space_group_name_H-M 'P-3'
_symmetry_space_group_number 147

_refine_date '12- 2-2018'
_refine_method 'generated from Wien2k code'
_refine_special_details
;
Structure converted from Wien2k struct file, Version 9.1
Title 'rt13a'
;

loop_
_symmetry_equiv_pos_as_xyz
+x,+y,+z
-y,+x-y,+z
-x+y,-x,+z
-x,-y,-z
+y,-x+y,-z
+x-y,+x,-z
loop_
_atom_site_label
_atom_site_type_symbol
_atom_site_fract_x
_atom_site_fract_y
_atom_site_fract_z
_atom_site_U_iso_or_equiv
O0001 O 0.22340310 0.21900732 0.04774593 0.05000000
O0002 O 0.14901262 0.39166970 0.05009195 0.05000000
O0003 O 0.16804902 0.53994566 0.04211745 0.05000000
O0004 O 0.29912330 0.52249972 0.04688048 0.05000000
O0005 O 0.40614182 0.47105462 0.04556120 0.05000000
O0006 O 0.16748671 0.12768716 0.14013093 0.05000000
O0007 O 0.26137414 0.06167558 0.13542610 0.05000000
O0008 O 0.38791491 0.03975877 0.14513500 0.05000000
O0009 O 0.49950554 0.98949216 0.14537902 0.05000000
O0010 O 0.03486548 0.13815380 0.13704865 0.05000000

```

O0011	O	0.17693534	0.27352446	0.13705630	0.05000000
O0012	O	0.07569228	0.08567567	0.04628455	0.05000000
O0013	O	0.41162578	0.19063543	0.14363784	0.05000000
O0014	O	0.65254567	0.11180004	0.14480236	0.05000000
O0015	O	0.11625802	0.45595317	0.14245415	0.05000000
O0016	O	0.24364152	0.43706264	0.14194404	0.05000000
O0017	O	0.33649730	0.37140841	0.13224146	0.05000000
O0018	O	0.57347257	0.30074881	0.14230786	0.05000000
O0019	O	0.25657798	0.58370971	0.13556942	0.05000000
O0020	O	0.09634734	0.04049016	0.23372662	0.05000000
O0021	O	0.25164042	0.12606906	0.23378224	0.05000000
O0022	O	0.47249943	0.05368709	0.23769768	0.05000000
O0023	O	0.09057123	0.23257722	0.04292425	0.05000000
O0024	O	0.32962472	0.43413778	0.23381261	0.05000000
O0025	O	0.17751451	0.35015544	0.23399524	0.05000000
O0026	O	0.25525312	0.27373547	0.22729147	0.05000000
O0027	O	0.50251425	0.21013408	0.23439524	0.05000000
O0028	O	0.38970889	0.25906048	0.24464517	0.05000000
O0029	O	0.55158310	0.36854612	0.23473095	0.05000000
O0030	O	0.46573402	0.57060706	0.23924538	0.05000000
O0031	O	0.63343816	0.68615405	0.24282930	0.05000000
O0032	O	0.78931387	0.81912335	0.23116003	0.05000000
O0033	O	0.25822188	0.67256095	0.23110030	0.05000000
O0034	O	0.30273196	0.00916195	0.04680440	0.05000000
O0035	O	0.32578788	0.16080836	0.04769765	0.05000000
O0036	O	0.44941506	0.13554633	0.04772217	0.05000000
O0037	O	0.55417880	0.08482967	0.05222706	0.05000000
O0038	O	0.67999702	0.06408864	0.04431315	0.05000000
O0039	O	0.60844957	0.24303853	0.04773991	0.05000000
O0040	O	0.23146619	0.60050489	0.31925597	0.05000000
O0041	O	0.01136549	0.09170228	0.32567698	0.05000000
O0042	O	0.29403502	0.46524881	0.32376729	0.05000000
O0043	O	0.32118597	0.32601531	0.31932373	0.05000000
O0044	O	0.93648021	0.78147488	0.32452528	0.05000000
O0045	O	0.76903161	0.74956356	0.31991147	0.05000000
O0046	O	0.69293154	0.84717658	0.32838004	0.05000000
Sr047	Sr	0.41252402	0.97597567	0.04712501	0.05000000
Sr048	Sr	0.31315926	0.23207466	0.13939952	0.05000000
Sr049	Sr	0.38686076	0.53511080	0.13436968	0.05000000
Sr050	Sr	0.07469536	0.31185851	0.13771918	0.05000000
Sr051	Sr	0.18337370	0.05226593	0.04481759	0.05000000
Sr052	Sr	0.61487698	0.45787192	0.15730338	0.05000000
Sr053	Sr	0.12253724	0.17056730	0.22634739	0.05000000
Sr054	Sr	0.37633101	0.10366913	0.24432064	0.05000000
Sr055	Sr	0.58840729	0.04333438	0.24443261	0.05000000
Sr056	Sr	0.66666667	0.33333333	0.24039864	0.05000000
Sr057	Sr	0.19398270	0.48118710	0.23044943	0.05000000
Sr058	Sr	0.49035767	0.28234214	0.05466797	0.05000000
Sr059	Sr	0.26012617	0.36202643	0.04123085	0.05000000
Sr060	Sr	0.33333333	0.66666667	0.03845031	0.05000000
Sr061	Sr	0.00000000	0.00000000	0.13647476	0.05000000
Ti062	Ti	0.07773708	0.31039017	0.99918369	0.05000000
Ti063	Ti	0.38544154	0.53954739	0.99611116	0.05000000
Ti064	Ti	0.94775272	0.12877775	0.90993003	0.05000000

```

Ti065  Ti  0.25864529  0.36147561  0.90313365  0.05000000
Ti066  Ti  0.56189766  0.59044409  0.90424593  0.05000000
Ti067  Ti  0.48743747  0.28319946  0.90955976  0.05000000
Ti068  Ti  0.54052539  0.16823973  0.72294611  0.05000000
Ti069  Ti  0.23415782  0.93754333  0.72052873  0.05000000
Ti070  Ti  0.00000000  0.00000000  0.29274946  0.05000000
Ti071  Ti  0.18099027  0.05445116  0.29775940  0.05000000
Ti072  Ti  0.07392080  0.29647914  0.28104598  0.05000000
Ti073  Ti  0.25497345  0.36446106  0.29755403  0.05000000
Ti074  Ti  0.17932902  0.05161479  0.17990017  0.05000000
Ti075  Ti  0.48673309  0.28003043  0.19784764  0.05000000
Ti076  Ti  0.25502792  0.35864467  0.17849382  0.05000000
Ti077  Ti  0.33333333  0.66666667  0.17483534  0.05000000
Ti078  Ti  0.56138562  0.58702459  0.19298334  0.05000000
Ti079  Ti  0.33333333  0.66666667  0.90038570  0.05000000
Ti080  Ti  0.66666667  0.33333333  0.70473539  0.05000000
Ti081  Ti  0.00000000  0.00000000  0.00000000  0.05000000
#End data_Wien2k_Data

```

### RT13b:

```

data_Wien2k_Data
_cell_length_a  19.943713
_cell_length_b  19.943713
_cell_length_c  24.186845
_cell_angle_alpha  90.000000
_cell_angle_beta  90.000000
_cell_angle_gamma  120.000000
_cell_measurement_temperature 0.0
_diffrn_ambient_temperature 0.0
_symmetry_space_group_name_H-M      'P-3      '
_symmetry_space_group_number  147

_refine_date  ' 5-10-2017'
_refine_method 'generated from Wien2k code'
_refine_special_details
;
Structure converted from Wien2k struct file, Version 9.1
Title 'rt13b'
;

loop_
_symmetry_equiv_pos_as_xyz
  +x,+y,+z
  -y,+x-y,+z
  -x+y,-x,+z
  -x,-y,-z
  +y,-x+y,-z
  +x-y,+x,-z
loop_
_atom_site_label
_atom_site_type_symbol
_atom_site_fract_x
_atom_site_fract_y
_atom_site_fract_z

```

_atom_site_U_iso_or_equiv					
O0001	O	0.22279274	0.21903112	0.04633844	0.05000000
O0002	O	0.15211983	0.39306663	0.04814111	0.05000000
O0003	O	0.17215720	0.54069499	0.03966657	0.05000000
O0004	O	0.30211234	0.52435590	0.04905888	0.05000000
O0005	O	0.41004498	0.47496193	0.04809209	0.05000000
O0006	O	0.16840656	0.12615603	0.13834259	0.05000000
O0007	O	0.26483833	0.06126693	0.13831699	0.05000000
O0008	O	0.40079520	0.05015595	0.14250427	0.05000000
O0009	O	0.50347428	0.99364592	0.15140464	0.05000000
O0010	O	0.03616772	0.14043627	0.13818950	0.05000000
O0011	O	0.18067256	0.27367909	0.13762604	0.05000000
O0012	O	0.07447897	0.08644393	0.04625715	0.05000000
O0013	O	0.41107954	0.19210599	0.14110765	0.05000000
O0014	O	0.65465533	0.11445879	0.14226759	0.05000000
O0015	O	0.11079716	0.45462870	0.13507035	0.05000000
O0016	O	0.24213872	0.43552265	0.14196033	0.05000000
O0017	O	0.33733951	0.37207943	0.13273658	0.05000000
O0018	O	0.57454321	0.30270898	0.14268058	0.05000000
O0019	O	0.25739847	0.58150237	0.13787004	0.05000000
O0020	O	0.09608054	0.04232012	0.23261974	0.05000000
O0021	O	0.25201275	0.12900596	0.23324418	0.05000000
O0022	O	0.45859558	0.03712394	0.25269808	0.05000000
O0023	O	0.09094544	0.23340417	0.04454628	0.05000000
O0024	O	0.33415893	0.43619959	0.23413092	0.05000000
O0025	O	0.17798082	0.35184149	0.23459956	0.05000000
O0026	O	0.25532624	0.27629442	0.23052766	0.05000000
O0027	O	0.49899520	0.20619219	0.23057142	0.05000000
O0028	O	0.38947673	0.25861590	0.24376870	0.05000000
O0029	O	0.55003029	0.36944773	0.23445305	0.05000000
O0030	O	0.47853825	0.59145138	0.23676740	0.05000000
O0031	O	0.63809979	0.68504232	0.22880399	0.05000000
O0032	O	0.78995097	0.81493584	0.23377726	0.05000000
O0033	O	0.25224375	0.66171884	0.23387942	0.05000000
O0034	O	0.30275276	0.00753164	0.04879661	0.05000000
O0035	O	0.32237818	0.15906259	0.04756480	0.05000000
O0036	O	0.44735849	0.13608506	0.04350036	0.05000000
O0037	O	0.55284101	0.08456985	0.05277963	0.05000000
O0038	O	0.67901139	0.06207087	0.04373559	0.05000000
O0039	O	0.60543741	0.24293013	0.04850342	0.05000000
O0040	O	0.23283608	0.60512198	0.32646767	0.05000000
O0041	O	0.01474744	0.09398549	0.32291323	0.05000000
O0042	O	0.45491985	0.52148111	0.32643963	0.05000000
O0043	O	0.28361206	0.45955860	0.32107001	0.05000000
O0044	O	0.32422501	0.32511008	0.32008256	0.05000000
O0045	O	0.93407337	0.78117520	0.32452556	0.05000000
O0046	O	0.76734596	0.74804862	0.32157260	0.05000000
O0047	O	0.60172036	0.69604149	0.32614856	0.05000000
O0048	O	0.71106702	0.86466484	0.32263883	0.05000000
Sr049	Sr	0.41150837	0.97430869	0.04280892	0.05000000
Sr050	Sr	0.31133735	0.23204385	0.13932133	0.05000000
Sr051	Sr	0.38685330	0.53660447	0.13983025	0.05000000
Sr052	Sr	0.07763575	0.30908309	0.13927969	0.05000000
Sr053	Sr	0.18090373	0.05132369	0.04489361	0.05000000

Sr054	Sr	0.61419781	0.45383074	0.15374637	0.05000000
Sr055	Sr	0.12114517	0.17388060	0.23546028	0.05000000
Sr056	Sr	0.36677492	0.10382542	0.23490218	0.05000000
Sr057	Sr	0.59007019	0.04257577	0.25512758	0.05000000
Sr058	Sr	0.66666667	0.33333333	0.23828861	0.05000000
Sr059	Sr	0.20883373	0.48446561	0.23038637	0.05000000
Sr060	Sr	0.49019270	0.28284792	0.05403900	0.05000000
Sr061	Sr	0.26017950	0.36097367	0.04346507	0.05000000
Sr062	Sr	0.33333333	0.66666667	0.04049301	0.05000000
Sr063	Sr	0.00000000	0.00000000	0.14024102	0.05000000
Ti064	Ti	0.07753145	0.30935961	0.00025950	0.05000000
Ti065	Ti	0.38528767	0.53922931	0.99709478	0.05000000
Ti066	Ti	0.94900227	0.12934719	0.90845102	0.05000000
Ti067	Ti	0.25625858	0.36061422	0.90584224	0.05000000
Ti068	Ti	0.56186641	0.59095491	0.90315780	0.05000000
Ti069	Ti	0.48867391	0.28187514	0.91067939	0.05000000
Ti070	Ti	0.53710455	0.15952889	0.70997426	0.05000000
Ti071	Ti	0.59822177	0.05158804	0.70441540	0.05000000
Ti072	Ti	0.23242784	0.93577305	0.71957591	0.05000000
Ti073	Ti	0.00000000	0.00000000	0.29094210	0.05000000
Ti074	Ti	0.18189898	0.05139561	0.29755354	0.05000000
Ti075	Ti	0.07722142	0.30639158	0.28828789	0.05000000
Ti076	Ti	0.25412773	0.35900141	0.29707562	0.05000000
Ti077	Ti	0.17920267	0.05070887	0.18109790	0.05000000
Ti078	Ti	0.48579415	0.28020857	0.19711786	0.05000000
Ti079	Ti	0.25677672	0.35950375	0.18026785	0.05000000
Ti080	Ti	0.33333333	0.66666667	0.18026669	0.05000000
Ti081	Ti	0.56609338	0.59274548	0.18288440	0.05000000
Ti082	Ti	0.33333333	0.66666667	0.90134139	0.05000000
Ti083	Ti	0.66666667	0.33333333	0.70152975	0.05000000
Ti084	Ti	0.00000000	0.00000000	0.00000000	0.05000000

#End data\_Wien2k\_Data